Investigation of Correlation Functions in Low-Dimensional Quantum Antiferromagnets by Quantum Monte Carlo Methods

Inaugural-Dissertation

zur

Erlangung des Doktorgrades

der Mathematisch-Naturwissenschaftlichen Fakultät

der Universität zu Köln

vorgelegt von

Carsten Hinrich Aits

aus Wermelskirchen

2005

Contents

1. Motivation

The theoretical description of strongly correlated electron systems is a major challenge in solid state physics. In these systems, the local interaction between the electrons leads to the formation of a collective, strongly interacting ensemble, whose properties cannot be described in a simple one-electron picture. As a result, even a small change in an external parameter such as doping, pressure, or a magnetic field can have a dramatic effect on the nature of both the ground state and the elementary excitations of the system [Sac00]. Apart from the influence of thermal fluctuations, this effect leads to a rich variety of competing phases in the phase diagrams of strongly correlated materials. Prominent examples are the high-temperature copper oxide superconductors [BM86, OM00, Sac03] or the manganese oxides as a prototype for the occurrence of colossal magnetoresistance [TN00].

In connection with these phenomena, the understanding of the distinct physical properties of *Mott insulators* is of significant importance [And87]. A Mott insulating phase is found to exist in many transition metal oxides. Although these materials have a partially filled electron band at the Fermi surface, they are good insulators, because correlations in the motion of the electrons induced by their Coulomb interaction lead to localization effects. The important difference to the usual band insulator is that the internal degrees of freedom, spin and orbital, survive in the Mott insulator, giving rise to interesting collective behavior. In many cases, the low energy physics of the system is well described by an effective magnetic model in a low-dimensional geometry, which is a consequence of spatial anisotropies in the crystal structure. For example, a two-dimensional magnetic structure is found in the undoped parent compounds of the high-temperature superconductors such as La_2CuO_4 [EYB$^+$88, YKE$^+$89].

To illustrate these features, it is instructive to consider the *Hubbard model*, which is a generic model to describe the motion of the conduction band electrons in the atomic limit [Gut63, Hub63, Aue94]. In the case of there being only one electron band at the Fermi surface, one can neglect the orbital degrees of freedom, and the Hubbard Hamiltonian reads

$$H = - \sum_{\vec{r},\vec{r}',s} t(\vec{r},\vec{r}')\, c_{\vec{r}s}^{\dagger} c_{\vec{r}'s} + U \sum_{\vec{r}} n_{\vec{r}\uparrow} n_{\vec{r}\downarrow}. \tag{1.0.1}$$

Here the first term describes hopping processes of the electrons with spin s according to the site-dependent hopping integral $t(\vec{r},\vec{r}')$. In the *tight binding limit*, one retains a minimal set of short-range hopping amplitudes $t(\vec{r},\vec{r}')$ on the lattice. The second term in Eq. (1.0.1) stems from the Coulomb repulsion of the electrons and penalizes double occupancies of the individual lattice sites. In particular for a half-filled band and in the limit of large Coulomb repulsion U, a Mott-insulating state with one electron per site is energetically favored. In this case and in the leading

order in $\frac{t}{U}$, an expansion of the Hamiltonian (1.0.1) yields the *spin-$\frac{1}{2}$ Heisenberg model*

$$H = \sum_{\vec{r},\vec{r}'} J(\vec{r},\vec{r}')\,\vec{S}_{\vec{r}}\vec{S}_{\vec{r}'}, \tag{1.0.2}$$

where the site-dependent antiferromagnetic exchange integral is given by $J(\vec{r},\vec{r}') = 2t(\vec{r},\vec{r}')^2/U$ in terms of the original parameters. Evidently, the effective dimension of the spin system (1.0.2) is reduced if the crystal structure disadvantages hopping processes of electrons along certain lattice directions. Furthermore, only short-range Heisenberg interactions survive in the tight binding approximation.

In recent years, the class of models described by the Heisenberg Hamiltonian (1.0.2) both for spin-$\frac{1}{2}$ and for larger spins has been studied extensively, because their magnetic properties depend sensitively on the dimensionality, the effective lattice structure, and the range of the magnetic interactions. In addition to this, higher order terms which are neglected in the low energy Hamiltonian (1.0.2) like e. g. a four-spin ring exchange [RHD83] can produce interesting physics. An even larger class of magnetic models is obtained by further coupling the spins to an external magnetic field, or by taking into account interactions between orbital or lattice degrees of freedom and the magnetic system.

Due to the complex interplay of the various interaction mechanisms, quantum spin systems in low dimensions provide typical examples for the occurrence of *quantum phase transitions*, i. e. qualitative changes in the nature of the ground state due to a variation of one or more model parameters [Sac00, Voj03]. Similarly, there is a fundamental difference in the nature of the elementary excitations on either side of the transition. For this reason the existence of such a zero temperature transition has an intense impact on the finite temperature properties of the system. One way to examine the nature of the ground state is the analysis of correlation functions at low finite temperatures.

To illustrate this, let us consider the antiferromagnetic Heisenberg model with spin-$\frac{1}{2}$ and couplings between nearest neighbors only. On a cubic lattice, the large coordination number tends to stabilize long-range antiferromagnetic i. e. *Néel order* even at finite temperatures, which is characterized by a finite sublattice magnetization and long-range spin correlations. In particular, the spin correlation length diverges algebraically at the temperature of the *Néel transition* from the paramagnetic to the ordered phase [San98a]. In one and two dimensions, the situation is somewhat different because thermal fluctuations are known to destroy the long-range Néel order at finite temperatures [MW66]. Nevertheless, in both cases there do exist ordered ground states. As far as the square lattice Heisenberg model is concerned, there is a finite sublattice magnetization at zero temperature [And52, Bar91, San97], accompanied by an exponential divergence of the spin correlation length as $T \rightarrow 0$ [CHN89, DM90, Bar91, BBGW98]. In the Heisenberg chain, the situation is more complicated, because there the quantum fluctuations are so strong that only *quasi* long-range order can be established, i. e. there is an algebraic decay of the spin correlations in the ground state. In addition to this, the corresponding correlation length diverges algebraically upon cooling down the system to absolute zero [KBI93, Tak99]. A common feature both in one and two dimensions is that there is a delicate dependence of the nature of the ground state on perturbations of the Heisenberg Hamiltonian. Frequently, these perturbations drive the system towards

a paramagnetic ground state, and thus a finite spin correlation length both in the ground state and at finite temperatures is found. Prominent examples where this situation is realized are the frustrated Heisenberg chain [ON92, Egg96b] or the coupled ladder antiferromagnet on the square lattice [Sac00].

In this thesis, basically two different types of quantum spin models will be investigated. The first system is the one-dimensional spin-$\frac{1}{2}$ Heisenberg model with anisotropic spin exchange between nearest neighbors, the *XXZ chain*. Here we will especially focus on the quantum critical regime of the model, i. e. we consider values $-1 < \Delta \leq 1$ for the anisotropy parameter Δ of the system. Although this model is exactly soluble by means of the *Bethe ansatz* [Bet31, KBI93, Tak99], there remain a couple of unresolved questions concerning the decay of correlation functions. It will be demonstrated that certain analytical expressions for the asymptotic behavior of two-point correlations as predicted by *conformal field theory* provide a good starting point to examine the spin and dimer correlations of the system at intermediate distances. The second class of models which play a central part in this dissertation are quasi two-dimensional Heisenberg systems coupled to lattice vibrations. From the theoretical point of view, there is a consistent picture on how this *spin-phonon coupling* influences the properties of quasi one-dimensional spin systems. In particular, this mechanism is known to be responsible for the occurrence of the *spin-Peierls transition* in a number of substances like e. g. $CuGeO_3$ [HTU93], which is a structural phase transition at finite temperatures accompanied by fundamental changes in the magnetic excitation spectrum [Pyt74, CF79]. In contrast to this, little is known about the impact of the spin-phonon coupling on quasi two-dimensional systems. In this thesis, we will tackle this problem by considering the spin-$\frac{1}{2}$ square lattice Heisenberg model coupled to phonons. In the first step, the ground state properties of a strictly two-dimensional model will be analyzed by studying spin correlations at low finite temperatures. Afterwards, we will consider statically dimerized systems as the effective models to describe the physics of spin layers coupled to three-dimensional lattice vibrations in the adiabatic limit. In particular, we will see that an analysis of the dimer correlations of the square lattice Heisenberg model is the key to establish a theory for the two-dimensional analog of the spin-Peierls transition.

In contrast to the special case of the XXZ chain, most of the theoretical models which are of importance in the field of strongly correlated electron systems cannot be solved analytically. Therefore along with approximative analytical approaches as e. g. the linear spin wave theory [And52], the perturbation theory, or the application of field-theoretical instruments, numerical techniques play a central part in modern condensed matter physics. In this thesis, we will make use of various versions of the *loop cluster algorithm* [ELM93], which belongs to the extended class of *quantum Monte Carlo* algorithms. In particular, the loop algorithm is best suited to evaluate finite temperature correlation functions of quantum spin models. In contrast to other standard numerical techniques like the density matrix renormalization group (DMRG) [Whi92, Whi93] or the flow equation method [Weg94, KU00], which basically apply to one-dimensional models, the quantum Monte Carlo method is not obstructed by the dimensionality of the system. Furthermore, it is possible to study significantly larger system sizes than those being accessible to the Lanczos algorithm [Lan50].

This thesis is divided into three main parts, each of which contains a separate introduction to

highlight the importance of the particular topic in the framework of condensed matter physics. In the following chapter, we first give a detailed derivation of the various versions of the loop algorithm for those quantum spin models which are investigated in this dissertation. The subsequent Chapter 3 deals with the issue of spin and dimer correlation functions in the XXZ chain. Afterwards in Chapt. 4, we turn our attention to the square lattice Heisenberg model with spin-phonon coupling. A comprehensive summary of the thesis can be found in Chapt. 5, which also contains an outlook for future investigations. In the Appendix, the detailed derivations of some crucial identities are given which have been left out of the main part to allow for a comprehensible presentation of matters. The thesis closes with an abstract both in English and in German.

2. Quantum Monte Carlo loop algorithm

2.1. Introduction to quantum Monte Carlo

Quantum Monte Carlo (QMC) is a stochastic method to investigate the finite-temperature properties of quantum many body systems. Especially in the case of low-dimensional non-frustrated quantum spin models, results obtained by QMC have contributed significantly to a deeper understanding of both thermodynamic and ground state properties of such systems. Besides the development of fast computing machines this is mainly due to a rapid development of cluster algorithms during the past decade. In this work we present numerical results for correlation functions obtained by means of the loop cluster algorithm [ELM93], whose formulation for various models is described in this chapter. Before discussing the details of the loop algorithm, however, we start with a short survey of the development of the QMC method and modern algorithms in QMC.

In 1953, Metropolis *et. al.* realized that stochastic decisions can be used to simulate the statistics of classical many body systems [MRR$^+$53]. In principle, the method works by setting up a *Markov chain* of classical configurations which are distributed according to their Boltzmann weight $W(\mathcal{C}) \equiv e^{-\beta E(\mathcal{C})}/Z$, where $E(\mathcal{C})$ is the energy of a given configuration $\mathcal{C}$, Z the partition function and β the inverse temperature of the system. Starting from a given configuration $\mathcal{C}$, a new configuration $\mathcal{C}'$ is generated randomly and accepted according to the *Metropolis probability*

$$p(\mathcal{C} \to \mathcal{C}') = \begin{cases} 1 & \text{if } W(\mathcal{C}) \leq W(\mathcal{C}'), \\ \frac{W(\mathcal{C}')}{W(\mathcal{C})} & \text{else,} \end{cases} \tag{2.1.1}$$

by drawing a random number. Such a procedure is called an *update*. In particular, the update probability (2.1.1) is chosen such that the *detailed balance* condition

$$W(\mathcal{C})p(\mathcal{C} \to \mathcal{C}') = W(\mathcal{C}')p(\mathcal{C}' \to \mathcal{C}) \tag{2.1.2}$$

is fulfilled. Assuming also *ergodicity* of the algorithm, i. e. starting from an arbitrary configuration any other configuration of the configuration space can be generated within a finite number of updates, the detailed balance condition (2.1.2) guarantees that the configurations of the Markov sequence take the correct distribution. Numerical estimates for physical observables are determined by taking the mean value over all configurations of the Markov chain. Note that in practice when starting the simulation a certain number of configurations is not taken into account for the measurement of physical quantities to allow the algorithm to reach thermal equilibrium, i. e. to *thermalize*.

For quantum many body systems, basically the same procedure can be applied if one succeeds in mapping the quantum system to a classical system. Such an attempt was first done by Handscomb

in 1962 for the ferromagnetic spin-$\frac{1}{2}$ Heisenberg model [Han62]. This approach is based on a series expansion of the partition function in β. The applicability of his method, however, first seemed to be very limited because in practice one needs to calculate the full traces of products of certain bond operators analytically. This problem was overcome by Sandvik and Kurkijärvi in 1991 with the *stochastic series expansion* (SSE) method [SK91]. There the traces are written as a sum of diagonal matrix elements in a suitably chosen basis. The matrix elements can be calculated easily and the sum is sampled along with the operator sequences.

An alternative approach is based on a path integral representation of the partition function. By making use of the *generalized Trotter-Suzuki formula*, a d-dimensional quantum system is mapped to a $(d + 1)$-dimensional classical system [Tro59, Suz76]. A QMC algorithm based on this construction was first applied in 1977 by Suzuki *et. al.* for the spin-$\frac{1}{2}$ XY model in one and two dimensions [SMK77]. In case of the spin-$\frac{1}{2}$ XXZ model, which will be of special interest in this work, the Trotter-Suzuki decomposition of the partition function corresponds to a mapping to the *six vertex model* of statistical physics [Bax82].

As they relied on local update procedures, one main problem of early QMC algorithms was that they suffered severly from *autocorrelation effects*, i. e. statistical errors of measured quantities grow because subsequent configurations of the Markov chain are not statistically independent. More quantitatively, the *integrated autocorrelation time* τ_{int} is a measure for the importance of autocorrelation effects in a Monte Carlo algorithm. Roughly spoken, from u configurations generated by the update procedure only $u/2\tau_{\text{int}}$ are statistically independent. In the vicinity of continuous phase transitions autocorrelation times are connected to the correlation length ξ of the system according to $\tau_{\text{int}} \sim \xi^z$, where z is a dynamical critical exponent. Thus at a critical point, Monte Carlo algorithms with non-vanishing z become inefficient because the correlation length diverges. This phenomenon is called *critical slowing down*.

Historically it turned out that the problem of large autocorrelation times could be overcome by constructing update procedures which alter the configurations of the Markov sequence globally, i. e. the development of cluster algorithms. In the case of QMC based on the path integral formulation, this was first achieved by the development of the loop cluster algorithm by Evertz *et. al.* in 1993, for which autocorrelation times stay of the order of unity [ELM93]. A further achievement was the formulation of the loop algorithm in *continuous time* by Beard and Wiese in 1996, which removed the systematic errors due to an artificial discretization of the time direction when applying the Trotter-Suzuki breakup [BW96]. An alternative to the loop algorithm within the path integral approach is the *worm algorithm* which was developed by Prokof'ev *et. al.* in 1998 [PST98a, PST98b]. In the same year Sandvik showed that cluster algorithms could also be constructed for sampling in the SSE representation [San98b]. In this context the clusters are called *operator-loops*. The approach was generalized to SSE algorithms based on *directed loops* in 2002, which was shown to be equivalent to the formulation of the loop algorithm in continuous time in the same paper [SS02].

The progress which has been made in the field of cluster algorithms in the past decade can be illustrated by considering e. g. numerical investigations of the spin correlation function in the two-dimensional spin-$\frac{1}{2}$ Heisenberg model on a square lattice at low temperatures. In 1990, Ding and

Makivić studied the system by applying a QMC algorithm based on the path integral formulation with local spin updates, simulating systems of maximum 128×128 sites and reaching temperatures which correspond to correlation lengths up to 28 lattice spacings [DM90]. In 1998, Beard *et. al.* investigated the system with up to 160×160 sites by means of a continuous time loop algorithm. By further applying finite-size scaling methods to the QMC results, they were able to reach correlation lengths of 352.000 lattice spacings [BBGW98].

To list all of the applications of the QMC method would go beyond the scope of this work. It has been successfully applied to non-frustrated spin systems (also in the presence of magnetic fields), to bosonic and one-dimensional fermionic systems. Review articles on the loop algorithm in the path integral representation [Eve01, KH04] as well as on the directed loop method in the SSE representation [SS02] include lists of the relevant literature.

We close this survey with the remark that in spite of all the success of the QMC method there is a class of models to which the method only provides limited access. These are frustrated quantum spin systems and fermionic models in $d > 1$ dimensions, for which the mapping of the quantum system to a classical system may yield configurations with negative Boltzmann weight (the *sign problem*) [TW04]. In these systems, the occurence of negative weights results in an exponential growth of the statistical error and hence of computation time with the system size.

This chapter is organized as follows. In Sect. 2.2, we give a detailed description of the loop algorithm for the antiferromagnetic spin-$\frac{1}{2}$ XXZ chain and for the two-dimensional Heisenberg model. We then derive how the loop algorithm can be applied for a Heisenberg model coupled to bond phonons in one and two spatial dimensions (Sect.2.3). In Sect. 2.4, we finally discuss rules for the measurement of correlation functions. In the same section, we present a more precise discussion on the issue of numerical error analysis.

2.2. Loop algorithm for the XXZ model

In this part we elaborate the construction of the loop algorithm for Heisenberg-like quantum spin models, see also Refs. [Eve01, KH04]. We start by considering the case of the XXZ chain, and construct the path integral representation of the partition function in the next subsection. In Sect. 2.2.2, the discrete time version of the loop algorithm is derived for this model. We then generalize the procedure to continuous time, see Sect. 2.2.3. Afterwards we investigate the special case of the isotropic Heisenberg model and transfer our findings to the two-dimensional case including bond disorder (Sect. 2.2.4). The results of this part are summarized in a sketch of the algorithm in Par. 2.2.5.

2.2.1. Model Hamiltonian and Trotter-Suzuki decomposition

The Hamiltonian of the antiferromagnet spin-$\frac{1}{2}$ XXZ chain reads

$$H = \sum_{i=1}^{N} H_i \equiv \sum_{i=1}^{N} \frac{J}{2}(\sigma_i^x \sigma_{i+1}^x + \sigma_i^y \sigma_{i+1}^y + \Delta\,\sigma_i^z \sigma_{i+1}^z). \tag{2.2.3}$$
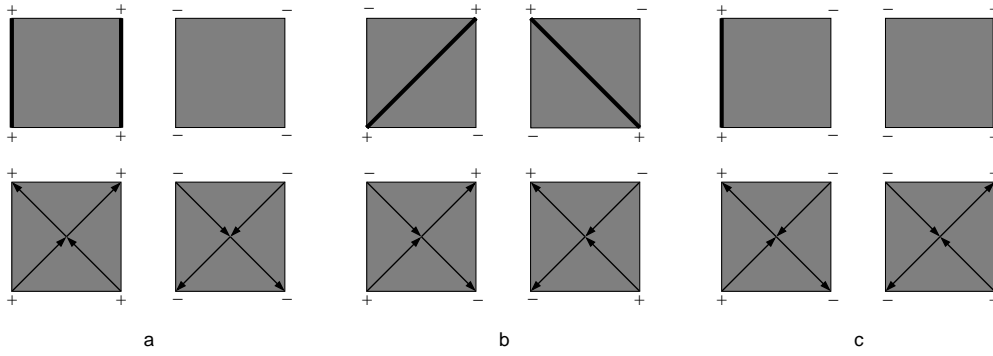
Fig. 2.1.: Graphical representation of the six plaquette configurations with non-vanishing plaquette weight *a* (left), *b* (middle), and *c* (right). The worldline representation is shown in the top row, while the vertex picture is visualized in the bottom row.

Here the exchange coupling J is chosen to be positive, while the anisotropy parameter takes values $\Delta \in [0, 1]$. The symbols σ_i^α ($\alpha = x, y, z$) denote the components of Pauli spin operators at the lattice sites $i = 1, \ldots, N$. Note that we assume an even number N of lattice sites and periodic boundary conditions. The physical properties of the model will be discussed in Chapt. 3, where we especially focus on the behavior of spin and dimer correlation functions.

We now construct the path integral formulation of the partition function Z of the system. After splitting the Hamiltonian (2.2.3) into even and odd parts,

$$H = H_{\text{even}} + H_{\text{odd}}, \qquad \text{with} \tag{2.2.4}$$

$$H_{\text{even}} = \sum_i H_{2i}, \qquad H_{\text{odd}} = \sum_i H_{2i+1},$$

we can apply the generalized Trotter formula [Tro59, Suz76] and write

$$Z = \text{Tr}\, e^{-\beta H} = \lim_{M \to \infty} Z_M \equiv \lim_{M \to \infty} \text{Tr}\, \left(e^{-\frac{\beta}{M} H_{\text{even}}} e^{-\frac{\beta}{M} H_{\text{odd}}} \right)^M. \tag{2.2.5}$$

The number M is called *Trotter number*.

In the following, we keep this number fixed and consider the Mth approximant Z_M of the partition function. We insert $(2M - 1)$ complete sets of σ^z eigenstates between the exponentials in Eq. (2.2.5) and find the partition function of a classical system

$$Z_M = \sum_{\{s_i^k\}} W(\{s_i^k\}) = \sum_{\{s_i^k\}} \prod_p W_p(\{s_p\}), \tag{2.2.6}$$

where the sum $\sum_{\{s_i^k\}}$ extends over Ising spins $s_i^k = \pm 1$. The index $k = 0, \ldots, 2M - 1$ labels the Trotter slices in imaginary time direction. In the second step we have exploited the observation that the summands of $H_{\text{even/odd}}$ commute, and therefore the weight $W(\{s_i^k\})$ of one configuration $\{s_i^k\}$ of Ising spins can be decomposed into a product of *plaquette weights* $W_p(\{s_p\})$ depending on the spin configurations $\{s_p\}$ on the shaded plaquettes of a $(1+1)$-dimensional checkerboard lattice. On the plaquette lattice, the construction implies periodic boundary conditions both in space and

time direction. The plaquette weights only depend on the four adjacent spins, i. e. they are given by the expression

$$W_p(\{s_p\}) = \langle s_i^k\, s_{i+1}^k | e^{-\beta H_i/M} | s_i^{k+1} s_{i+1}^{k+1} \rangle, \tag{2.2.7}$$

where the index i is even (odd) for even (odd) values of k due to the structure of the decomposition. Because the summands H_i of the Hamiltonian (2.2.3) conserve the z-component of the total spin on each plaquette, there are only six non-vanishing plaquette weights. They can be calculated easily, see App. A.1. We only denote the result here, which is

$$a \equiv \langle + + | e^{-\beta H_i/M} | + + \rangle = \langle - - | e^{-\beta H_i/M} | - - \rangle = e^{-\beta J \Delta/2M}, \tag{2.2.8}$$

$$b \equiv \langle + - | e^{-\beta H_i/M} | - + \rangle = \langle - + | e^{-\beta H_i/M} | + - \rangle = e^{\beta J \Delta/2M} \sinh(\beta J/M), \tag{2.2.9}$$

$$c \equiv \langle + - | e^{-\beta H_i/M} | + - \rangle = \langle - + | e^{-\beta H_i/M} | - + \rangle = e^{\beta J \Delta/2M} \cosh(\beta J/M). \tag{2.2.10}$$

Note that the matrix element b is originally proportional to $\sinh(-\beta J/M)$. Here we implicitly assume the application of a unitary transformation

$$U = \prod_i \sigma_{2i}^z \tag{2.2.11}$$

to the Hamiltonian of the system, which guarantees that all the plaquette weights are positive to avoid negative Boltzmann weights.

The six non-vanishing plaquette weights can be represented graphically by making use of the *wordline* and *vertex* pictures, respectively, see Fig. 2.1. In the first case, on each plaquette the spins pointing upwards are connected by thick solid lines, the so-called worldlines. In this picture, a configuration which contributes to the partition function is given by a set of closed worldlines on the shaded plaquettes of the $(1 + 1)$-dimensional checkerboard lattice. In the latter case, arrows which connect the center of each plaquette to its corners are drawn. These vertices are directed along the imaginary time direction if the spin on the corner is pointing upwards, otherwise against it. In the vertex representation, the connection between the XXZ model and the six-vertex model [Bax82] which was mentioned in the introduction of this chapter becomes obvious. An example for a configuration with non-vanishing Boltzmann weight on a checkerboard lattice with $N = 4$ sites and $2M = 6$ Trotter slices is given in Fig. 2.2.

In its original formulation [ELM93], the loop algorithm was constructed in discrete time, i. e. the simulations were carried out for classical systems with the partition function (2.2.6), keeping the Trotter number M fixed. This way of proceeding will be described in the following subsection. In Sect. 2.2.3 we then discuss how the algorithm can be formulated directly in the continuum limit $M \to \infty$.

2.2.2. Plaquette breakups and loop construction

Early QMC algorithms for the XXZ model were based on update procedures with local deformations of worldlines [HSSB81, CL83]. In addition to the problem of critical slowing-down, such algorithms were not ergodic because they conserved both the temporal and spatial *winding numbers*, i. e. the number of times a worldline winds around the $(1 + 1)$-dimensional checkerboard lattice. However, the latter problem could be overcome by introducing additional global updates [DM90, DM91].
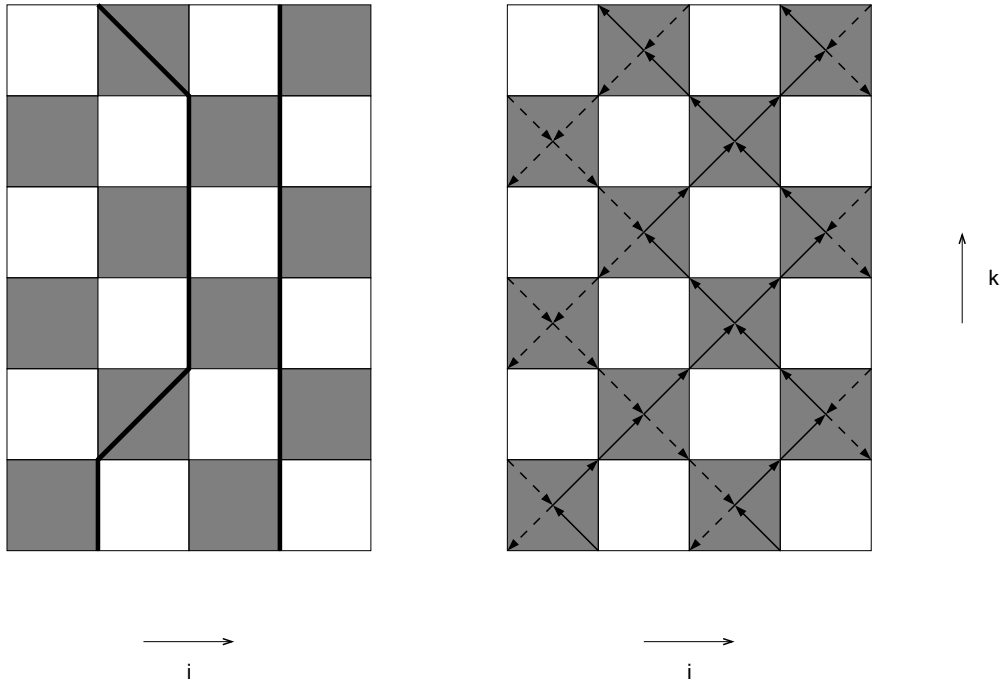
Fig. 2.2.: Example for a configuration with non-vanishing Boltzmann weight on the checkerboard lattice of shaded plaquettes. Taking the periodic boundary conditions into account, there are two closed worldlines in the worldline representation (left). The same configuration in the vertex picture is shown in the right panel.

The main advantage of the loop algorithm is that it allows global changes of a given configuration by taking local stochastic decisions. In particular, the number of worldlines as well as winding numbers may be changed significantly within one single update step. Furthermore, the principle of *importance sampling* is incorporated, which means that the configurations of the Markov sequence are sampled directly according to their Boltzmann weight. This guarantees that the computer is not occupied with generating configurations which are rejected immediately.

An update within the loop algorithm consists of two steps. First, for a given worldline (or vertex) configuration a set of closed loops is constructed by specifying loop segments on each shaded plaquette of the $(1+1)$-dimensional checkerboard lattice. These *breakups* are determined stochastically and depend on the spin configuration on each plaquette. The loops are built in such a fashion that each spin belongs to a single loop. In the second step, each loop is flipped (i. e. all the spins belonging to the same loop are inverted) with a certain probability. By construction of the algorithm this yields a new configuration with non-vanishing Boltzmann weight. An example for an update of the configuration from Fig. 2.2 with a single loop flip is shown in Fig. 2.3.

The way the loops are constructed can be understood most easily in the vertex picture. For a given configuration of vertices, we pick an arbitrary spin s_i^k on the plaquette lattice and follow its vertex into the adjacent plaquette. At the center of the plaquette, there are two possibilities of arrows to follow. We arbitrarily choose one direction to get to a new plaquette, where we apply
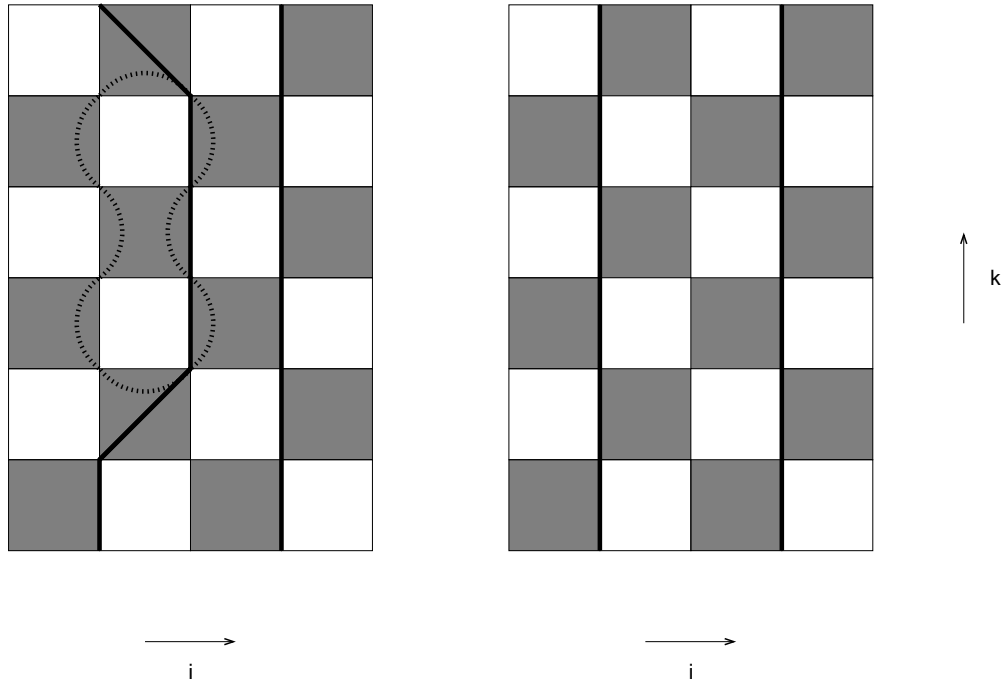
Fig. 2.3.: Example for a loop flip in the worldline configuration from Fig. 2.2. In the left panel, the original worldline configuration is shown. The dashed line shows a single loop along which the spins are inverted during the update. This results in a new worldline configuration which is depicted in the right panel.

the same scheme. If we have met a certain plaquette before, we move along the vertex which has not been selected yet, since we do not allow the loop to overlap itself. This way of proceeding is repeated successively until we reach the spin where the construction of the loop started. Now we can start with another spin which does not belong to the first loop and construct a second loop in the same fashion. We repeat this procedure until each spin of the lattice has been assigned to a loop.

Equivalently, we can select a breakup on each plaquette, which means that the vertex configuration on the plaquette is split into two loop segments. For each of the plaquette configurations with non-vanishing plaquette weights as shown in Fig. 2.1, there are two possibilities of breakups, see Fig. 2.4. For the two configurations with weight a, we can choose vertical and diagonal breakups. For the plaquette configurations with weight b, horizontal and diagonal breakups are possible, while for plaquettes with weight c vertical and horizontal breakups can be selected, respectively. For each type of plaquette, there is also another choice of breakup which is called *freezing*. Freezing can be viewed as consisting of two connected loop segments. Thus two loops entering a plaquette with freezing are glued together to a *cluster* of loops which have to be flipped together. Upon flipping such a cluster the weight of the plaquette is conserved, i. e. it is frozen. The set of all the clusters on the lattice will be called a *graph* in the following.

To specify both the probabilities for the selection of plaquette breakups and for the loop flips we need a more technical description, see also Ref. [Eve01]. We first observe that by constructing
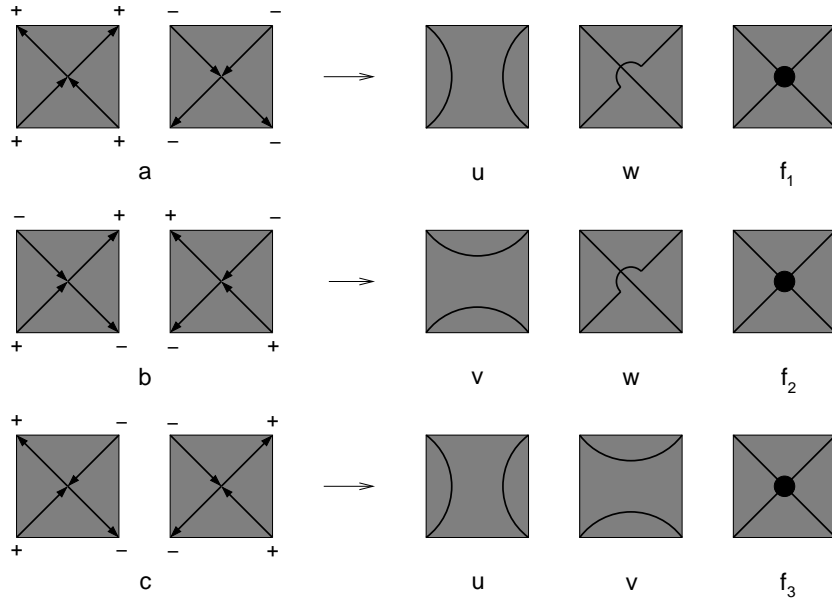
Fig. 2.4.: Possible breakups for the six plaquette configurations with non-vanishing plaquette weights *a* (top), *b* (middle), and *c* (bottom) shown in the vertex representation. For each spin configuration, there are two choices of breakups and, in addition, the possibility of freezing. The breakup weights are *u*, *v* and *w* for vertical, horizontal, and diagonal breakups, respectively, and f_i ($i = 1, 2, 3$) for each type of freezing.

a graph G, we have mapped a wordline configuration of spins $\{s_i^k\}$ with weight $W(\{s_i^k\})$ to a combination of worldlines and loops $(\{s_i^k\}, G)$ with a certain weight $W(\{s_i^k\}, G)$. On each plaquette, this corresponds to assigning a *breakup weight* $W_p(\{s_p\}, B_p)$ to the combination of plaquette configuration $\{s_p\}$ and breakup B_p, for which we demand

$$\sum_{B_p} W_p(\{s_p\}, B_p) = W_p(\{s_p\}), \tag{2.2.12}$$

$$W_p(\{s_p\}, B_p) \geq 0. \tag{2.2.13}$$

The update procedure of the loop algorithm now consists of two steps:

1. On each plaquette with spin configuration $\{s_p\}$, select a breakup according to the probability

$$p(\{s_p\} \to (\{s_p\}, B_P)) = \frac{W_p(\{s_p\}, B_p)}{W_p(\{s_p\})}. \tag{2.2.14}$$

The conditions (2.2.12) and (2.2.13) guarantee that the breakup probabilities are positive and normalized correctly. Relation (2.2.12) further implies

$$\sum_G W(\{s_i^k\}, G) = \sum_G \prod_{\cup B_p = G} W_p(\{s_p\}, B_p) = \prod_p \sum_{B_p} W_p(\{s_p\}, B_p) \overset{(2.2.12)}{=}$$

$$\prod_p W_p(\{s_p\}) = W(\{s_i^k\}). \tag{2.2.15}$$

2. After having identified the clusters constituting the graph G, determine which of the clusters are flipped. A flip of a single cluster yields a new configuration $\{s_i^k\}'$ with non-vanishing Boltzmann weight, keeping the graph G fixed. One possible choice for the transition probability into the new configuration is the *heat bath probability*

$$p(\,(\{s_i^k\}, G) \to (\{s_i^k\}', G)\,) = \frac{W(\{s_i^k\}', G)}{W(\{s_i^k\}, G) + W(\{s_i^k\}', G)}, \tag{2.2.16}$$

which can be shown easily to satisfy the detailed balance condition (2.1.2).

In the following we determine the breakup weights $W_p(\{s_p\}, B_p)$ for the XXZ model. It is possible to derive simple expressions for the breakup weights if we demand

$$W_p(\{s_p\}, B_p) = W_p(\{s_p\}', B_p), \tag{2.2.17}$$

i.e. the weight $W_p(\{s_p\}, B_p)$ only depends on the type of breakup B_p and not on the spin configuration $\{s_p\}$ on the plaquette. For this reason we only have six different breakup weights u, v, w, and f_i ($i = 1, 2, 3$) for the six types of breakups as shown in Fig. 2.4. Making use of the abbreviations for the plaquette weights as introduced in Eqs. (2.2.8),(2.2.9), and (2.2.10), relation (2.2.12) now reads

$$u + w + f_1 = a, \tag{2.2.18}$$

$$v + w + f_2 = b, \tag{2.2.19}$$

$$u + v + f_3 = c. \tag{2.2.20}$$

We can see that there are only three equations to determine the six breakup weights. We thus have the freedom to construct a solution with vanishing freezing weights $f_i = 0$ ($i = 1, 2, 3$). It is useful to search for solutions with minimal freezing weights because freezing is known to increase autocorrelation effects due to the formation of clusters. If the size of the clusters becomes comparable to the system size, the update scheme becomes inefficient. Heuristically, this can be explained by observing that in the extreme case that there is only one single cluster, only the same or the inverse configuration can be reached by one update. Excluding the possibility of freezing, we find the solutions

$$u = \frac{1}{2}(a - b + c), \tag{2.2.21}$$

$$v = \frac{1}{2}(-a + b + c), \tag{2.2.22}$$

$$w = \frac{1}{2}(a + b - c), \tag{2.2.23}$$

for the breakup weights.

We finally have to specify the loop flip probability $p(\,(\{s_i^k\}, G) \to (\{s_i^k\}', G)\,)$. From the condition (2.2.17), we first see that

$$W(\{s_i^k\}, G) = \prod_p W_p(\{s_p\}, B_p) = \prod_p W_p(\{s_p\}', B_p) = W(\{s_i^k\}', G). \tag{2.2.24}$$

By inserting this result into the relation (2.2.16), we find that each loop is flipped with probability $\frac{1}{2}$.
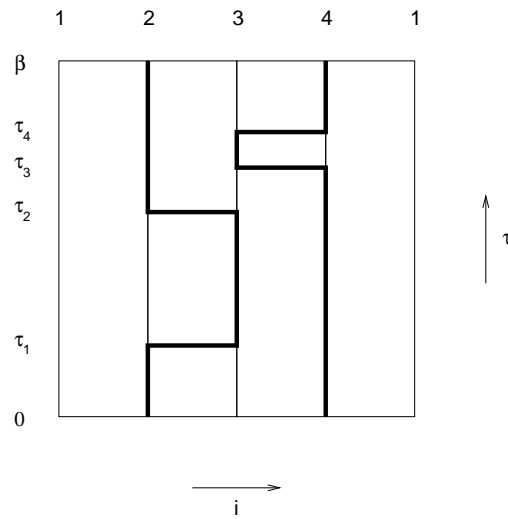
Fig. 2.5.: Example for a worldline configuration in the continuum limit $M \to \infty$. There are four worldline jumps which can be specified by the times τ_α ($\alpha = 1, \ldots, 4$) of the transitions and the spatial indices of the lattice sites involved.

2.2.3. Continuous time

The artificial discretization of the Trotter direction which was used in the preceeding two subsections leads to systematic errors, because the continuum limit $M \to \infty$ in Eq. (2.2.5) can only be taken into account by extrapolating the Monte Carlo estimates of physical quantities after running the simulation with several finite values of M. In addition to this effect, for large values of the Trotter number the algorithm is slowed down because the number of Ising spins on the checkerboard lattice increases linearly with M. In this section we describe how these problems can be overcome by formulating the loop algorithm directly in continuous time [BW96].

In the continuum limit, the worldline picture can still be used to visualize configurations which contribute to the partition function (2.2.5) of the system. The discrete index k, however, which we have used so far to label the Trotter slices in imaginary time direction, is replaced by a continuous time variable τ taking values in $[0, \beta)$. Instead of having to store the values of $N \times 2M$ Ising spins $\{s_i^k\}$ on the discrete checkerboard lattice, now the values of only N Ising spins $\{s_i(\tau)\}$ at one certain point of time (e. g. $\tau = 0$) plus the relevant information on worldline jumps are required to specify a configuration. A transition of a worldline between two adjacent sites is characterized by the time of the transition plus the spatial indices of the two Ising spins connected by the worldline jump. An example with four such transition events on a lattice with $N = 4$ sites is depicted in Fig. 2.5.

We are now going to discuss the construction of loops in continuous time. Similarly to the case of worldline configurations, the loops are specified by transition events of loops jumping to an adjacent site. In the discrete time version of the algorithm, there are in principle two possibilities of breakups where a loop changes the lattice site. These are horizontal and diagonal breakups, see also Fig. 2.4. The correspondence for $M \to \infty$ is that a jump of a loop is either accompanied
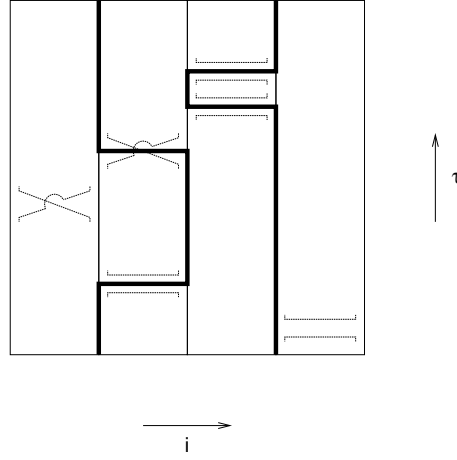
Fig. 2.6.: A possible choice of loop transition events represented by the thin lines for the worldline configuration from Fig. 2.5. For each of the four worldline jumps, there is a corresponding loop jump. The type of the loop transition is determined from the probabilities (2.2.30) and (2.2.31). Additionally, two more transitions of loops have been determined according to the transition rates (2.2.27) and (2.2.29). Connecting the horizontal and diagonal lines by vertical ones yields a graph consisting of closed loops.

by a reversal of the loop direction (a horizontal breakup in discrete time) or the direction of the loop remains unchanged (corresponding to a diagonal breakup). Which type of transition occurs depends on the underlying worldline configuration as in the discrete time version of the algorithm.

In practice transition events of loops are determined bond by bond. According to the underlying worldline configuration, on each bond the time interval $[0, \beta)$ is cut into a number of intervals $[\tau_\alpha, \tau_{\alpha+1})$ with constant worldline configuration on the two adjacent sites. For example, on the bond between lattice sites 2 and 3 in Fig. 2.5 there are five such intervals. We first consider a time interval where the two adjacent sites are both empty or occupied by worldlines. In our example, this is the case for times $\tau \in [\tau_3, \tau_4)$. In discrete time, on each plaquette with this worldline configuration we would either choose a vertical or a diagonal breakup. According to Eq. (2.2.14), the probability for the selection of a diagonal breakup is

$$p = \frac{w}{a} = \frac{1}{2}\left(1 + \frac{b}{a} - \frac{c}{a}\right) = \frac{1}{2}\left(1 - e^{-\frac{\beta}{M}J(1-\Delta)}\right), \qquad (2.2.25)$$

where we have used the result (2.2.23) and the expressions (2.2.8),(2.2.9), and (2.2.10) for the plaquette weights from Sect. 2.2.1. Expanding the exponential to first order in $\Delta\tau \equiv \beta/M$, this becomes

$$p = \Delta\tau \frac{J}{2}(1 - \Delta). \qquad (2.2.26)$$

Hence in continuous time, we can assign transition events of loops which conserve the loop direction according to a constant probability per unit time, i. e. a *transition rate*

$$\lambda_{\text{diag}} = \frac{p}{\Delta\tau} = \frac{J}{2}(1 - \Delta). \qquad (2.2.27)$$

Note that the time segments between two such transitions take an exponential distribution[1]

---

[1]This result is identical to the lifetime distribution of a radioactive nucleus with decay rate λ_{diag}.

$\sim e^{-\lambda_{\text{diag}}\tau}$.

We can proceed in an analogous way for time intervals in which only one of the adjacent sites is empty, e. g. the interval $[0, \tau_1)$ on the bond between sites 2 and 3 in Fig. 2.5. For finite M, such a worldline configuration enables us to select vertical and horizontal breakups on the individual plaquettes. The probability for a horizontal breakup is given by

$$p = \frac{v}{c} = \frac{1}{2}(1 - \frac{a}{c} + \frac{b}{c}) = \frac{e^{\Delta\tau J} - e^{-\Delta\tau J\Delta}}{2\cosh(\Delta\tau J)} \overset{\Delta\tau \ll 1}{\approx} \Delta\tau \frac{J}{2}(1 + \Delta). \tag{2.2.28}$$

Thus we have a transition rate

$$\lambda_{\text{hor}} = \frac{J}{2}(1 + \Delta) \tag{2.2.29}$$

for loop transitions accompanied by a reversal of the loop direction.

We finally discuss what happens if the two spins interacting on the selected bond are connected by a worldline jump. On the bond we have chosen in our example such an event takes place at the times τ_1 and τ_2. In discrete time, a transition of a worldline corresponds to a single plaquette with plaquette weight b on which we can either choose a horizontal or diagonal breakup. From this rule we conclude that for $M \to \infty$ a worldline jump always leads to a loop transition event. To specify the type of the event, we have to evaluate the limit $\Delta\tau \to 0$ of the probabilities $\frac{v}{b}$, $\frac{w}{b}$ for horizontal and diagonal breakups, respectively. By applying the rule of de L'Hospital, one can prove easily that

$$p_{\text{hor}} = \frac{v}{b} = \frac{1}{2}(1 - \frac{a}{b} + \frac{c}{b}) = \frac{e^{\Delta\tau J} - e^{-\Delta\tau J\Delta}}{2\sinh(\Delta\tau J)} \overset{\Delta\tau \to 0}{=} \frac{1}{2}(1 + \Delta), \tag{2.2.30}$$

$$p_{\text{diag}} = 1 - p_{\text{hor}} = \frac{1}{2}(1 - \Delta). \tag{2.2.31}$$

After having applied this scheme for all of the bonds on the lattice, one ends up with a set of loop transition events, see Fig. 2.6. We can now connect the horizontal and diagonal line segments by drawing vertical lines between them, and obtain a graph consisting of closed loops as in the discrete time version of the algorithm. The loops can be flipped independently to reach a new worldline configuration. The loop flip probability remains unchanged in the continuum limit, i. e. each loop is flipped with probability $\frac{1}{2}$ as discussed in the previous subsection.

2.2.4. One- and two-dimensional isotropic Heisenberg model and bond disorder

We are now going to describe how the results of the preceeding three subsections can be generalized to formulate the loop algorithm for two-dimensional quantum spin systems. We restrict the discussion to the case of the isotropic Heisenberg model on a square lattice, however including the possibility of bond disorder, i. e. we allow for different values of the exchange coupling on different bonds.

Before we focus on the two-dimensional case, it is instructive to consider the isotropic XXX chain for which the loop construction rules from the previous two subsections take an especially simple form. For later use, we examine the implications of the choice $\Delta = 1$ in the Hamiltonian (2.2.3) for both the discrete and continuous time version of the algorithm. We first observe that

by setting $\Delta = 1$, we find the relation $a + b = c$ for the plaquette weights (2.2.8),(2.2.9), and (2.2.10). This implies that the solution (2.2.23) for the breakup weight w vanishes, while we get $u = a$ and $v = b$ for the other two breakup weights (2.2.21) and (2.2.22). Thus there are no diagonal breakups, and loops are only constructed by selecting vertical and horizontal breakups on the individual plaquettes. In particular, only on plaquettes with spin configurations corresponding to the weight c a stochastic decision on the choice of breakup has to be made. Here the probability for the selection of a horizontal breakup becomes $\frac{v}{c} = \frac{b}{c} = \tanh(\beta J/M)$. On plaquettes with weight a and b, the choice is unique, namely vertical and horizontal breakups, respectively.

These results are consistent with the findings for $M \to \infty$. From the result (2.2.27) we see that λ_{diag} vanishes, and we only have to assign loop jumps accompanied by a reversal of the loop direction according to the decay rate (see Eq. (2.2.29))

$$\lambda_{\text{hor}} = J \qquad (2.2.32)$$

in time intervals where only one of the adjacent sites of a bond is carrying a worldline. As in the discrete time version, we assign a horizontal breakup if we encounter a worldline jump, because from relation (2.2.30) we find $p_{\text{hor}} = 1$.

With this knowledge we can now concentrate on the two-dimensional Heisenberg model on a square lattice

$$H = \sum_{i,j=1}^{N} (H_{ij}^x + H_{ij}^y) \equiv \sum_{i,j=1}^{N} \left(\frac{J}{2} \vec{\sigma}_{ij} \vec{\sigma}_{i+1,j} + \frac{J}{2} \vec{\sigma}_{ij} \vec{\sigma}_{i,j+1} \right), \qquad (2.2.33)$$

where the symbols $\vec{\sigma}_{ij}$ denote Pauli spin operators at the lattice sites. As for the Hamiltonian (2.2.3), we assume an antiferromagnetic coupling $J > 0$ and periodic boundary conditions. We will comment on the physics of the model in Chapt. 4 in the context of two-dimensional spin models with spin-phonon coupling.

As in Sect. 2.2.1, we start with the construction of the path integral formulation of the partition function. In two dimensions, the decomposition (2.2.4) of the one-dimensional Hamiltonian (2.2.3) into even and odd parts can be generalized by splitting the Hamiltonian (2.2.33) into four terms according to

$$H = H_{\text{even}}^x + H_{\text{odd}}^x + H_{\text{even}}^y + H_{\text{odd}}^y, \qquad \text{with} \qquad (2.2.34)$$

$$H_{\text{even}}^x = \sum_{ij} H_{2i,j}^x, \quad H_{\text{odd}}^x = \sum_{ij} H_{2i+1,j}^x, \quad H_{\text{even}}^y = \sum_{ij} H_{i,2j}^y, \quad H_{\text{odd}}^y = \sum_{ij} H_{i,2j+1}^y.$$

We can now follow the argumentation from Sect. 2.2.1 and carry out a Trotter-Suzuki breakup [Tro59, Suz76]

$$Z = \text{Tr } e^{-\beta H} = \lim_{M \to \infty} Z_M \equiv \lim_{M \to \infty} \text{Tr } \left(e^{-\frac{\beta}{M} H_{\text{even}}^x} e^{-\frac{\beta}{M} H_{\text{odd}}^x} e^{-\frac{\beta}{M} H_{\text{even}}^y} e^{-\frac{\beta}{M} H_{\text{odd}}^y} \right)^M. \qquad (2.2.35)$$

After inserting $(4M - 1)$ complete sets of σ^z eigenstates between the exponentials, the Mth approximant of the partition function becomes (compare Eq. (2.2.6))

$$Z_M = \sum_{\{s_{ij}^k\}} W(\{s_{ij}^k\}) = \sum_{\{s_{ij}^k\}} \prod_p W_p(\{s_p\}), \qquad (2.2.36)$$
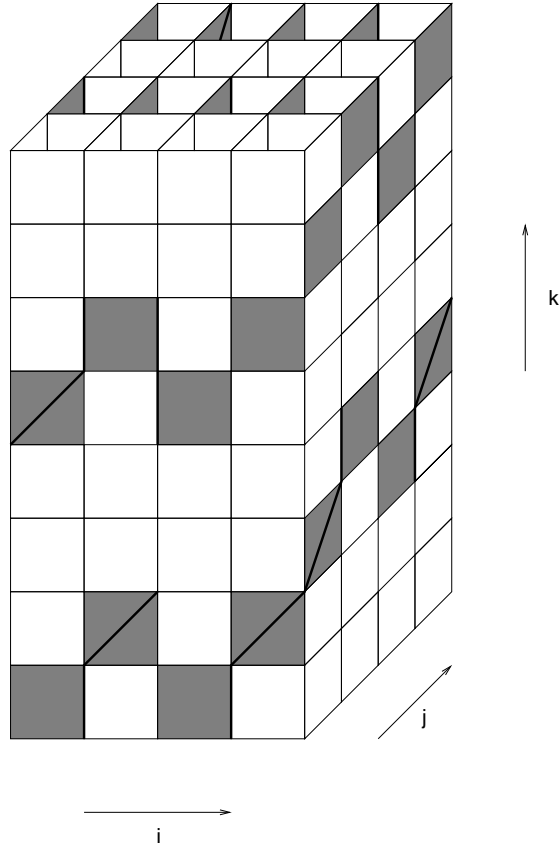
Fig. 2.7.: Example for the $(2 + 1)$-dimensional generalized checkerboard lattice for the two-dimensional Heisenberg model with $N = 4$ and $M = 2$. As in the one-dimensional case, a configuration with non-vanishing Boltzmann weight is defined by a set of closed worldlines on the lattice. Visible segments of these worldlines are sketched by the thick solid lines.

where we have exploited the fact that the summands of $H^{x/y}_{\text{even/odd}}$ commute in the last step. In complete analogy to the one-dimensional case, we thus arrive at the partition function of a classical system of Ising spins $s^k_{ij} = \pm 1$ ($k = 0, \ldots, 4M-1$) interacting on the shaded plaquettes of a $(2+1)$-dimensional generalized checkerboard lattice as depicted in Fig. 2.7. With $\Delta = 1$, we find the same expressions (2.2.8), (2.2.9), and (2.2.10) for the non-vanishing plaquette weights as for the one-dimensional model.[2] As a result we can still use the worldline and vertex pictures to visualize the configurations which contribute to the partition function (2.2.36). Worldline segments belonging to a set of closed worldlines which characterize a given configuration are also sketched in the example of Fig. 2.7.

Due to the analogy of this construction to our approach for the XXX chain, we can immediately formulate the loop algorithm for the two-dimensional model. In the discrete time version, we can construct closed loops by specifying loop breakups on the individual plaquettes of the generalized

---

[2]In two dimensions, we have to apply a unitary transformation $U = \prod_{ij} \sigma^z_{2i,2j}\sigma^z_{2i+1,2j+1}$ to guarantee that the plaquette weight b is positive on all plaquettes of the $(2 + 1)$-dimensional generalized plaquette lattice.

checkerboard lattice. As the argumentation from Sect. 2.2.2 and the beginning of this subsection does not depend on the dimensionality of the system, we obtain the same results for the breakup selection probabilities and the loop flip probability as in the one-dimensional case. In addition, the algorithm can immediately be formulated in continuous time. As for the one-dimensional model, each worldline jump is accompanied by a horizontal breakup. Furthermore, we can proceed bond by bond and identify time intervals with one empty adjacent site to assign loop transition events accompanied by a reversal of the loop direction. Again the transition rate is given by the relation (2.2.32). Then each loop is flipped with probability $\frac{1}{2}$.

We finally address the case of bond disorder, i. e. we allow for spatial variations of the magnetic exchange coupling J. Formally, this situation can be expressed by replacing

$$J \to J_{ij}^{x/y} \tag{2.2.37}$$

in the summands of $H_{ij}^{x/y}$ of the Hamiltonian (2.2.33). However, we still assume antiferromagnetic couplings[3] $J_{ij}^{x/y} \geq 0$. Note that the choice (2.2.37) includes the case of statically dimerized models for which the coupling constants $J_{ij}^{x/y}$ take only two different values $J(1 \pm \delta)$ with $\delta \in [0, 1]$. Such models will be of particular interest in this thesis, see Chapt. 4.

The update procedure described in this section can be extended easily to models with bond disorder. The only difference to the case of the Heisenberg model with uniform couplings is that the replacement (2.2.37) has to be taken into account in the expressions (2.2.8), (2.2.9), and (2.2.10) for the plaquette weights (with $\Delta = 1$). For finite M, this means that the probability $\frac{v}{c}$ for selecting a horizontal breakup on plaquettes with weight c becomes bond dependent. Equivalently, in the continuum limit $M \to \infty$ the transition rate (2.2.32) now depends on the selected bond of the lattice. There are no other changes.

2.2.5. Summary: sketch of the algorithm

We close our discussion of the loop algorithm for Heisenberg-like spin models by giving a sketch of the update procedure in the continuous time version of the algorithm. To study the properties of the XXZ chain and the two-dimensional Heisenberg model with bond disorder, the algorithm sketched below was implemented as a computer program, using a C++ code in both cases.

We assume starting with a worldline configuration with non-vanishing Boltzmann weight. Such a configuration is specified by storing the values of N Ising variables $\{s_i(\tau = 0)\}$ (N^2 Ising spins $\{s_{ij}(\tau = 0)\}$ in two dimensions) at a fixed point of time (here $\tau = 0$) plus a linked list consisting of the times of and the sites connected by worldline jumps. An update now consists of the following steps:

1. For each bond of the lattice, identify time intervals with constant worldline configuration on the two adjacent sites. In each time interval, assign two types of loop jumps according to the transition rates (2.2.27) and (2.2.29) in dependence on the underlying worldline configuration.

---

[3]On bonds with $J_{ij}^{x/y} = 0$, the plaquette weight b as well as the breakup weight v become zero. Therefore we can incorporate the case of vanishing local couplings if we permit both worldline jumps and horizontal breakups on the plaquettes associated with such a bond.

For models with isotropic exchange, i. e. $\Delta = 1$, only time intervals with one worldline on the adjacent sites have to be considered, where loop jumps accompanied by a reversal of the loop direction are assigned according to the transition rate (2.2.32). Bond disorder can be taken into account by considering the replacement (2.2.37). For a given time interval $[\tau_1, \tau_2)$, the transition times are determined by drawing a random number $x \in (0, 1]$ and calculating

$$\tau' = \frac{-\ln x}{\lambda_{\text{diag/hor}}}. \tag{2.2.38}$$

If $\tau' < \tau_2 - \tau_1$ holds, assign a loop jump at time $\tau_1 + \tau'$ and repeat the procedure by taking $\tau_1 + \tau'$ as the new lower boundary of the time interval. Otherwise proceed with a new time interval with constant worldline configuration.

2. At each worldline jump, assign a loop transition event corresponding to a horizontal or diagonal breakup according to the probabilities (2.2.30) and (2.2.31), respectively. For models with isotropic exchange, each worldline jump is accompanied by a loop transition with a reversal of the loop direction. One ends up with a list consisting of the types and times of loop transitions plus the sites connected by the loop jumps.

3. Identify loops. By following vertical connections between the loop segments defined by the loop transition events, a search through the lattice for each loop is involved. The loop identification is finished if a loop number has been assigned to each of the two loop segments of the individual loop jumps.

4. Determine which of the loops are flipped according to the loop flip probability $\frac{1}{2}$.

5. Flip the loops to generate a new worldline configuration. In practice, all of the loop flips determined in the previous step can be performed at once by considering the individual loop transition events. Depending on the type of the loop jump, the underlying worldline configuration, and on which of the two loops entering the breakup are flipped, a loop transition event might translate into a worldline jump. At last, update the values of the Ising variables at $\tau = 0$.

6. Measure observables. This step is only performed after the algorithm has thermalized. The rules for measuring both diagonal and off-diagonal operators are derived in Sect. 2.4.

2.3. Loop algorithm for the bond coupling model

In this part we discuss the application of the loop algorithm to the spin-$\frac{1}{2}$ Heisenberg model coupled to bond phonons, see also Refs. [Kühne01] and [Ait02] for a description of the algorithm in one and two dimensions, respectively. We proceed in the same fashion as in Sect. 2.2. We start by introducing the model Hamiltonian in one dimension and mapping the system to a classical one in the following subsection. In Sect. 2.3.2, we then discuss how the loop algorithm can be modified to update the spin degrees of freedom of the system. The update procedure for the phonons is described in Par. 2.3.3. After generalizing our findings to the two-dimensional case (Sect. 2.3.4), we give a sketch of the algorithm in Sect. 2.3.5.

2.3.1. Model Hamiltonian and Trotter-Suzuki decomposition

We consider the one-dimensional isotropic Heisenberg model coupled to dispersionless Einstein phonons on the bonds of the lattice. For a chain with periodic boundary conditions and an even number N of lattice sites, the Hamiltonian reads [KL99]

$$H = H_{sp} + H_{ph}, \qquad \text{with} \tag{2.3.39}$$

$$H_{sp} = \sum_{i=1}^{N} H_i \equiv \sum_{i=1}^{N} \frac{J}{2}(\vec{\sigma}_i\vec{\sigma}_{i+1} - 1)(1 + g[a_i^\dagger + a_i]), \qquad H_{ph} = \omega \sum_{i=1}^{N} a_i^\dagger a_i.$$

As before, the symbols $\vec{\sigma}_i$ denote Pauli spin operators at the lattice sites. The phonon degrees of freedom on the bonds are characterized by boson creation and annihilation operators $a_i^\dagger$ and a_i. The part H_{sp} describes the dependence of the nearest neighbor Heisenberg exchange (exchange coupling $J > 0$) on lattice distortions $x_i \sim [a_i^\dagger + a_i]$ up to first order in the spin-phonon coupling constant $g \geq 0$. The loss in elastic energy due to the deformation of the lattice is given by the contribution H_{ph}, where the phonons with frequency $\omega \geq 0$ are treated in the harmonic approximation.

For a detailed discussion of the bond coupling model in one and two dimensions we refer to Chapt. 4. However, for later use we mention that the Hamiltonian (2.3.39) is equivalent to the phenomenologically more realistic model

$$H = \frac{1}{2}\sum_{i=1}^{N}(J' + g'[a_i^\dagger + a_i])\,\vec{\sigma}_i\vec{\sigma}_{i+1} + \omega \sum_{i=1}^{N} a_i^\dagger a_i, \tag{2.3.40}$$

which is obtained from Eq. (2.3.39) by shifting the phonon operators according to [RLUK02]

$$a_i \to a_i + \frac{gJ}{2\omega}, \tag{2.3.41}$$

and neglecting a constant energy contribution. Note that the coupling constants of the model (2.3.40) are given by $J' = J(1 + \frac{g^2 J}{\omega})$ and $g' = gJ$ in terms of the original couplings.

The construction of the path integral formulation for the partition function of the system (2.3.39) is similar to our approach for the XXZ model in Sect. 2.2.1. After splitting the contribution H_{sp} in (2.3.39) into even and odd parts,

$$H_{sp} = H_{even} + H_{odd}, \qquad \text{with} \tag{2.3.42}$$

$$H_{even} = \sum_i H_{2i}, \qquad H_{odd} = \sum_i H_{2i+1},$$

we apply the generalized Trotter-Suzuki formula [Tro59, Suz76] as usual and find

$$Z = \operatorname{Tr} e^{-\beta H} = \lim_{M \to \infty} Z_M \equiv \lim_{M \to \infty} \operatorname{Tr}\left(e^{-\frac{\beta}{M} H_{even}} e^{-\frac{\beta}{M} H_{odd}} e^{-\frac{\beta}{M} H_{ph}}\right)^M. \tag{2.3.43}$$

For fixed M, a suitable choice for the basis of the Hilbert space is now given by the combined tensor product of the eigenstates of N Pauli spin matrices σ_i^z and N occupation number operators $n_i \equiv a_i^\dagger a_i$. After inserting $(3M - 1)$ complete sets of such states between the exponentials in relation (2.3.43), we arrive at the partition function

$$Z_M = \sum_{\{s_i^k, n_i^k\}} W(\{s_i^k, n_i^k\}) = \sum_{\{s_i^k, n_i^k\}} \left(\prod_p W_p(\{s_p, n_p\})\right) W_{ph}(\{n_i^k\}). \tag{2.3.44}$$

Here the sum $\sum_{\{s_i^k, n_i^k\}}$ extends over Ising spins $s_i^k = \pm 1$ and phonon occupation numbers $n_i^k \in \mathbb{N}_0$, where the index $k = 0, \ldots, 3M - 1$ labels the time slices in Trotter direction according to our usual notation. The structure of the decomposition implies that the weight $W(\{s_i^k, n_i^k\})$ of a configuration factorizes into two contributions:

1. The factor $\prod_p W_p(\{s_p, n_p\})$ corresponds to the action of the terms $e^{-\frac{\beta}{M} H_{\text{even/odd}}}$ in Eq. (2.3.43). Because the individual summands of $H_{\text{even/odd}}$ commute, their contribution can be written as a product of $(N/2) \times (2M)$ plaquette weights

$$W_p(\{s_p, n_p\}) = \langle s_i^k \, s_{i+1}^k \, n_i^k | e^{-\beta H_i/M} | s_i^{k+1} s_{i+1}^{k+1} n_i^{k+1} \rangle. \tag{2.3.45}$$

The plaquettes are defined on a $(1 + 1)$-dimensional modified checkerboard lattice (see also Fig. 2.8), i. e. there are only plaquettes between Trotter slices with $k = 3l$, $k = 3l + 1$ (mediating the action of H_{even}) and $k = 3l + 1$, $k = 3l + 2$ (corresponding to H_{odd}), respectively. We point out that in addition to the spin variables the plaquette weights also depend on the two phonon occupation numbers $n_i^{k/k+1}$ on the selected bond. Fluctuations of the phonon occupation numbers can only occur on the shaded plaquettes of the modified checkerboard lattice.

2. The factor $W_{\text{ph}}(\{n_i^k\})$ arises from the action of the terms $e^{-\frac{\beta}{M} H_{\text{ph}}}$ (see relation (2.3.43)) between Trotter slices with $k = 3l + 2$, $k = 3(l + 1)$. Between these slices, the classical variables for both spins and phonons cannot change because H_{ph} is diagonal with respect to the chosen basis of the Hilbert space. In addition, we can immediately write down the result

$$W_{\text{ph}}(\{n_i^k\}) = \prod_{i, k=3l} e^{-\frac{\beta}{M} \omega n_i^k}. \tag{2.3.46}$$

To be able to construct the loop algorithm for the bond coupling model (2.3.39) we still need the explicit expressions for the plaquette weights (2.3.45). In analogy to the case of the XXZ model, there are only six spin configurations with non-vanishing plaquette weight, for a detailed calculation see App. A.2. Introducing the abbreviation $\eta \equiv 2\beta J/M$, the results are

$$a(n, n') \equiv \langle + + n | e^{-\beta H_i/M} | + + n' \rangle = \langle - - n | e^{-\beta H_i/M} | - - n' \rangle = \delta_{n,n'}, \tag{2.3.47}$$

$$b(n, n') \equiv \langle + - n | e^{-\beta H_i/M} | - + n' \rangle = \langle - + n | e^{-\beta H_i/M} | + - n' \rangle$$

$$= \frac{1}{2}[A(g, \eta, n, n') - \delta_{n,n'}], \tag{2.3.48}$$

$$c(n, n') \equiv \langle + - n | e^{-\beta H_i/M} | + - n' \rangle = \langle - + n | e^{-\beta H_i/M} | - + n' \rangle$$

$$= \frac{1}{2}[A(g, \eta, n, n') + \delta_{n,n'}], \tag{2.3.49}$$

where the quantity A is given by the expression

$$A(g, \eta, n, n') = \begin{cases} e^{\eta} \delta_{n,n'} & \text{if } g\eta = 0, \\ e^{\eta(1 + \frac{1}{2}\eta g^2)} \sqrt{n! n'!} \sum_{k=\max\{0, n'-n\}}^{n'} \frac{(g\eta)^{n-n'+2k}}{k!(n-n'+k)!(n'-k)!} & \text{else.} \end{cases} \tag{2.3.50}$$

Note that the plaquette weights (2.3.47),(2.3.48),and (2.3.49) are all positive or equal to zero because the relation $A(g, \eta, n, n') \geq \delta_{n,n'}$ holds.[4]

---

[4]As in Sect. 2.2.1, we assume having applied the unitary transformation (2.2.11) to the Hamiltonian to guarantee
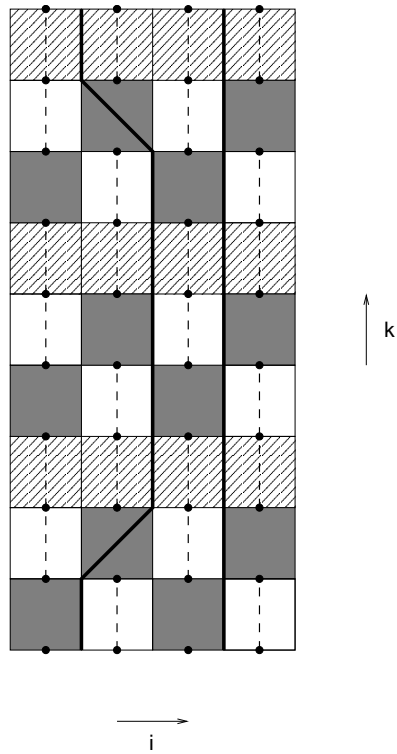
Fig. 2.8.: Illustration of the modified checkerboard lattice for the bond coupling model (2.3.39). The slices with diagonal stripes indicate the action of $e^{-\frac{\beta}{M}H_{\text{ph}}}$. The thick solid lines represent a set of closed worldlines for the spin degrees of freedom. The circles correspond to the phonon degrees of freedom which can only fluctuate on the shaded plaquettes of the lattice, i. e. the occupation numbers of phonons in the same block (indicated by the dashed lines) take the same value.

In particular, our results imply that we can still use the worldline (or vertex) picture to visualize the spin degrees of freedom on the modified $(1 + 1)$-dimensional checkerboard lattice. We first introduce the convention that between Trotter slices connected by the action of $e^{-\frac{\beta}{M}H_{\text{ph}}}$, we simply draw vertical worldline segments between Ising spins with positive spin (or a vertical arrow pointing in imaginary time direction in the vertex picture). Otherwise no wordline is drawn (the arrow is pointing against the Trotter time direction). On the shaded plaquettes of the lattice, we follow our usual convention. Then as for the XXZ model, the spin part of a configuration which contributes to the partition function is given by a set of closed worldlines on the modified plaquette lattice. An example for a worldline configuration on a lattice with $N = 4$ sites and $3M = 9$ Trotter slices is given in Fig. 2.8.

We are now in the state to construct a QMC algorithm for the model (2.3.39). Due to the coupling between spin and lattice degrees of freedom, however, it is difficult to derive an algorithm which works directly in the continuous time limit $M \to \infty$. For this reason a discrete time algorithm was used to simulate the finite-temperature behavior of the model and its counterpart in two

---

that the plaquette weight b is positive.

dimensions. As we have mentioned before, such an approach requires an extrapolation of the numerical data to infinite Trotter number. Alternatively, the simulations have to be carried out for values of M large enough that the systematic error due to the discretization of the time direction becomes smaller than the statistical error of measured quantities. The algorithm consists of two independent parts: the spin degrees of freedom are updated by means of a modified version of the loop algorithm for the XXX chain (with finite M) as discussed in Sect. 2.2.4. We comment on the details in the following subsection. For the phonon occupation numbers, we apply an update procedure which is based on local updates of *blocks* of three phonons indicated by the dashed lines in Fig. 2.8. We discuss this procedure in Sect. 2.3.3 and show that, depending on the underlying spin configuration, the algorithm can be improved by identifying *clusters* of such blocks which can be updated simultaneously.

We close this subsection with a remark concerning the choice of the summands H_i in the spin-phonon part H_{sp} of the Hamiltonian (2.3.39). In principle, the generalized Trotter-Suzuki formula has only been proven for bounded operators. Since they contain the displacement operators $[a_i^\dagger + a_i]$, the summands H_i do not fulfill this requirement. However, a number of numerical results based on the QMC algorithm described in this section have been compared to numerical data obtained from the flow equation and high temperature series expansion methods [RLUK02, Büh03, BUO04]. The comparison yields a convincing agreement between the different approaches, which justifies the application of the generalized Trotter-Suzuki formula in our case.

2.3.2. Modified loop update

In this subsection we briefly comment on the loop updates for the spin degrees of freedom $\{s_i^k\}$ on the $(1+1)$-dimensional modified checkerboard lattice as introduced in the previous subsection. We point out that during a spin update, we keep the phonon occupation numbers $\{n_i^k\}$ fixed. In principle, the loops are constructed in the same way as for the XXZ chain. On each of the shaded plaquettes of the lattice, we specify a breakup of vertices. As ususal, the possible choices of breakups depend on the underlying spin configuration as depicted in Fig. 2.4, see Sect. 2.2.2. Between Trotter slices connected by the action of $e^{-\frac{\beta}{M}H_{ph}}$, we simply draw vertical loop segments between adjacent spins in imaginary time direction. By using this convention, we assure that the two spins of each pair s_i^k, s_i^{k+1} lie on the same loop, where $k = 3l+2$. Thus upon flipping the loop, the two spins remain in the same state. By applying this scheme we arrive at a graph consisting of clusters of closed loops on the modified plaquette lattice.

Because the weight $W(\{s_i^k, n_i^k\})$ of a given configuration factorizes into a product of plaquette weights $W_p(\{s_p, n_p\})$ and the phonon contribution $W_{ph}(\{n_i^k\})$ (see Eq.(2.3.44)), the formal description is completely analogous to the one in Sect. 2.2.2. By identifying the weight $W(\{s_i^k\})$ from Par. 2.2.2 with the product $\prod_p W_p(\{s_p, n_p\})$ and omitting the dependence of the plaquette and breakup weights on the phonon occupation numbers, we receive the same solutions for the breakup weights as for the XXZ model. In particular, this means that the freezing weights f_i ($i = 1, 2, 3$) vanish and that the relations (2.2.21), (2.2.22), and (2.2.23) still hold. Furthermore, the loop flip probability of $\frac{1}{2}$ remains the same.

In addition, we have to stress that the plaquette weights (2.3.47), (2.3.48), and (2.3.49) obey

the relation $a + b = c$ as in the case of the isotropic Heisenberg chain. This means that the results from the beginning of Sect. 2.2.4 directly apply to the loop update procedure for the bond coupling model. Hence we only have to take a stochastic decision for the type of breakup on plaquettes with weight c. On these plaquettes, the probability for choosing a horizontal breakup is given by the fraction $\frac{b}{c}$.

2.3.3. Phonon updates

We now discuss the update procedure for the phonon occupation numbers $\{n_i^k\}$. During a phonon update, the values for the spin variables $\{s_i^k\}$ are kept fixed. In contrast to the global loop update for the spin degrees of freedom, the update scheme for the phonons is based on local changes of the phonon occupation numbers. Therefore to minimize autocorrelation effects, it is useful to repeat the phonon update procedure from this subsection several times between successive loop updates.

As we have mentioned in Sect. 2.3.1, the phonons on the modified plaquette lattice can be grouped into blocks consisting of three phonons $n_i^k, n_i^{k+1}, n_i^{k+2}$, with $k = 3l + 1$ ($k = 3l + 2$) for even (odd) values of i. Due to the structure of the Trotter-Suzuki decomposition, the phonons of each block take the same value and hence have to be updated simultaneously. Thus in principle, a full update of the whole set of phonon occupation numbers $\{n_i^k\}$ consists of $N \times M$ local updates of the phonons of each block. In practice this can be done blockwise, i. e. the occupation numbers in each block are updated block by block until the whole lattice has been visited.

Now let us consider such a block where the three numbers $n_i^k, n_i^{k+1}, n_i^{k+2}$ take a certain value n_1. Similarly, we assume that the phonon occupation numbers of the two adjacent blocks with respect to the imaginary time axis are given by n_0 and n_2. The situation is visualized in the left part of Fig. 2.9. According to Eq. (2.3.44), the weight of the whole configuration can be written as

$$W(\{n_i^k\}) = W_{\text{rest}}(\{n_i^k\})\, W_{p_1}(n_0, n_1)\, W_{p_2}(n_1, n_2)\, e^{-\frac{\beta}{M}\omega n_1}, \tag{2.3.51}$$

where we have omitted all dependences on the spin variables for the moment. Here $W_{p_1}(n_0, n_1)$ and $W_{p_2}(n_1, n_2)$ denote the plaquette weights of the two plaquettes at the boundaries of the block, while the factor $e^{-\frac{\beta}{M}\omega n_1}$ corresponds to the n_1-dependent part of the contribution W_{ph} from Eq. (2.3.46). The abbreviation $W_{\text{rest}}(\{s_i^k, n_i^k\})$ contains all the plaquette weights and factors of W_{ph} which do not depend on the occupation number n_1 of the block. In the following we suggest a change $n_1 \rightarrow n_1'$ in the block. This corresponds to a change $\{n_i^k\} \rightarrow \{n_i^k\}'$ of the configuration of phonons on the plaquette lattice, which we accept according to the heat bath probability (compare also Eq. (2.2.16))

$$\begin{aligned} p(\{n_i^k\} \rightarrow \{n_i^k\}') &= \frac{W(\{n_i^k\}')}{W(\{n_i^k\}) + W(\{n_i^k\}')} \\ &= \frac{W_{p_1}(n_0, n_1')W_{p_2}(n_1', n_2)e^{-\frac{\beta}{M}\omega n_1'}}{W_{p_1}(n_0, n_1)W_{p_2}(n_1, n_2)e^{-\frac{\beta}{M}\omega n_1} + W_{p_1}(n_0, n_1')W_{p_2}(n_1', n_2)e^{-\frac{\beta}{M}\omega n_1'}}. \end{aligned} \tag{2.3.52}$$

Here we have taken advantage of the fact that the factor $W_{\text{rest}}(\{n_i^k\})$ cancels in the second line. The choice (2.3.52) guarantees that the condition of detailed balance (2.1.2) is fulfilled.
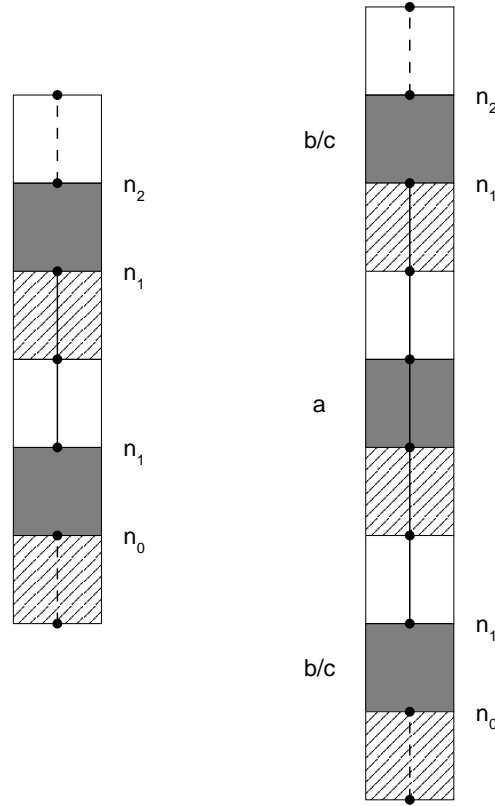
Fig. 2.9.: Visualization of a block (left) and a cluster consisting of two blocks (right) with phonon occupation number n_1 on a bond with even index i. The occupation numbers in the adjacent blocks (clusters) are n_0 and n_2.

In the following we discuss an important observation which leads us to a significant improvement of this update scheme. Let us imagine that on one of the two plaquettes at the boundary of the selected block, we have a spin configuration with plaquette weight a. Then we find that for any $n'_1 \neq n_1$ the weight $W(\{n_i^k\}')$ and hence the update probability (2.3.52) vanishes due to the Kronecker symbol in the expression (2.3.47). This implies that the phonon occupation number of the block is frozen until we apply a spin update to alter the underlying configuration of Ising spins.

We can avoid this problem by building clusters of blocks. Such a cluster can be constructed as follows. Starting on a plaquette with weight $W_{p_1} \neq a$, we move along the time direction and neglect all the plaquettes with weight a. After having passed by Q such plaquettes, we finally reach a plaquette with weight $W_{p_2} \neq a$. Grouping the blocks together, we obtain a cluster consisting of $(Q+1)$ blocks with one common phonon occupation number. An example for a cluster with $Q = 1$ is given in the right panel of Fig. 2.9. To construct an update for this number, we first note that Eq. (2.3.51) can be generalized by writing

$$W(\{n_i^k\}) = W_{\mathrm{rest}}(\{n_i^k\}) \, W_{p_1}(n_0, n_1) \, W_{p_2}(n_1, n_2) \, e^{-\frac{\beta}{M}\omega(Q+1)n_1}, \tag{2.3.53}$$

because the contribution of each of the Q intermediate plaquettes with weight a is equal to unity.

The abbreviation $W_{\text{rest}}(\{n_i^k\})$ now includes all the factors which do not depend on the occupation number n_1 of the cluster. Then a change $n_1 \to n_1'$ in the whole cluster is accepted with probability (compare Eq. (2.3.52))

$$p(\{n_i^k\} \to \{n_i^k\}') = \frac{W_{p_1}(n_0, n_1')W_{p_2}(n_1', n_2)e^{-\frac{\beta}{M}\omega(Q+1)n_1'}}{W_{p_1}(n_0, n_1)W_{p_2}(n_1, n_2)e^{-\frac{\beta}{M}\omega(Q+1)n_1} + W_{p_1}(n_0, n_1')W_{p_2}(n_1', n_2)e^{-\frac{\beta}{M}\omega(Q+1)n_1'}}. \tag{2.3.54}$$

It is obvious how these formulae have to be modified for the special case $Q = M$, i. e. the cluster extends over all Trotter slices in imaginary time direction (or for the case $Q = M - 1$, which means that all of the plaquettes except for one have the plaquette weight a). Applying the cluster updates for the phonon degrees of freedom, it becomes evident immediately that the whole algorithm satisfies the ergodicity condition.

We add that for practical applications, one cannot allow the phonon occupation numbers to take any natural number. Instead of this we have to introduce a *cutoff* n_{max} for the phonons, i. e. we only allow for values $n_i^k \leq n_{\text{max}}$. Evidently, this way of proceeding leads to systematical errors during the simulation. These deviations, however, are well controlled if the measured mean occupation numbers stay significantly smaller than the value selected for the cutoff. Such an analysis has been done for the algorithm both in one and two dimensions [KL99, AL03].

We finally comment on how the concept of importance sampling can be incorporated for the update procedure described above. As before, we consider a cluster consisting of Q blocks and calculate the quantities

$$S(n_1') = \sum_{j=0}^{n_1'} W_{p_1}(n_0, j) W_{p_2}(j, n_2) e^{-\frac{\beta}{M}\omega(Q+1)j}, \qquad n_1' = 0, \ldots, n_{\text{max}}. \tag{2.3.55}$$

In addition we define $S(-1) \equiv 0$. If we now draw a random number $x \in [0, 1)$, there is always an integer n_1' with

$$\frac{S(n_1' - 1)}{S(n_{\text{max}})} \leq x < \frac{S(n_1')}{S(n_{\text{max}})}, \tag{2.3.56}$$

which we take as the new occupation number for the cluster. This implies

$$p(\{n_i^k\} \to \{n_i^k\}') = \frac{W_{p_1}(n_0, n_1')W_{p_2}(n_1', n_2)e^{-\frac{\beta}{M}\omega(Q+1)n_1'}}{S(n_{\text{max}})} \tag{2.3.57}$$

for the update probability, which is the natural extension of relation (2.3.54) and can be shown easily to satisfy detailed balance.

2.3.4. Two-dimensional model

In analogy to the argumentation for the Heisenberg model in Sect. 2.2.4, we can immediately generalize the loop algorithm for the spin-phonon coupling model (2.3.39) to a QMC algorithm for

its two-dimensional counterpart

$$H = H_{\text{sp}} + H_{\text{ph}}, \qquad \text{with} \tag{2.3.58}$$

$$H_{\text{sp}} = \sum_{i,j=1}^{N} \{H_{ij}^x + H_{ij}^y\}$$

$$\equiv \sum_{i,j=1}^{N} \left\{ \frac{J}{2}(\vec{\sigma}_{ij}\vec{\sigma}_{i+1,j} - 1)(1 + g[a_{ij}^\dagger + a_{ij}]) + \frac{J}{2}(\vec{\sigma}_{ij}\vec{\sigma}_{i,j+1} - 1)(1 + g[b_{ij}^\dagger + b_{ij}]) \right\},$$

$$H_{\text{ph}} = \omega \sum_{ij=1}^{N} (a_{ij}^\dagger a_{ij} + b_{ij}^\dagger b_{ij}),$$

According to our usual notation, the symbols $\vec{\sigma}_{ij}$ denote Pauli spin matrices at the sites of a square lattice with $N \times N$ sites and periodic boundary conditions. Since there are two bonds per lattice site, we have to introduce two types of phonon creation (annihilation) operators $a_{ij}^\dagger$, $b_{ij}^\dagger$ (a_{ij}, b_{ij}) corresponding to the bonds oriented along the i- and j-direction, respectively. As in one dimension, we have $J > 0$ and $g, \omega \geq 0$ for the coupling constants of the model. The (unphysical) static terms $-\frac{gJ}{2}(a_{ij}^\dagger + a_{ij})$, $-\frac{gJ}{2}(b_{ij}^\dagger + b_{ij})$ can be avoided by considering the two-dimensional analog of the phonon shift (2.3.41) from Par. 2.3.1. For a detailed discussion on the properties of the model we refer to Chapt. 4.

We first mention that by transferring our results from the preceeding three sections to the two-dimensional case we do not gain fundamental new insights. For this reason we keep the following discussion as short as possible, which is given for the sake of completeness. We split the part H_{sp} from Eq. (2.3.58) into four parts

$$H_{\text{sp}} = H_{\text{even}}^x + H_{\text{odd}}^x + H_{\text{even}}^y + H_{\text{odd}}^y, \qquad \text{with} \tag{2.3.59}$$

$$H_{\text{even}}^x = \sum_{ij} H_{2i,j}^x, \quad H_{\text{odd}}^x = \sum_{ij} H_{2i+1,j}^x, \quad H_{\text{even}}^y = \sum_{ij} H_{i,2j}^y, \quad H_{\text{odd}}^y = \sum_{ij} H_{i,2j+1}^y,$$

and apply the usual Trotter-Suzuki breakup [Tro59, Suz76]

$$Z = \text{Tr}\, e^{-\beta H} = \lim_{M \to \infty} Z_M \equiv \lim_{M \to \infty} \text{Tr}\, \left(e^{-\frac{\beta}{M}H_{\text{even}}^x} e^{-\frac{\beta}{M}H_{\text{odd}}^x} e^{-\frac{\beta}{M}H_{\text{even}}^y} e^{-\frac{\beta}{M}H_{\text{odd}}^y} e^{-\frac{\beta}{M}H_{\text{ph}}} \right)^M. \tag{2.3.60}$$

This time we have to insert $(5M - 1)$ complete sets of eigenstates of the operators σ_{ij}^z for all the sites, and of the operators $n_{ij} \equiv a_{ij}^\dagger a_{ij}$, $m_{ij} \equiv b_{ij}^\dagger b_{ij}$ for all the bonds of the lattice to obtain the partition function of a $(2 + 1)$-dimensional classical model

$$Z_M = \sum_{\{s_{ij}^k, n_{ij}^k, m_{ij}^k\}} W(\{s_{ij}^k, n_{ij}^k, m_{ij}^k\}) = \sum_{\{s_{ij}^k, n_{ij}^k, m_{ij}^k\}} \left(\prod_p W_p(\{s_p, n_p/m_p\}) \right) W_{\text{ph}}(\{n_{ij}^k, m_{ij}^k\}). \tag{2.3.61}$$

The partition function (2.3.61) depends on classical Ising spins $s_{ij}^k = \pm 1$ and phonon occupation numbers $n_{ij}^k, m_{ij}^k \in \mathbb{N}$, where $k = 0, \ldots, 5M - 1$ is the index for the Trotter direction as usual. The lattice of the classical system can be characterized as a $(2+1)$-dimensional generalized checkerboard lattice similar to the one depicted in Fig. 2.7, see Sect. 2.2.4. In analogy to Fig. 2.8 for the one-dimensional model, however, we have to insert an additional striped slice indicating the action of

$e^{-\frac{\beta}{M}H_{\mathrm{ph}}}$ between the slices with plaquettes corresponding to the terms $e^{-\frac{\beta}{M}H^y_{\mathrm{odd}}}$ and $e^{-\frac{\beta}{M}H^x_{\mathrm{even}}}$. In addition to the spin degrees of freedom $\{s_p\}$, the plaquette weights W_p of plaquettes associated with the action of $e^{-\frac{\beta}{M}H^x_{\mathrm{even/odd}}}$ ($e^{-\frac{\beta}{M}H^y_{\mathrm{even/odd}}}$) also depend on two phonon occupation numbers $\{n_p\}$ (or $\{m_p\}$) as indicated in Eq. (2.3.61). In principle, they are given by the same matrix elements (2.3.45) as in one dimension, i. e. the explicit expressions for the non-vanishing plaquette weights (2.3.47), (2.3.48), and (2.3.49) are still valid.[5] The result for W_{ph} becomes

$$W_{\mathrm{ph}}(\{n^k_{ij}, m^k_{ij}\}) = \prod_{i,j,k=5l} e^{-\frac{\beta}{M}\omega(n^k_{ij}+m^k_{ij})} \tag{2.3.62}$$

in two dimensions.

Using the same conventions as for the spin-phonon chain, we can still apply the worldline (or vertex) picture to visualize the spin part of a given configuration. Furthermore, we have argued that the results for the plaquette weights do not depend on the dimensionality of the system. In particular, this means that the relation $a + b = c$ holds for the non-vanishing matrix elements on the plaquettes. Hence we can apply the discrete time version of the loop algorithm for the two-dimensional Heisenberg model as described in Sect. 2.2.4 as a valid update procedure for the spin degrees of freedom. As has been motivated in Sect. 2.3.2, we only have to set up vertical loop segments between adjacent sites (with respect to the imaginary time axis) in Trotter slices connected by the action of $e^{-\frac{\beta}{M}H_{\mathrm{ph}}}$ to join those parts of loops which have been specified by the breakups on the individual plaquettes.

The update procedure for the phonons is identical to the one described in Par. 2.3.3. Here each block consists of five phonon occupation numbers which take the same value and hence have to be updated simultaneously. Because the phonon degrees of freedom in the Hamiltonian (2.3.58) are defined on the bonds of the lattice we can proceed bondwise, identify clusters and update the phonon occupation number of each cluster successively.

2.3.5. Summary: sketch of the algorithm

As already done for the pure spin models, we will now summarize the update procedure for the bond coupling model in one and two dimensions by giving a short sketch of the algorithm. The algorithm was implemented as a C++ program to compute correlation functions for the one- and two-dimensional bond coupling model.

We assume starting with a configuration which contributes to the partition function (2.3.44) (Eq. (2.3.61) in two dimensions). Such a configuration is specified by storing the values of $N \times (3M)$ Ising variables $\{s^k_i\}$ plus the values of $N \times (3M)$ phonon occupation numbers $\{n^k_i\}$ (for the two-dimensional model, we need each $(N^2) \times (5M)$ values for the numbers $\{s^k_{ij}\}$, $\{n^k_{ij}\}$, and $\{m^k_{ij}\}$). Then an update of both spin and phonon degrees of freedom consists of the following steps.

1. Loop update for spin variables:

   a) Specify breakups on the individual plaquettes of the lattice. On plaquettes with spin configurations corresponding to the plaquette weights a and b the choice is unique,

---

[5]We assume having applied the same unitary transformation to the Hamiltonian as for the two-dimensional Heisenberg model in Sect. 2.2.4.

namely vertical and horizontal breakups, respectively. On plaquettes with weight c, select a horizontal breakup with probability $\frac{b}{c}$ and a vertical breakup otherwise.

b) Identify loops. By adding vertical loop segments between Trotter slices connected by the action of $e^{-\frac{\beta}{M}H_{\mathrm{ph}}}$ on each site of the lattice, the loop segments defined by the breakups combine to a set of closed loops. The individual loops are identified by following the loop segments through the lattice. The loop identification is finished if a loop number has been assigned to each of the $N \times (3M)$ spin variables $\{s_i^k\}$ (or $(N^2) \times (5M)$ spins $\{s_{ij}^k\}$ in the two-dimensional case).

c) Determine which of the loops are flipped according to the loop flip probability $\frac{1}{2}$.

d) Flip the loops by inverting the Ising spins which belong to the loops determined in the previous step.

2. Cluster updates for phonon occupation numbers:

a) Identify clusters. This is done bondwise by analyzing the spin configuration on the individual plaquettes.

b) On each bond of the lattice, update the phonon occupation numbers in each cluster by applying the importance sampling procedure from Sect. 2.3.3. Proceed cluster by cluster until each cluster on the selected bond has been visited. Repeat this procedure several times (e. g. 30 times).

3. Measure observables. This step is only performed if the algorithm has thermalized. The rules for the measurement of thermodynamic quantities are described in the following section.

2.4. Measurement of correlation functions and numerical error analysis

In this part we will ask the question how one can measure thermal expectation values within the loop algorithm. We restrict ourselves to the case of arbitrary spin correlation functions and, to simplify matters, derive measurement rules on the basis of the loop algorithm for the XXZ chain in discrete time, see Sects. 2.2.1 and 2.2.2. One can proof easily that the same rules hold for the other types of models from Sects. 2.2 and 2.3. Furthermore, they can be generalized trivially to the continuous time limit. In the next subsection, we first consider the simple case of diagonal operators with respect to the chosen basis of the Hilbert space. We then concentrate on two-point correlations (Sect. 2.4.2), and show that in principle both diagonal and off-diagonal spin correlators can be calculated efficiently by evaluating the loop properties of a given worldline configuration. In Sect. 2.4.3, we formalize this idea and address the case of general n-point correlations. We close by discussing the issues of numerical error analysis and autocorrelation effects in Sect.2.4.4.

2.4.1. Diagonal operators

In this subsection, we concentrate on operators which are diagonal with respect to the basis of the Hilbert space. In our description of the loop algorithm for the XXZ chain, we have characterized the spin degrees of freedom in a basis of σ^z eigenstates, see Sect. 2.2.1. Thus focussing on equal-time correlations for the beginning, we are interested in expectation values of diagonal operators of the type

$$D \equiv \prod_{\alpha=1}^{n} \sigma_{i_\alpha}^z, \tag{2.4.63}$$

i. e. we assume that D factorizes into a product of n Pauli spin matrices $\sigma_{i_\alpha}^z$ acting on the spins at those lattice sites characterized by the indices i_α. For example, in case of the longitudinal two-point spin correlation function we have $D = \sigma_i^z \sigma_j^z$. We start by making use of the Suzuki-Trotter decomposition from Sect. 2.2.1, and write

$$\langle D \rangle = \frac{1}{Z} \mathrm{Tr} \left(D e^{-\beta H} \right) = \lim_{M \to \infty} \langle D \rangle_M \equiv \lim_{M \to \infty} \frac{1}{Z_M} \mathrm{Tr}\, D \left(e^{-\frac{\beta}{M} H_{\mathrm{even}}} e^{-\frac{\beta}{M} H_{\mathrm{odd}}} \right)^M, \tag{2.4.64}$$

where Z and Z_M are given by the expressions (2.2.5) and (2.2.6), respectively. In the following, we keep the Trotter number M fixed and consider the Mth approximant $\langle D \rangle_M$, using the same notation as is Par. 2.2.1. In analogy to our treatment of the partition function Z_M, we insert $(2M - 1)$ complete sets of σ^z eigenstates between the exponentials in Eq. (2.4.64). Furthermore, we apply the operator D to the additional set of eigenstates stemming from the trace symbol, which we label with the index $k = 0$ in the following. Since D is diagonal, we immediately find

$$\langle D \rangle_M = \frac{1}{Z_M} \sum_{\{s_i^k\}} W(\{s_i^k\}) \prod_{\alpha=1}^{n} s_{i_\alpha}^0. \tag{2.4.65}$$

We can generalize this result easily to the case of time-dependent correlations, i. e. now we consider operators

$$D \equiv \prod_{\alpha=1}^{n} \sigma_{i_\alpha}^z(\tau_\alpha). \tag{2.4.66}$$

Since we discuss the loop algorithm in discrete time, we assume that the times τ_α are integer multiples[6] of $\Delta\tau \equiv \frac{\beta}{M}$. This implies that we can write $\tau_\alpha \equiv l_\alpha \Delta\tau$ with integers $0 \leq l_\alpha \leq M - 1$. The time dependence of the individual factors $\sigma_{i_\alpha}^z(\tau_\alpha)$ is due to a translation in imaginary time direction, which is given by

$$A(\tau) \equiv e^{-\tau H} A\, e^{\tau H} \tag{2.4.67}$$

for any (not necessarily diagonal) operator A. Thus we can apply each factor $\sigma_{i_\alpha}^z(\tau_\alpha)$ from the definition (2.4.66) to the set of eigenstates characterized by the index $k = 2l_\alpha$, and the relation (2.4.65) is replaced by

$$\langle D \rangle_M = \frac{1}{Z_M} \sum_{\{s_i^k\}} W(\{s_i^k\}) \prod_{\alpha=1}^{n} s_{i_\alpha}^{2l_\alpha}. \tag{2.4.68}$$

---

[6]In continuous time, the times τ_α can take arbitrary values in the interval $[0, \beta)$.

Note that this result is identical to the formula one obtains for the operator $\tilde{D} = U^\dagger D U$, where U is the unitary transformation (2.2.11) which we applied to the Hamiltonian in Sect. 2.2.1 to avoid negative plaquette weights.

From the relation (2.4.68), we can immediately read the measurement rule for diagonal operators (2.4.66) in a QMC simulation. One obtains a numerical estimate for the quantity $\langle D \rangle_M$ by averaging

$$\langle D \rangle_M^{\mathrm{MC}} = \frac{1}{u} \sum_{\{s_i^k\}}' \prod_{\alpha=1}^{n} s_{i_\alpha}^{2l_\alpha}, \qquad (2.4.69)$$

where u is the number of Monte Carlo updates (after the algorithm has thermalized), and the sum $\sum_{\{s_i^k\}}'$ extends over the individual configurations of the Markov chain.

Before we address the case of off-diagonal operators, we add a remark concerning the extrapolation to infinite Trotter number. To obtain a reliable estimate $\langle D \rangle^{\mathrm{MC}}$ for the expectation value $\langle D \rangle = \lim_{M \to \infty} \langle D \rangle_M$, one needs to calculate the numerical estimate (2.4.69) for various values of M. Afterwards these numbers have to be extrapolated to the limit $M \to \infty$, which is well controlled because in leading order the relation $\langle D \rangle_M \sim \frac{1}{M^2}$ holds [Suz85]. As has been mentioned earlier, such an extrapolation can be avoided if the value for the Trotter number is that large that the systematic error due to the discretization of time is significantly smaller than the statistical error (see Sect. 2.4.4) due to the finite number u of configurations generated during the simulation. The best choice, however, is to run the simulation in continuous time and to compute the expectation value $\langle D \rangle^{\mathrm{MC}}$ directly.

2.4.2. Improved estimators and off-diagonal correlation functions

We are now going to concentrate on the issue of expectation values of non-diagonal operators. The concept behind the evaluation of such correlators can be best understood if we restrict ourselves to the case of two-point correlation functions, for which we illustrate the basic ideas in this subsection. A formal description and the more complicated case of general n-point correlations will be discussed in the following section.

In Sect. 2.2.2 we have already mentioned that by selecting a breakup on the individual plaquettes of the $(1+1)$-dimensional checkerboard lattice, we have mapped a worldline configuration of spins $\{s_i^k\}$ to a combination of worldlines and loops $(\{s_i^k\}, G)$. This construction enables us not only to measure an operator in each configuration of the Markov chain, but also in all configurations related by loop flips. We first construct such an *improved estimator* for the simple case of the (time-dependent) two-point function $\langle \sigma_x^z \sigma_y^z \rangle$, using a simplified notation by omitting the subindex M for expectation values and introducing indices x, y which label both space and Trotter time, i. e. $x \equiv (i, \tau_1)$ and $y \equiv (j, \tau_2)$. According to our results from the previous section, each worldline configuration gives a contribution of $s_x s_y$ to the numerical estimate for this correlation function, compare Eq. (2.4.69). However, one obtains a better estimate by averaging this contribution over all configurations which can be constructed by (virtually) flipping the loops of the underlying graph. In our example, we have to distinguish between two cases. We first assume that the two spins s_x, s_y belong to different loops. In this case we have to average over four different worldline configurations, because each of the two loops can either be flipped or not. This means that we have
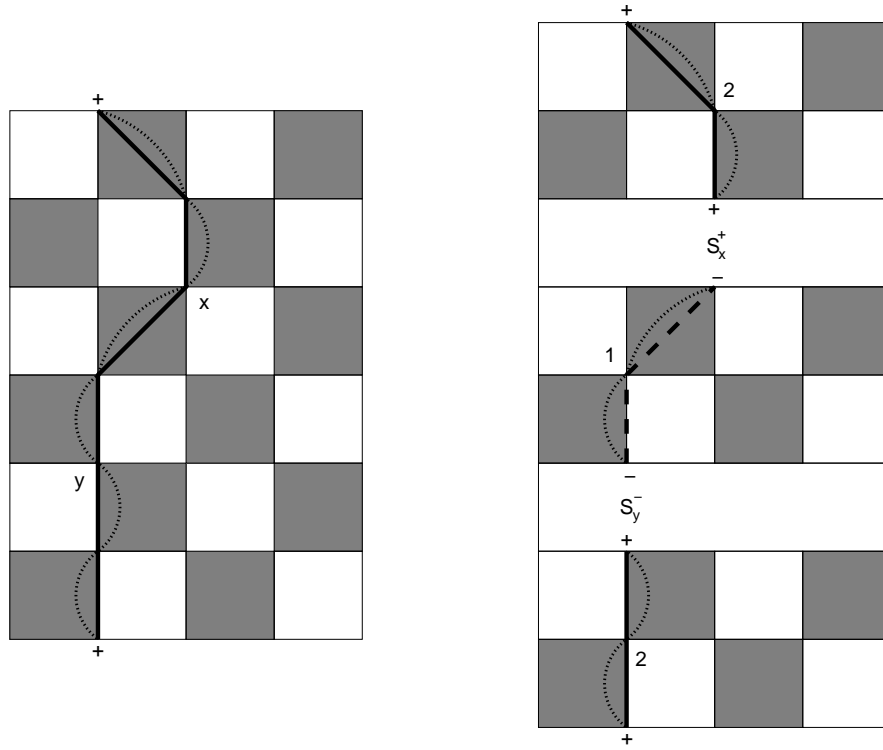
Fig. 2.10.: Example for a configuration which contributes to $\langle S_x^+ S_y^- \rangle$. On the left, a spin configuration with one closed worldline is shown. The spins on the sites x, y are connected by a loop which is depicted by the dashed line. The right panel illustrates the modified checkerboard lattice after the insertion of two extra Trotter slices for the action of S_x^+ and S_y^-. After inverting the spins on the partial loop marked by the number 1, one obtains the desired propagator.

$\frac{1}{4}[s_x s_y + s_x(-s_y) + (-s_x)s_y + (-s_x)(-s_y)] = 0$ for the total contribution. The second possibility is that both spins belong to the same loop, which can either change or keep its direction. Then the total contribution is $\frac{1}{2}[s_x s_y + (-s_x)(-s_y)] = s_x s_y$. Hence we find

$$\langle \sigma_x^z \sigma_y^z \rangle \rightarrow \begin{cases} s_x s_y & \text{if } s_x, s_y \text{ belong to the same loop,} \\ 0 & \text{else,} \end{cases} \tag{2.4.70}$$

for the improved estimator. We see that besides the spin configuration the improved estimator (2.4.70) also explicitly depends on the particular graph.

In the following we argue that the same concept can be used to calculate off-diagonal correlations [BCW98, AG00]. As an example, we consider the correlation function $\langle S_x^+ S_y^- \rangle$, where $S^{\pm} = \frac{1}{2}(\sigma^x \pm i\sigma^y)$ are the ladder operators of the spin algebra for spin-$\frac{1}{2}$. For example, measurement rules for this expectation value are needed when calculating transversal spin correlations, because one can apply the identity $\langle \sigma_x^x \sigma_y^x \rangle = \frac{1}{2}\langle \sigma_x^x \sigma_y^x + \sigma_x^y \sigma_y^y \rangle = \langle S_x^+ S_y^- + S_x^- S_y^+ \rangle$. We first observe that the worldline configurations generated by the loop algorithm never contribute to this correlation function. To see this, we consider the same construction as we have used for diagonal operators in the previous section. As we did there for the individual factors $\sigma_{i_\alpha}^z(\tau_\alpha)$ from the product (2.4.66), we apply the

operators S_x^+, S_y^- on the complete sets of σ^z eigenstates at times τ_1 and τ_2, respectively. Then the contribution either vanishes due to the identity $S^\pm|\pm\rangle = 0$, or one obtains plaquettes which violate the conservation of the number of worldlines on the plaquette lattice. We can visualize the configurations which contribute to $\langle S_x^+ S_y^- \rangle$ if we introduce two extra Trotter slices for the action of S_x^+, S_y^- at the corresponding Trotter times (or one extra slice if $\tau_1 = \tau_2$ holds). On this modified checkerboard lattice, the configurations with non-vanishing contributions are characterized by a partial worldline or *propagator* connecting the two sites x, y, because then the z-component of the total spin on each plaquette of the original lattice is conserved. From this point of view it becomes even clearer that the worldline configurations generated during the simulation do not contribute because for such configurations all worldlines are closed by construction. However, within the loop algorithm we can measure $\langle S_x^+ S_y^- \rangle$ by virtually flipping partial loops and hence creating the desired propagator virtually. Again we have to distinguish between two cases. If s_x and s_y belong to different loops, there is no contribution because we cannot construct a partial worldline which connects the two spins. Only if s_x and s_y belong to the same loop, we can virtually flip one of the two partial loops between the two spins to obtain the desired propagator. This amounts to a total contribution of $\frac{1}{2}(1+0) = \frac{1}{2}$, because we can either flip the partial loop or not. Which part of the loop has to be considered depends on the current worldline configuration. An example is shown in Fig. 2.10. In summary, we find an improved estimator

$$\langle S_x^+ S_y^- \rangle \rightarrow \begin{cases} \frac{1}{2}(-1)^{i+j} & \text{if } s_x, s_y \text{ belong to the same loop,} \\ 0 & \text{else.} \end{cases} \tag{2.4.71}$$

The additional factor of $(-1)^{i+j}$ appears if one takes into account the unitary transformation (2.2.11) from Sect. 2.2.2.

2.4.3. Formal description

We now turn our attention to the case of general n-point correlation functions. To derive the measurement rules in question, we need to formalize the ideas of the preceeding subsection. A more detailed presentation is given in Ref. [AG00].

Our starting point is the mapping of a configuration $\{s_i^k\}$ of Ising spins to a combination $(\{s_i^k\}, G)$ of worldlines and loops by choosing breakups on the plaquettes. We further observe that we were able to find the solutions (2.2.21),(2.2.22), and (2.2.23) for the non-vanishing breakup weights by imposing the condition (2.2.17), i. e. the breakup weights only depend on the type of breakup and not on the spin configurations on the plaquettes. For this reason we can rewrite the partition function (2.2.6) in terms of a statistical model of *directed loops*, where the direction of a loop is given by the direction of the vertices of the worldline configuration. Starting from a loop configuration $\{\ell\}$ consisting of N_ℓ directed loops, we can construct 2^{N_ℓ} different configurations of directed loops by either flipping the individual loops or not. As can be seen from the identity (2.2.24), all these configurations have the same weight $W(\{\ell\}) \equiv W(\{s_i^k, G\})$. Hence we obtain

$$Z = \sum_{\{\ell\}} W(\{\ell\})\, 2^{N_\ell} = \sum_{\{\ell\}} W(\{\ell\}) \prod_{\ell \in \{\ell\}} \text{Tr}_\ell \prod_\mu \sigma^{\gamma_\mu}. \tag{2.4.72}$$

For the second equality we have rewritten our result as a weighted sum of traces over individual loops. The notation can be understood as follows. We first note that each loop consists of a number of loop segments defined by the breakups on the plaquettes. Each loop segment is identified with a 2×2 matrix σ^{γ_μ}. Because vertical and diagonal loop segments do not change the loop direction, they correspond to the identity matrix $\sigma^0 = \begin{pmatrix} 1 & 0 \\ 0 & 1 \end{pmatrix}$. A horizontal loop segment, on the other hand, does change the direction of the loop, and is therefore identified with the matrix $\sigma^x = \begin{pmatrix} 0 & 1 \\ 1 & 0 \end{pmatrix}$ in our notation. By using these conventions we can follow the course of a loop and collect a factor σ^{γ_μ} for each loop segment. For each closed loop, there is an even number of σ^x matrices under the trace in the relation (2.4.72). Because all the other loop segments correspond to the insertion of identity matrices and the identity $(\sigma^x)^2 = \sigma^0$ holds, we find a factor of $\mathrm{Tr}\,\sigma^0 = 2$ for each loop (two possible loop directions) and thus a total factor of 2^{N_ℓ} for the whole loop configuration as demanded.

We are now in the state to treat the issue of expectation values of general operators

$$O = \prod_{\alpha=1}^{n} S_{x_\alpha}^{\gamma_\alpha}, \tag{2.4.73}$$

where the symbols $S_{x_\alpha}^{\gamma_\alpha}$ correspond to operators $\sigma^z, S^\pm$ acting on the spins with spacetime indices $x_\alpha \equiv (i_\alpha, \tau_\alpha)$. In terms of the loop model as defined by Eq. (2.4.72), the action of each factor $S_{x_\alpha}^{\gamma_\alpha}$ is given by the insertion of an additional 2×2 matrix $\sigma_{x_\alpha}^{\gamma_\alpha}$ (to be specified below) between the two matrices σ^{γ_μ} which correspond to the two loop segments adjacent to the spin s_{x_α}. Therefore we have

$$\langle O \rangle = \frac{1}{Z} \sum_{\{\ell\}} W(\{\ell\}) \mathcal{T} \left(\prod_\alpha \sigma_{x_\alpha}^{\gamma_\alpha} \prod_{\ell \in \{\ell\}} \mathrm{Tr}_\ell \prod_\mu \sigma^{\gamma_\mu} \right), \tag{2.4.74}$$

where the symbol $\mathcal{T}$ denotes proper time and space ordering for the insertion of the additional matrices. Note that the insertion of extra factors under the traces in Eq. (2.4.74) corresponds to the introduction of additional Trotter slices which was discussed in the context of the correlations $\langle S_x^+ S_y^- \rangle$ in the previous subsection.

We now specify which kind of matrices $\sigma_{x_\alpha}^{\gamma_\alpha}$ have to be inserted for the factors $S_{x_\alpha}^{\gamma_\alpha}$ from the definition (2.4.73). Depending on the loop direction at the site x, the replacement is

$$\begin{Bmatrix} \sigma_x^z \\ S_x^+ \\ S_x^- \end{Bmatrix} \rightarrow \begin{Bmatrix} \sigma^z(\sigma^z) \\ \sigma^+(\sigma^-) \\ \sigma^-(\sigma^+) \end{Bmatrix} \tag{2.4.75}$$

for loops running along (against) the imaginary time direction, with 2×2 matrices $\sigma^z = \begin{pmatrix} 1 & 0 \\ 0 & -1 \end{pmatrix}$, $\sigma^+ = \begin{pmatrix} 0 & 1 \\ 0 & 0 \end{pmatrix}$, and $\sigma^- = \begin{pmatrix} 0 & 0 \\ 1 & 0 \end{pmatrix}$.

In the following we throw more light on these results by reproducing the improved estimators (2.4.70) and (2.4.71) from Sect. 2.4.2 for the two-point correlators $\langle \sigma_x^z \sigma_y^z \rangle$ and $\langle S_x^+ S_y^- \rangle$, respectively. As we did in the previous subsection, we first consider the case that the spins s_x, s_y lie on different loops. Then Eq. (2.4.74) implies that we have two factors of the type

$$\mathrm{Tr}\,(\sigma^{z/\pm} \prod_\mu \sigma^{\gamma_\mu}) = \mathrm{Tr}\,\sigma^{z/\pm} = 0, \tag{2.4.76}$$

s_x	s_y	contribution to $\langle \sigma_x^z \sigma_y^z \rangle$	contribution to $\langle S_x^+ S_y^- \rangle$
+1	+1	$\frac{1}{2}\mathrm{Tr}\,(\sigma^z\sigma^z) = 1$	$\frac{1}{2}\mathrm{Tr}\,(\sigma^+\sigma^-) = \frac{1}{2}$
-1	-1	$\frac{1}{2}\mathrm{Tr}\,(\sigma^z\sigma^z) = 1$	$\frac{1}{2}\mathrm{Tr}\,(\sigma^-\sigma^+) = \frac{1}{2}$
+1	-1	$\frac{1}{2}\mathrm{Tr}\,(\sigma^z\sigma^x\sigma^z\sigma^x) = -1$	$\frac{1}{2}\mathrm{Tr}\,(\sigma^+\sigma^x\sigma^+\sigma^x) = \frac{1}{2}$
-1	+1	$\frac{1}{2}\mathrm{Tr}\,(\sigma^z\sigma^x\sigma^z\sigma^x) = -1$	$\frac{1}{2}\mathrm{Tr}\,(\sigma^-\sigma^x\sigma^-\sigma^x) = \frac{1}{2}$

Table 2.1.: Verification of the results (2.4.70), (2.4.71) from Sect. 2.4.2 in the case that the spins s_x, s_y belong to the same loop.

because we can omit the σ^0 matrices for vertical and diagonal loop segments, and the σ^x matrices for horizontal loop segments only appear in pairs because each loop is closed. Hence only a non-vanishing contribution is found if the two spins belong to the same loop. In this case we can exploit the same observations. We only have to keep two σ^x-matrices for a change of the loop direction if the two spins s_x, s_y take different values. The one-loop contributions to $\langle \sigma_x^z \sigma_y^z \rangle$ and $\langle S_x^+ S_y^- \rangle$ in dependence on the loop orientation are given in Table 2.1. Note that the prefactors $\frac{1}{2}$ stem from the normalization factor $\frac{1}{Z}$ in Eq. (2.4.74). We see that the results coincide with our findings from the previous subsection if we take into account that the unitary transformation (2.2.11) generates an additional minus sign for each factor $S_{x_\alpha}^\pm$ with an even space index i_α in the definition (2.4.73).

We finally return to the general case of arbitrary n-point correlation functions. In principle, one can derive similar rules for these expectation values by analyzing the implications of Eq. (2.4.74). To do this in a systematic way, it is useful to consider all possible distributions of the n factors from relation (2.4.73) to $m \leq n$ different loops. In a second step, the traces over the loops containing such operators have to be calculated. In this thesis, we only need measurement rules for operators with $n \leq 4$. In this case, the result (2.4.76) implies that only loop configurations with each loop containing an even number (or none) of the spins s_{x_α} contribute. This leads to the conclusion that the expectation values for all possible choices (2.4.73) with $n = 1, 3$ vanish. For $n = 2$, we have already discussed the relevant correlation functions extensively. For a derivation of the measurement rules for those operators with $n = 4$ factors which are needed for a determination of dimer correlations we refer to App. A.3.

2.4.4. Numerical error analysis

We have not discussed the issue of numerical error analysis so far. Since QMC is a numerical technique, it is particularly important to have reliable error estimates for measured quantities from a Monte Carlo simulation. In Sect. 2.1, we have already pointed out that autocorrelation effects have to be taken into account for a correct determination of the measurement errors. In this subsection, we discuss how autocorrelation times are defined and how they can be measured in practice, which yields a possibility to deduce the correct numerical errors.

We follow the argumentation from Ref. [Eve01], and first define a Monte Carlo average of an

observable $\mathcal{O}$ over u configurations $\mathcal{C}_i$,

$$\langle \mathcal{O} \rangle^{\text{MC}} = \frac{1}{u} \sum_{i=1}^{u} \mathcal{O}(\mathcal{C}_i), \tag{2.4.77}$$

see e. g. Eq. (2.4.69) from Sect. 2.4.1 for the case of diagonal operators. If the configurations $\{\mathcal{C}_i\}$ of the Markov chain were statistically independent, the error of the mean value (2.4.77) would be $\sigma/\sqrt{u}$ with the standard deviation

$$\sigma^2 = \frac{u}{u-1} \left[\langle \mathcal{O}^2 \rangle^{\text{MC}} - (\langle \mathcal{O} \rangle^{\text{MC}})^2 \right]. \tag{2.4.78}$$

However, subsequent configurations generated by the update procedure are not statistically independent, and therefore the relation (2.4.78) underestimates the correct size of numerical error bars. To treat this issue, we define the *autocorrelation function*

$$\Gamma_{\mathcal{O}}(t) \equiv \frac{C_{\mathcal{O}}(t)}{C_{\mathcal{O}}(0)} \qquad \text{with} \tag{2.4.79}$$

$$C_{\mathcal{O}}(t) = \langle \mathcal{O}(\mathcal{C}_i)\mathcal{O}(\mathcal{C}_{i+t}) \rangle^{\text{MC}} - \langle \mathcal{O}(\mathcal{C}_i) \rangle^{\text{MC}} \langle \mathcal{O}(\mathcal{C}_{i+t}) \rangle^{\text{MC}},$$

which can be used to calculate the integrated autocorrelation time

$$\tau_{\text{int}}^{\mathcal{O}} \equiv \frac{1}{2} + \sum_{t=1}^{\infty} \Gamma_{\mathcal{O}}(t). \tag{2.4.80}$$

By making use of this definition one can prove that the correct numerical error is given by $\sigma_{\text{int}}/\sqrt{u}$, with

$$\sigma_{int}^2 \simeq 2\tau_{\text{int}}^{\mathcal{O}} \sigma^2, \qquad \text{if } u \gg \tau_{\text{int}}^{\mathcal{O}}. \tag{2.4.81}$$

It is useful to add some remarks at this point. We first have to stress that – according to the definitions (2.4.79) and (2.4.80) – different observables have different autocorrelation times. Therefore in the introduction to this chapter, we have been somewhat unprecise talking of a single autocorrelation time τ_{int}. What remains valid is the conclusion that a Monte Carlo run with u measurements contains only $u/2\tau_{\text{int}}^{\mathcal{O}}$ independent samples with respect to the observable $\mathcal{O}$. We also have to comment on the question of convergence of the sum in Eq. (2.4.80). Typically, one can expect the sum to converge because the function $\Gamma_{\mathcal{O}}$ decays exponentially at large t. We only mention that this dependence $\sim e^{-t/\tau_{exp}^{\mathcal{O}}}$ defines the *exponential autocorrelation time* $\tau_{exp}^{\mathcal{O}}$ of the observable $\mathcal{O}$, which is an upper bound for the value of $\tau_{\text{int}}^{\mathcal{O}}$.

Evidently, one cannot use the relation (2.4.80) to determine the integrated autocorrelation times in a computer simulation, because a direct evaluation of the autocorrelation function (2.4.79) for each observable $\mathcal{O}$ and all times t is very ineffective. For the numerical data presented in this work, the *binning of time series* technique was used instead. The idea is to group the u configurations of the Markov chain into k bins of length $l = \frac{u}{k}$. Then one computes the bin averages

$$\langle \mathcal{O}(l) \rangle_b^{\text{MC}} \equiv \frac{1}{l} \sum_{i=(b-1)l+1}^{bl} \mathcal{O}(\mathcal{C}_i), \qquad b = 1, \ldots, k, \tag{2.4.82}$$

and the variance of these averages

$$\sigma^2(l) = \frac{1}{k-1} \sum_{b=1}^{k} \left[\langle \mathcal{O}(l) \rangle_b^{\mathrm{MC}} - \langle \mathcal{O} \rangle^{\mathrm{MC}} \right]^2. \qquad (2.4.83)$$

These numbers are used to evaluate the quantity

$$\tau_{\mathrm{int}}^{\mathcal{O}}(l) \equiv \frac{l\sigma^2(l)}{2\sigma^2}, \qquad (2.4.84)$$

with the standard deviation σ from Eq. (2.4.78). It can be shown that the function (2.4.84) grows monotonically in l, and it converges to the integrated autocorrelation time for $l \gg \tau_{\mathrm{int}}^{\mathcal{O}}$. Hence by choosing l sufficiently large, one obtains a reliable numerical estimate for $\tau_{\mathrm{int}}^{\mathcal{O}}$ and hence for the corresponding statistical error due to the identity (2.4.81). Note that in practice l should not be too large, because otherwise the number k of bins becomes too small and the quantity (2.4.84) starts to fluctuate.

3. Conformal invariance and correlation functions of the XXZ chain

3.1. Known properties of the XXZ model: a survey

In this chapter we concentrate on the issue of correlation functions of the one-dimensional spin-$\frac{1}{2}$ XXZ model

$$H = \frac{J}{2} \sum_{i=1}^{N} (\sigma_i^x \sigma_{i+1}^x + \sigma_i^y \sigma_{i+1}^y + \Delta\, \sigma_i^z \sigma_{i+1}^z), \tag{3.1.1}$$

compare Eq. (2.2.3) from Sect. 2.2.1. We first give a short survey of the physics of the system for $J > 0$ and arbitrary values of Δ in this section. Note that by choosing these values for the coupling constants, we cover both the antiferromagnetic and ferromagnetic regimes of the model, because there is a correspondence $(J, \Delta) \leftrightarrow (-J, -\Delta)$ mediated by the unitary transformation (2.2.11) from Par. 2.2.1.

The XXZ chain has been studied extensively during the past decades and is one of the best understood models in quantum many body physics. For this reason and due to its generic structure, it serves as a reference system in the field of quantum magnetism. The magnetic properties of a couple of quasi one-dimensional non-frustrated compounds are well described by the model. For example, the isotropic antiferromagnetic Heisenberg model or XXX chain with $\Delta = 1$ is realized by the cuprates Sr_2CuO_3 and Ca_2CuO_3 [Egg96a, KFL$^+$97]. An example for an inorganic substance with considerably anisotropic exchange is Cs_2CoCl_4, where $\Delta = 0.25$ is realized [DOB$^+$81, YSSH83]. The Hamiltonian (3.1.1) also plays a significant role in the context of fermionic models. By means of a Jordan-Wigner transformation, the spin system (3.1.1) can be mapped to a one-dimensional model of interacting spinless fermions ($n_i \equiv c_i^\dagger c_i$)

$$H = -t \sum_{i=1}^{N} (c_i^\dagger c_{i+1} + c_i\, c_{i+1}^\dagger) + U \sum_{i=1}^{N} n_i n_{i+1}, \tag{3.1.2}$$

where the coupling constants of the fermionic model are given by[1] $t = -\frac{J}{2}$ and $U = \frac{J\Delta}{2}$.

The XXZ chain is an integrable system, i. e. it is exactly soluble by means of the Bethe ansatz. This approach was introduced by Bethe in 1931 to study the isotropic cases $\Delta = \pm 1$ [Bet31]. Lieb, Schultz, and Mattis investigated the free fermion case $\Delta = 0$ in 1961 [LSM61]. In 1966, Yang and Yang were able to construct the ground state of the system for general values of Δ using the Bethe ansatz [YY66a, YY66b, YY66c]. Today the nature of the ground state and the

---

[1]The derivation of the fermionic model (3.1.2) from the XXZ Hamiltonian (3.1.1) involves the neglect of a constant energy contribution.
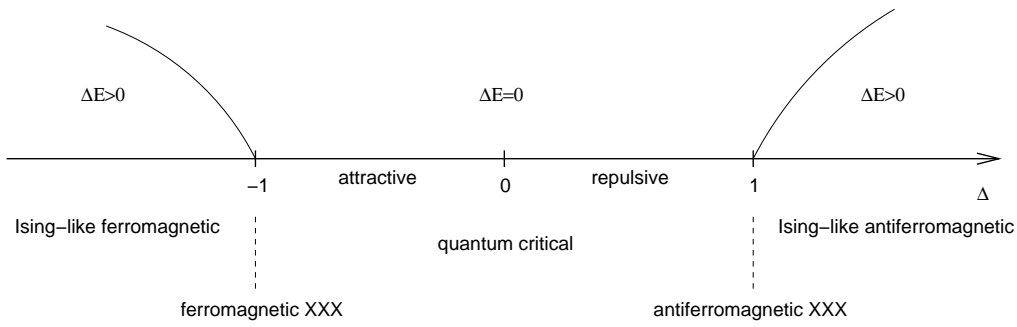
Fig. 3.1.: Ground state phase diagramm of the XXZ model with $J > 0$. In the Ising-like regions $|\Delta| > 1$, there is an energy gap $\Delta E > 0$. For $-1 \leq \Delta \leq 1$, the excitation spectrum is gapless ($\Delta E = 0$).

elementary excitations as well as the excitation spectrum are well understood. Similarly, thermodynamic quantities like the free energy, the specific heat and the magnetic susceptibility have attracted considerable attention. The thermodynamics of the XX model were studied by Katsura in 1962 [Kat62]. For $\Delta \neq 0$, investigations of the model at finite temperatures are based on the *algebraic Bethe ansatz* [Klü93]. Review articles on the properties of the XXZ model can be found in Refs. [KBI93, Tak99].

The ground state phase diagram of the system in the thermodynamic limit ($N \to \infty$ in Eq. (3.1.1)) is sketched in Fig. 3.1. We start by discussing the isotropic cases $\Delta = \pm 1$ which play a special role because they are $SU(2)$-symmetric. The ferromagnetic XXX model with $\Delta = -1$ has an infinite number of degenerate ground states, spontanously breaking the $SU(2)$-symmetry of the Hamiltonian. The system shows long-range ferromagnetic order at $T = 0$, because the ground state can be characterized by a non-vanishing magnetization. The elementary excitations have spin one and are interpreted as spin waves or *magnons*, whereas the low lying states of the gapless excitation spectrum can be characterized as *m*-magnon bound states or *m-strings*. For the antiferromagnetic XXX chain ($\Delta = 1$) the situation is somewhat different. Here a unique ground state with a complicated correlated structure is found. There is no long-range order because the staggered magnetization vanishes. The spectrum is gapless as in the ferromagnetic case, but the excited states are superpositions of elementary spin-$\frac{1}{2}$ excitations, so-called *spinons* [FT81, HZ93]. Spinons can only be excited in pairs which either form a singlet or a triplet state. A spinon can be illustrated as a domain wall between antiferromagnetically ordered domains, compare Fig. 3.2. Similar results as for $\Delta = 1$ are valid in the region $-1 < \Delta < 1$, where the system has a unique complicated ground state as well. In addition, there is no gap to the excited states. The nature of the massless excitations, however, depends on the choice of Δ. In the repulsive region $0 < \Delta < 1$, one finds pairs of spinons similarly to the isotropic antiferromagnetic case. In the attractive region $-1 < \Delta < 0$, two kinds of excited states exist. The first is a superposition of elementary spin-$\frac{1}{2}$ excitations as in the repulsive case. The second kind can be characterized as *m*-magnon bound states as in the ferromagnetic XXX chain.

For $|\Delta > 1|$, the system behaves *Ising-like*, i. e. the system shows long-range order and a gap in the excitation spectrum. In the ferromagnetic regime $\Delta < -1$, there is a twofold degenerate
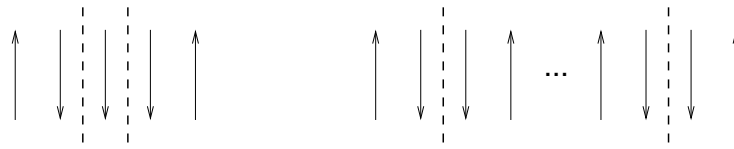
Fig. 3.2.: Illustration of a pair of spinons. Starting with the Néel state $|+-+\ldots\rangle$, a spinflip creates two domain walls or spinons (left), which can propagate through the system (right).

ferromagnetic ground state $|+++\ldots\rangle$ (and the spin-flipped state). The elementary excitations can be characterized as massive magnons. In the Ising-like antiferromagnetic sector $\Delta > 1$, the two ground states show a Néel-type order with a finite sublattice magnetization. However, the structure of the ground state is more complicated than in the Ising-limit $\Delta \to \infty$, where two *Néel states* of the form $|+-+\ldots\rangle$ (and the inverse state) become the exact ground states of the system. As for $\Delta = 1$, the elementary excitations can be characterized as pairs of spinons.

Although the Bethe ansatz provides a powerful instrument to analyze the system (3.1.1), it is a challenge to evaluate correlation functions for the XXZ model analytically. One exception is the ferromagnetic regime $\Delta \leq -1$ at $T = 0$. Here one can evaluate arbitrary correlation functions immediately due to the simple structure of the ground state. The most interesting correlation function is certainly the static *longitudinal spin correlation function*

$$G_\parallel(x) \equiv \langle \sigma_i^z \sigma_{i+x}^z \rangle, \tag{3.1.3}$$

which takes a finite value of $G_\parallel(x) = 1$ for all distances x. We can see that the correlations of the operator associated with the order parameter of the system reflect the long-range order in the ground state. In analogy to this observation, one expects that for $x \to \infty$ the absolute value of $G_\parallel$ takes a finite value in the gapped antiferromagnetic sector $\Delta > 1$. Another simple case is the XX model, for which simple expressions for $G_\parallel$ and the *transversal spin correlation function*

$$G_\perp(x) \equiv \langle \sigma_i^x \sigma_{i+x}^x \rangle \tag{3.1.4}$$

both in the ground state and at finite temperatures were derived in the 1960s [LSM61,McC68]. For general values of Δ, there exist certain multiple integral representations of the static spin correlation functions at $T = 0$ [KMST02]. The approach has been generalized to finite temperatures recently [GKS04]. Because of their complicated structure, however, it is hard to evaluate these expressions, even numerically. In 2004, numbers for the third neighbor spin correlation functions as well as for some four spin correlators in the ground state were published [KSTS04]. Further progress has been made in Ref. [SST05], where the two-point spin correlations of the antiferromagnetic XXX model up to $x = 8$ habe been calculated.

In the quantum critical region $-1 < \Delta \leq 1$, the leading asymptotic expressions for two-point correlation functions can be obtained from a combination of conformal field theory (CFT) and Bethe ansatz results [KBI93]. The conformal approach is motivated by the observation [LP75] that the low energy physics of the lattice Hamiltonian (3.1.2) can be described by an effective one-dimensional quantum field theory, the fermionic *Thirring model* [Thi58]. Quantum field theories in

one dimension in general turn out to be conformal invariant at a quantum critical point. For this reason general results from CFT for the properties of correlation functions can be applied to the XXZ model. In the ground state, CFT predicts an algebraic decay of the spin correlations $G_{\parallel/\perp}$ and of the *dimer correlation function*

$$G_{\mathrm{d}}(x) \equiv \langle D_i D_{i+x} \rangle - \langle D_i \rangle \langle D_{i+x} \rangle, \qquad (3.1.5)$$

where $D_i \equiv \vec{\sigma}_i \vec{\sigma}_{i+1}$ is the local energy operator of the XXX model. The critical exponents which govern this *quasi long-range order* have been deduced both for spin [KBI93] and dimer correlations [Klü98] in the literature. For $\Delta = 1$, the competition between the quasi long-range Néel and dimer orders reflects the tendency of the system to undergo a spin-Peierls transition towards a non-magnetic dimerized ground state [Klü98]. This kind of phase transition plays an important role in systems with spin-phonon coupling [Pyt74, CF79]. A detailed analysis of Heisenberg-like systems coupled to lattice degrees of freedom in one and two dimensions will be given in Chapt. 4.

We emphasize that CFT reveals a deep connection between the algebraic decay of correlations in the ground state and the exponential decay which is found at low finite temperatures. The same numbers that define the critical exponents at $T = 0$ also determine the correlation lengths at $T > 0$. In particular, a smooth crossover between the low temperature and the ground state behavior is predicted. However, despite of its success the conformal approach cannot be applied to determine the correlation amplitudes. Furthermore, algebraic and logarithmic corrections to asymptotic scaling for $-1 < \Delta < 1$ and $\Delta = 1$, respectively, are not accessible. These corrections are due to the lattice nature of the model. Fortunately for $G_{\parallel/\perp}$, alternative field theoretical methods have been applied successfully in this context during the past years [LZ97, Luk99, LT03]. In Ref. [LT03], Lukyanov and Terras give closed expressions for the correlation amplitudes. In addition, they discuss the leading algebraic and logarithmic corrections in the ground state. The analytical results for the correlation amplitudes have been confirmed numerically by means of the DMRG method [HF98, Luk99, HF01, HF04]. Deviations between analytical and numerical results close to the isotropic point $\Delta = 1$, however, are not discussed by the authors. In Ref. [HF04], numerical estimates for the correlation amplitudes of certain four-point correlators are given as well, but the authors do not consider the full dimer correlation function (3.1.5). The analytical results for logarithmic corrections in the antiferromagnetic XXX model have also been compared to DMRG data [HHM95] in Ref. [LT03]. There is a good coincidence even down to very small distances.

The argumentation from this section shows that numerical techniques are needed to fully understand the correlations of the XXZ chain. As has been mentioned above, exact analytical results have only been obtained for distances $x \leq 8$ so far. In this chapter, we present a detailed numerical investigation [AL05] of low temperature data at intermediate distances on the basis of the QMC loop algorithm from the Sects. 2.2.3 and 2.2.5 in the gapless repulsive region $0 \leq \Delta \leq 1$. We concentrate on the crossover between low temperature and ground state properties. Here we especially pose the question to what extent the relations from CFT can be used to extract ground state properties from finite temperature data. This is done to deduce independent numerical estimates for the correlation amplitudes. Besides a comparison of the results for spin correlations to previous analytical and numerical results, one main goal is to determine the amplitudes for the dimer corre-

lation function which has not been done in the literature so far. We also ask the question in which range of distances x the results from CFT are valid. Here we especially focus on the algebraic and logarithmic corrections at $T = 0$ as given in Ref. [LT03] .

We emphasize that our analysis of the QMC data is based on the asymptotic expressions from CFT. As the relevant literature is rather extensive, we give a detailed review of the concept of conformal invariance in the next section. In particular, we focus on the general properties of two-point correlation functions in conformal invariant theories. For the reader who is only interested in our analysis of the numerical data, we recommend to skip this part and to continue with Sect. 3.3. There we briefly comment on the Bethe ansatz solution of the XXZ model, and give the asymptotic expressions for the correlation functions in question. In the same section, we also present a review of the results for the correlation amplitudes and the corrections to asymptotic scaling from the literature. Finally in Sect. 3.4, the numerical data are analyzed and compared to the findings from Sect. 3.3.

3.2. Conformal field theory in two dimensions

In this section we give a detailed review of the general properties of two-point correlation functions in conformal invariant theories. For further information on CFT and its application to statistical physics we refer to Refs. [BPZ84, GO86, Gin90, Car90]. In the following subsection, we first introduce the conformal group in d dimensions, and after restricting ourselves to the two-dimensional case we determine the commutation relations of the conformal algebra for classical scalar fields. In Par. 3.2.2, we then define the energy momentum tensor and motivate why quantum field theories in two dimensions are conformal invariant at a quantum critical point. In the next step (Sect. 3.2.3), we explain the concept of radial quantization, which is very helpful when showing that the modes of the energy momentum tensor are the generators of the conformal algebra, see Par. 3.2.4. In the subsequent Sect. 3.2.5, a definition of primary fields is given, which obey a particularly simple transformation law under a conformal mapping. In particular, we discuss the properties of two-point correlators of primary fields in the vacuum state of the theory. In Sect. 3.2.6, we introduce the concept of conformal families, which is used to extract the asymptotic behavior of two-point correlations of arbitrary fields in the ground state, see Sect. 3.2.7. Finally in Par. 3.2.8, we derive asymptotic expressions for correlation functions in a strip geometry, which provide an instrument to study finite-size effects at $T = 0$ and the asymptotics of two-point correlation functions at low finite temperatures.

3.2.1. Classical conformal algebra in two dimensions

We consider the space $\mathbb{R}^d$ with metrics $g_{\mu\nu}$ and line element $ds^2 = g_{\mu\nu} dx^\mu dx^\nu$. Under a change of coordinates $x \to x'$ the metrics transforms like

$$g_{\mu\nu} \to g'_{\mu\nu}(x') = \frac{\partial x^\alpha}{\partial x'^\mu} \frac{\partial x^\beta}{\partial x'^\nu} g_{\alpha\beta}. \tag{3.2.6}$$

A *conformal transformation* is a mapping of coordinates which leaves the metrics invariant up to a scale change

$$g'_{\mu\nu} = \Omega(x)g_{\mu\nu}. \tag{3.2.7}$$

The set of conformal transformations constitutes the *conformal group*.

It is useful to understand the implications of the definition (3.2.7) for an infinitesimal conformal mapping $x^\mu \to x'^\mu = x^\mu + \epsilon^\mu(x)$. Neglecting terms $\mathcal{O}(\epsilon^2)$, we find[2]

$$g'_{\mu\nu} = g_{\mu\nu} + \partial_\mu\epsilon_\nu + \partial_\nu\epsilon_\mu. \tag{3.2.8}$$

The comparison of this result to Eq. (3.2.7) yields $\Omega(x) = 1 + \frac{2}{d}(\partial \cdot \epsilon)$. Therefore an infinitismal conformal transformation fulfills the condition

$$\partial_\mu\epsilon_\nu + \partial_\nu\epsilon_\mu = \frac{2}{d}(\partial \cdot \epsilon)g_{\mu\nu}. \tag{3.2.9}$$

In the introduction 3.1 to this chapter we have already mentioned that the critical behavior of the XXZ model can be described by an effective one-dimensional quantum field theory, the Thirring model. In such a theory the partition function Z of the system is given by a field integral

$$Z = \int \mathcal{D}A \, e^{-S[A]}, \tag{3.2.10}$$

where the action $S[A]$ can be written as a $(1+1)$-dimensional integral over some Lagrange density which depends on a set of local fields $[A]$. For this reason we restrict ourselves to the case $d = 2$ in the rest of Sect. 3.2.

After having defined how a conformal transformation acts in coordinate space, the next step is to determine the commutation relations of the corresponding Lie algebra. In this section, we search for a representation of the conformal group in the special case of classical scalar fields. For this choice it is straightforward to determine the infinitesimal generators of the conformal algebra and the corresponding commutation relations. Later we will discuss the case of critical quantum field theories in two dimensions and show that the modes of the energy momentum tensor are the generators of the conformal algebra in the quantum case.

In the following we choose $d = 2$ and the Euclidean metrics $g_{\mu\nu} \equiv \delta_{\mu\nu}$. In this case there is no difference between covariant and contravariant notation, and we only use subindices to label components of the quantities in consideration. Note that we still make use of the sum convention if we denote indices by Greek letters. From the relation (3.2.9), we find the Cauchy-Riemann equations

$$\partial_0\epsilon_0 = \partial_1\epsilon_1, \tag{3.2.11}$$

$$\partial_0\epsilon_1 = -\partial_1\epsilon_0. \tag{3.2.12}$$

Hence it is convenient to switch to complex coordinates $z = x_0 + ix_1$ and $\overline{z} = x_0 - ix_1$. Then an infinitesimal transformation takes the two equivalent forms $\epsilon(z) = \epsilon_0 + i\epsilon_1$ and $\overline{\epsilon}(\overline{z}) = \epsilon_0 - i\epsilon_1$. At this point the reader may be reminded that Eq. (3.2.9) is a local condition. Conformal

---

[2] The reader may be reminded that the metric tensor $g_{\mu\nu}$ acts as the mediator between covariant and contravariant notation, i. e. $x_\nu = g_{\mu\nu}x^\mu$.

transformations in two dimensions thus coincide with meromorphic functions which can be written as the Laurent series

$$\epsilon(z) = -\sum_{n=-\infty}^{\infty} a_n z^{n+1}, \qquad \overline{\epsilon}(\overline{z}) = -\sum_{n=-\infty}^{\infty} b_n \overline{z}^{n+1}. \tag{3.2.13}$$

We now determine how an infinitesimal conformal transformation acts on classical scalar fields $f(z)$. Using the identity $f(z + \epsilon) = f(z) + \frac{df}{dz}(z)\epsilon + \mathcal{O}(\epsilon^2)$ and inserting the expansion (3.2.13) for $\epsilon(z)$, one obtains

$$f(z + \epsilon) = (1 - \sum_n a_n z^{n+1} \frac{\partial}{\partial z}) f(z) \tag{3.2.14}$$

(for $\overline{\epsilon}(\overline{z})$ analogously). Therefore we can identify the corresponding infinitesimal generators

$$\ell_n = -z^{n+1} \frac{\partial}{\partial z}, \qquad \overline{\ell}_n = -\overline{z}^{n+1} \frac{\partial}{\partial \overline{z}}, \qquad n \in \mathbb{Z}. \tag{3.2.15}$$

The ℓ's satisfy the commutation relations

$$[\ell_m, \ell_n] = (m - n)\ell_{m+n}. \tag{3.2.16}$$

This algebra is called the *Virasoro algebra* $\mathcal{V}_0$. Simultaneously the relation

$$[\overline{\ell}_m, \overline{\ell}_n] = (m - n)\overline{\ell}_{m+n} \tag{3.2.17}$$

holds, and since we also have $[\ell_m, \overline{\ell}_n] = 0$, the local conformal algebra is the direct sum of two isomorphic subalgebras. In Sect. 3.2.4 we will discuss that in the quantum case the relations (3.2.16) and (3.2.17) are modified by an extra term on the right-hand side, the central extension.

So far we have only used the local conditions (3.2.11) and (3.2.12). The global conformal group in two dimensions is defined by the set of conformal transformations that are well-defined and invertible on the Riemann sphere $\mathbb{C} \cup \infty$. It can be shown that this corresponds to transformations which are generated by $\{\ell_{-1}, \ell_0, \ell_1\} \cup \{\overline{\ell}_{-1}, \overline{\ell}_0, \overline{\ell}_1\}$.

3.2.2. Scale invariance and energy momentum tensor

We now explain why any quantum field theory in $(1 + 1)$ dimensions is conformal invariant at a quantum critical point. This question naturally leads to the definition of the energy momentum tensor, which provides an instrument to construct a representation of the conformal algebra in the quantum case.

To start with, we consider a quantum system on a lattice like the XXZ chain (3.1.1). At its critical point, the system is scale invariant, i. e. the correlation length ξ of correlations of the operator associated with the order parameter is infinite. Sufficiently close to the critical point, i. e. for large correlation lengths $\xi \gg a$ (a is the lattice spacing), the behavior of the system on large length scales does not depend on whether the system is defined on a lattice or in a continuum, and we can assume that an effective field theory of the form (3.2.10) will describe the critical behavior of the system properly.

In the following we discuss how the action $S[A]$ in Eq. (3.2.10) changes under an arbitrary infinitesimal coordinate transformation $x_\mu \rightarrow x_\mu + \alpha_\mu(x)$. In general we cannot expect S to be

invariant under such a transformation, and the leading term in the change δS of the action is given by

$$\delta S = \frac{-1}{2\pi} \int d^2x \, T_{\mu\nu}(x)\partial_\mu\alpha_\nu. \tag{3.2.18}$$

This equation defines the *energy momentum tensor* $T_{\mu\nu}(x)$. Scale invariance at the critical point means that the partition function Z from the relation (3.2.10) does not change under dilatations $x_\mu \to x_\mu/\lambda$ (which can be identified with a transformation $a \to \lambda a$ on the lattice, and corresponds to the infinitesimal transformation $\alpha_\mu = [\frac{1}{\lambda} - 1]x_\mu$). This condition is certainly fulfilled if S is invariant, which means $\delta S = 0$ in the identity (3.2.18). This is the case if we demand

$$T_{\mu\nu}(x)\partial_\mu\alpha_\nu = 0. \tag{3.2.19}$$

Using $\partial\alpha_\mu/\partial x_\nu = [\frac{1}{\lambda} - 1]\delta_{\mu\nu}$, we find that $T_{\mu\nu}$ is traceless: $T_{00} + T_{11} = 0$. If we further assume that the theory is rotational invariant, we have $T_{01} = T_{10}$. Hence the energy momentum tensor has only two independent components. By making use of these findings the integrand in Eq. (3.2.18) becomes

$$T_{00}(\partial_0\alpha_0 - \partial_1\alpha_1) + T_{01}(\partial_0\alpha_1 + \partial_1\alpha_0). \tag{3.2.20}$$

In the last subsection we have seen that any infinitesimal conformal transformation $\alpha \equiv \epsilon$ fulfills the Cauchy-Riemann equations (3.2.11) and (3.2.12). Therefore, if α is a conformal mapping, the integrand (3.2.20) indeed obeys the condition (3.2.19). For this reason any (rotational invariant) $(1+1)$-dimensional field theory is conformal invariant at a quantum critical point [Car90].

We close this subsection with some further remarks concerning the properties of the energy momentum tensor in conformal invariant theories. If we demand $\delta S = 0$ and integrate the relation (3.2.18) by parts, we find

$$\partial_\mu T_{\mu\nu} = 0. \tag{3.2.21}$$

As we did in Sect. 3.2.1 we switch to complex coordinates and define

$$T(z) \equiv \frac{1}{2}(T_{00} - iT_{01}), \qquad \overline{T}(\overline{z}) \equiv \frac{1}{2}(T_{00} + iT_{01}). \tag{3.2.22}$$

Then the insertion of $T_{00} = -T_{11}$ and $T_{01} = T_{10}$ into the identity (3.2.21) again reveals the Cauchy-Riemann equations, and we find that $T(z)$ is (locally) analytic.

3.2.3. Conserved charges and radial quantization

From the Noether theorem one knows that it is possible to construct a *current* j which satifies the continuity equation

$$\partial_\mu j_\mu = 0, \tag{3.2.23}$$

if the underlying theory is invariant under a continuous group of transformations α. In this case an arbitrary field $A(z, \overline{z})$ transforms[3] according to

$$A \to A + \delta_\alpha A. \tag{3.2.24}$$

---

[3]Due to the structure of the conformal algebra as discussed in Sect. 3.2.1 we explicitly keep the dependence of the fields on $\overline{z}$. In terms of the original coordinates $(x_0, x_1) \in \mathbb{R}^2$, this amounts to taking instead $(x_0, x_1) \in \mathbb{C}^2$, and then the transformation to $(z, \overline{z})$ coordinates is just a change of variables. One can recover the original real coordinates by considering the surface defined by $\overline{z} = z^*$ in $\mathbb{C}^2$ (in contrast to our usual notation here $*$ means complex conjugation).
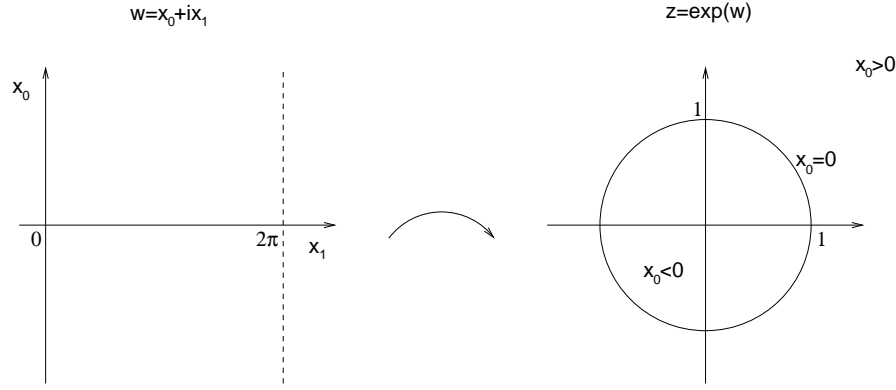
Fig. 3.3.: Radial quantization. A cylinder with periodic boundary conditions along the x_1-direction is mapped to the complex plane. Circles in the plane correspond to slices with fixed time variable x_0 on the cylinder.

Here the variation $\delta_\alpha A$ is given by the expression

$$\delta_\alpha A = [Q_\alpha, A], \tag{3.2.25}$$

where

$$Q_\alpha = \int dx_1 \, j_0(x_0, x_1) \tag{3.2.26}$$

is the conjugated *conserved charge*. For the integration the time x_0 is kept fixed. However, it can be shown that Q_α does not depend on the specific choice of x_0. Note that the operator Q_α is not only conserved, it also acts as a generator of the symmetry [Wei95].

In a conformal invariant theory, we can identify $\alpha \equiv \epsilon$, and the corresponding current is given by

$$j_\mu = T_{\mu\nu}\epsilon_\nu, \tag{3.2.27}$$

while the conjugated charge becomes

$$Q_\epsilon = \int dx_1 \, T_{0\mu}\epsilon_\mu. \tag{3.2.28}$$

To verify whether j fulfills the continuity equation (3.2.23) we consider

$$\partial_\mu j_\mu = \partial_\mu(T_{\mu\nu}\epsilon_\nu) = (\partial_\mu T_{\mu\nu})\epsilon_\nu + T_{\mu\nu}\partial_\mu\epsilon_\nu. \tag{3.2.29}$$

By inserting the relations (3.2.21) and (3.2.19) from Sect. 3.2.2 we can see that both summands vanish.

As we did in the previous subsections, we switch to complex coordinates $w = x_0 + ix_1$, because then the theory of analytic functions can be applied. In the following we make use of the concept of *radial quantization*. We first compactify the space coordinate x_1, i. e. we assume having mapped the complex plane to a cylinder with periodic boundary conditions in the x_1-direction: $x_1 \equiv x_1 + 2\pi$. Next we consider the transformation $w \to z = \exp(w)$ (see also Fig. 3.3). Then the expression (3.2.28) takes the especially simple form

$$Q_\epsilon = \frac{1}{2\pi i}\oint dz \, T(z)\epsilon(z) + \frac{1}{2\pi i}\oint d\bar{z} \, \overline{T}(\bar{z})\bar{\epsilon}(\bar{z}) \tag{3.2.30}$$

in terms of the new coordinates. The line integrals are performed over some circle of fixed radius (corresponding to a fixed value for the time variable x_0 in Eq. (3.2.28)), using the sign convention that both the dz and the $d\overline{z}$ integrations are taken in the counter-clockwise sense.

3.2.4. Mode expansion of the energy momentum tensor

We are now in the position to derive a procedure how to determine a representation of the conformal algebra in a critical quantum field theory. At the end of Par. 3.2.2, it was shown that $T(z)$ is locally analytic. Therefore it is possible to write down the Laurent series

$$T(z) = \sum_{n=-\infty}^{\infty} \frac{L_n}{z^{n+2}}, \qquad \overline{T}(\overline{z}) = \sum_{n=-\infty}^{\infty} \frac{\overline{L}_n}{\overline{z}^{n+2}}. \tag{3.2.31}$$

These expansions are formally inverted by the expressions

$$L_n = \frac{1}{2\pi i} \oint dz\, z^{n+1} T(z), \qquad \overline{L}_n = \frac{1}{2\pi i} \oint d\overline{z}\, \overline{z}^{n+1} \overline{T}(\overline{z}). \tag{3.2.32}$$

We now consider an infinitesimal conformal transformation ϵ and evaluate Q_ϵ. By inserting the expansions (3.2.31) into the result (3.2.30), one finds (we set $\overline{\epsilon} \equiv 0$ for the moment)

$$\begin{aligned}
Q_\epsilon &= \frac{1}{2\pi i} \sum_n L_n \oint dz\, \frac{1}{z^{n+2}} \epsilon(z) \\
&\overset{(3.2.13)}{=} \frac{-1}{2\pi i} \sum_{m,n} a_m L_n \oint dz\, \frac{1}{z^{n-m+1}} \\
&= -\sum_{m,n} a_m L_n \delta_{n-m+1,1} \\
&= -\sum_n a_n L_n.
\end{aligned} \tag{3.2.33}$$

Here we have used the result $\oint \frac{dz}{z^{n-m+1}} = 2\pi i\, \delta_{n-m+1,1}$ in the third step. Using Eq. (3.2.33) one can show that the relation (3.2.25) from the preceeding subsection for $\alpha \equiv \epsilon$ defines a representation of the conformal algebra indeed. To see this, we consider two infinitesimal conformal transformations $\epsilon(z) \equiv -\sum_n a_n z^{n+1}$ and $\zeta(z) \equiv -\sum_n b_n z^{n+1}$. Then we have

$$\begin{aligned}
\delta_{\epsilon+\zeta} A &\overset{(3.2.25)}{=} [Q_{\epsilon+\zeta}, A] \\
&= [-\sum_n (a_n + b_n) L_n, A] \\
&= -\sum_n a_n [L_n, A] - \sum_n b_n [L_n, A] \\
&= [-\sum_n a_n L_n, A] + [-\sum_n b_n L_n, A] \\
&= [Q_\epsilon, A] + [Q_\zeta, A] \overset{(3.2.25)}{=} \delta_\epsilon A + \delta_\zeta A.
\end{aligned} \tag{3.2.34}$$

Furthermore, the relation (3.2.33) implies that the modes L_n (and $\overline{L}_n$ if we take the dependence of Q_ϵ on $\overline{\epsilon}$ into account) of the energy momentum tensor are the generators of the conformal

algebra in a critical $(1+1)$-dimensional quantum field theory. For a theory which is specified by the action $S[A]$ (see Eq. (3.2.10)) we can construct the generators as follows: first determine $T(z)$ and $\overline{T}(\overline{z})$ according to the results (3.2.18) and (3.2.22), then evaluate the L's and $\overline{L}$'s by means of Eq. (3.2.32).

We now have to specify the commutation relations of the L's (and $\overline{L}$'s). In quantum field theory, we have to extend the classical Virasoro algebra $\mathcal{V}_0$ from Sect. 3.2.1 by postulating

$$[L_n, L_m] = (n - m)L_{n+m} + \frac{c}{12}n(n^2 - 1)\delta_{n,-m}. \tag{3.2.35}$$

Simultaneously we demand

$$[\overline{L}_n, \overline{L}_m] = (n - m)\overline{L}_{n+m} + \frac{c}{12}n(n^2 - 1)\delta_{n,-m}, \tag{3.2.36}$$

and $[L_n, \overline{L}_m] = 0$ as in Sect. 3.2.1. The algebra (3.2.35) is called the *extended Virasoro algebra* $\mathcal{V}_c$ and differs from the result (3.2.16) by adding an extra term proportional to the *central charge* c, the *central extension*. Note that the central charge is real and satisfies $c \geq 0$. It serves as a free parameter of the theory, i. e. it describes the particular realization of conformal symmetry. In principle it can be determined by comparing predictions for the finite-size behavior of e. g. the ground state energy based on CFT to independent analytical or numerical results. We will consider this point in Sect. 3.2.8. Note that − as in the classical case − global conformal transformations are generated by the infinitesimal generators $\{L_{-1}, L_0, L_1\} \cup \{\overline{L}_{-1}, \overline{L}_0, \overline{L}_1\}$.

3.2.5. Primary fields

We have not discussed the behavior of correlation functions so far. As we are interested in the critical behavior of our theory, it is reasonable to search for fields $\phi(z, \overline{z})$ which show an especially simple transformation law under a conformal mapping $(z, \overline{z}) \rightarrow (f(z), \overline{f}(\overline{z}))$, i. e.

$$\phi(z, \overline{z}) \rightarrow \left(\frac{df}{dz}\right)^{\Delta_\phi} \left(\frac{d\overline{f}}{d\overline{z}}\right)^{\overline{\Delta}_\phi} \phi\left(f(z), \overline{f}(\overline{z})\right). \tag{3.2.37}$$

Fields with the transformation property (3.2.37) are called *primary fields*, and the real numbers $(\Delta_\phi, \overline{\Delta}_\phi)$ are the *anomalous dimensions* of the field ϕ.

In the framework of statistical physics, the relation (3.2.37) means that each primary field is a scaling operator. This can be seen if we consider a scale change $(z, \overline{z}) \rightarrow (\frac{z}{\lambda}, \frac{\overline{z}}{\lambda})$. Then the transformation property (3.2.37) becomes

$$\phi(z, \overline{z}) \rightarrow \lambda^{-\Delta_\phi} \lambda^{-\overline{\Delta}_\phi} \phi\left(\frac{z}{\lambda}, \frac{\overline{z}}{\lambda}\right), \tag{3.2.38}$$

which indeed implies that ϕ is a scaling operator, and the corresponding scaling dimensions are given by $(\Delta_\phi, \overline{\Delta}_\phi)$. In the context of the renormalization group, scaling operators are important when describing the system in the vicinity of a critical fixed point, see e. g. Ref. [Car96].

To study the properties of primary fields more closely we consider the change of $\phi(z)$ under an infinitesimal conformal transformation $z \rightarrow z + \epsilon(z)$. In the following we simplify our notation by omitting the dependence of ϕ on $\overline{z}$. It can be shown easily that taking the dependence on $\overline{z}$ into

account leads to analogous results. Therefore we will generalize our results to the properties of fields depending on both z and $\overline{z}$ later. We first evaluate

$$\left(\frac{\partial f}{\partial z}\right)^{\Delta_\phi} = \left(1 + \frac{d\partial\epsilon}{\partial z}\right)^{\Delta_\phi} = 1 + \Delta_\phi \frac{\partial\epsilon}{\partial z} + \mathcal{O}(\epsilon^2), \tag{3.2.39}$$

$$\phi(f(z)) = \phi(z + \epsilon(z)) = \phi(z) + \epsilon(z)\frac{\partial\phi}{\partial z} + \mathcal{O}(\epsilon^2). \tag{3.2.40}$$

Inserting these identities into the relation (3.2.37) and neglecting terms $\mathcal{O}(\epsilon^2)$, we obtain

$$\phi(z) \to (1 + \Delta_\phi \frac{\partial\epsilon}{\partial z})\,[\phi(z) + \epsilon(z)\frac{\partial\phi}{\partial z}] \approx$$

$$\phi(z) + \epsilon(z)\frac{\partial\phi}{\partial z} + \Delta_\phi \phi(z)\frac{\partial\epsilon}{\partial z} \overset{(3.2.13)}{=}$$

$$\phi(z) - \sum_n a_n \left(z^{n+1}\frac{\partial\phi}{\partial z} + \Delta_\phi(n+1)z^n\phi(z)\right). \tag{3.2.41}$$

On the other hand we know from Sect. 3.2.3 that $\phi \to \phi + \delta_\epsilon\phi$ with $\delta_\epsilon\phi = [Q_\epsilon, \phi]$. Now we can make use of the mode expansion (3.2.33), and find

$$\delta_\epsilon\phi = -\sum_n a_n[L_n, \phi]. \tag{3.2.42}$$

If we compare this result to Eq. (3.2.41), we obtain the commutation relations of the generators of the conformal group and primary fields

$$[L_n, \phi(z,\overline{z})] = z^{n+1}\frac{\partial\phi}{\partial z} + \Delta_\phi(n+1)z^n\phi(z,\overline{z}). \tag{3.2.43}$$

Taking the dependence on $\overline{z}$ into account, one can prove the analogous equation

$$[\overline{L}_n, \phi(z,\overline{z})] = \overline{z}^{n+1}\frac{\partial\phi}{\partial\overline{z}} + \overline{\Delta}_\phi(n+1)\overline{z}^n\phi(z,\overline{z}). \tag{3.2.44}$$

The relations (3.2.43) and (3.2.44) provide a powerful tool to evaluate correlation functions of *quasiprimary fields*. These are the fields which fulfill Eq. (3.2.43) only for $n = -1, 0, 1$. Note that each primary field is quasiprimary.

In the following we determine the properties of two-point correlation functions of quasiprimary fields in the vacuum state $|0\rangle$ (which will be associated to the ground state in case of the critical XXZ model later). Before we start, however, we have to make one further assumption. We demand that the expectation value $\langle 0|T(z)|0\rangle$ is analytic at $z = 0$. Taking into account the property $L_n^\dagger = L_{-n}$, which we do not want to prove here, this implies

$$L_n|0\rangle = 0 = \langle 0|L_n, \qquad n = -1, 0, 1. \tag{3.2.45}$$

Hence we immediately have the result ($n = -1, 0, 1$)

$$0 = \langle 0|[L_n, \phi_1(z_1)\phi_2(z_2)]|0\rangle$$

$$= \langle 0|\phi_1(z_1)[L_n, \phi_2(z_2)]|0\rangle + \langle 0|[L_n, \phi_1(z_1)]\phi_2(z_2)|0\rangle, \tag{3.2.46}$$

with two independent quasiprimary fields ϕ_1 and ϕ_2 depending on coordinates z_1 and z_2, respectively. We now evaluate Eq. (3.2.46) by making use of the relation (3.2.43):

1. The case $n = -1$ yields

$$(\partial_{z_1} + \partial_{z_2})\langle 0|\phi_1(z_1)\phi_2(z_2)|0\rangle = 0. \tag{3.2.47}$$

   If we change coordinates according to $v = z_1 + z_2$, $w = z_1 - z_2$, this is equivalent to $\partial_v\langle 0|\phi_1(z_1)\phi_2(z_2)|0\rangle = 0$, which means

$$\langle 0|\phi_1(z_1)\phi_2(z_2)|0\rangle = f(z_1 - z_2). \tag{3.2.48}$$

2. By inserting $n = 0$ and making use of the property (3.2.48), we obtain the differential equation

$$(\Delta_{\phi_1} + \Delta_{\phi_2})f(z_1 - z_2) + (z_1 - z_2)\frac{\partial f(z_1 - z_2)}{\partial z_1} = 0, \tag{3.2.49}$$

   (with Δ_{ϕ_1} and Δ_{ϕ_2} being the anomalous dimensions of the fields ϕ_1 and ϕ_2, respectively) which has the solution

$$f(z_1 - z_2) = \frac{C}{(z_1 - z_2)^{\Delta_{\phi_1} + \Delta_{\phi_2}}}. \tag{3.2.50}$$

   Here C is a constant number.

3. For $n = 1$ we arrive at

$$(z_1 + z_2)(\Delta_{\phi_1} - \Delta_{\phi_2}) = 0. \tag{3.2.51}$$

   Since z_1 and z_2 can take any value this means $\Delta_{\phi_1} = \Delta_{\phi_2}$. Thus only two-point correlators of quasiprimary fields with themselves have nontrivial properties.

We see that the two-point correlators of quasiprimary fields ϕ_i, ϕ_j in conformal invariant theories vanish for $i \neq j$, and they show an algebraic decay for $i = j$. We can summarize the results of this subsection if we remember that ϕ_i and ϕ_j also depend on $\overline{z}$. This leads to the generalized expression

$$\langle 0|\phi_i(z_1, \overline{z}_1)\phi_j(z_2, \overline{z}_2)|0\rangle = \delta_{ij}\frac{C}{(z_1 - z_2)^{2\Delta_\phi}(\overline{z}_1 - \overline{z}_2)^{2\overline{\Delta}_\phi}}, \tag{3.2.52}$$

with $(\Delta_\phi, \overline{\Delta}_\phi) \equiv (\Delta_{\phi_i}, \overline{\Delta}_{\phi_i})$. Note that Eq. (3.2.52) further implies $\Delta_\phi, \overline{\Delta}_\phi \geq 0$, because otherwise the correlations would increase with increasing distance which is unphysical.

3.2.6. Descendant fields and conformal families

In statistical physics, the asymptotic behavior of correlation functions in the vicinity of a critical fixed point is determined by the simple scaling properties of scaling operators. At the beginning of the previous section, we explained that in CFT each primary field is also a scaling operator. On the other hand we cannot conclude that each scaling operator is a primary field, i. e. we cannot expect that the relevant fields of the effective theory close to a quantum phase transition have the simple transformation property (3.2.37) under conformal transformations. However, in this subsection we argue that conformal invariance provides an instrument to classify all the fields composing the operator algebra, and the primary fields play a crucial part in this argumentation.

To start with, we consider a primary field ϕ with anomalous dimensions $(\Delta_\phi, \overline{\Delta}_\phi)$ and construct *secondary* or *descendant fields*

$$\phi^{(\{-k\},\{-\overline{k}\})}(z, \overline{z}) \equiv L_{-k_1} \ldots L_{-k_n}\overline{L}_{-\overline{k}_1} \ldots \overline{L}_{-\overline{k}_m}\phi(z, \overline{z}). \tag{3.2.53}$$

level	dimension	fields
0	Δ_ϕ	$\phi(z)$
1	$\Delta_\phi + 1$	$L_{-1}\phi$
2	$\Delta_\phi + 2$	$L_{-2}\phi, L_{-1}^2\phi$
...	...	...

Table 3.1.: The primary field ϕ and its descendant fields, which comprise the conformal family $[\phi]$, ordered according to their dimension. To simplify matters, we have omitted the dependence of the fields on $\overline{z}$.

In this definition the numbers $k_i, \overline{k}_j$ have to be positive or equal to zero since the relations

$$L_n\phi(z,\overline{z}) = 0 = \overline{L}_n\phi(z,\overline{z}) \qquad \forall n > 0, \tag{3.2.54}$$

hold.

In the following we consider the dimensions of secondary fields. In contrast to the case of primary fields, we cannot expect that secondary fields are scaling operators. This means that under a scale change $z \to z/\lambda$, secondary fields do not obey the simple transformation law (3.2.38) from the preceeding subsection, and it does not make sense to speak of the scaling dimension of a secondary field. However, due to their construction (3.2.53) we can expect that in leading order, the correlations of descendants show an algebraic decay analogously to Eq. (3.2.52), but the anomalous dimensions $(\Delta_\phi, \overline{\Delta}_\phi)$ will be replaced by the *dimensions* of the fields (in the case of scaling operators, the scaling dimension and the dimension are identical). Note that in principle higher order terms come into play, but we do not discuss them here since we are only interested in the leading asymptotic behavior. We first mention that by considering $[Q_\epsilon, T(z)]$, inserting the mode expansions (3.2.31) and (3.2.33), then making use of the Virasoro algebra (3.2.35) and finally comparing the result to the relation (3.2.43), it can be shown that the energy momentum tensor $T(z)$ is quasiprimary with anomalous dimension $\Delta_T = 2$. Then it follows from the mode expansion (3.2.31) that we have $L_n \to \lambda^n L_n$ under a scale change $z \to z/\lambda$. This means that L_{-n} has the scaling dimension n (for $\overline{L}_{-n}$ analogous), and the dimensions of the secondary fields as defined in Eq. (3.2.53) are given by

$$\left(\Delta_\phi + \sum_{i=1}^{n} k_i \ , \ \overline{\Delta}_\phi + \sum_{j=1}^{m} \overline{k}_j \right). \tag{3.2.55}$$

We see that the primary field ϕ and its descendants form a series of fields with integer-spaced dimensions, see also Table 3.1. The numbers $l \equiv \sum_{i=1}^{n} k_i$ and $\overline{l} \equiv \sum_{j=1}^{m} \overline{k}_j$ are the *levels* of the descendant field $\phi^{(\{-k\},\{-\overline{k}\})}$. We call such a series a *conformal family*, and we denote it by $[\phi]$ after the primary field which in a sense serves as the ancestor of the family. Due to the property

$$\phi^{(-1,-k_1,\ldots,-k_n,-\overline{k})} = \frac{\partial}{\partial z}\phi^{(-k_1,\ldots,-k_n,-\overline{k})} \tag{3.2.56}$$

(and analogously for $\overline{z}$) a conformal family naturally contains all the derivatives of each field involved.

In principle, all the correlation functions of secondary fields are given by certain differential operators acting on those of primary fields. It is difficult, however, to write down closed expressions for those operators. From the result (3.2.52), we see that two-point functions of descendants of different primary fields vanish. For correlators of two secondary fields belonging to the same conformal family the leading order is given by Eq. (3.2.52), with the exponent $2\Delta_\phi$ ($2\overline{\Delta}_\phi$) replaced by $2\Delta_\phi + l_1 + l_2$ ($2\overline{\Delta}_\phi + \overline{l}_1 + \overline{l}_2$), where the numbers $(l_i, \overline{l}_i)$, $i = 1, 2$, denote the levels of the two fields.

We finally discuss how a secondary field $\phi^{(\{-k\}, \{-\overline{k}\})}$ changes under an infinitesimal conformal mapping ϵ. For this case it can be shown that the variation $\delta_\epsilon \phi^{(\{-k\}, \{-\overline{k}\})}$ can be fully expressed in terms of fields belonging to the same conformal family $[\phi]$. On the other hand, we know that the variation of ϕ is given by the expression (3.2.25), with Q_ϵ acting as a generator of the symmetry (see also Sects. 3.2.3 and 3.2.4). Therefore the conformal families $[\phi]$ correspond to irreducible representations of the conformal algebra, i. e. there are no subspaces invariant under conformal transformations. This observation leads to an important conclusion concerning the structure of the complete set of fields $\{A_n\}$ composing the operator algebra, namely that it consists of some number (which can be infinite) of conformal families $[\phi_i]$,

$$\{A_n\} = \bigoplus_i [\phi_i]. \tag{3.2.57}$$

This property implies that correlations of arbitrary fields (and therefore especially of scaling operators) in principle are given by the corresponding expressions for primary and secondary fields. Since correlations of descendants can be expressed in terms of those of primary fields, the decay of correlation functions in a conformal invariant theory is governed by the values of the anomalous dimensions $(\Delta_{\phi_i}, \overline{\Delta}_{\phi_i})$ of the primary fields ϕ_i which appear in the relation (3.2.57).

Before we analyze the two-point correlations of arbitrary fields in the following two subsections, we make one further comment concerning unitarity. In quantum field theory, unitarity guarantees the conservation of probabilities. For this reason it is important to search for values of the central charge c for which the Virasoro algebra has unitary representations. For $c < 1$, it turns out that only the values of c given by [FQS84]

$$c = 1 - \frac{6}{m(m+1)}, \qquad m \in \mathbb{N}_{\geq 3}, \tag{3.2.58}$$

are allowed, and for each value of m, there is only a finite number of representations (conformal families). For $c \geq 1$ no such restrictions are known, which is especially important for the case of the XXZ model, where $c = 1$ is valid (see Sect. 3.3.2).

3.2.7. Two-point correlations at $T = 0$

We now concentrate on the behavior of two-point correlation functions of arbitrary fields in the infinite-size geometry and in the vacuum state, which will be identified with the ground state in the following. We further assume that the effective continuum model has gapless excitations with a linear dispersion close to the Fermi points. Then we can write $z = x + i v_F \tau$ (v_F is the Fermi

velocity). The factor v_F is introduced so that both the real and imaginary part of z have the same physical dimension.

On the lattice, we are interested in correlations of physical quantities (e. g. spin or dimer operators) which correspond to certain fields $A(x, t) \equiv A(z, \overline{z})$ in the effective continuum model. Due to the property (3.2.57), we can decompose A according to

$$A(z, \overline{z}) = \sum_Q B(Q)\phi_Q(z, \overline{z}), \tag{3.2.59}$$

where $\phi_Q \equiv \phi_i^{(\{-k_i\}, \{-\overline{k_i}\})}$, i. e. the index Q labels both primary and descendant fields composing the operator algebra. From the previous subsection, we know that the two-point correlators of fields from different conformal families vanish, and in leading order the correlations of fields belonging to the same conformal family are determined by the anomalous dimensions of the primary field and the levels of its descendants. For this reason the leading asymptotic behavior of the two-point correlator of the field A in the ground state is given by the correlations of that primary field ϕ which has minimal values $(\Delta_\phi, \overline{\Delta}_\phi)$ for the anomalous dimensions and a non-vanishing weight B in the relation (3.2.59). According to Eq. (3.2.52), we therefore obtain

$$\langle 0|A(z_1, \overline{z}_1)A(z_2, \overline{z}_2)|0\rangle \simeq \frac{C}{(z_1 - z_2)^{2\Delta_\phi}(\overline{z}_1 - \overline{z}_2)^{2\overline{\Delta}_\phi}}. \tag{3.2.60}$$

By setting $z_1 = x + iv_F t$ and $z_2 = 0$, this gives an algebraic decay

$$\langle A(x, \tau)A(0, 0)\rangle_{T=0} \simeq \frac{C}{(x + iv_F\tau)^{2\Delta_\phi}(x - iv_F\tau)^{2\overline{\Delta}_\phi}}, \tag{3.2.61}$$

for the (Euclidean) dynamical two-point correlations at $T = 0$, which simplifies to

$$\langle A(x)A(0)\rangle_{T=0} \simeq Cx^{-2(\Delta_\phi + \overline{\Delta}_\phi)} \tag{3.2.62}$$

for the equal-time correlation function if we set $\tau = 0$.

3.2.8. Finite-size effects

In this subsection, we close our digression on CFT by discussing finite-size effects. We start with an analysis of the asymptotics of two-point correlations in a finite system [KBI93]. For this reason we consider the mapping[4] $f(z) = \frac{L}{2\pi} \log z$, which is a conformal transformation since it is analytical in the complex plane except for the origin $z = 0$. By applying this transformation and writing $f = u + iv$, the complex plane is mapped onto a strip (cylinder) with periodic boundary conditions along the v-direction: $v \equiv v + L$. The implications of this transformation can be used to study finite-size effects at $T = 0$ if we set $u \equiv v_F\tau$, $v \equiv x$, and $L \equiv N$. On the other hand, by setting $u \equiv x$, $v \equiv v_F\tau$, and $L = \frac{v_F}{T}$, the system gets finite along the time direction, and it is possible to extract the asymptotics of correlations in the infinite system at finite temperatures. To apply the results for $T > 0$ to the original lattice model, however, the temperature has to be sufficiently low, so that the condition $\xi \gg a$ is fulfilled.

---

[4]For $L = 2\pi$, this transformation is the inverse of the mapping we used in the context of radial quantization, see also Fig. 3.3 in Sect. 3.2.3.

The key observation when analyzing the finite-size behavior of correlations of arbitrary fields is that we can still make use of the decomposition (3.2.59). Then from an argumentation which is completely analogous to our approach in the preceeding section, it follows that the leading asymptotic behavior is determined by the correlations of that primary field ϕ with minimal anomalous dimensions $(\Delta_\phi, \overline{\Delta}_\phi)$ and non-vanishing coefficient B in Eq. (3.2.59). For this reason we only discuss the behavior of primary fields here.

For any primary field $\phi(z, \overline{z})$, the two-point correlations in the strip geometry can be evaluated by making use of the transformation property (3.2.37) and the result (3.2.52) for the infinite system. To simplify matters, we neglect the dependence of ϕ on $\overline{z}$ and generalize our result later as usual. We find

$$\langle 0|\phi(f_1)\phi(f_2)|0\rangle \overset{(3.2.37)}{=} \left(\frac{dz_1}{df_1}\right)^{\Delta_\phi} \left(\frac{dz_2}{df_2}\right)^{\Delta_\phi} \langle 0|\phi(z_1)\phi(z_2)|0\rangle$$

$$\overset{(3.2.52)}{=} \left(\frac{dz_1}{df_1}\right)^{\Delta_\phi} \left(\frac{dz_2}{df_2}\right)^{\Delta_\phi} \frac{C}{(z_1 - z_2)^{2\Delta_\phi}}. \tag{3.2.63}$$

If we now insert $z = \exp(\frac{2\pi}{L}f)$ and take the dependence on $\overline{z}$ into account, we arrive at

$$\langle 0|\phi(f_1, \overline{f}_1)\phi(f_2, \overline{f}_2)|0\rangle = C \left(\frac{\frac{\pi}{L}}{\sinh[\frac{\pi}{L}(f_1 - f_2)]}\right)^{2\Delta_\phi} \left(\frac{\frac{\pi}{L}}{\sinh[\frac{\pi}{L}(\overline{f}_1 - \overline{f}_2)]}\right)^{2\overline{\Delta}_\phi}, \tag{3.2.64}$$

which becomes

$$\langle 0|\phi(u_1, v_1)\phi(u_2, v_2)|0\rangle = C \frac{\left(\frac{2\pi}{L}\right)^{2(\Delta_\phi + \overline{\Delta}_\phi)}}{\left[2\cosh\left(\frac{2\pi}{L}(u_1 - u_2)\right) - 2\cos\left(\frac{2\pi}{L}(v_1 - v_2)\right)\right]^{\Delta_\phi + \overline{\Delta}_\phi}}, \tag{3.2.65}$$

if we replace $f = u + iv$. In the following we discuss the implications of this result for the following two cases:

1. Correlations in a finite chain of length N at $T = 0$ ($u_1 = v_F\tau$, $v_1 = x$, $u_2 = v_2 = 0$, and $L = N$):
   Then Eq. (3.2.65) becomes

$$\langle\phi(x, \tau)\phi(0, 0)\rangle^N_{T=0} = C \frac{\left(\frac{2\pi}{N}\right)^{2(\Delta_\phi + \overline{\Delta}_\phi)}}{\left[2\cosh\left(\frac{2\pi}{N}v_F\tau\right) - 2\cos\left(\frac{2\pi}{N}x\right)\right]^{\Delta_\phi + \overline{\Delta}_\phi}}. \tag{3.2.66}$$

   By inserting $\tau = 0$, this yields for the static correlation function

$$\langle\phi(x)\phi(0)\rangle^N_{T=0} = C \frac{\left(\frac{2\pi}{N}\right)^{2(\Delta_\phi + \overline{\Delta}_\phi)}}{\left[2 - 2\cos\left(\frac{2\pi}{N}x\right)\right]^{\Delta_\phi + \overline{\Delta}_\phi}}. \tag{3.2.67}$$

2. Low temperature correlations in the infinite system ($u_1 = x$, $v_1 = v_F\tau$, $u_2 = v_2 = 0$, and $L = \frac{v_F}{T}$):
   In this case one obtains from Eq. (3.2.65)

$$\langle\phi(x, \tau)\phi(0, 0)\rangle_{T>0} = C \frac{\left(\frac{2\pi T}{v_F}\right)^{2(\Delta_\phi + \overline{\Delta}_\phi)}}{\left[2\cosh\left(\frac{2\pi T}{v_F}x\right) - 2\cos\left(2\pi T\tau\right)\right]^{\Delta_\phi + \overline{\Delta}_\phi}}. \tag{3.2.68}$$

With $\tau = 0$, this implies for the equal-time correlation function

$$\langle \phi(x)\phi(0) \rangle_{T>0} = C \frac{\left(\frac{2\pi T}{v_F}\right)^{2(\Delta_\phi + \overline{\Delta}_\phi)}}{\left[2\cosh\left(\frac{2\pi T}{v_F}x\right) - 2\right]^{\Delta_\phi + \overline{\Delta}_\phi}}. \tag{3.2.69}$$

This is the result which will be exploited extensively when analyzing the low temperature data from QMC for the XXZ chain in Sect. 3.4. In particular, Eq. (3.2.69) implies that the algebraic exponent $2(\Delta_\phi + \overline{\Delta}_\phi)$ and the correlation amplitude C which govern the correlations at $T = 0$ (compare relation (3.2.62)) also determine the asymptotic decay at low finite temperatures. We further point out that the result (3.2.69) guarantees a smooth crossover to the corresponding expression (3.2.62) in the ground state, because we can expand $\cosh\left(\frac{2\pi T}{v_F}x\right) = 1 + \frac{1}{2}\left(\frac{2\pi T}{v_F}x\right)^2 + \mathcal{O}(T^4)$ for small temperatures T. Note that for $x \gg 1$, Eq. (3.2.69) also yields the expected exponential decay

$$\langle \phi(x)\phi(0) \rangle_{T>0} \simeq C \left(\frac{2\pi T}{v_F}\right)^{2(\Delta_\phi + \overline{\Delta}_\phi)} e^{-x/\xi(T)}, \tag{3.2.70}$$

with the correlation length

$$\xi^{-1}(T) = \frac{2\pi T}{v_F}(\Delta_\phi + \overline{\Delta}_\phi). \tag{3.2.71}$$

We see that ξ diverges linearly with the inverse temperature β as $T \to 0$.

We now need a procedure to determine the anomalous dimensions $(\Delta_\phi, \overline{\Delta}_\phi)$ of primary fields and the central charge c of the underlying Virasoro algebra in the effective theory. These numbers cannot be determined from CFT alone. However, one can compare the findings from the conformal approach concerning finite-size effects for the energy and momentum spectra to independent analytical or numerical results for the lattice model to deduce the quantities in question. The argument is as follows. We consider the result (3.2.65) with $u = v_F\tau$, $v = x$ and $L = N$, which has the expansion [Car86]

$$\langle 0|\phi(x_1, \tau_1)\phi(x_2, \tau_2)|0\rangle$$
$$= \left(\frac{2\pi}{N}\right)^{2(\Delta_\phi + \overline{\Delta}_\phi)} \sum_{m,\overline{m}=0}^{\infty} a_m a_{\overline{m}}\, e^{-\frac{2\pi v_F}{N}(\Delta_\phi + \overline{\Delta}_\phi + m + \overline{m})(\tau_1 - \tau_2) + i\frac{2\pi}{N}(\Delta_\phi - \overline{\Delta}_\phi + m - \overline{m})(x_1 - x_2)}, \tag{3.2.72}$$

where $a_m \equiv \frac{\Gamma(\Delta_\phi + \overline{\Delta}_\phi + m)}{\Gamma(\Delta_\phi + \overline{\Delta}_\phi)m!}$.

On the other hand one can analyze the correlations of the corresponding operator in the finite lattice model. This model is defined by a quantum Hamiltonian such as Eq. (3.1.1) for the XXZ chain, for which we want to assume translational invariance. Then it is possible to construct a basis of the Hilbert space which consists of common eigenstates of the Hamiltonian H and the total momentum operator P,

$$H|n, k_n\rangle = E_n(N)|n, k_n\rangle, \tag{3.2.73}$$

$$P|n, k_n\rangle = k_n(N)|n, k_n\rangle. \tag{3.2.74}$$

On the lattice, the field $\phi(x, \tau)$ corresponds to an operator $\hat{\phi}_x(\tau)$ acting on the Hilbert space. According to Eq. (2.4.67) from Par. 2.4.1, the dependence of $\hat{\phi}_x$ on τ is given by a Heisenberg representation (in imaginary time $t \equiv i\tau$) of the form $\hat{\phi}_x(\tau) = e^{-\tau H} \hat{\phi}_x \, e^{\tau H}$. Similarly, we can translate $\hat{\phi}_x$ according to $\hat{\phi}_x = e^{ixP} \hat{\phi}_0 \, e^{-ixP}$. Hence we have

$$\langle 0|\hat{\phi}_{x_1}(\tau_1)\hat{\phi}_{x_2}(\tau_2)|0\rangle = \sum_{n, k_n}\langle 0|\hat{\phi}_{x_1}(\tau_1)|n, k_n\rangle\langle n, k_n|\hat{\phi}_{x_2}(\tau_2)|0\rangle$$

$$= \sum_{n, k_n}|\langle 0|\hat{\phi}_0|n, k_n\rangle|^2 \; e^{-(E_n - E_0)(\tau_1 - \tau_2) + i(k_n - k_0)(x_1 - x_2)}, \tag{3.2.75}$$

where we have inserted a complete set of (H, P)-eigenstates in the first step. Then the comparison to Eq. (3.2.72) yields

$$E_n(N) - E_0(N) = \frac{2\pi v_F}{N}(\Delta_\phi + \overline{\Delta}_\phi + m + \overline{m}), \tag{3.2.76}$$

$$k_n(N) - k_0(N) = \frac{2\pi}{N}(\Delta_\phi - \overline{\Delta}_\phi + m - \overline{m}) + 2k_F D. \tag{3.2.77}$$

Here we have also included excitations where D particles are transferred from one Fermi point at $k = k_F$ to the other at $k = -k_F$. The relations (3.2.76) and (3.2.77) together with Eq. (3.2.75) imply that the anomalous dimensions of the primary field ϕ determine the energy and momentum of excitations mediated by the action of the operator $\hat{\phi}_0$ on the ground state if the system is placed on a cylinder of circumference N. Therefore, if it is possible to evaluate the energies and momenta of these excitations independently (in the case of the XXZ model this is done using the Bethe ansatz, see Sect. 3.3.1), one can determine the numbers $(\Delta_\phi, \overline{\Delta}_\phi)$.

We finally discuss the finite-size behavior of the ground state energy E_0 under the assumption of periodic boundary conditions, which yields a possibility to determine the central charge c. Since we deal with ground state properties again, we make use of the conformal mapping defined at the beginning of this subsection and set $f = v_F\tau + ix$. In principle, the change in E_0 under the transformation f can be obtained from the relation (3.2.18) in Par. 3.2.2. Therefore it is necessary to analyze the transformation behavior of the energy momentum tensor $T(z)$, which is a quasiprimary field (see also Sect. 3.2.6). For a detailed derivation we refer to the literature. We only give the main result here, which is

$$E_0(N) = N\epsilon_0 - c\frac{\pi v_F}{6N}, \tag{3.2.78}$$

where ϵ_0 is the ground state energy density (or ground state energy per lattice site) in the infinite system. We see that by comparing this expression to independent results from analytical or numerical techniques the central charge of the underlying Virasoro algebra can be extracted.

3.3. Bethe ansatz solution and asymptotics of correlation functions for the XXZ model

In this part we apply our findings from CFT for the asymptotic behavior of two-point correlations to the critical XXZ model with $-1 < \Delta \leq 1$. According to the argumentation from Par. 3.2.8,

however, we first need analytical results for the finite-size behavior of the model in order to determine the anomalous dimensions of primary fields and the central charge of the effective quantum field theory at low energies. For this reason we sketch how the XXZ chain can be solved analytically, and discuss the outcomes required in the context of correlation functions in the following subsection. Then in Sect. 3.3.2, these findings are combined with the expressions from CFT to derive the asymptotics of spin and dimer correlations which are needed for the numerical analysis in Sect. 3.4. We also turn to the topic of correlation amplitudes, especially focussing on the results for $G_{\parallel/\perp}$ from the literature (see Sect. 3.3.3). In Par. 3.3.4, we close this section with a discussion of algebraic and logarithmic corrections to asymptotic scaling at $T = 0$.

3.3.1. The idea of the coordinate Bethe ansatz

In this subsection we consider the Hamiltonian

$$\tilde{H} = \frac{J}{2} \sum_{i=1}^{N} (\sigma_i^x \sigma_{i+1}^x + \sigma_i^y \sigma_{i+1}^y + \Delta\,[\sigma_i^z \sigma_{i+1}^z - 1]), \qquad (3.3.79)$$

assuming periodic boundary conditions. Note that the model (3.3.79) differs from Eq. (3.1.1) by an energy shift of $-\frac{NJ\Delta}{2}$ which will simplify our notation below. In the following we present the idea of the *coordinate* Bethe ansatz solution for this system, allowing for arbitrary values[5] of the anisotropy parameter. For a more detailed review, we recommend Refs. [KBI93, Tak99].

The first observation one can exploit is that $\tilde{H}$ conserves the z-component of the total spin,

$$[\tilde{H}, S_{\text{tot}}^z] \equiv \left[\tilde{H}, \frac{1}{2}\sum_{i=1}^{N}\sigma_i^z\right] = 0. \qquad (3.3.80)$$

Therefore the Hilbert space decomposes according to

$$\mathcal{H} = \bigoplus_{M=0}^{N} \mathcal{H}_M, \qquad (3.3.81)$$

i. e. we can characterize the eigenstates of $\tilde{H}$ by the number M of down-spins, which is connected to the total magnetization by the relation

$$\langle S_{\text{tot}}^z \rangle = \frac{N}{2} - M. \qquad (3.3.82)$$

A basis in each subspace $\mathcal{H}_M$ is given by the states $(i_1 < i_2 < \ldots < i_M)$

$$|i_1 i_2 \ldots i_M\rangle \equiv \sigma_{i_1}^- \sigma_{i_2}^- \ldots \sigma_{i_M}^- |++\ldots+\rangle. \qquad (3.3.83)$$

The state $|++\ldots+\rangle$ is called *reference state* or *Bethe ansatz vacuum*, and obviously forms a basis of $\mathcal{H}_0$. As has been mentioned in the introduction 3.1 to this chapter, it is also a ground state of the system in the ferromagnetic sector $\Delta \leq -1$. However, for values $\Delta > -1$ the reference state is not the ground state and therefore should not be confused with the vacuum state $|0\rangle$ from

---

[5]We explicitly include the case of the XX model here, which can be solved analytically without Bethe ansatz methods [LSM61, McC68].

Sect. 3.2. The states defined in Eq. (3.3.83) differ from the Bethe ansatz vacuum by M spins overturned at the sites $i_1, i_2, \ldots, i_M$. An arbitrary state in $\mathcal{H}_M$ can be written as a superposition

$$|\psi_M\rangle = \sum_{i_1 < i_2 < \ldots < i_M} a(i_1, i_2, \ldots, i_M)|i_1 i_2 \ldots i_M\rangle. \qquad (3.3.84)$$

We see that solving the Schrödinger equation for the XXZ model is equivalent to the problem of determining the coefficients $a(i_1, i_2, \ldots, i_M)$ for the eigenstates of the Hamiltonian (3.3.79).

The key idea behind the coordinate Bethe ansatz is to represent these coefficients as a superposition of plane waves with a fixed set of wavenumbers $\{q_j\}$,

$$a(i_1, i_2, \ldots, i_M) = \sum_{P \in S_M} A_P \, e^{i(q_{P_1} i_1 + \ldots + q_{P_M} i_M)}, \qquad (3.3.85)$$

where S_M denotes the set of all permutations P of $\{1, 2, \ldots, M\}$. By inserting the linear combination (3.3.84) together with the ansatz (3.3.85) into the Schrödinger equation $\tilde{H}|\psi_M\rangle = E_M|\psi_M\rangle$ and exploiting the periodic boundary conditions, one receives M nonlinear coupled equations for the wavenumbers $\{q_j\}$

$$e^{iq_j N} \prod_{l \neq j} S(q_j, q_l) = 1, \qquad j, l = 1, 2, \ldots, M. \qquad (3.3.86)$$

Here the quantity $S(q_j, q_l)$ is given by

$$S(q_j, q_l) = -e^{-i\theta(q_j, q_l)}, \qquad (3.3.87)$$

with

$$\theta(q_j, q_l) = 2 \arctan\left(\frac{\Delta \sin([q_j - q_l]/2)}{\cos([q_j + q_l]/2) - \Delta \cos([q_j - q_l]/2)}\right). \qquad (3.3.88)$$

The equations (3.3.86) are the *Bethe ansatz equations* for the XXZ model, and $S(q_j, q_l)$ is called *two-particle scattering matrix*. Note that neither of the quasi-momenta $\{q_j\}$ can be equal because otherwise the wave function $|\psi_M\rangle$ vanishes, and furthermore, these numbers are not necessarily real. Similarly to the result (3.3.86), the amplitudes A_P in Eq. (3.3.85) can be expressed by A_I (I is the identity) and the scattering matrix in a unique way. The energy of $|\psi_M\rangle$ can be written as a sum of one-particle energies

$$E_M = \sum_{j=1}^M E(q_j) = 2J \sum_{j=1}^M (\cos(q_j) - \Delta). \qquad (3.3.89)$$

In analogy to the linear spin wave theory the plane waves in (3.3.85) are interpreted as magnons. For $\Delta \leq -1$, where the Bethe ansatz vacuum is also a ground state of the system, these particles are the elementary excitations of the system. As we have explained in Sect. 3.1, this is not the case in the quantum critical region $-1 < \Delta \leq 1$ and in the Ising-like antiferromagnetic sector $\Delta > 1$ of the phase diagram.

We now restrict ourselves to the case $-1 < \Delta \leq 1$. We do not discuss how the Bethe ansatz equations (3.3.86) are solved in the quantum critical regime. We only give the results which are needed to determine the asymptotics of correlation functions.

In the following we assume that the number N of lattice sites is even. Like the Néel state, the ground state of the system in the quantum critical regime can be characterized by $M = \frac{N}{2}$, i. e. it can be written as a (complicated) superposition of states with an equal number of up- and down-spins. In the thermodynamic limit, the ground state energy density is given by the expression

$$\epsilon_0 = -2J \sin^2 \gamma \int_{-\infty}^{\infty} \frac{d\lambda}{\cosh(\pi\lambda)(\cosh(2\gamma\lambda) - \cos\gamma)}. \qquad (3.3.90)$$

Here we have parametrized the anisotropy by defining $\gamma \equiv \arccos \Delta$, i. e. γ takes values in $[0, \pi)$. Note that for the original Hamiltonian (3.1.1), one has to add an additional contribution of $\frac{J\Delta}{2}$. For the antiferromagnetic XXX model, the result (3.3.90) reduces to $\epsilon_0 = -2J \ln 2$, which becomes

$$\epsilon_0 = \frac{J}{2} - 2J \ln 2 \qquad (3.3.91)$$

for the model (3.1.1) without energy shift. We have already described the nature of the gapless elementary excitations in Sect. 3.1. As has been mentioned there, one has to distinguish between the attractive and repulsive sectors of the quantum critical regime. However, a common feature for both regimes is the result

$$v_F = \frac{\pi J \sin \gamma}{\gamma} \qquad (3.3.92)$$

for the Fermi velocity, which is obtained from the dispersion relation of the two-spinon excitations with $S_{\text{tot}}^z = 0$. Note that the expression (3.3.92) becomes $v_F = \pi J$ in the isotropic limit $\Delta = 1$. The Fermi momentum is $k_F = \frac{\pi}{2}$.

In order to make use of the expressions derived from CFT in Sect. 3.2, we also need the Bethe ansatz results for the finite-size behavior of the system. For periodic boundary conditions, the finite-size correction to the ground state energy is

$$E_0(N) = N\epsilon_o - \frac{\pi v_F}{6N}, \qquad (3.3.93)$$

while the expressions for the energy and momentum of the low lying excitations are [KBI93]

$$E_n(N) - E_0(N) = \frac{2\pi v_F}{N} \left[\frac{\eta}{2}(\Delta M)^2 + \frac{1}{2\eta}D^2 + m + \overline{m} \right], \qquad (3.3.94)$$

$$k_n(N) - k_0(N) = \frac{2\pi}{N}(D\,\Delta M + m - \overline{m}) + 2k_F D, \qquad (3.3.95)$$

with

$$\eta \equiv \frac{\pi - \gamma}{\pi}. \qquad (3.3.96)$$

Note that by denoting these formulae, higher order contributions are neglected. Here the low lying excitations are classified in terms of the particles (spin-down sites) from Eq. (3.3.85). For the derivation of the results (3.3.94) and (3.3.95) only the following three processes are important:

1. The number of particles can be changed by ΔM as compared to the ground state.

2. D particles can jump over the sea of filled one-particle states from one Fermi point to the other (backscattering processes).

3. In practice, the Bethe ansatz equations (3.3.86) are solved by using their logarithmic representation

$$q_j N - \sum_{l \neq j} \theta(q_j, q_l) = n_j \pi, \tag{3.3.97}$$

where n_j is integer (half-integer) if N is odd (even). Then the number $m \in \mathbb{N}$ accounts for processes where n_j for the particle at one Fermi point is changed by m. Analogously, the number n_j for the particle at the other Fermi point may be changed by $\overline{m}$.

3.3.2. Asymptotics from the conformal approach

The expressions for the ground state and the excited states obtained from the Bethe ansatz are too complicated to evaluate the correlation functions $G_{\|/\perp/d}$ as defined in Eqs. (3.1.3), (3.1.4), and (3.1.5) directly. However, the results from Sect. 3.2 can be combined with the findings from the previous subsection to obtain the asymptotic expressions for the correlation functions. In this subsection, we give the relevant formulae for equal-time correlations in the thermodynamic limit for both $T = 0$ and low finite temperatures.

We first determine the central charge c and the anomalous dimensions $(\Delta_\phi, \overline{\Delta}_\phi)$ of those primary fields which are important for the correlations of the XXZ model [KBI93, Klü98]. To do this, we follow the method given in Par. 3.2.8. Comparing Eq. (3.3.93) to the result (3.2.78), we find $c = 1$ and therefore no restrictions on possible values for the anomalous dimensions due to unitarity. In addition, the values for $(\Delta_\phi, \overline{\Delta}_\phi)$ can be obtained by comparing the formulae (3.3.94) and (3.3.95) from the Bethe ansatz solution to the CFT results (3.2.76) and (3.2.77), respectively. Here we only denote the expression for the sum

$$\Delta_\phi + \overline{\Delta}_\phi = \frac{\eta}{2}(\Delta M)^2 + \frac{1}{2\eta} D^2, \tag{3.3.98}$$

because only this quantity appears in the results (3.2.62) and (3.2.69) for static correlations from the conformal approach. We now have to specify how the spin operators σ_i^z, $S_i^\pm$ and the dimer operator D_i act on the ground state. Note that for $G_\perp$, we consider the operators $S_i^\pm$ instead of σ_i^x because of the identity $\langle \sigma_i^x \sigma_j^x \rangle = \frac{1}{2} \langle \sigma_i^x \sigma_j^x + \sigma_i^y \sigma_j^y \rangle = \langle S_i^+ S_j^- + S_i^- S_j^+ \rangle$.

In the case of the longitudinal spin correlations, we obviously have $\Delta M = 0$, i. e. the action of σ_i^z on the ground state involves no change of the number of down-spins. The same statement holds[6] for the dimer correlations, because we can write $D_i = \vec{\sigma}_i \vec{\sigma}_{i+1} = 2P_{i,i+1} - 1$, where $P_{i,i+1}$ is the permutation operator which interchanges the spins on the sites i and $i + 1$. Therefore the fields which dominate the asymptotic behavior of both correlation functions $G_{\|/d}$ (i. e. with minimal scaling dimensions) are characterized by the following choices for $Q \equiv (\Delta M, D, m, \overline{m})$ in the decomposition (3.2.59), see Sect. 3.2.7.

1. $Q = (0, 1, 0, 0)$:

---

[6]From the viewpoint of the QMC loop algorithm, the evaluation of dimer correlations involves the numerical calculation of certain four-point correlations as described in App. A.3. In the context of CFT, the correlation function G_d is interpreted as the two-point correlator of the local energy operator D_i.

According to Eq. (3.3.98), this choice corresponds to a primary field with

$$\Delta_\phi + \overline{\Delta}_\phi = \frac{1}{2\eta}. \tag{3.3.99}$$

The contribution of this field to the asymptotics of $G_{\parallel/\mathrm{d}}$ is given by the Eqs. (3.2.62) and (3.2.69), respectively. We add that it can be shown [KBI93] that the dependence of the weight $B(Q)$ in Eq. (3.2.59) on D is given by ($z = v_\mathrm{F} t + ix$)

$$B(Q) \propto e^{-2ixk_\mathrm{F}D}.$$

With $D = 1$ and $k_\mathrm{F} = \frac{\pi}{2}$ for the XXZ model this amounts to an additional factor of $(-1)^x$.

2. $Q = (0, 0, 1, 0), (0, 0, 0, 1)$:
   These choices correspond to secondary fields and determine the subleading order of the decay of $G_{\parallel/\mathrm{dim}}$. Their leading contribution is also given by the results (3.2.62) and (3.2.69) if we replace

$$\Delta_\phi + \overline{\Delta}_\phi \ \rightarrow \ \Delta_\phi + \overline{\Delta}_\phi + m + \overline{m} = 1. \tag{3.3.100}$$

As far as the transversal spin correlations are concerned, we have $\Delta M = 1$, because the operators $S_i^\pm$ may alter the number of down-spins by one. Therefore the leading and subleading orders of the asymptotic decay of $G_\perp$ can be read from the Eqs. (3.2.62) and (3.2.69) as usual, where we have

1. $Q = (1, 0, 0, 0)$:
   This corresponds to a primary field with

$$\Delta_\phi + \overline{\Delta}_\phi = \frac{\eta}{2}. \tag{3.3.101}$$

2. $Q = (1, 1, 0, 0)$:
   In contrast to $G_{\parallel/\mathrm{d}}$, the subleading order of $G_\perp$ is also controlled by a primary field with

$$\Delta_\phi + \overline{\Delta}_\phi = \frac{\eta}{2} + \frac{1}{2\eta}. \tag{3.3.102}$$

Again we have to include an additional factor of $(-1)^x$ because we have $D = 1$.

We are now in the position to sum up our results. The asymptotics of the longitudinal and transversal spin correlation functions in the ground state are given by

$$G_\parallel(x) \simeq (-1)^x \frac{C_{\parallel,1}}{x^{\frac{1}{\eta}}} \ + \ \frac{C_{\parallel,2}}{x^2}, \tag{3.3.103}$$

$$G_\perp(x) \simeq \frac{C_{\perp,1}}{x^\eta} \ + \ (-1)^x \frac{C_{\perp,2}}{x^{\eta + \frac{1}{\eta}}}. \tag{3.3.104}$$

For the dimer correlations, we omit the subleading order term and find

$$G_\mathrm{d}(x) \simeq (-1)^x \frac{C_\mathrm{d}}{x^{\frac{1}{\eta}}}. \tag{3.3.105}$$

With respect to the numerical analysis in Sect. 3.4, we are particularly interested in the corresponding expressions for low finite temperatures. These are

$$G_{\parallel}(x) \simeq \frac{C_{\parallel,1}(-1)^x \left(\frac{2\pi T}{v_F}\right)^{\frac{1}{\eta}}}{\left[2\cosh\left(\frac{2\pi T}{v_F}x\right) - 2\right]^{\frac{1}{2\eta}}} + \frac{C_{\parallel,2}\left(\frac{2\pi T}{v_F}\right)^2}{\left[2\cosh\left(\frac{2\pi T}{v_F}x\right) - 2\right]}, \tag{3.3.106}$$

$$G_{\perp}(x) \simeq \frac{C_{\perp,1}\left(\frac{2\pi T}{v_F}\right)^{\eta}}{\left[2\cosh\left(\frac{2\pi T}{v_F}x\right) - 2\right]^{\frac{\eta}{2}}} + \frac{C_{\perp,2}(-1)^x \left(\frac{2\pi T}{v_F}\right)^{\eta+\frac{1}{\eta}}}{\left[2\cosh\left(\frac{2\pi T}{v_F}x\right) - 2\right]^{\frac{\eta}{2}+\frac{1}{2\eta}}}, \tag{3.3.107}$$

$$G_{d}(x) \simeq \frac{C_{d}(-1)^x \left(\frac{2\pi T}{v_F}\right)^{\frac{1}{\eta}}}{\left[2\cosh\left(\frac{2\pi T}{v_F}x\right) - 2\right]^{\frac{1}{2\eta}}}, \tag{3.3.108}$$

where the Fermi velocity v_F is given by Eq. (3.3.92). As expected, the expressions for longitudinal and transversal spin correlation coincide (apart from a trivial factor of $(-1)^x$) in the isotropic limit $\Delta = 1$. We further emphasize that in the free fermion case $\Delta = 0$, which can be diagonalized easily without making use of the Bethe ansatz, our findings for $G_{\parallel,\perp}$ are consistent with the results obtained in Refs. [LSM61, McC68].

3.3.3. Correlation amplitudes

We have seen that the combination of CFT and Bethe ansatz results provides a powerful instrument to determine the exponents of the asymptotic decay of correlation functions in critical theories. To evaluate the correlation amplitudes and the leading corrections to asymptotic scaling, however, one needs a quantitative relation between lattice operators and the fields which are important in the effective critical theory. This cannot be achieved within the framework of conformal invariance, and substantially different approaches have to be applied.

As we have pointed out in Sect. 3.1, closed expressions for the correlation amplitudes $C_{\parallel/\perp,1/2}$ as well as corrections to the asymptotic behavior of spin correlations at $T = 0$ have been derived for the quantum critical regime $-1 < \Delta \leq 1$ in the literature [LZ97, Luk99, LT03]. The approach is based on an asymptotic series expansion of the lattice Hamiltonian (2.2.3) in terms of the lattice spacing a, where the leading order is given by the (conformal invariant) effective quantum field theory at low energies, i. e. the Thirring model which is equivalent to the bosonic *Gaussian field theory*. In terms of statistical physiscs, the higher order terms in this expansion correspond to irrelevant (or marginal) scaling operators. For the lattice spin operators one can write down similar series expansions in a. A quantitative relation between lattice operators and scaling fields can be obtained by moving slightly away from the critical regime and considering the more general XYZ model

$$H = \frac{1}{2}\sum_{i=1}^{N}(J_x\sigma_i^x\sigma_{i+1}^x + J_y\sigma_i^y\sigma_{i+1}^y + J_z\sigma_i^z\sigma_{i+1}^z), \tag{3.3.109}$$

which contains the Hamiltonian (3.1.1) in the special case $J_x = J_y$. The effective quantum field theory which describes the low energy physics of the XYZ model properly is the *sine-Gordon*

model. By comparing certain exact results obtained for the XYZ and the sine-Gordon models, one can quantitatively connect lattice spin operators to scaling fields. This provides access to both correlation amplitudes and to the leading corrections to asymptotic scaling for the critical XXZ model. For more details we refer to the literature. However, for later use we write down the results for the correlation amplitudes from Ref. [LT03], which are

$$
C_{\parallel,1} = \frac{8}{\pi^2} \left[\frac{\Gamma(\frac{\eta}{2-2\eta})}{2\sqrt{\pi}\Gamma(\frac{1}{2-2\eta})} \right]^{\frac{1}{\eta}} \exp \left\{ \int_0^\infty \frac{dt}{t} \left(\frac{\sinh((2\eta-1)t)}{\sinh(\eta t)\cosh((1-\eta)t)} - \frac{2\eta-1}{\eta} e^{-2t} \right) \right\},
$$

$$
\tag{3.3.110}
$$

$$
C_{\parallel,2} = -\frac{1}{\pi^2 \eta},
\tag{3.3.111}
$$

for the longitudinal spin correlation function, while the findings are

$$
C_{\perp,1} = \frac{1}{2(1-\eta)^2} \left[\frac{\Gamma(\frac{\eta}{2-2\eta})}{2\sqrt{\pi}\Gamma(\frac{1}{2-2\eta})} \right]^{\eta} \exp \left\{ -\int_0^\infty \frac{dt}{t} \left(\frac{\sinh(\eta t)}{\sinh(t)\cosh((1-\eta)t)} - \eta e^{-2t} \right) \right\},
$$

$$
\tag{3.3.112}
$$

$$
C_{\perp,2} = \frac{2}{\eta(1-\eta)} \left[\frac{\Gamma(\frac{\eta}{2-2\eta})}{2\sqrt{\pi}\Gamma(\frac{1}{2-2\eta})} \right]^{\eta+\frac{1}{\eta}}
$$

$$
\times \exp \left\{ -\int_0^\infty \left(\frac{\cosh(2\eta t)e^{-2t}-1}{2\sinh(\eta t)\sinh(t)\cosh((1-\eta)t)} + \frac{1}{\sinh(\eta t)} - \frac{\eta^2+1}{\eta} e^{-2t} \right) \right\},
$$

$$
\tag{3.3.113}
$$

for the prefactors of transversal correlations. Note that $C_{\parallel/\perp,1}$ both diverge as $\Delta \uparrow 1$. This indicates the presence of logarithmic corrections in the isotropic XXX model. In the case of the dimer correlations, the amplitude C_d has not been determined in the literature.

3.3.4. Algebraic and logarithmic corrections to asymptotic scaling

In the last subsection, we have argued that the lattice nature of the XXZ model causes corrections to the effective Gaussian field theory. As long as $-1 < \Delta < 1$, the operators involved turn out to be irrelevant, giving rise to additive algebraic corrections to the asymptotics of correlations in the ground state. Although these corrections can be neglected at large distances, they might be important when analyzing numerical data at intermediate distances. In the case of the spin correlations $G_{\parallel/\perp}$, these corrections have also been determined by Lukyanov and Terras [LT03]. In this thesis, we only analyze the leading corrections to the leading order terms, which can be expressed by replacing

$$
C_{\parallel,1} \to C_{\parallel,1}(x) \equiv C_{\parallel,1} \left(1 - \frac{B_z}{x^{\frac{2}{\eta}-2}} \right),
\tag{3.3.114}
$$

$$
C_{\perp,1} \to C_{\perp,1}(x) \equiv C_{\perp,1} \left(1 - \frac{B}{x^{\frac{4}{\eta}-4}} \right),
\tag{3.3.115}
$$

in the asymptotic results (3.3.103) and (3.3.104). For analytical expressions of the constants B_z and B see Ref. [LT03]. Note that for G_d no such result has been derived in the literature.

The situation is somewhat different at the isotropic point $\Delta = 1$, where one of the operators involved becomes marginal. This gives rise to multiplicative logarithmic corrections [AGSZ89, GS89, SFS89, Klü98]. In Ref. [LT03], the authors also derive a precise expression for these corrections in the case of the spin correlations. As above, we only give the corrections to the leading order term here. Similarly to the Eqs. (3.3.114) and (3.3.115), we express the result by assigning a dependence on x to $C_{\parallel,1}$,[7]

$$C_{\parallel,1}(g) = \sqrt{\frac{2}{\pi^3 g}}\left[1 - \frac{1}{8}g - \frac{19}{128}g^2 + \left(\frac{13\zeta(3)}{32} - \frac{127}{1024}\right)g^3 + \mathcal{O}(g^4)\right]. \qquad (3.3.116)$$

Here g depends on x and can be determined by solving

$$\sqrt{g}\,e^{\frac{1}{g}} = 2\sqrt{2\pi}e^{\gamma_E+1}x, \qquad (3.3.117)$$

which has to be done numerically in practice. The number $\gamma_E \approx 0.5772$ is the Euler constant. For large x, Eq. (3.3.116) yields the asymptotic result $C_{\parallel,1} \sim (\ln x)^{\frac{1}{2}}$ which had been found in Refs. [AGSZ89, GS89, SFS89]. As has been mentioned before, we have $G_{\parallel}(x) = (-1)^x G_{\perp}(x)$ for $\Delta = 1$. For the dimer correlations, it is known that the leading logarithmic correction is of the order $C_d \sim (\ln x)^{-\frac{3}{2}}$ [AGSZ89, Klü98].

3.4. Analysis of low temperature data

In this section we analyze the QMC data of correlation functions at low finite temperatures, restricting ourselves to the gapless repulsive regime $0 \leq \Delta \leq 1$ of the model [AL05]. The numerical estimates for $G_{\parallel/\perp/d}$ were obtained by means of the continuous time loop algorithm as described in Sects. 2.2.3 and 2.2.5, applying the measurement rules from Sects. 2.4.2 and App. A.3 for the correlation functions. The simulations were carried out for temperatures $T = 0.02J, 0.025J, \ldots, 0.1J$ and values of the anisotropy parameter $\Delta = 0.0, 0.1, \ldots, 1.0$ in chains with $N = 1000$ sites and periodic boundary conditions. In each run, a number of 10^5 spin updates was taken for the thermalization of the algorithm. Furthermore, for the measurement of correlation functions 2×10^6 configurations were evaluated to reach a high accuracy of the numerical results.

The section is organized as follows. In Par. 3.4.1, we focus on the spin correlation functions $G_{\parallel/\perp}$ and discuss to what extent the results from the Sects. 3.3.2 and 3.3.3 coincide with the numerical data. Then in Par. 3.4.2, we concentrate on the crossover from low temperatures to the ground state, and analyze the algebraic and logarithmic corrections to asymptotic scaling. The properties of the dimer correlation function G_d are analyzed in an analogous fashion in the Sects. 3.4.3 and 3.4.4. There we especially focus on the correlation amplitude C_d, which has not been determined in the literature. In the first of the two subsections we derive a rough numerical estimate for C_d by directly fitting the asymptotic expression from CFT to the numerical data. The second subsection is dedicated to the corrections to asymptotic scaling. In particular, we will see that this analysis provides a possibility to deduce more reliable numerical estimates for the prefactor C_d.

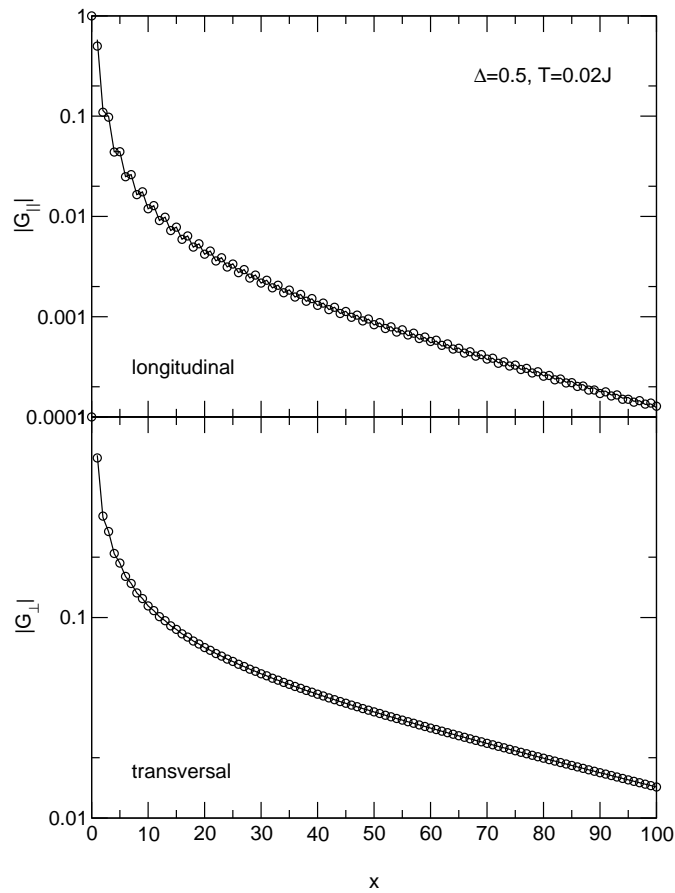[7]We set $c = 1$ in Eq. (5.25) from Ref. [LT03].

Fig. 3.4.: Numerical values (circles) and fits (solid lines) for the absolute value of $G_\parallel$ (top) and $G_\perp$ (bottom) vs. distance for $T = 0.02J$. The value of the anisotropy parameter is $\Delta = 0.5$. The numerical errors are smaller than the symbol size.

3.4.1. Spin correlations: direct fits of asymptotic expressions

The predictions from Sect. 3.3.2 for the low temperature behavior of the longitudinal and transversal spin correlations can be tested directly by considering the fitfunction

$$f(x) = \frac{C_1(-1)^x \left(\frac{2\pi T}{v}\right)^{2x_{\phi,1}}}{\left[2\cosh\left(\frac{2\pi T}{v}x\right) - 2\right]^{x_{\phi,1}}} + \frac{C_2 \left(\frac{2\pi T}{v}\right)^{2x_{\phi,2}}}{\left[2\cosh\left(\frac{2\pi T}{v}x\right) - 2\right]^{x_{\phi,2}}} \qquad (3.4.118)$$

with five free parameters v, $x_{\phi,1/2}$, and $C_{1/2}$, see the formulae (3.3.106) and (3.3.107) for the decay of $G_{\parallel/\perp}$. The periodic boundary conditions are taken into account by fitting the symmetrized form

$$g(x) \equiv f(x) + f(N - x) \qquad (3.4.119)$$

to the numerical data. Since we are interested in asymptotic properties, it is reasonable to fit the numerical data for distances x as large as possible. If the separation x is too large, on the other hand, the absolute values of the Monte Carlo estimates become too small to be reliable. A good
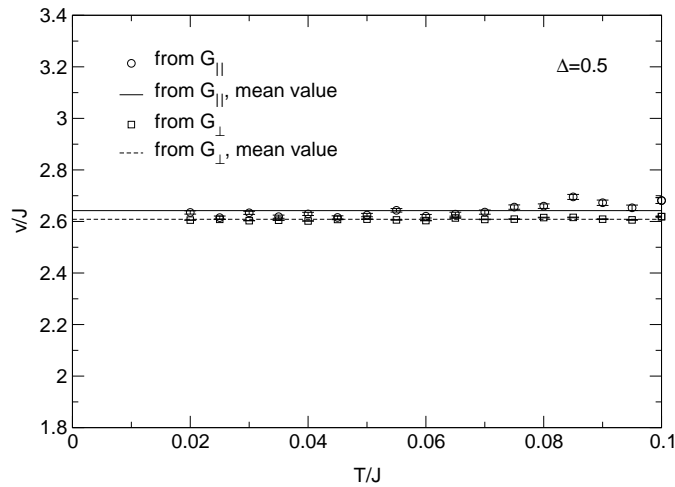
Fig. 3.5.: Fitting parameter v against temperature for $\Delta = 0.5$ from fits of $G_\parallel$ (circles) and $G_\perp$ (squares). The solid (dashed) line represents the average of the values over all temperatures extracted from $G_\parallel$ ($G_\perp$).
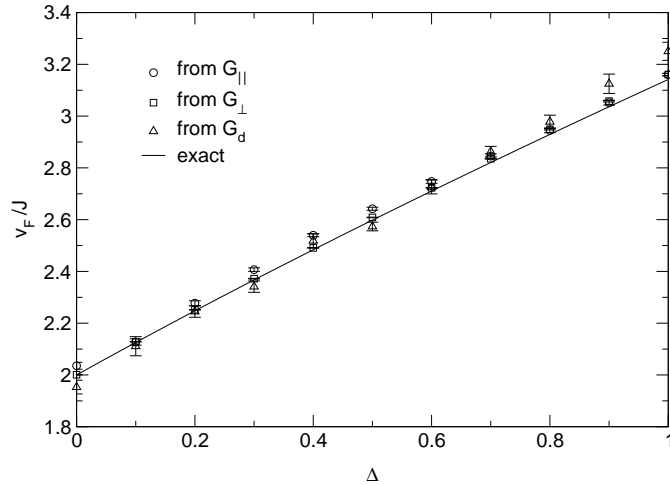

Fig. 3.6.: Comparison of averaged values for v from longitudinal (circles) and transversal spin correlations (squares) to the exact result (3.3.92) (solid line) for v_F from Sect. 3.3.1. The triangles are the numbers derived from the fits of G_d, see Par. 3.4.3.

fitting performance is achieved by choosing $x_{min} = 7$ for the left boundary of the fitting interval. The right boundary varies and is determined by the condition $|G_{\parallel/\perp}(x_{max})| \geq 10^{-4}$. Note that for $G_\parallel$, this condition is applied for odd values of x only, because we have $G_\parallel(x) = 0$ for x even in the XX model ($\Delta = 0$) [LSM61, McC68]. To illustrate the quality of the fits, we give a typical example in Fig. 3.4.

The number v can be viewed as a control parameter for the reliability of our approach. For fixed anisotropy Δ and sufficiently low temperatures in an infinite system, we expect that v takes the constant value v_F for all temperatures, which is given by Eq. (3.3.92) from Par. 3.3.1. On a finite
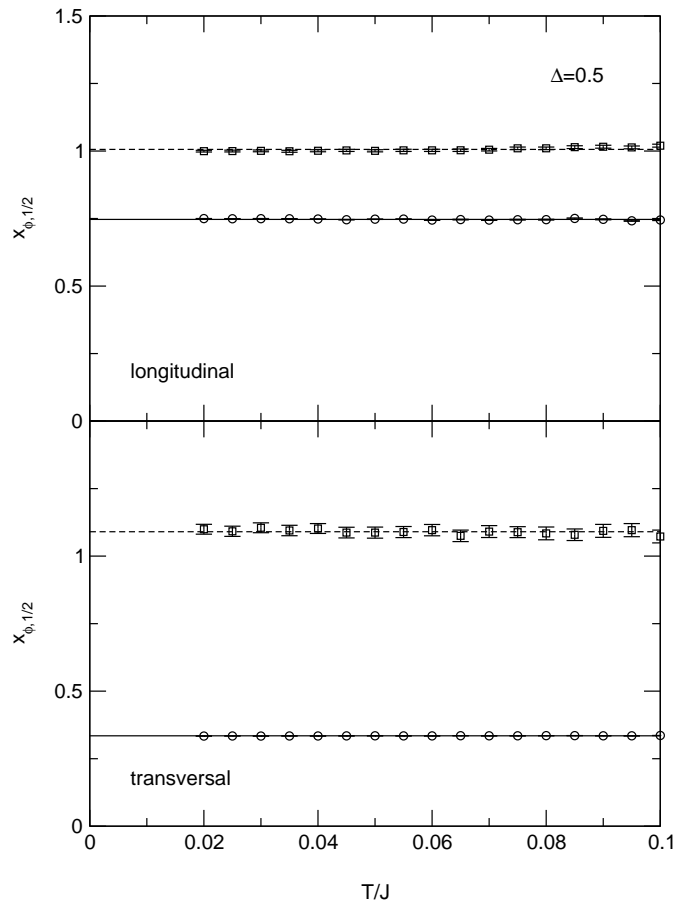
Fig. 3.7.: Temperature dependence of the fitting parameters $x_{\phi,1/2}$ for the leading (circles) and subleading orders (squares) from direct fits to the data of $G_{\parallel}$ (top) and $G_{\perp}$ (bottom). The value for the anisotropy parameter is $\Delta = 0.5$. In both panels the solid (dashed) line corresponds to the averaged value as an estimate for the correlation exponent of the leading (subleading) order.

lattice, however, significant deviations from this behavior should appear as soon as the temperature becomes smaller than the gap in the excitation spectrum which opens due to the finite-size effect. In Fig. 3.5, it is illustrated that the parameter v obtained by fitting both $G_{\parallel}$ and $G_{\perp}$ stays constant in the whole temperature range indeed. Neglecting small fluctuations at higher temperatures, we can therefore extract numerical estimates for the Fermi velocity by averaging the values of v over all temperatures. The results for various choices of Δ are compared to the expression (3.3.92) in Fig. 3.6. They coincide well with the exact result, although the mean values from the fits of $G_{\parallel}$ slightly overestimate v_F. From this analysis we conclude that the temperature range chosen is sufficiently low to see the asymptotic behavior predicted by CFT on the one hand, and larger than the finite-size gap in the excitation spectrum on the other hand.

From the other fitting parameters, one can derive numerical estimates for the correlation exponents and amplitudes. Similarly to the values of v, we expect that for fixed Δ the fitting parameters $x_{\phi,1/2}$ and $C_{1/2}$ stay constant in the whole range of temperatures. For $\Delta = 0.5$, it is shown ex-
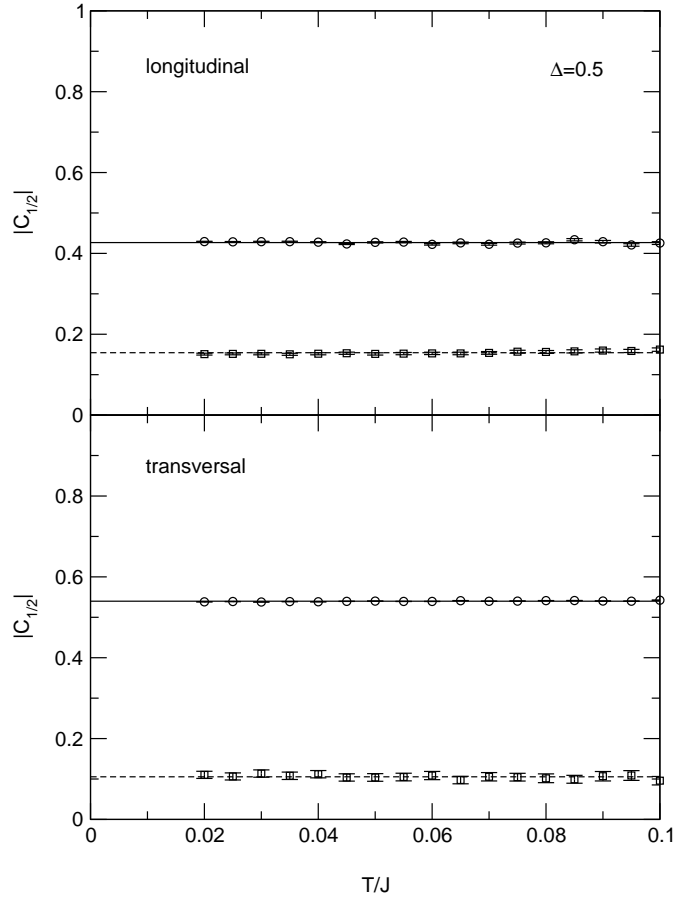
Fig. 3.8.: Absolute values of the fitting parameters $C_{1/2}$ vs. temperature for the leading (circles) and subleading orders (squares) of $G_\parallel$ (top) and $G_\perp$ (bottom) for $\Delta = 0.5$. The solid (dashed) lines depict the average over all temperatures for the leading (subleading) contribution.

emplarily in the Figs. 3.7 and 3.8 that this expectation is fulfilled very convincingly. Even for the subleading order terms, the fluctuations of the fitting parameters with the temperature are small. As we did for the Fermi velocity, we therefore determine numerical estimates for the exponents and amplitudes by averaging the numbers obtained from the fits over the whole temperature range.

As far as the correlation exponents are concerned, we have seen in Sect. 3.3.2 that $x_{\phi,1/2}$ should take the constant values $\frac{1}{2\eta}$ and 1 for $G_\parallel$, while they should be equal to $\frac{\eta}{2}+\frac{1}{2\eta}$ and $\frac{\eta}{2}$ for $G_\perp$, compare the Eqs. (3.3.106) and (3.3.107), respectively. The comparison to the numerical estimates is shown in Fig. 3.9. In the case of the longitudinal correlations the leading order is reproduced well by the Monte Carlo results for $0 \leq \Delta \leq 0.5$, while the subleading order coincides with the result from CFT in the whole range of the anisotropy parameter Δ. For values $\Delta > 0.5$, however, deviations from the predicted behavior in the leading order are visible. This discrepancy can be ascribed to the fact that the QMC data are fitted at values for x which are too small to fully reach the asymptotic regime. As has been discussed in Sect. 3.3.4, at $T = 0$ the correlation amplitude $C_{\parallel,1}$ has an
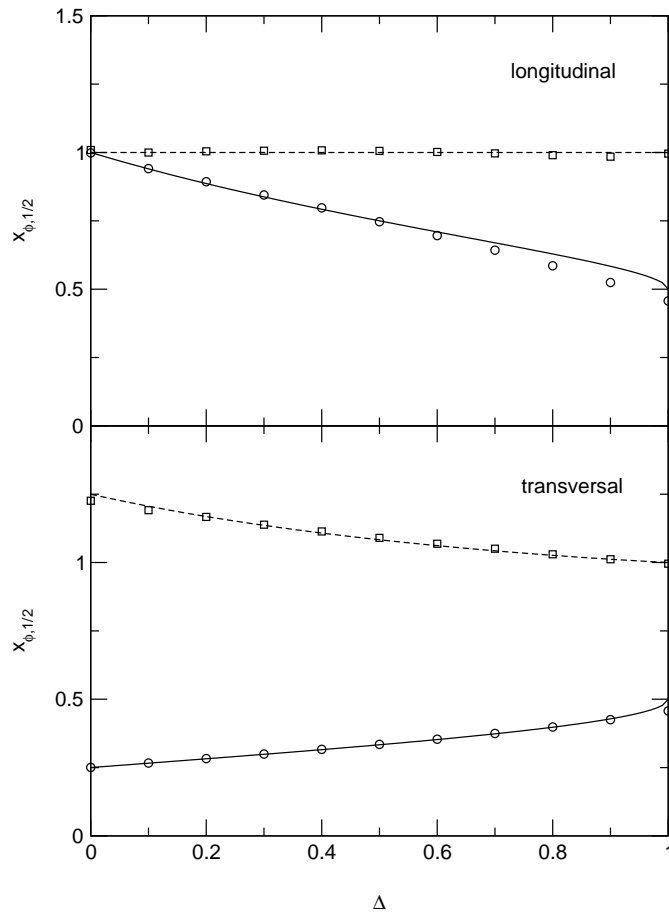
Fig. 3.9.: Correlation exponents for longitudinal (top) and transversal spin correlations (bottom). The circles represent the QMC results for the leading order, the squares for the subleading order. The solid lines represent the leading exponents from CFT ($\frac{1}{2\eta}$ and $\frac{\eta}{2}$), while the exact results for the subleading order (1 and $\frac{\eta}{2} + \frac{1}{2\eta}$) are depicted by the dashed lines. The numerical errors are smaller than the size of the symbols.

algebraic correction of the order $x^{2-\frac{2}{\eta}}$, compare the relation (3.3.114). Hence the influence of this correction grows as $\Delta \uparrow 1$. Due to the close connection between ground state and low temperature properties, a similar correction should play a part at low finite temperatures. For $\Delta = 1$, one cannot expect that the procedure applied in this subsection gives correct results because of the presence of logarithmic corrections. Similar statements hold in the case of transversal correlations. As far as the leading order is concerned though, the algebraic correction to $C_{\perp,1}$ at $T = 0$ is of the order $x^{4-\frac{4}{\eta}}$ (see Eq. (3.3.115)) and therefore less important than the corresponding correction for $G_{\parallel}$. For this reason deviations only appear for $\Delta = 1$. Close to the free fermion point $\Delta = 0$, it is difficult to extract the correct exponent of the subleading order. This is mainly due to the large difference of the leading and subleading exponents in this parameter range.

The findings for the correlation amplitudes $C_{\parallel/\perp,1/2}$ support these observations, see Fig. 3.10.
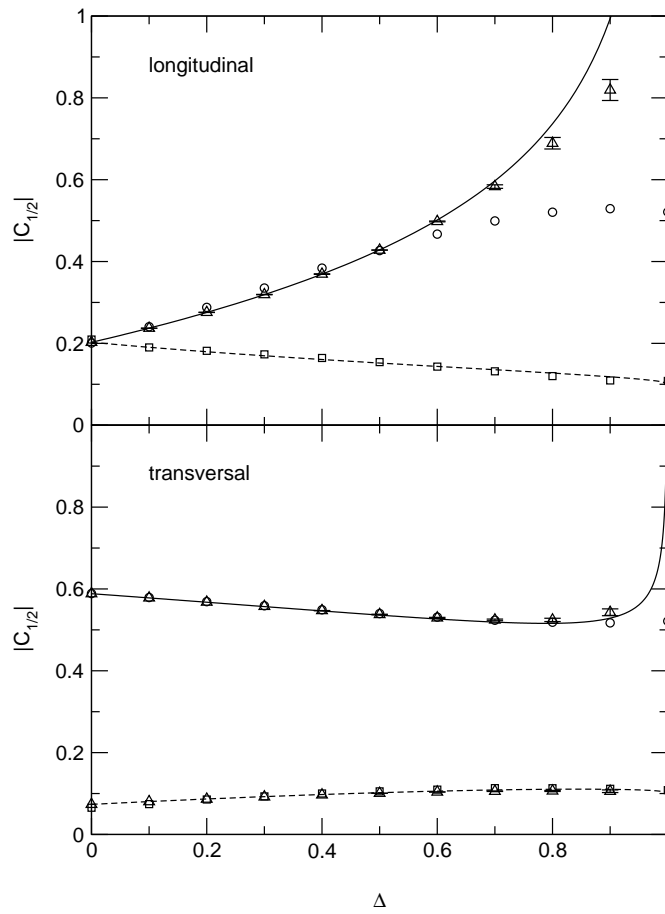
Fig. 3.10.: Absolute values of the correlation amplitudes for the longitudinal (top) and transversal spin correlation functions (bottom). As in Fig. 3.9, the circles and squares are the QMC results for the leading and subleading orders, respectively. The errors are smaller than the symbols. The solid lines represent the exact results (3.3.110) and (3.3.112), the dashed lines Eqs. (3.3.111) and (3.3.113) from Ref. [LT03], see Sect. 3.3.3. The numerical estimates derived from DMRG data in Ref. [HF04] are given by the triangles.

The numerical estimates confirm the expressions (3.3.110), (3.3.111), (3.3.112) and (3.3.113) from Sect. 3.3.3 in the ranges for Δ described above. The values for Δ, where the QMC results for the amplitudes deviate from the analytical asymptotic results, fully coincide with the discrepancies observed for the correlation exponents. This supports the assumption that algebraic and logarithmic corrections have to be taken into account close to and at the isotropic point $\Delta = 1$, respectively. From the figure we can also conclude that the numerical values obtained from DMRG data in Ref. [HF04] give a better estimate of the correlation amplitudes as compared to the QMC results. This is an expected result because DMRG is an instrument to investigate the ground state properties of the system directly. In addition, the errorbars of quantities computed with DMRG are usually very small. Close to $\Delta = 1$ and similarly to the QMC findings, however, the numbers from Ref. [HF04] also show deviations from the analytical expressions due to the neglect of algebraic corrections.

We will discuss this aspect in more detail in the next subsection.

We close this subsection with a remark concerning the crossover behavior from low finite temperatures to $T = 0$. In Sect. 3.2.8 it has been explained that in CFT, the factor $\left(\frac{2\pi T}{v}\right)^{2(\Delta_\phi + \overline{\Delta}_\phi)}$ in the numerator of Eq. (3.2.69) guarantees a smooth connection to the ground state correlator (3.2.62) from Par. 3.2.7 as $T \to 0$. In Ref. [FM99], however, the authors point out that this point has not yet been shown numerically. Since the fitting ansatz (3.4.118) includes such a temperature dependence and the numbers obtained from the fits stay constant in the whole temperature range, the QMC data clearly support this type of crossover behavior.

3.4.2. Spin correlations: algebraic and logarithmic corrections

In the last subsection we saw that, close to $\Delta = 1$, one cannot determine the correct correlation exponents and amplitudes by fitting the asymptotic expressions from Sect. 3.3.2 directly to the numerical data at intermediate distances. For $\Delta \lesssim 1$, we suspected that this is mainly due to algebraic corrections, while in the XXX model logarithmic corrections play a part. We now investigate this point in more detail. Since we were well able to reproduce the exact results for the subleading order terms in our analysis, we restrict the discussion to the leading order terms of $G_\parallel$ and $G_\perp$.

A systematic way to describe deviations from the asymptotic behavior at finite temperatures is to formally keep the asymptotic expressions (3.3.106) and (3.3.107) from Sect. 3.3.2, but to assign a dependence on distance and temperature to the correlation amplitudes, i. e.

$$C_{\parallel/\perp,1} \to C_{\parallel/\perp,1}(x, T). \tag{3.4.120}$$

Such an approach is justified if we get back to the expressions (3.3.114), (3.3.115) (for $\Delta < 1$), and (3.3.116) (for $\Delta = 1$) from Par. 3.3.4 in the limit $T \to 0$ and for $x \gg 1$, because in this case a smooth crossover to the behavior in the ground state is ensured. Note that this is a nontrivial assumption which has to be verified when analyzing the numerical data. The distance and temperature dependent prefactors $C_{\parallel/\perp,1}(x, T)$ can be extracted as follows: for each value of x and T, the QMC estimates for $G_\parallel$ and $G_\perp$ are inserted into the symmetrized form (3.4.119) of Eqs. (3.3.106) and (3.3.107), then the resulting equations are solved for $C_{\parallel,1}$ and $C_{\perp,1}$, respectively. This procedure involves a subtraction of the subleading order, for which we make use of the exact asymptotic results (3.3.111) and (3.3.113) for $C_{\parallel,2}$ and $C_{\perp,2}$. At this point a systematic error comes into our analysis due to the neglect of both corrections to the subleading order terms and of higher order contributions, but one can expect these corrections to be of minor importance when investigating the leading order.

For $G_\parallel$ and $\Delta = 0.8, 0.9$, the results for four different temperatures are plotted in Fig. 3.11. As can be clearly seen, the values for $C_{\parallel,1}(x, T)$ deviate strongly from the asymptotic constant value (3.3.110) which is given by the dashed lines in the figure. As expected, these deviations from the CFT prediction increase with higher temperatures. At any fixed temperature, the difference to the asymptotic result grows when Δ is increased. This behavior is consistent with the influence of the algebraic correction $\sim x^{2-\frac{2}{\eta}}$ in the ground state, whose impact grows as $\Delta \uparrow 1$. The values for $C_{\parallel,1}(x, T)$ can be extrapolated to $T = 0$. Reliable estimates for the values in the ground state are
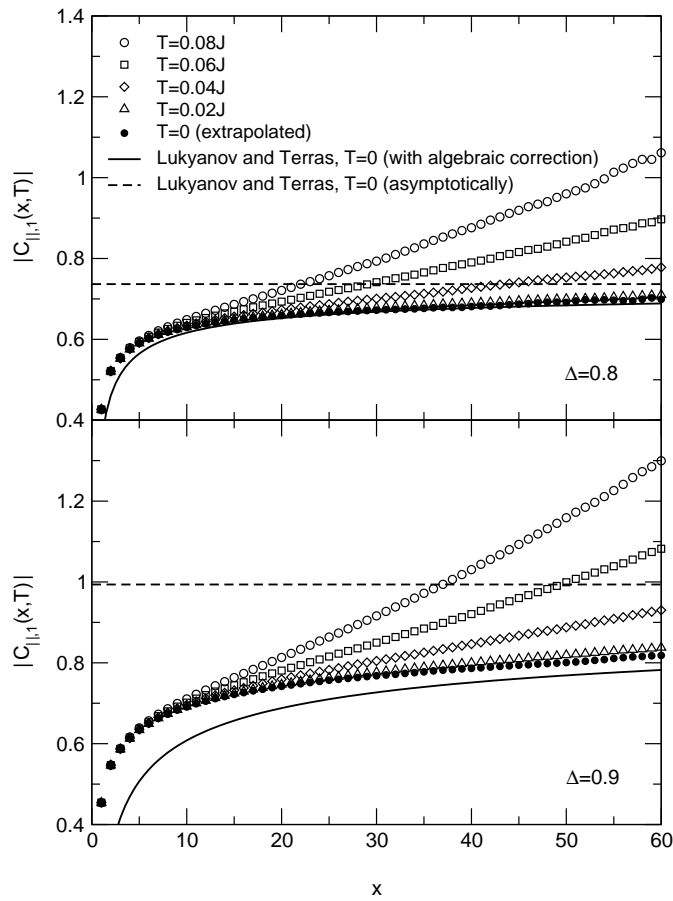
Fig. 3.11.: Absolute value of temperature and distance dependent prefactors $C_{\|,1}(x,T)$ vs. x for $\Delta = 0.8$ (top) and $\Delta = 0.9$ (bottom). The open symbols represent the numerical results for four different finite temperatures, while the extrapolated values to $T = 0$ are given by the filled circles. Also shown are the asymptotic result (3.3.110) (dashed lines) and the asymptotics including the leading algebraic correction (3.3.114) (solid lines). Note that the numerical errors are smaller than the size of the symbols.

determined by fitting a power law ansatz

$$C_{\|,1}(x,T) = C_{\|,1}(x,T=0) + \alpha T^\beta \tag{3.4.121}$$

for fixed x with three free parameters $C_{\|,1}(x,T=0), \alpha, \beta$ to the data at temperatures $T = 0.02J, 0.025J, \ldots, 0.1J$. An example for the quality of the fits is given in Fig. 3.12. The extrapolated values for $C_{\|,1}(x,T=0)$ which we obtain in this way are also plotted in Fig. 3.11. In the whole range of x shown in the figure and for both choices of the anisotropy parameter, the numbers are clearly smaller than the asymptotic correlation amplitude. Again this effect grows when increasing Δ. This result explains why – close to $\Delta = 1$ – one cannot expect to find the correct correlation exponents and amplitudes by fitting the asymptotic expression (3.3.106) directly to the numerical data for $x \geq 7$, as we did in the last subsection. In particular it can be seen that within such a procedure the values for $C_{\|,1}$ are strongly underestimated, see also Fig. 3.10. When moving away
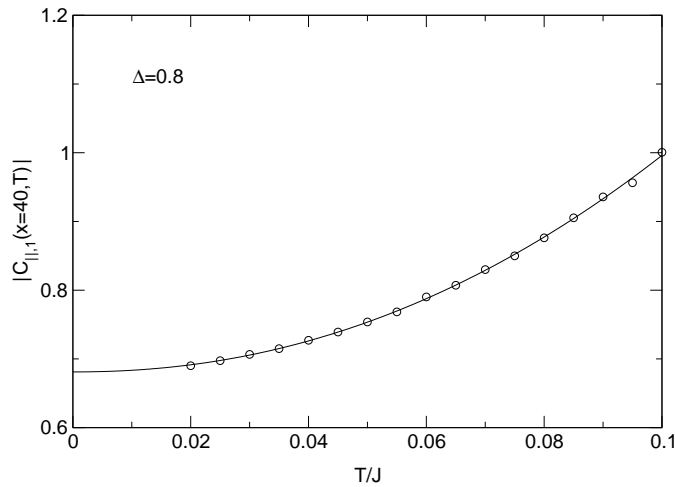
Fig. 3.12.: Temperature dependence of $|C_{\parallel,1}(x,T)|$ for fixed $x = 40$ and $\Delta = 0.8$ (circles). The data are extrapolated to $T = 0$ by fitting the relation (3.4.121) (solid line). The numerical errors are smaller than the size of the circles.

from $\Delta = 1$, on the other hand, where algebraic corrections get less important, the estimates from the last subsection should become more reliable. The extrapolated values for $C_{\parallel,1}(x, T = 0)$ can also be compared to the result (3.3.114) from Ref. [LT03] including algebraic corrections. For $\Delta = 0.8$ and $x \gtrsim 25$, there is a good agreement between the two curves. Note that discrepancies for $x \gtrsim 45$ can mainly be assigned to technical difficulties in the extrapolation scheme. For $\Delta = 0.9$ and $x \leq 60$, the result (3.3.114) does not coincide with the numerical data. Obviously it is not sufficient to take into account only the leading algebraic correction to $C_{\parallel,1}$ in order to correctly describe the decay of $G_{\parallel}$ at intermediate distances and in the proximity of $\Delta = 1$.

For the transversal correlations and $\Delta < 1$, we expect similar results as in the case of longitudinal spin correlations. Deviations from the asymptotic behavior, however, should be smaller because for $G_{\perp}$ the algebraic correction to the leading order in the ground state is only of the order $\sim x^{4-\frac{4}{\eta}}$, see Eq. (3.3.115) from Par. 3.3.4. Both expectations are found to be confirmed in Fig. 3.13, where the numbers $C_{\perp,1}(x, T)$ are plotted for $\Delta = 0.9$. As for the longitudinal spin correlations, deviations from the asymptotic constant (3.3.112) (see Sect. 3.3.3) show up, which increase with higher temperature, although the relative difference to the asymptotic value is much smaller than for $G_{\parallel}$. The extrapolated numbers to $T = 0$ only slightly differ from the constant value (3.3.112), and the curve coincides with the result (3.3.115) including algebraic corrections for $x \gtrsim 25$. Since the deviations from the asymptotic result as predicted by CFT are so small, in retrospective it is clear why for $G_{\perp}$ and for all $\Delta < 1$ the numerical results from the direct fits coincided well with the expectations from CFT in the last subsection.

We now turn our attention towards logarithmic corrections in the isotropic XXX model. Here $G_{\parallel}$ and $G_{\perp}$ become − apart from a trivial factor of $(-1)^x$ − identical. As we did in the previous cases for $\Delta < 1$, we derive amplitudes $C_{\parallel,1}(x, T)$ from the QMC data and extrapolate these numbers to zero temperature. The results are given in Fig. 3.14. For $T > 0$, one finds large deviations
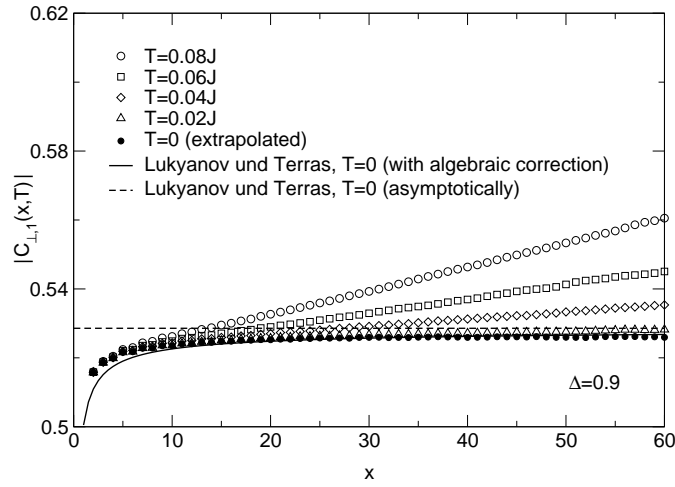
Fig. 3.13.: Absolute value of the prefactors $C_{\perp,1}(x, T)$ against distance for $\Delta = 0.9$. As in Fig. 3.11 the open symbols represent the numerical results for four different finite temperatures, while the extrapolated values to $T = 0$ are given by the filled circles. The dashed and solid lines are the asymptotic results (3.3.112) and (3.3.115) without and with algebraic correction. All numerical errors are smaller than the symbol sizes.
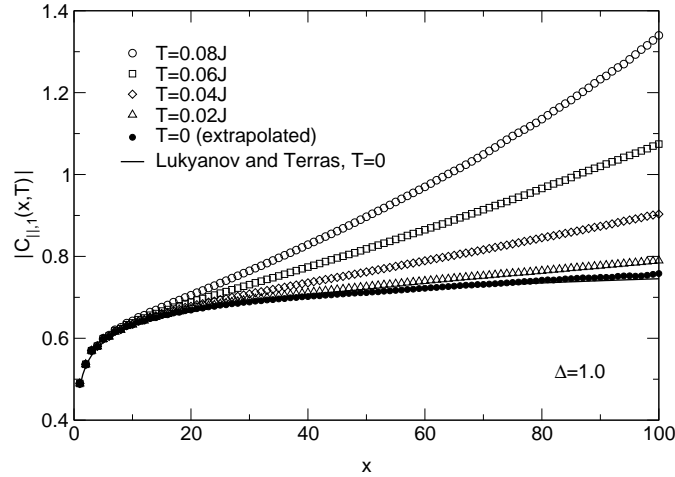
Fig. 3.14.: Absolute values of the amplitudes $C_{\|,1}(x, T)$ vs. x for $\Delta = 1.0$. The open symbols are derived from the QMC data for four different finite temperatures, while the filled circles show the extrapolated values to $T = 0$. The exact result (3.3.116) including logarithmic corrections is given by the solid line. The numerical errors are smaller than the symbols.

from the CFT behavior which also show a strong dependence on temperature. This is an expected result since CFT does not take into account multiplicative corrections. The values for $T = 0$ can be compared to the expression (3.3.116) from Par. 3.3.4. The two curves coincide very well even down to small distances $x \gtrsim 5$. The same result has already been found in Ref. [LT03], where the analytical expression (3.3.116) has been compared to DMRG data from Ref. [HHM95]
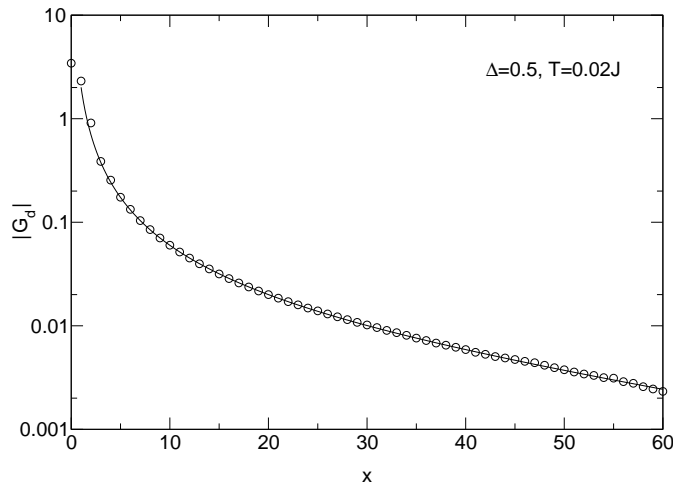
Fig. 3.15.: Numerical values (circles) and fit (solid line) for the absolute value of G_d vs. distance for $T = 0.02J$. As in Fig. 3.4, the value of the anisotropy parameter is $\Delta = 0.5$. The errorbars are smaller than the symbols.

computed by Hallberg *et al.* In that reference, however, the datapoints for $G_{\parallel}$ at $T = 0$ have only been computed for $x \leq 30$. By means of our analysis, we can confirm the relation (3.3.116) very precisely up to $x \approx 80$. For larger distances, deviations arise from inaccuracies in the extrapolation scheme to zero temperature.

To finish our investigation of the spin correlations, we emphasize that we were able to confirm the analytical expressions (3.3.114) and (3.3.115) for algebraic and Eq. (3.3.116) for logarithmic corrections to the asymptotic behavior at $T = 0$. In retrospective, the assumption (3.4.120) to describe deviations from CFT therefore was justified.

3.4.3. Dimer correlations: direct fits of CFT results

We now turn our attention to the dimer correlation function G_d. Similarly to our approach for $G_{\parallel}$ and $G_{\perp}$, we directly fit the symmetrized form (3.4.119) of

$$f(x) = \frac{C(-1)^x \left(\frac{2\pi T}{v}\right)^{2x_\phi}}{\left[2\cosh\left(\frac{2\pi T}{v}x\right) - 2\right]^{x_\phi}} \tag{3.4.122}$$

with three free parameters v, x_ϕ, and C to the QMC data. The left boundary for the fitting interval is $x_{\min} = 7$, while $x_{\max}$ is determined from the condition $|G_d(x_{\max})| \geq 3 \times 10^{-4}$. This condition for $x_{\max}$ reflects the fact that the numerical estimates for G_d are less reliable than those for the spin correlations, since in the context of the loop algorithm G_d is a four-point function. For this reason we also neglect any subleading contributions in the ansatz (3.4.122). From a direct examination of the decay of G_d at finite temperatures, however, one can conclude that subleading order terms are less important for the dimer correlations. This can also be seen in Fig. 3.15, where a typical example for the quality of the fits is shown.
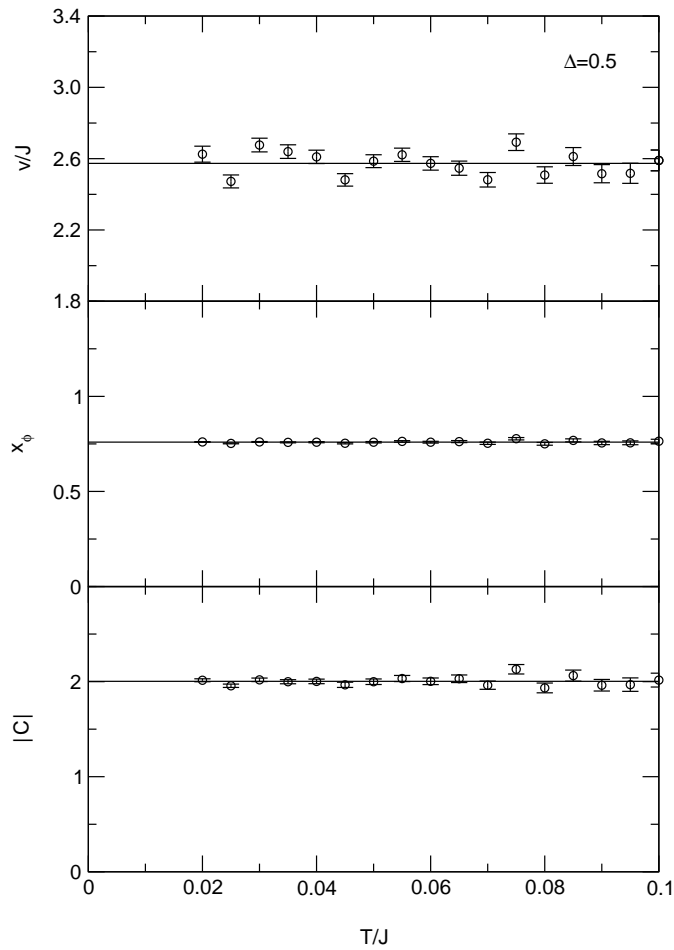
Fig. 3.16.: Temperature dependence of the fitting parameters v (top), x_ϕ (middle) and C (bottom). The lines give the mean values averaged over all temperatures.

By comparing the fitfunction (3.4.122) to the asymptotic expression (3.3.108) from Par. 3.3.2 we expect that, for fixed Δ and for all temperatures, the parameters v, x_ϕ and C take the constant values v_F, $\frac{1}{2\eta}$ and C_d, respectively. The results for $\Delta = 0.5$ are shown in Fig. 3.16. Although stronger fluctuations than in the case of the spin correlations are visible especially for the parameter v, this condition is fulfilled sufficiently. Note that − in analogy to the discussion for $G_\parallel$ and $G_\perp$ − this means that we find a smooth crossover from finite temperatures to $T = 0$ as predicted by CFT. Next we extract numerical estimates for v_F and the correlation exponents and amplitudes by averaging the numbers from the fits over the whole temperature range.

The results for the Fermi velocity are given in Fig. 3.6, see Sect. 3.4.1. From the discussion given above it is evident that the numerical errors are larger than in the case of $G_{\parallel/\perp}$. For $\Delta \leq 0.8$, the estimates for v_F coincide with the exact result (3.3.92) within the numerical errors. Close to $\Delta = 1$ systematic deviations appear. Again this is probably due to algebraic and logarithmic corrections close to and at the isotropic point. The differences to the exact result are more pronounced for
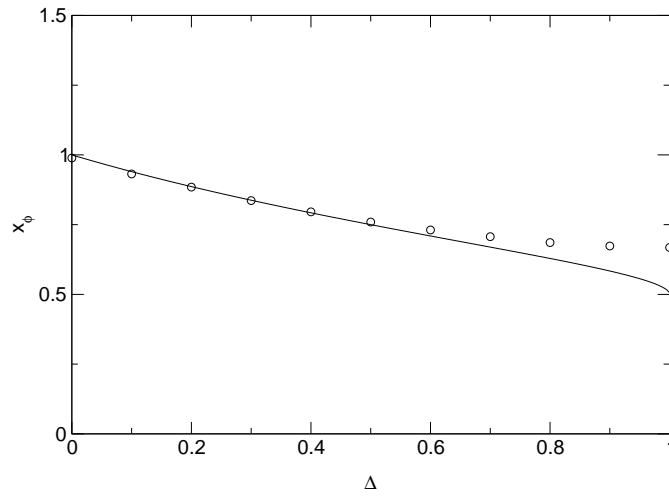
Fig. 3.17.: Numerical estimates for the correlation exponent x_ϕ vs. Δ (circles). The solid line shows the asymptotic expectation $\frac{1}{2\eta}$ from CFT. The errorbars are smaller than the size of the symbols.
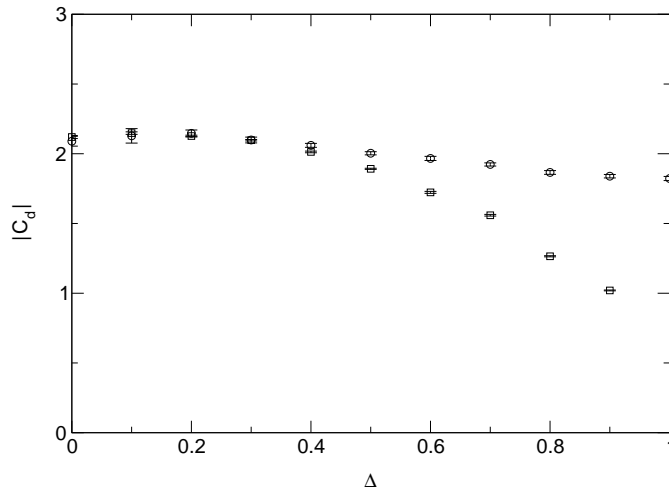
Fig. 3.18.: Numerical estimates for the absolute value of the correlation amplitudes C_d against anisotropy. The circles represent the averaged values for the parameters C from direct fits as described in Par. 3.4.3. The estimates extracted from an analysis of distance dependent prefactors $C_d(x, T = 0)$, see Sect. 3.4.4, are given by the squares.

the conformal dimensions, see Fig. 3.17. Here the behavior is very similar to the leading order of the longitudinal spin correlation function. For $0 \leq \Delta < 0.5$, the numerical values coincide with the prediction from Sect. 3.3.2. For $\Delta \geq 0.5$ though, the results become less reliable. As for $G_\parallel$ the interpretation is that close to $\Delta = 1$ irrelevant operators induce algebraic corrections to the correlation amplitude C_d, i. e. the values for x chosen in the fitting procedure are too small to reach the asymptotic regime. Exactly at the isotropic point $\Delta = 1$, logarithmic corrections are brought forward. In contrast to the case of $G_\parallel$, where the correlation exponents close to $\Delta = 1$ are

underestimated by the QMC results, here the numbers for x_ϕ overestimate the asymptotic values. In the XXX model, this effect can easily be understood by observing that on the one hand, the exponent of the multiplicative logarithmic correction at $T = 0$ is positive $(\frac{1}{2})$ for $G_\parallel$, while it is negative $(-\frac{3}{2})$ for G_d, see also Sect. 3.3.4. On the other hand these logarithmic corrections are not taken into account when considering the fitfunctions (3.4.118) and (3.4.122). Close to $\Delta = 1$, algebraic corrections should create similar effects.

Comparing these results to our findings from the analysis of the spin correlations in the last subsection, we conclude that for $\Delta < 0.5$, where the QMC numbers for the correlation exponents coincide with the CFT result, the averaged values of C give good estimates for the amplitudes C_d. These numbers are represented by the open circles in Fig. 3.18. As $\Delta \uparrow 1$, however, we expect $C_d \to 0$ due to the logarithmic correction $\sim (\ln x)^{-\frac{3}{2}}$ at $T = 0$. As can be seen in the figure, this limit is not realized by the data from the direct fits. More precise values for C_d in the vicinity of $\Delta = 1$ will be derived in the next subsection.

3.4.4. Dimer correlations: deviations from the asymptotic behavior

In analogy to our approach for the spin correlations in Sect. 3.4.2, a systematic way to describe deviations from the CFT predictions is to allow for dependences

$$C_d \to C_d(x, T) \tag{3.4.123}$$

in the Eqs. (3.3.105) and (3.3.108) from Par. 3.3.2. The temperature and distance dependent amplitudes $C_d(x, T)$ are derived from the QMC data by − for fixed Δ and each value of x and T − inserting the numerical values into the symmetrized form (3.4.119) of relation (3.3.108), and then solving the resulting equations for C_d. For each distance x, a numerical estimate for the corresponding number $C_d(x, T = 0)$ in the ground state can be extracted by fitting a power law function as given in Eq. (3.4.121) with three free parameters to the data. Since the QMC estimates for G_d at large distances and high temperatures have larger statistical errors than those for $G_{\parallel/\perp}$, we only take into account the datapoints from the ten lowest temperatures $0.02J \le T \le 0.065J$ in this part of our analysis.

For $\Delta = 0.9$, the results for four different finite temperatures and the extrapolated values to $T = 0$ are shown in Fig. 3.19. The curves show a similar behavior as those for the spin correlations. With higher temperatures we find an increasing difference to the extrapolated curve for $T = 0$. One main difference to the properties of $G_\parallel$ and $G_\perp$ is that the finite temperature curves approach the one for $T = 0$ from below. For the range of distances shown in the figure, the numbers $C_d(x, T = 0)$ show a strong dependence on x. This indicates the presence of strong algebraic corrections to the asymptotic behavior in the system. The number of datapoints, however, is too small to determine the exponent of the algebraic correction from the $T = 0$ data. It is possible though to extract an estimate for the asymptotic value C_d from the curve in the ground state. This is done by applying a linear fit in $\frac{1}{x}$ to the $T = 0$ data for $x \ge 10$. The result of the fit is shown in Fig. 3.19 as well.

In the same way one can determine numerical estimates for C_d for the other choices of $\Delta < 1$. Note that upon moving away from the isotropic point $\Delta = 1$, the number of datapoints where
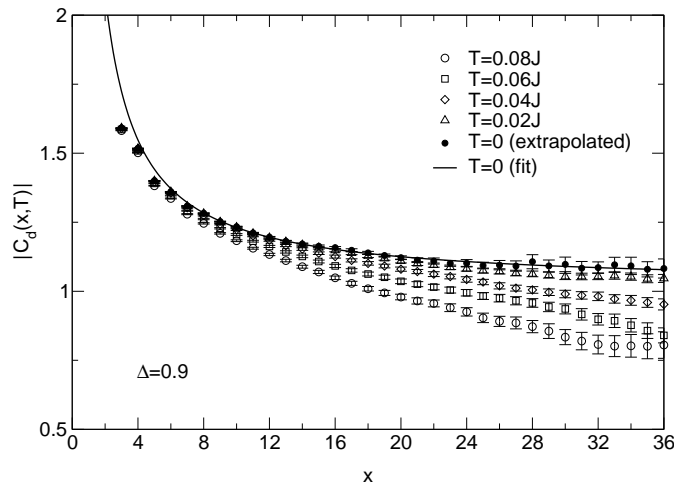
Fig. 3.19.: Absolute value of temperature and distance dependent prefactors $C_d(x, T)$ for $\Delta = 0.9$. The open symbols are the numerical results for four different finite temperatures, while the filled circles represent the extrapolated values to $T = 0$. The solid line is an asymptotic fit to the $T = 0$ values for $x \geq 10$.
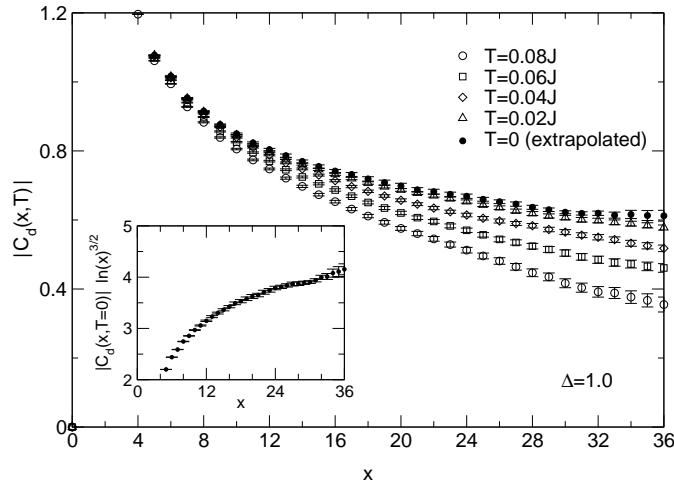
Fig. 3.20.: Absolute value of corrections to the asymptotic behavior from CFT $C_d(x, T)$ vs. x at $\Delta = 1$. The open symbols represent $C_d(x, T)$ for temperatures $T = 0.02J, \ldots, 0.08J$, while the filled circles are the extrapolated values for the ground state. The inset shows the estimates at $T = 0$ times $(\ln x)^{\frac{3}{2}}$ in a plot against distance.

the asymptotic fit can be applied decreases because G_d decays more rapidly in the ground state, compare Eq.(3.3.105). The opposite effect is that with decreasing Δ the numbers $C_d(x, T = 0)$ show a smaller dependence on x because algebraic corrections get less pronounced. For this reason our extrapolation scheme gives reliable results even in the vicinity of the XX model. The numbers we obtain are shown and compared to the results of the previous subsection in Fig. 3.18. For $\Delta < 0.5$, where we consider the estimates for C_d from the direct fits to be reliable, both results coincide.

For $\Delta \to 1$, the numbers from this subsection show a more realistic tendency. In particular they seem to obey the condition $C_d \to 0$ as $\Delta \uparrow 1$ which is expected due to the logarithmic correction $\sim (\ln x)^{-\frac{3}{2}}$ in the ground state of the XXX model.

We finally discuss the deviations from the conformal behavior for $\Delta = 1$, see Fig. 3.20. As for $\Delta < 1$, the curves for finite temperatures approach the result for $T = 0$ from below. We make use of the extrapolated values to the ground state to test the exponent of the multiplicative logarithmic correction. Plotting $|C_d(x, T = 0)| \times (\ln x)^{\frac{3}{2}}$ against x in the inset of Fig. 3.20, we can see that the numerical values saturate to a constant value ≈ 4 for $x \gg 1$, indicating that the correct asymptotic behavior is visible even at intermediate distances.

4. Two-dimensional systems with spin-phonon coupling

4.1. Introduction to spin systems with spin-phonon coupling

Quasi one-dimensional antiferromagnets with spin-phonon coupling have attracted considerable attention during the past decades. Although the models taking into account this mechanism are rather complicated, they are well understood because they can be studied by a wide range of analytical and numerical techniques. In contrast to this, little is known about the physics of two-dimensional spin systems with spin-lattice coupling, which will be investigated by means of the QMC method in this chapter. Before we start with our analysis, however, we give an outline of the relevant literature in this section.

In Sect. 3.1 we have mentioned that for spin-$\frac{1}{2}$, the mechanism of the spin-phonon coupling is closely connected to the phenomenon of the spin-Peierls transition. A theoretical understanding of this type of phase transition was established by the fundamental work of Pytte [Pyt74] and Cross and Fisher [CF79] in the 1970s, who considered a cubic lattice consisting of linear chains

$$H = \sum_{i=1}^{N} \frac{J_i}{2} \vec{\sigma}_i \vec{\sigma}_{i+1}. \tag{4.1.1}$$

The spins only interact between nearest neighbors along the chain direction according to the site-dependent antiferromagnetic exchange integral J_i. Expanding the exchange coupling in terms of the displacement vectors $\vec{u}_i$ of the two magnetic ions adjacent to a particular bond, one obtains

$$J_i = J + g\sqrt{2}(\vec{u}_i - \vec{u}_{i+1}) + \mathcal{O}(u^2), \tag{4.1.2}$$

i. e. the spin degrees of freedom are coupled to three-dimensional lattice vibrations with a spin-phonon coupling constant $g > 0$. By means of a Jordan-Wigner transformation, the spin Hamiltonian (4.1.1) can be mapped to a model of spinless interacting fermions. In the fermionic description, there is a structural similarity to quasi one-dimensional half-filled electronic systems coupled to lattice degrees of freedom. These systems are known to exhibit a metal-insulator transition accompanied by a structural phase transition upon decreasing the temperature, the *Peierls transition* [Pei55]. The spin-Peierls transition is the analogous phenomenon for the spin model (4.1.1). Treating the phonon degrees of freedom in the random phase approximation, one finds a renormalization

$$\omega^2(q) = \omega_0^2(q) + \Pi(q, \Omega) \tag{4.1.3}$$

of the bare phonon frequencies ω_0 for momenta q directed along the chains. Here the *polarizability* Π describes the response of the lattice to the magnetic degrees of freedom due to the spin-phonon
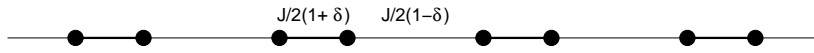
Fig. 4.1.: Schematic illustration of the spin-Peierls state. The spins of each chain group into pairs, leaving a magnetic structure described by the Hamiltonian (4.1.4) with alternating couplings $\frac{J}{2}(1 \pm \delta)$.

coupling. In principle, Π can be determined from the (Euclidean) dynamical structure factor of the dimer correlation function in the uniform, i. e. undistorted, Heisenberg model. While Pytte determined this quantity by treating the interaction part of the Hamiltonian in the Hartree-Fock approximation, Cross and Fisher improved on his calculation by applying bosonization techniques. As $T \to 0$, the polarizability at[1] $q = \pi$ and $\Omega = 0$ diverges like $-\frac{J}{T}$ [CF79]. Hence when decreasing the temperature, the phonon with $q = \pi$ gets *softened* until at a certain critical value T_c, the right-hand side of Eq. (4.1.3) vanishes. This indicates a structural instability towards a *dimerized* state, i. e. a distorted state which can be characterized by the magnetic ions of each chain moving together in pairs. The result is a structure of alternating bond lengths along the chains as depicted in Fig. 4.1. At the same time, a gap opens in the magnetic excitation spectrum. The loss in elastic energy due to the lattice distortions is overcompensated by a gain in the magnetic energy which reflects the tendency of the spins of each pair to form singlet states.

Since $\omega(q = \pi)$ vanishes as $T \downarrow T_c$, an adiabatic treatment is a good approximation to describe the magnetic properties of the system. In a mean-field approximation, the effective magnetic model in the adiabatic limit is the *statically dimerized spin chain*

$$H = \frac{J}{2} \sum_{i=1}^{N} (1 + (-1)^i \delta) \, \vec{\sigma}_i \vec{\sigma}_{i+1}. \tag{4.1.4}$$

Here the *dimerization* $\delta \equiv \delta(T) \geq 0$ is proportional to the local lattice distortion of the original model, which serves as the order parameter of the transition. Hence the dimerization takes positive values below T_c, while δ vanishes at all temperatures above the spin-Peierls transition. In addition, we have $\delta = 0$ at $T = T_c$, which reflects the fact that the transition is continuous. Note that as soon as $\delta > 0$ holds, the elementary excitations of the model (4.1.4) cannot be characterized as massless spinons like in the isotropic Heisenberg chain. Instead, there is a gapped excitation spectrum consisting of triplet-like excitations (so-called *triplons* [SKU04]) above a paramagnetic ground state. A quantitative analysis of the thermodynamics of the spin-Peierls transition based on the adiabatic approach has been performed recently by means of bosonization and the thermodynamic Bethe ansatz [OC04].

Two years after Pytte's theoretical prediction, the existence of the spin-Peierls transition was proven experimentally in the organic compounds TTFCuBDT and TTFAuBDT [JBJ+76]. For both systems, the adiabatic treatment yielded a convincing explanation of the experimental results. In the subsequent years, further quasi one-dimensional organic substances showing the spin-Peierls transition were discovered, namely the compounds MEM-$(TCNQ)_2$ [HKS+79], $(TMTTF)_2PF_6$ and $(TMTTF)_2AsF_6$ [PMC+82, LCG+84, MFFM85] as well as $(BCPTTF)_2PF_6$ [LRP+93].

In 1993, the interest in systems with spin-lattice coupling was renewed when Hase *et al.* found

---

[1] In this chapter, we set $a \equiv 1$ for the lattice constant of the models under consideration.
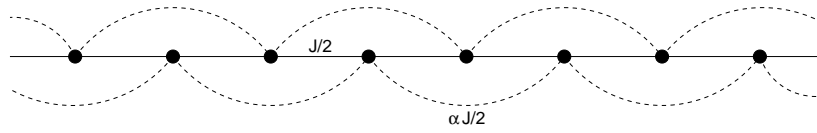
Fig. 4.2.: Sketch of the frustrated Heisenberg chain Eq. (4.1.5) with competing nearest and next-nearest neighbor antiferromagnetic exchange (coupling constants $\frac{J}{2}$ and $\frac{\alpha J}{2}$, respectively).

evidence of the spin-Peierls transition in the inorganic $CuGeO_3$ [HTU93]. Providing the possibility to grow single crystals, this compound is more convenient for experimental studies. However, a careful analysis of neutron scattering data revealed that the phonon-softening described by Eq. (4.1.3) was absent in $CuGeO_3$ [LHS$^+$94, HSH$^+$95, BWL$^+$96]. Furthermore, a comparison between the experimental curves and theoretical predictions of the magnetic susceptibility showed that the Heisenberg model with nearest neighbor interactions only is not sufficient to describe the magnetic properties of the system. Instead, the proper effective spin model [CCE95] for the high-temperature phase of $CuGeO_3$ is the *frustrated Heisenberg chain*

$$H = \frac{J}{2} \sum_{i=1}^{N} (\vec{\sigma}_i \vec{\sigma}_{i+1} + \alpha\,\vec{\sigma}_i \vec{\sigma}_{i+2}), \tag{4.1.5}$$

compare Fig. 4.2. It is a characteristic feature of this model that the next-nearest neighbor interaction provides an alternative mechanism to obtain a dimerized ground state. At $T = 0$, the system shows a quantum phase transition from a Néel ordered state to a non-magnetic phase for values of $\alpha > \alpha_c$, with a critical frustration of $\alpha_c \approx 0.2412$ [ON92, Egg96b].

The occurrence of a significant spin-phonon coupling has also been proven for $(VO)_2P_2O_7$ [GLG$^+$00, KTP$^+$02], although this system exhibits no structural phase transition accompanied by the opening of a spin gap. However, a disputive discussion on its magnetic structure revealed [JJGJ87, GNT$^+$97, PBA$^+$98, UN98, YNK$^+$99] that the system is a good realization of the alternating Heisenberg chain (4.1.4). Recently, the inorganic TiOCl has been suggested as another candidate for the spin-Peierls transition. Here susceptibility measurements indicate two different phase transitions in the low temperature regime [SMC$^+$03]. While the role of the orbital degrees of freedom is not settled for this system [KBM$^+$03, SDVRG04], both the opening of a spin gap [SMC$^+$03, LCC$^+$04] as well as considerable phonon anomalies due to the spin-lattice coupling [LCV$^+$05] have been reported in the literature.

As a result of the experimental studies on $CuGeO_3$, strictly one-dimensional dynamical models have been proposed to investigate the influence of the spin-phonon coupling in the non-adiabatic regime. Restricting ourselves to one-dimensional lattice distortions $u_i = (a_i^\dagger + a_i)/\sqrt{2}$ in Eq. (4.1.2), and coupling the spins to dispersionless Einstein phonons of frequency ω for simplicity, we obtain the *difference coupling model*

$$H = \frac{1}{2} \sum_{i=1}^{N} (J + g\,[a_{i+1}^\dagger + a_{i+1} - a_i^\dagger - a_i])\,\vec{\sigma}_i \vec{\sigma}_{i+1} + \omega \sum_{i=1}^{N} a_i^\dagger a_i\,. \tag{4.1.6}$$

In the antiadibatic limit $J/\omega \to 0$, one can integrate out the phonon degrees of freedom and map the system to the frustrated Heisenberg chain (4.1.5) [KF87, Uhr98]. In leading order in $\frac{J}{\omega}$ and in
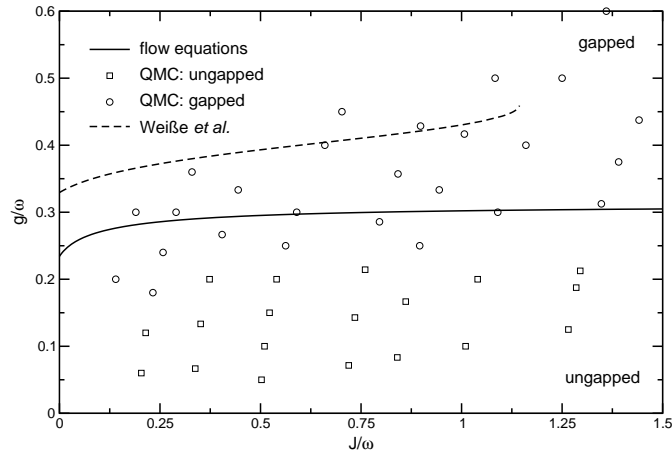
Fig. 4.3.: Ground state phase diagram of the bond coupling model (4.1.7) from Ref. [RLUK02]. The solid line is the phase separation line between the Néel ordered (ungapped) and the dimerized (gapped) ground state obtained by the flow equation method. The squares and circles represent QMC results obtained by means of the algorithm from Sect. 2.3. The dashed line is the result from Ref. [WWF99] based on a perturbative series expansion.

terms of the original coupling constants, the frustration parameter of the effective model is given by $\alpha = \frac{g^2}{\omega J + 2g^2}$. Hence for sufficiently large numbers of the spin-phonon coupling, the frustration exceeds the critical value α_c. This corresponds to a quantum phase transition from a (quasi) Néel ordered to a dimerized ground state. The interpretation is that the occurence of a soft phonon mode is non-generic for the spin-Peierls transition, i. e. the adiabatic treatment only covers one possible scenario to find a dimerized ground state. The ground state phase diagram of the model (4.1.6) in the entire frequency range has been analyzed by means of exact diagonalization and perturbative series expansions [WWF99], DMRG [BMH99], renormalization group techniques [SSB00], and flow equations [RBU01]. Recently, the DMRG method has also been applied to a model with difference coupling which couples the spins to one-dimensional dispersive phonons [BB05]. Note that models which describe a difference coupling mechanism are not accessible to QMC because there is a non-trivial sign problem.

A second model which has been proposed is the *bond coupling model*

$$H = \frac{1}{2} \sum_{i=1}^{N} (J + g[a_i^\dagger + a_i]) \, \vec{\sigma}_i \vec{\sigma}_{i+1} + \omega \sum_{i=1}^{N} a_i^\dagger a_i \,, \qquad (4.1.7)$$

compare Eq. (2.3.40) from Sect. 2.3.1. Here the spins are coupled to phonon degrees of freedom defined on the bonds of the lattice, which is considered to be a more realistic scenario for $CuGeO_3$. There according to the *Goodenough-Kanamori-Anderson rules* [Goo55, Kan59, And63, GK96], a displacement of the oxygen ions between adjacent copper sites significantly influences the bond angle of the Cu-O-Cu superexchange path and hence the corresponding exchange integral [KGM96, WGB99, FW00]. The model (4.1.7) is accessible to the QMC algorithm described in Sect. 2.3, which has been applied to study the thermodynamics of the system in Refs. [KL99, Kühne01, RLUK02]. In

addition, an alternative QMC algorithm based on the SSE representation [SSC97, SC99] as well as high temperature series expansions [Büh03, BUO04] have been used to investigate the behavior of the system at finite temperatures. The thermodynamic quantities are influenced significantly by a non-vanishing spin-phonon coupling. In particular, the maximum of the magnetic susceptibilty is suppressed and shifted to higher temperatures as compared to the uniform Heisenberg model. The nature of the ground state and the magnetic excitations have also been studied in a number of publications relying on QMC [KL99, SSC97, SC99, RLUK02, SSC03], exact diagonalization [WFK98], perturbative series expansions [WWF99, TEM01] and flow equations [RLUK02]. Even the influence of a non-vanishing interchain coupling between adjacent spin chains has been analyzed [Sen03], which is usually neglected in numerical studies. The ground state phase diagram of the model taken from Ref. [RLUK02] is shown in Fig. 4.3. Similarly to the case of difference coupling, the system exhibits a quantum phase transition from a gapless to a gapped state even in the antiadiabatic regime. The exact shape of the phase separation line, however, differs between the two models. For example, this can be seen from the values for the critical coupling $\frac{g_c}{\omega}$ in the antiadiabatic limit $\frac{J}{\omega} \to 0$. While this number vanishes for the difference coupling model (4.1.6), it takes a finite value for the bond coupling mechanism as described by Eq. (4.1.7), compare also Fig. 4.3.

In principle, a coupling between the spin and lattice degrees of freedom is a generic feature regardless of the dimensionality and lattice structure of a magnetic system, since the vibrations of the lattice ions always influence the magnetic exchange. Hence it is always possible to write down a Taylor expansion of the type (4.1.2) for the exchange integrals. Therefore besides its relevance for one-dimensional spin systems, the spin-phonon coupling is expected to play a part in certain materials with a two-dimensional magnetic structure. For example, there are indications that this mechanism is relevant for $LuMnO_3$ and $YMnO_3$, which are realizations of the spin-2 Heisenberg model on a triangular lattice [JH05]. In this work, we focus on the spin-$\frac{1}{2}$ Heisenberg model on a square lattice because it describes the magnetism of the undoped parent compounds of the high temperature superconductors such as La_2CuO_4 [EYB+88, YKE+89]. As in one dimension, one expects that the spin-lattice coupling leads to a phonon softening analogously to Eq. (4.1.3), where the renormalization of the bare phonon frequencies is given by certain structure factors of the two-dimensional dimer correlations. In contrast to the one-dimensional case though one cannot assume that these quantities diverge since the square lattice Heisenberg model shows long-range Néel order in the ground state [And52, Bar91, San97] accompanied by an exponentially diverging spin correlation length as $T \to 0$ [CHN89, DM90, Bar91, BBGW98]. A quantitative analysis if and under which circumstances the response of the lattice to the magnetic degrees of freedom is sufficiently large to drive the system into a structural instability has not yet been done in the literature.

The published articles on this issue are mainly restricted to statically dimerized models [KKK99b, KKK99a, AO00, SKH02], i. e. two-dimensional generalizations of the Hamiltonian (4.1.4) on a square lattice. In the spirit of Pytte's approach, such systems are interpreted as effective models to describe the magnetic properties of distorted spin layers coupled to three dimensional phonons in the adiabatic limit. A more general starting point to obtain this class of models is the two-
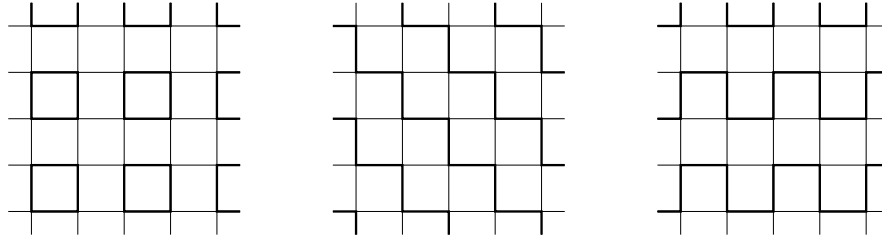
Fig. 4.4.: The three possible arrangements of alternating couplings along each linear chain on a square lattice with a minimal 2×2 unit cell are the plaquette (left), the stair (middle), and the meander model (right). As in Fig. 4.1, thick and thin lines correspond to couplings $\frac{J}{2}(1 \pm \delta)$.

dimensional square lattice Hubbard model coupled to lattice vibrations, the *Peierls-Hubbard model*. In the adiabatic limit of this model, one receives dimerized hopping amplitudes for the electrons and thus a dimerized spin exchange in the limit of infinite on-site Coulomb repulsion [TH88, ZP88, Maz89, TH89, YNK01, YK02]. The question which dimerization pattern is energetically favored is an unresolved issue. In principle, the optimal pattern is expected to consist of truly two-dimensional lattice modulations which correspond to commensurate wave vectors. However, even by restricting oneself to those patterns characterized by alternating couplings $\frac{J}{2}(1 \pm \delta)$ along each linear chain of the square lattice (i. e. there is an equal number of strong and weak bonds) there remains an infinite number of possibilites. In the literature, only three such models with a minimal 2×2 unit cell as shown in Fig. 4.4 have been investigated, revealing an ambiguous picture. In Ref. [SKH02], the authors determine the ground state energies of the three models by applying linear spin wave theory and conclude that a stair-like distortion has the largest gain in magnetic energy. This result contradicts an older analysis based on exact diagonalization, which supports the plaquette model as the optimal configuration [TH88]. Note that such a comparison of ground state energies for the effective spin models does not take into account possible differences in the elastic energy loss due to the lattice distortions.

The search for the energetically favored dimerization pattern is motivated by the fact that the nature of the lattice modulation determines whether a transition to a paramagnetic phase is possible. In one-dimensional spin-Peierls systems, the structural transition from the uniform to the distorted phase coincides with a magnetic phase transition from a magnetically ordered to a non-magnetic phase. As far as two-dimensional spin systems are concerned, quantum fluctuations are known to be less important due to the larger coordination number. For this reason one expects that the long-range antiferromagnetic order in the ground state is more stable towards dimerization. Indeed at $T = 0$, each of the three models from Fig. 4.4 has an extended phase characterized by the coexistence of dimerization (i. e. $\delta > 0$) and long-range magnetic order [SKH02]. In case of the stair and meander models, it is believed that there is no transition to a state with short-range magnetic correlations in the whole interval $\delta \in [0, 1]$. This is consistent with the observation that for $\delta = 1$, the stairs and meanders decouple to independent chains of infinite length with quasi long-range order in the ground state. However, the situation is different to the plaquette model, which exhibits a quantum phase transition to a paramagnetic phase at a critical dimerization

$0 < \delta_c < 1$. The exact value of δ_c is controversial. While the estimate $\delta_c \approx 0.798$ based on the linear spin wave calculation from Ref. [SKH02] very likely overestimates the accurate number, the result $\delta_c \approx 0.30$ based on a series expansion starting from uncoupled plaquettes seems to be more realistic [KKK99b]. We add that the plaquette model from Fig. 4.4 has also been analyzed to understand the gapped excitation spectrum of CaV_4O_9. This substance is a realization of the 1/5 depleted square lattice Heisenberg model which is topologically equivalent to a different type of plaquette lattice [KKK99b, KKK99a].

We close this survey by noting that an analysis of two-dimensional spin-phonon systems in the non-adiabatic regime is an even more challenging task. Here most of the analytical and numerical instruments which have successfully been applied to the one-dimensional models are not available. However, since the applicability of the QMC method is not hampered by the dimensionality of the system, it is possible to make use of the loop algorithm from Sect. 2.3.4 to investigate the two-dimensional counterpart of the bond coupling model (4.1.7). So far only thermodynamic properties such as the magnetic susceptibility or the specific heat have been analyzed [Ait02, AL03], showing that the spin-phonon coupling has a similar impact on these quantities as in one dimension.

This chapter is organized as follows. In the following section, we analyze the ground state properties of the two-dimensional bond coupling model. There we especially focus on the non-adiabatic regime and try to clarify to what extent the long-range Néel order of the square lattice Heisenberg model is affected by the spin-phonon coupling. In Sect. 4.3, we then consider statically dimerized spin models as effective models in the adiabatic limit. In particular, we develop an approach to compare the magnetic energy gain for all possible patterns with an equal number of strong and weak bonds. By assuming a bond coupling mechanism, this treatment also allows for a quantitative discussion of the two-dimensional counterpart of the spin-Peierls transition. In Sect. 4.4, the same idea is applied to a difference coupling model with a more realistic assumption for the lattice potential, which will enable us to study phonon dispersion curves and hence the softening of phonon modes.

4.2. Ground state properties of the two-dimensional bond coupling model

In this part we focus on the two-dimensional bond coupling model, i. e. the generalization of the spin-phonon chain (4.1.7) on the square lattice. The Hamiltonian reads

$$
\begin{aligned}
H = &\frac{1}{2} \sum_{ij=1}^{N} (J + g\,[a_{ij}^{\dagger} + a_{ij}])\vec{\sigma}_{ij}\vec{\sigma}_{i+1,j} \\
&+ \frac{1}{2} \sum_{ij=1}^{N} (J + g\,[b_{ij}^{\dagger} + b_{ij}])\vec{\sigma}_{ij}\vec{\sigma}_{i,j+1} \\
&+ \omega \sum_{ij=1}^{N} (a_{ij}^{\dagger}a_{ij} + b_{ij}^{\dagger}b_{ij}).
\end{aligned}
\tag{4.2.8}
$$

One main difference to the linear chain is that on the square lattice there are two bonds per lattice site. Therefore we have to distinguish between two types of phonons defined on bonds oriented along the i- (phonon operators a_{ij}, $a_{ij}^\dagger$) and j-direction (phonon operators b_{ij}, $b_{ij}^\dagger$), respectively.

The aim of this section is to answer the question to what extent the spin-phonon coupling in Eq. (4.2.8) affects the long-range antiferromagnetic order which is found in the ground state of the square lattice Heisenberg model. In particular, we are interested in the non-adiabatic regime of the model. The influence of the spin-lattice coupling is studied by exemplarily analyzing the spin correlations of two systems with fundamentally different choices for the coupling constants [AL03]. For the first system, we select $g = 0.1J$ and $\omega = 8J$, i. e. the value of the fraction $\frac{g}{\omega}$ is so small that we cannot expect the spin-phonon interaction to have a significant influence on the nature of the ground state. However, this statement does not hold for the second system, where we arbitrarily choose $g = \omega = 0.67J$ which corresponds to a considerably large value of $\frac{g}{\omega}$.

Another goal of this section is to study the influence of the dimensionality of the system. For this reason we first discuss the finite temperature correlations of the one-dimensional bond coupling model (4.1.7) for both sets of parameters in the following subsection. Then in Par. 4.2.2, we apply a similar approach to the model (4.2.8) and compare our findings to the results from Sect. 4.2.1.

4.2.1. Spin correlation length in one dimension

In the introduction 4.1 to this chapter, we have already discussed the properties of the one-dimensional bond coupling model (4.1.7). As far as the two systems with $g = 0.1J$, $\omega = 8J$ and $g = \omega = 0.67J$ are concerned, we can see from the ground state phase diagram in Fig. 4.3 that the first system behaves Heisenberg-like, i. e. it shows quasi long-range Néel order at $T = 0$ like the one-dimensional XXX model. The latter choice of coupling constants, on the other hand, corresponds to a strongly dimerized system with a gapped excitation spectrum.

In the following we demonstrate that the nature of the ground state is reflected by the behavior of the spin correlation function $\langle \sigma_0^z \sigma_x^z \rangle$ at low finite temperatures. According to our discussion from the beginning of Par. 2.3.1, the Hamiltonian (4.1.7) is accessible to the loop algorithm from Sect. 2.3, which provides a tool to evaluate the spin correlations in question. It is therefore possible to extract the spin correlation length ξ^{1d} of the two systems by fitting an exponential decay

$$f(x) = a\,e^{-x/\xi^{1d}} \tag{4.2.9}$$

with two free parameters a, ξ^{1d} to the numerical data at intermediate distances. While applying 30 phonon updates per loop update with a value of 40 for the phonon cutoff, a number of 1.25×10^5 spin updates was taken for the thermalization of the algorithm, and 3.75×10^5 configurations were evaluated to obtain reliable numerical estimates for the expectation values in question. For the system with $g = 0.1J$ and $\omega = 8J$, the choice for the Trotter number was $M = 160$ which is large enough to avoid an effect of the finite Trotter number. Furthermore, the system sizes were chosen so large that finite-size effects are negligible ($N = 500$ for $T = 0.025J, 0.05J$, $N = 400$ for $T = 0.075J, 0.125J$, and $N = 300$ for $T = 0.1J, 0.15J$), i. e. the system size is significantly larger than the values for ξ^{1d} extracted from the fits. As far as the system with $g = \omega = 0.67J$ is concerned, the correlation lengths are found to be so small that a chain length of $N = 200$
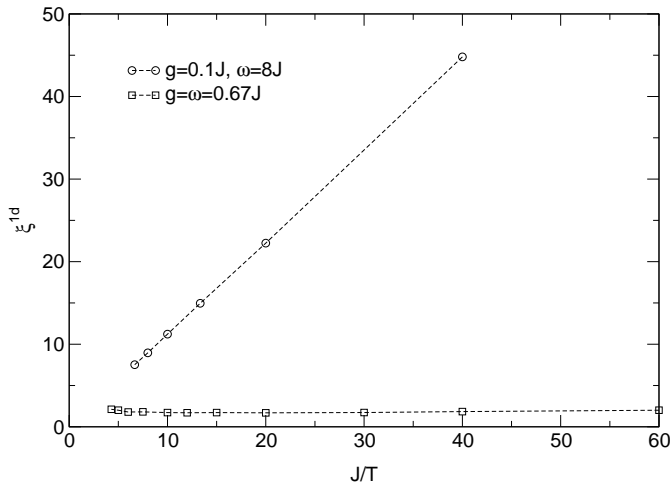
Fig. 4.5.: Correlation length ξ^{1d} of the one-dimensional bond-coupling model (4.1.7) vs. inverse temperature $\frac{J}{T}$ for the two sets of parameters as described in the text.

is sufficient to make statements about the thermodynamic limit. In this system, the influence of the finite Trotter number is more important. For $M = 400$ at the lowest temperatures, however, this effect is smaller than the error which comes into the analysis during the fitting procedure (the simulations were run with $M = 400$ for $T = 0.017J, 0.025J, 0.033J$, $M = 360$ for $T = 0.05J$, and $M = 160$ for $T \geq 0.067J$). Note that with these choices, autocorrelation effects are well under control in both systems.

The results for the correlation lengths are depicted in Fig. 4.5, where the fitting parameter ξ^{1d} is plotted against $\frac{J}{T}$. They unambiguously show the expected behavior. For $g = 0.1J$ and $\omega = 8J$, the correlation length grows linearly with the inverse temperature. This is an expected result, because in this system the spin-phonon coupling is only an irrelevant perturbation of the XXX Hamiltonian. Hence according to our discussion from Chapt. 3, the low temperature physics of the system is well described by an effective conformal invariant field theory, and the formulae (3.2.70) and (3.2.71) from Par. 3.2.8 (with $\Delta_\phi + \overline{\Delta}_\phi = \frac{1}{2}$ as for the XXX chain, see Sect. 3.3.2) determine the leading asymptotic behavior of the spin correlation function. Non-universal effects only enter in the correlation amplitude C and in the Fermi velocity v_F (i. e. the slope of the straight line in Fig. 4.5). Note that in order to obtain reliable quantitative results for this system, a better ansatz for the fitfunction would be given by Eq. (3.4.118) from Par. 3.4.1, which is based on the more accurate result (3.2.69) (see Sect. 3.2.8) for the decay of primary fields at low finite temperatures. However, we are only interested in the qualitative behavior of the spin correlations in this section (for the same reason we do not give any error bars for correlation lengths obtained from numerical fits in this and the next subsection). Furthermore and in contrast to Eq. (3.4.118), the ansatz (4.2.9) should also apply to the gapped region of the phase diagram and hence to the system with $g = \omega = 0.67J$. As can be seen from the figure, for this choice the correlation length ξ^{1d} shows a paramagnetic behavior as anticipated, i. e. the spin correlations stay short-range even at very low temperatures due to the dimerization in the ground state.
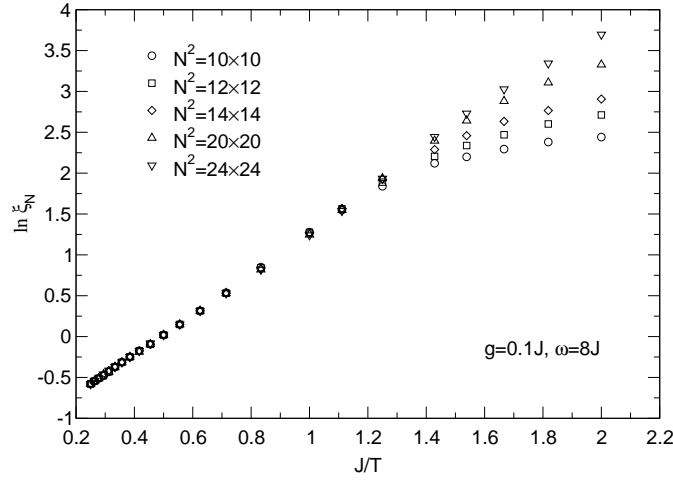
Fig. 4.6.: Logarithm of the finite system correlation lengths ξ_N vs. inverse temperature for $g = 0.1J$, $\omega = 8J$, and five different system sizes.

4.2.2. Spin correlations and staggered magnetization of the two-dimensional model

We now turn our attention to the two-dimensional bond coupling model (4.2.8). As we did for the one-dimensional case in the previous subsection, we first analyze the spin correlation length of the two systems with $g = 0.1J$, $\omega = 8J$, and $g = \omega = 0.67J$. Note that our discussion at the beginning of Par. 2.3.1 did not basically depend on the dimensionality of the system, i. e. the model (4.2.8) can be mapped exactly to the Hamiltonian (2.3.58). Hence we can apply the loop algorithm from Par. 2.3.4 and the improved estimator (2.4.70) from Sect. 2.4.2 to compute the two-point spin correlation function

$$G(\vec{x}) = \langle \sigma_0^z \sigma_{\vec{x}}^z \rangle \equiv \langle \sigma_{00}^z \sigma_{ij}^z \rangle \tag{4.2.10}$$

(i. e. $\vec{x} \equiv (i,j)$) for finite temperatures. As in the one-dimensional case, in both systems a number of 30 phonon updates per loop update (again with a value of 40 for the phonon cutoff) is sufficient to keep autocorrelation effects under control.

We first consider the system with $g = 0.1J$ and $\omega = 8J$. Similarly to the situation in one dimension, we expect that for this set of parameters the coupling between spin and lattice degrees of freedom is not sufficient to destroy the long-range Néel order which is present in the ground state of the Heisenberg model [And52, Bar91, San97]. Thus for reasons of universality, we can assume that the correlation function (4.2.10) obeys the known asymptotic result [CHN89, DM90, Bar91]

$$G(\vec{x}) \simeq C \, (-1)^{i+j} \, |\vec{x}|^{-\lambda} e^{-|\vec{x}|/\xi}, \tag{4.2.11}$$

with the algebraic exponent λ close to the classical Ornstein-Zernike value of $\frac{1}{2}$ [DM90]. In contrast to the linear dependence of ξ^{1d} on the inverse temperature in the XXX chain, here the correlation length ξ diverges exponentially with $\frac{J}{T}$ as $T \to 0$ [CHN89, DM90, Bar91, BBGW98]. For the system
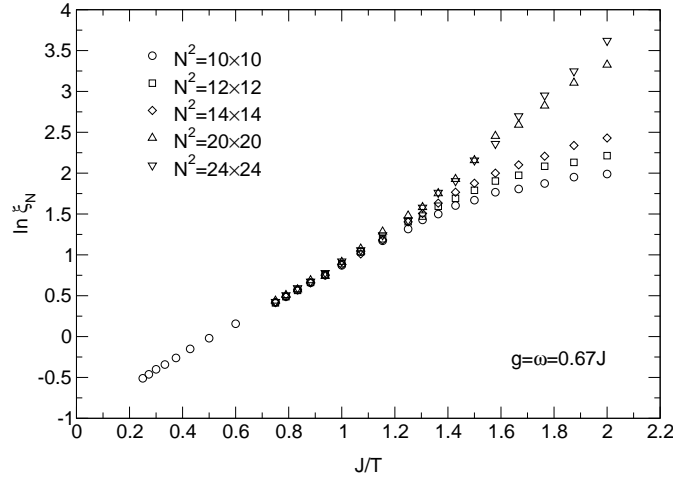
Fig. 4.7.: Semilogarithmic plot of the finite system correlation length ξ_N against $\frac{J}{T}$ for $g = \omega = 0.67J$, and the same set of system sizes as in Fig. 4.6.

with $g = 0.1J$ and $\omega = 8J$, we deduce numerical estimates for the finite system correlation lengths ξ_N by fitting the symmetrized function

$$f(x) = a\,(-1)^{i+j} \left(\frac{e^{-|\vec{x}|/\xi_N}}{\sqrt{|\vec{x}|}} + \frac{e^{-(N-|\vec{x}|)/\xi_N}}{\sqrt{N-|\vec{x}|}} \right) \qquad (4.2.12)$$

with two free parameters a and ξ_N to QMC data calculated in systems with linear system sizes $N = 10, 12, 14, 20, 24$. For the simulations, the total number of Monte Carlo sweeps per temperature was 10^5, while the first 25% of the configurations were skipped for thermalization of the algorithm. The values for the Trotter number of $M = 120$ for temperatures $0.5J \leq T \leq 0.9J$, and $M = 80$ for $T \geq J$, respectively, are sufficiently large to avoid finite-size effects in Trotter direction (for $N = 24$ the choice was $M = 120$ at all temperatures). The results are shown in Fig. 4.6, where the natural logarithm of ξ_N is plotted vs. $\frac{J}{T}$. They clearly reflect our expectations. At high temperatures, no dependence on the system size is visible, and we find the same exponential growth as in the Heisenberg model. When decreasing the temperature, finite-size effects become important. As soon as the estimates for ξ_N obtained from the fits become of the order of the linear system size, the curves branch off from the asymptotic behavior.

The ansatz (4.2.12) is also applied to fit the numerical data for the second system with $g = \omega = 0.67J$. While the linear system sizes and the number of loop updates were chosen to be identical to those given above, the values for the Trotter number were $M = 160$ for $0.5J \leq T \leq 0.63J$, $M = 120$ for $0.67J \leq T \leq 1.33J$, and $M = 80$ for $T \geq 1.67J$ (for $N = 20$ the number of configurations was 1.5×10^5, while it was 2×10^5 for $N = 24$ and $0.5J \leq T \leq 0.63J$). The results for the correlation lengths are depicted in Fig. 4.7. Surprisingly, the curves show a very similar behavior as compared to those given in Fig. 4.6. In retrospective, this justifies the application of the same fitting function (4.2.12) as for the system with $g = 0.1J$ and $\omega = 8J$. The conclusion is that we find Heisenberg-like behavior of the spin correlation length even for a fairly large value of the spin-phonon coupling. This is a striking difference to the one-dimensional bond coupling model,
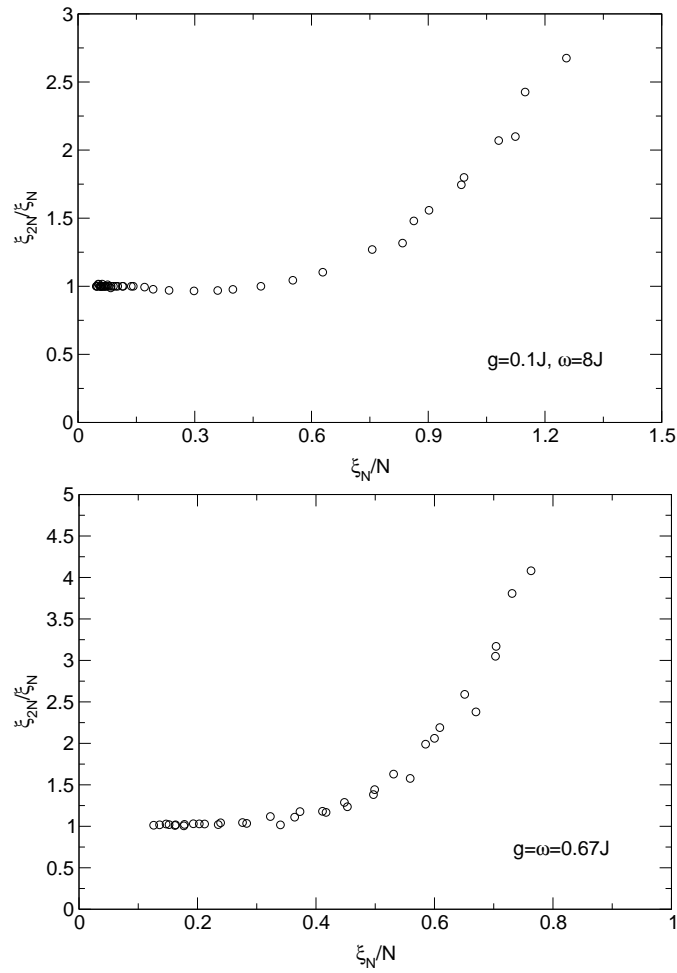
Fig. 4.8.: Test of the scaling prediction (4.2.13) for $g = 0.1J$, $\omega = 8J$ (top), and $g = \omega = 0.67J$ (bottom).

where the same choice corresponds to a strongly dimerized system, compare the discussion from Sect. 4.2.1. However, from our analysis we can also come to the conclusion that a strong spin-phonon coupling weakens the tendency of the system to establish antiferromagnetically ordered domains. From the Figs. 4.6 and 4.7 we see that at the same temperature, the correlation lengths in the system with $g = \omega = 0.67J$ are smaller than the corresponding values for $g = 0.1$ and $\omega = 8J$. We will discuss this aspect in more detail below.

At this point the reader might argue that an analysis of the spin correlation length at finite temperatures is not sufficient to draw reliable conclusions about the nature of the ground state. However, in the following we demonstrate that the data for ξ_N at $T > 0$ can be used to make direct statements about ground state properties. The argument is as follows: let us assume that the system shows long-range Néel order in the ground state. In terms of the renormalization group, this means that there is a critical fixed point at $T = 0$ which controls the system properties at low

temperatures. In this case the finite-size scaling relation [CEF$^+$95, CEPS95, BBGW98]

$$\frac{\xi_{2N}(T)}{\xi_N(T)} = F\left(\frac{\xi_N(T)}{N}\right) \tag{4.2.13}$$

holds, where F is a universal scaling function. With the data from the Figs. 4.6 and 4.7 it is possible to test the scaling prediction (4.2.13), see Fig. 4.8. There for both choices of coupling constants and $N = 10, 12$ the fraction $\frac{\xi_{2N}}{\xi_N}$ is plotted against $\frac{\xi_N}{N}$. For $g = 0.1J$ and $\omega = 8J$ as well as $g = \omega = 0.67J$ the data clearly collaps onto one curve. Thus the assumption that the two systems show long-range antiferromagnetic order in the ground state is valid indeed. Note that the shape of the scaling function F in Eq. (4.2.13) depends on the particular choice of coupling constants in Eq. (4.2.8).

A more quantitative understanding of the influence of the spin-phonon coupling can be achieved by considering the order parameter for a Néel ordered phase, which is the staggered magnetization

$$M_s = \lim_{N\to\infty}\left|\frac{1}{2N^2}\sum_{i,j=1}^{N}(-1)^{i+j}\langle\vec{\sigma}_{ij}\rangle\right|. \tag{4.2.14}$$

As long as $T > 0$ holds, M_s vanishes because due to thermal fluctuations no long-range antiferromagnetic order can be established. This is in accordance with the Mermin-Wagner theorem which states that in $d \leq 2$ dimensions there is no breaking of a continuous symmetry (here the $SU(2)$ symmetry of the Hamiltonian (4.2.8)) at finite temperatures [MW66]. As far as the square lattice spin-$\frac{1}{2}$ Heisenberg model at $T = 0$ is concerned, there is long-range order and hence a finite staggered magnetization [And52, Bar91, SSC97]. For this system, a comparison of the accurate numerical value of $M_s = 0.3070(3)$ obtained from QMC simulations [San97] to the number of $M_s = 0.5$ for a classical Néel state indicates that quantum fluctuations are of significant importance in two-dimensional quantum spin systems.

In the following we determine numerical estimates for M_s in the two systems with spin-phonon coupling at $T = 0$. We emphasize that a direct measurement of the observable (4.2.14) in the ground state is not possible since the QMC method can only be applied to finite systems at temperatures $T > 0$, where M_s vanishes. However, the staggered magnetization can be accessed by measuring

$$m_s^2(N) = \left\langle\left(\frac{1}{2N^2}\sum_{i,j=1}^{N}(-1)^{i+j}\sigma_{ij}^z\right)^2\right\rangle = \frac{1}{4N^2}\sum_{i,j=1}^{N}(-1)^{i+j}\langle\sigma_{00}^z\sigma_{ij}^z\rangle, \tag{4.2.15}$$

which is just the static structure factor of the two-point spin correlation function (4.2.10) at momentum (π, π). At sufficiently low temperatures, one can neglect the temperature-dependence of this quantity and the estimates for m_s^2 take their values in the ground state with numerical accuracy. In this case we can make use of the identity [RY88, Bar91, San97]

$$3m_s^2(N) = M_s^2 + \frac{b}{N} + \mathcal{O}\left(\frac{1}{N^2}\right) \tag{4.2.16}$$

to extrapolate to the thermodynamic limit, and we obtain the order parameter M_s in the ground state. Here b is a constant number and the factor of three on the left-hand side accounts for the
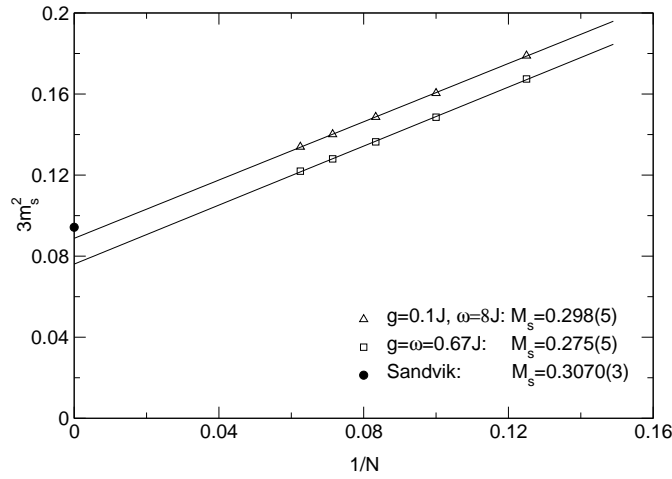
Fig. 4.9.: Extrapolation of the staggered magnetization M_s from finite-size data for $3m_s^2$ as defined in Eq. (4.2.15). The triangles are the datapoints for $g = 0.1J$, $\omega = 8J$, while the squares represent the QMC results for $g = \omega = 0.67J$. The error bars are smaller than the size of the symbols. The solid straight lines are the curves from a linear fit according to Eq. (4.2.16), and the filled circle corresponds to the result $M_s = 0.3070(3)$ for the square lattice Heisenberg model from Ref. [San97].

fact that the definition (4.2.14) makes use of the full spin operators $\vec{\sigma}_{ij}$, while the relation (4.2.15) is based on the two-point correlations of the corresponding z-components σ_{ij}^z.

We are now in the position to apply this scheme to the two systems with $g = 0.1J$, $\omega = 8J$ and $g = \omega = 0.67J$. The spin correlations were calculated in systems with $N = 8, 10, 12, 14, 16$, taking 5×10^5 spin updates (with 25% of the sweeps skipped for thermalization as before) and $M = 160$ for the Trotter number. The choice for the temperature was $T = 0.1J$, which is found to be sufficiently low to make quantitative statements about the staggered magnetization in the ground state. In Fig. 4.9, the values for $3m_s^2$ are plotted against $\frac{1}{N}$. The results show the correct finite-size behavior as predicted by Eq. (4.2.16), and therefore we can make use of linear regression to deduce the numerical estimates for M_s. For the system with $g = 0.1J$ and $\omega = 8J$ we have $M_s = 0.298(5)$, i. e. the spin-phonon interaction only leads to a small reduction of the staggered magnetization as compared to the Heisenberg model. As far as the second system with $g = \omega = 0.67J$ is concerned, the result is $M_s = 0.275(5)$. Thus we find – in accordance with the finite-size scaling analysis of the correlation length in Fig. 4.8 – that there is long-range antiferromagnetic order in the ground state even for a large value of the fraction $\frac{g}{\omega}$. As expected, the reduction of M_s due to the spin-phonon coupling is significantly larger than for $g = 0.1$ and $\omega = 8J$. However, the value for the staggered magnetization is still so large that from our analysis, we cannot conclude that the model (4.2.8) shows a quantum phase transition towards a paramagnetic state like its one-dimensional counterpart (4.1.7).

To clarify whether the model (4.2.8) shows such a transition, one would have to move even further into the strong coupling regime and increase the fraction of $\frac{g}{\omega}$ drastically. In this case though, the loop algorithm from Sect. 2.3.4 strongly suffers from autocorrelation effects and is not

applicable in practice. This is mainly due to the local nature of the phonon update procedure as described in Par. 2.3.3. We further emphasize that from the analysis in this section, one cannot judge whether the weakening of the Néel order due to the spin-phonon coupling is accompanied by lattice distortions. To answer this question, it is necessary to measure the correlations of the local displacements operators $(a_{ij}^\dagger + a_{ij})$ and $(b_{ij}^\dagger + b_{ij})$. This amounts to a calculation of non-diagonal quantities composed of the phonon annihilation and creation operators, which is hampered even more by large autocorrelation times because the concept of improved estimators (see Sect. 2.4.2) cannot be applied. Furthermore and according to our discussion from Par. 4.1, it is not clear which operator exactly has to be measured to study a ground state with broken translational invariance because it is not known which type of distortion pattern is energetically favored. Note that in principle, even a finite temperature phase transition from the uniform to a distorted phase is conceivable. However, an analysis of the specific heat of the model does not give any hints on the occurrence of such a feature [Ait02, AL03].

4.3. Statically dimerized spin models and the optimal dimerization pattern

In the last section we saw that for large values of the fraction $\frac{g}{w}$, the loop algorithm from Par. 2.3.4 only provides limited access to the two-dimensional bond coupling model (4.2.8). Although we showed that the spin-lattice interaction tends to suppress the antiferromagnetic order in the ground state, we were not able to answer the question whether the model exhibits a quantum phase transition to a paramagnetic state. Furthermore, we were not capable of studying under which circumstances lattice distortions might come into play and which pattern of the distortions would be realized.

The aim of this section is to gain a deeper understanding of these problems by investigating statically dimerized spin models [ALKW05]. As in the case of quasi one-dimensional spin-phonon systems, the analysis of such models can be viewed as a mean field approach to investigate the influence of the spin-phonon coupling in the adiabatic limit. One way to derive this class of models is to consider the bond coupling Hamiltonian (4.2.8), and replace

$$g(a_{ij}^\dagger + a_{ij}) = \sqrt{2}\, g\, u_{ij}^x \quad \rightarrow \quad \sqrt{2}\, g\, \langle u_{ij}^x \rangle \equiv J A_{ij} \delta, \tag{4.3.17}$$

$$g(b_{ij}^\dagger + b_{ij}) = \sqrt{2}\, g\, u_{ij}^y \quad \rightarrow \quad \sqrt{2}\, g\, \langle u_{ij}^y \rangle \equiv J B_{ij} \delta. \tag{4.3.18}$$

Here we have $\delta \in [0, 1]$ and $A_{ij}, B_{ij} = \pm 1$, i. e. we only allow for two possible values $\pm\delta$ of the lattice distortions $\langle u_{ij}^{x/y} \rangle$ on the bonds of the lattice. Furthermore, we impose the constraint that there is an equal number of strong and weak bonds,

$$\sum_{i,j=1}^{N} (A_{ij} + B_{ij}) = 0. \tag{4.3.19}$$

For a treatment of arbitrary lattice distortions we refer to Sect. 4.4, where we focus on a two-dimensional difference coupling model (4.1.6) in the adiabatic limit. Note that the Ising-like variables $\{A_{ij}, B_{ij}\}$ have been introduced to encode the particular dimerization pattern. With the

replacements (4.3.17) and (4.3.18), the spin-phonon interaction part of Eq. (4.2.8) becomes

$$H = \frac{J}{2} \sum_{i,j=1}^{N} \left[(1 + A_{ij}\delta) \vec{\sigma}_{ij} \vec{\sigma}_{i+1,j} + (1 + B_{ij}\delta) \vec{\sigma}_{ij} \vec{\sigma}_{i,j+1} \right], \quad (4.3.20)$$

which can be viewed as the two-dimensional analog of the dimerized Heisenberg chain (4.1.4). We add that by assuming a bond coupling mechanism, the loss in elastic energy due to the lattice distortions does not depend on the particular dimerization pattern. Indeed in the limit of small phonon frequencies ω, the third line of Eq. (4.2.8) becomes

$$H_{\text{dis}} = \frac{K}{2} \sum_{i,j=1}^{N} \left[(A_{ij}\delta)^2 + (B_{ij}\delta)^2 \right] = KN^2\delta^2, \quad (4.3.21)$$

with an elastic constant K defined by $\omega^2 = \frac{K}{m}$ (m is the mass of the oscillating ions on the bonds). We see that it is sufficient to investigate the statically dimerized models (4.3.20) in order to draw conclusions about the full lattice Hamiltonian which is the sum of Eqs. (4.3.20) and (4.3.21). We further point out that – although here we have constructed the statically dimerized models starting from the bond coupling model (4.2.8) – the set of magnetic Hamiltonians defined by Eq. (4.3.20) is a very general starting point for our analysis. For example, these systems can also be viewed as possible candidates for effective spin models to describe the magnetism of independent spin layers coupled to three dimensional lattice vibrations.

In the following subsection, we first concentrate on the three models from Fig. 4.4 (see Sect. 4.1). With regard to the controversial discussion in the literature, we compare numerical estimates for the ground state energies and determine which of the three models has the largest energy gain in the magnetic sector. In the subsequent subsections, we develop a method to investigate the whole class of models defined by Eq. (4.3.20) with the confinement (4.3.19). We first explain the main ideas behind this approach for the well understood dimerized Heisenberg chain (4.1.4) in Par. 4.3.2. In particular, we show that by performing a Landau expansion of the free energy for this system it is possible to establish a mean field theory of the spin-Peierls transition. As the approach relies on a numerical computation of integrated dynamical dimer correlations, the analysis of the one-dimensional system provides a means to check the corresponding numerical routines which will also be needed in the two-dimensional case. In Sect. 4.3.3, we then turn to quasi two-dimensional systems and demonstrate that an analogous approach yields a possibility to compare all possible patterns in the region of small dimerization δ. By analyzing the numerical data for the two-dimensional dimer correlations, we obtain the optimal distortion pattern among all possibilities encoded by Eq. (4.3.20) (see Par. 4.3.4). Having determined this pattern, it is straightforward to generalize the ideas from Sect. 4.3.2 and to establish a Landau theory of the two-dimensional analog of the spin-Peierls transition in Par. 4.3.5. Under the assumption that the relation (4.3.21) correctly describes the elastic energy of the distorted system, we investigate the dependence of the transition temperature on the elastic constant K. A discussion on the order of the transition is also included. Finally in Par. 4.3.6, we return to the question from Sect. 4.2 whether a coupling between spin and lattice degrees of freedom can drive the system into a paramagnetic phase.

model	A_{ij}	B_{ij}
plaquette	$(-1)^i$	$(-1)^j$
stair	$(-1)^{i+j}$	$(-1)^{i+j}$
meander	$(-1)^{i+j}$	$(-1)^j$

Table 4.1.: Possible choices for $\{A_{ij}, B_{ij}\}$ in Eq. (4.3.20) to model the three dimerized lattices as depicted in Fig. 4.4 from Sect. 4.1.

4.3.1. Models with alternating couplings and minimal unit cell

In this subsection, we focus on the three models depicted in Fig. 4.4 from Sect. 4.1. As has been mentioned there, these systems are the only possibilities of dimerized systems on a square lattice with an equal number of strong and weak bonds, alternating couplings along each linear chain, and a minimal 2×2 unit cell. Obviously, the three models belong to the set of Hamilton operators defined by the Eqs. (4.3.20) and (4.3.19), see also Table 4.1. Being representations of the isotropic Heisenberg model with antiferromagnetic bond-dependent couplings, they are directly accessible to the continuous time loop algorithm as described in the Pars. 2.2.4 and 2.2.5.

In the introduction 4.1 to this chapter, we have already pointed out that the discussions in the literature reveal an ambiguous picture which of the three patterns has the largest gain in the magnetic energy as compared to the Heisenberg model (for fixed δ). While the Lanczos calculations on small lattices from Ref. [TH88] indicate that the plaquette model has the lowest ground state energy, the results from Ref. [SKH02] based on linear spin wave theory point towards the opposite direction, because there the authors find a stair-like distortion to be energetically favored.

In the following our aim is to clarify which of the two statements is true. We tackle this question by comparing numerical estimates for the ground state energy densities ϵ_0 of the three models in the whole regime $\delta \in [0, 1]$ of the dimerization parameter. These numbers can be deduced from QMC results for the internal energy per lattice site U, which is given by (see the Hamiltonian (4.3.20))

$$U \equiv \frac{\langle H \rangle}{N^2} = \frac{3J}{2N^2} \sum_{i,j=1}^{N} \left[(1 + A_{ij}\delta)\langle \sigma_{ij}^z \sigma_{i+1,j}^z \rangle + (1 + B_{ij}\delta)\langle \sigma_{ij}^z \sigma_{i,j+1}^z \rangle \right], \tag{4.3.22}$$

i. e. we need to compute the spin correlations between nearest neighbors on the dimerized square lattice. Note that by denoting Eq. (4.3.22), we have taken opportunity of the fact that at finite temperatures and for arbitrary pairs of spins $\vec{\sigma}_{ij}$, $\vec{\sigma}_{kl}$ the relation $\langle \vec{\sigma}_{ij} \vec{\sigma}_{kl} \rangle = 3\langle \sigma_{ij}^z \sigma_{kl}^z \rangle$ holds. The further argumentation is analogous to the one from Par. 4.2.2, where we have discussed how the staggered magnetization M_s in the ground state can be deduced from finite temperature data for the static structure factor of the two-point spin correlation function. For sufficiently low temperatures, the QMC results for U coincide with the ground state energy density $\epsilon_0(N)$ of the finite system with numerical accuracy. Then one can apply a finite-size scaling analysis based on the relation [Bar91, San97]

$$\epsilon_0(N) = \epsilon_0 + \frac{a}{N^3} + \mathcal{O}\left(\frac{1}{N^4}\right) \tag{4.3.23}$$

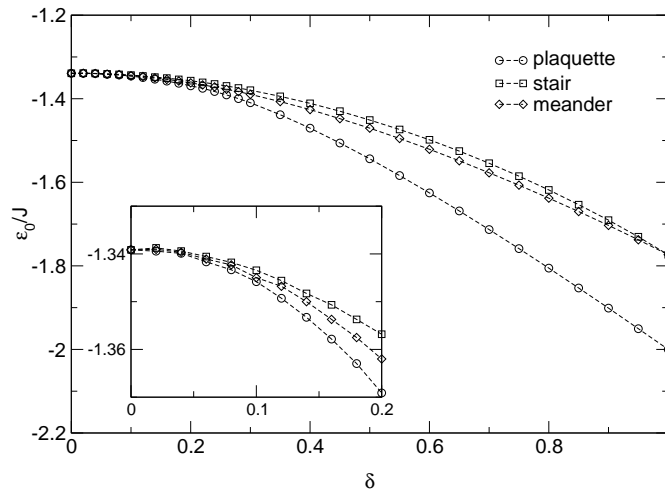to obtain the corresponding values for ϵ_0 in the thermodynamic limit $N \to \infty$.

Fig. 4.10.: Comparison of the ground state energy density ϵ_0 in dependence on δ for the plaquette (circles), stair (squares) and meander model (diamonds). The numerical error bars are smaller than the size of the symbols. The inset is a magnification of the region with small $\delta \in [0, 0.2]$.

The QMC estimates for the internal energy of the three models were computed in systems with linear systems sizes $N = 12, 16, \ldots, 32$ and values of $\delta = 0, 0.02, \ldots, 0.3$ and $\delta = 0.35, 0.4, \ldots, 1$ for the dimerization, respectively. A temperature of $T = 0.04J$ was found to be sufficiently low so that the ground state completely dominates the behavior of U. While the first 2×10^4 Monte Carlo sweeps were skipped for the thermalization of the algorithm, a number of 2×10^5 worldline configurations was taken for the evaluation of expectation values. Afterwards for each of the three models and each value of δ, a two-parameter fit according to Eq. (4.3.23) was applied to the QMC data for six different system sizes, providing the desired numerical estimates for ϵ_0 in the thermodynamic limit.

The reliability of this approach can be checked by considering the two special choices $\delta = 0$ and $\delta = 1$, where the results can be compared to independent exact or numerical findings. As far as the uniform square lattice Heisenberg model with $\delta = 0$ is concerned, we find $\epsilon_0/J = -1.3392(2)$, which – for our purposes – is in good accordance with the result of $\epsilon_0/J = 1.33887(1)$ from a very careful analysis of SSE data in Ref. [San97]. For the plaquette model with $\delta = 1$, the numerical result of $\epsilon_0/J = -1.99997(8)$ agrees perfectly with the exact value of $\epsilon_0/J = -2.0$ which can be determined easily, because in this limit the plaquette lattice consists of uncoupled and periodically closed XXX chains with only four sites. In case of the stair and meander models with $\delta = 1$, one has a set of uncoupled XXX chains of infinite length. Hence the exact result for the ground state energy is given by the Bethe ansatz result (3.3.91) for the one-dimensional Heisenberg model (see Par. 3.3.1) with the replacement $J \rightarrow J(1 + \delta) = 2J$, which yields $\epsilon_0/J \approx -1.7725887$. Again this is in sufficient agreement with the numerical value of $\epsilon_0/J = -1.7733(1)$. Note that the numerical errors given here are those obtained from the fitting procedure and do not account for systematic effects due to the simulation of finite temperatures or the neglect of higher order terms in the relation (4.3.23).

The comparison of the ground state energy densities for the three models with $\delta \in [0, 1]$ is given in Fig. 4.10. The results leave no doubt that for any fixed δ, the plaquette model has the largest gain in the magnetic energy. This statement also holds in the region of small δ (inset of Fig. 4.10), which is of particular interest in the context of systems with spin-phonon coupling, because in real solids the occurrence of large lattice distortions due to this mechanism is very unlikely. We see that our findings are in accordance with those from Ref. [TH88], while the application of linear spin wave theory in Ref. [SKH02] to determine the favored dimerization pattern turns out to be problematic.

4.3.2. Landau theory of the spin-Peierls transition: the dimerized chain revisited

In principle, the procedure to extract the ground state energies of dimerized spin models as described in the previous subsection applies to each of the models defined by the Eqs.(4.3.20) and (4.3.19). For this reason it would be straightforward to compare the gain in magnetic energy for a larger set of distortions patterns than just the three lattice modulations as depicted in Fig. 4.4. However, this way of proceeding is somewhat unsatisfactory because there always remains an infinite number of possibilities to arrange strong and weak bonds on the square lattice which are not taken into account. In the following subsections, we will develop a method to compare all possible patterns in the region of small but finite dimerizations δ. Before we focus our attention on this issue though, we discuss the basic ideas behind this approach in the context of quasi one-dimensional spin-Peierls systems in this subsection.

We follow the argumentation from Refs. [KRS99,RKS00], and consider the dimerized Heisenberg chain (4.1.4) with temperature dependent dimerization $\delta(T)$ as the effective model to describe the magnetism of a spin-Peierls system in the adiabatic limit, see also the discussion from Sect. 4.1. The loss in the elastic energy due to possible lattice distortions can be taken into account by adding a contribution

$$H_{\text{dis}} = \frac{K}{2} N \delta^2 \qquad (4.3.24)$$

to the magnetic Hamiltonian (4.1.4), see also the analogous expression (4.3.21) in the two-dimensional case. In the following we investigate the dependence of the transition temperature T_c of the spin-Peierls transition on the elastic constant K. We start by performing a Landau expansion [LL79] of the free energy per lattice site $f(T, \delta)$ for the Hamiltonian (4.1.4), which reads

$$f(T, \delta) = f_0(T) + \frac{1}{2} a(T) \delta^2 + \frac{1}{24} b(T) \delta^4 + \mathcal{O}(\delta^6). \qquad (4.3.25)$$

Here the odd orders in δ vanish because the Hamiltonian is invariant under the transformation $\delta \to -\delta$, and $f_0(T) \equiv f(T, \delta = 0)$ is the free energy of the uniform Heisenberg chain. The coefficient

$$a(T) \equiv \left. \frac{\partial^2}{\partial \delta^2} f(T, \delta) \right|_{\delta=0} \qquad (4.3.26)$$

of the second order will be called *'dimerizability'* in the following, because it describes the tendency of the system to establish a dimerized state. The critical temperature T_c can be determined if

we also take into account the lattice contribution (4.3.24). As soon as the free energy gain of $-\frac{1}{2}a(T)\delta^2$ in the magnetic sector (we expect that $a(T)$ takes negative values at all temperatures $T > 0$) outweighs the elastic energy loss of $\frac{K}{2}\delta^2$ per lattice site as given by Eq. (4.3.24), a dimerized state is energetically favored. Hence the condition to determine T_c is

$$-a(T_c) = K, \tag{4.3.27}$$

and an investigation of the transition temperature amounts to a calculation of the dimerizability for the uniform XXX chain.

In the following we derive an explicit expression for $a(T)$ in a finite system with N sites and periodic boundary conditions. Making use of the relation $f = -\frac{1}{\beta N}\ln Z$ (with $Z = \mathrm{Tr}\, e^{-\beta H}$ as usual) and $\frac{\partial f}{\partial \delta}\big|_{\delta=0} = 0$ due to the invariance under transformations $\delta \to -\delta$, Eq. (4.3.26) becomes

$$a(T) = -\frac{1}{\beta N Z_0}\frac{\partial^2 Z}{\partial \delta^2}\bigg|_{\delta=0}, \tag{4.3.28}$$

where we have introduced the abbreviation Z_0 for the partition function of the uniform Heisenberg chain with $\delta = 0$. In the next step, we consider the general identity

$$\frac{\partial^2}{\partial \delta^2}\bigg|_{\delta=0} \mathrm{Tr}\, e^{-\beta H + \delta A} = \frac{Z}{\beta}\int_0^\beta d\tau\, \langle A(0)A(\tau)\rangle, \tag{4.3.29}$$

where A is an arbitrary operator which does not necessarily commute with H. The partition function Z as well as the expectation values on the right-hand side are defined with respect to the unperturbed Hamiltonian H, and the time-dependence of $A(\tau)$ is given by a translation in imaginary time direction as defined by Eq. (2.4.67), see Par. 2.4.1. A proof of the relation (4.3.29) can be found in App. A.4. In the following we identify $H \equiv H(\delta = 0)$ and $A \equiv -\frac{\beta J}{2}\sum_i(-1)^i D_i$, where $D_i \equiv \vec{\sigma}_i \vec{\sigma}_{i+1}$ is the local dimer operator as introduced in Sect. 3.1, and apply the formula (4.3.29) to the relation (4.3.28). The result is

$$a(T) = -\frac{1}{\beta^2 N}\int_0^\beta d\tau\, \left\langle \left(-\frac{\beta J}{2}\sum_{i=1}^N(-1)^i D_i(0)\right)\left(-\frac{\beta J}{2}\sum_{j=1}^N(-1)^j D_j(\tau)\right)\right\rangle_{\delta=0}$$

$$= -\frac{J^2}{4}\sum_{i=1}^N(-1)^i\int_0^\beta d\tau\, \langle D_0(0)D_i(\tau)\rangle_{\delta=0}, \tag{4.3.30}$$

where we have exploited the translational invariance of the uniform Heisenberg chain and the periodic boundary conditions in the second step. We see that the gain in the magnetic energy due to the dimerization is controlled by the (Euclidean) dynamical structure factor of the dimer correlation function at zero frequency and momentum π, evaluated for the uniform Heisenberg model. This is in accordance with the findings from Refs. [Pyt74, CF79], see the discussion in the introduction 4.1 to this chapter. There in the context of softening of phonon modes as described by Eq. (4.1.3), we have mentioned that the same quantity governs the behavior of the polarizability $\Pi(q, \Omega)$ at momentum $q = \pi$ (with $\Omega = 0$), which is the relevant phonon mode to study in the context of the spin-Peierls transition. According to Ref. [CF79], the dimerizability diverges like $-\frac{J}{T}$ as $T \to 0$. This indicates that one cannot perform a Taylor expansion of the ground state energy
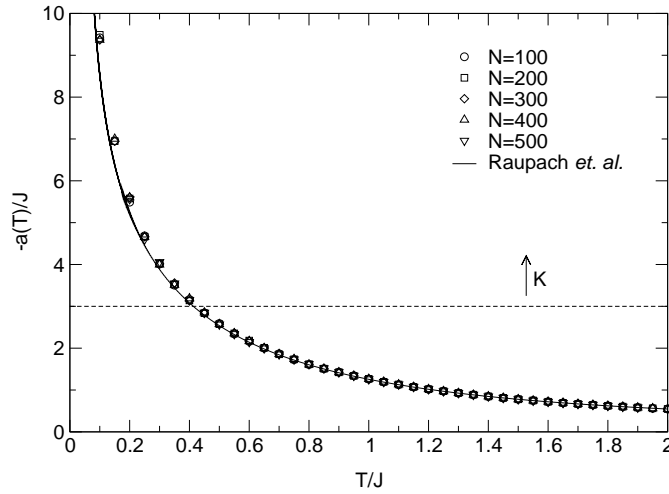
Fig. 4.11.: QMC data for the negative dimerizability evaluated via Eq. (4.3.30). The numerical errors are smaller than the size of the symbols. The solid line is the TMRG result from Ref. [RKS00]. The intersection point of the horizontal dashed line at $-a = K$ (here $K = 3J$) with the curve for $-a(T)$ yields the critical temperature T_c (here $T_c \approx 0.43J$) of the spin-Peierls transition.

in δ analogous to the expression (4.3.25) for the free energy at finite temperatures. Indeed in the vicinity of $\delta = 0$, the ground state energy gain of the model (4.1.4) scales like $\delta^{\frac{4}{3}}$ [CF79]. Thus regardless of the exact value of the elastic constant K, there is always a transition to a dimerized phase at finite temperatures.

The application of bosonization techniques in Ref. [CF79] only yields approximate results for the dimerizability, which should be checked against independent numerical findings. Numerical data for $a(T)$ have been obtained using the TMRG approach in Refs. [KRS99, RKS00]. Replacing the second derivative in Eq. (4.3.26) by the corresponding difference quotient, the authors find the identity

$$a(T) = \lim_{\delta \to 0} \frac{J}{4\delta} \left[\left\langle \vec{\sigma}_1 \vec{\sigma}_2 \right\rangle_\delta - \left\langle \vec{\sigma}_0 \vec{\sigma}_1 \right\rangle_\delta \right] . \tag{4.3.31}$$

This relation can be assessed by first computing the difference of the nearest neighbor spin correlations on bonds with different couplings $\frac{J}{2}(1 \mp \delta)$ for several dimerizations $\delta > 0$, and subsequently extrapolating to $\delta = 0$. The TMRG data were found to be in good qualitative agreement with the bosonization results from Ref. [CF79].

In the remainder of this subsection we show independent numerical data for $a(T)$ which have been obtained by applying the continuous time loop algorithm as described in Sects. 2.2.4 and 2.2.5. The computation is based on a direct evaluation of the identity (4.3.30), i. e. in contrast to the approach from Refs. [KRS99, RKS00] there is no extrapolation procedure involved. The measurement rules for the dynamical dimer correlations are given in App. A.3. Note that the integration over τ in Eq. (4.3.30) can be directly incorporated in the numerical routines. While 2×10^4 loop updates were applied for thermalization, a number of 5×10^5 configurations was evaluated for the calculation of expectation values. The results for $-a(T)$ with five different system sizes $N = 100, 200, \ldots, 500$ are shown in Fig. 4.11. For the temperature range given in the figure, there is no visible finite-

size effect, i. e. we can assume that the data represent the thermodynamic limit with sufficient accuracy. Besides the characteristic divergence as $T \to 0$, there is a good quantitative agreement to the TMRG data from Refs. [KRS99, RKS00]. The small deviations at low temperatures could indicate systematic errors of the TMRG data due to the extrapolation procedure mentioned above.

Given the curve for $-a(T)$ and a certain value of the elastic constant K, one can immediately assess the condition (4.3.27) to determine the critical temperature T_c of the spin-Peierls transition. Drawing a horizontal line at $-a = K$ in the figure, the value for T_c corresponds to the first coordinate of the intersection point of the two curves. For the example with $K = 3J$ as shown in Fig. 4.11, this procedure yields $T_c \approx 0.43J$.

Before we return to the dimerized spin models in two dimensions, we add the remark that the approach from this subsection is not sufficient to determine the values of $\delta(T)$ for temperatures below T_c. Furthermore, the ansatz cannot be applied to analyze the order of the spin-Peierls transition. Both issues would require an evaluation of the fourth order coefficient $b(T)$ in the Landau expansion (4.3.25), which amounts to a calculation of certain dynamical eight-point correlation functions. Although it is in principle feasible, this is an even larger challenge than the evaluation of the dynamical dimer correlations.

4.3.3. Effective Ising model for the dimerizability

We now return to the issue of two-dimensional statically dimerized spin models. In this section we develop a numerical method to compare the gain in the magnetic energy for all possible patterns defined by the Eqs. (4.3.20) and (4.3.19), which applies to the region of small dimerizations $\delta > 0$. The only restriction of this approach is due to the finite system size which can be treated in numerical simulations. We emphasize that focussing on small values of δ is not a severe limitation, because from the viewpoint of systems with spin-phonon coupling one only expects small lattice distortions to be important in real materials.

The key idea behind our analysis is to perform the same Landau expansion of the free energy of the two-dimensional Hamiltonian (4.3.20) as we did for the dimerized chain in the preceeding subsection. We then observe that for any choice of $\{A_{ij}, B_{ij}\}$ in Eq. (4.3.20), we obtain the same expression (4.3.25) for the free energy density as in one dimension. In particular, the odd orders in δ vanish due to the constraint (4.3.19). Thus for any fixed but small value of δ, it is sufficient to analyze the dependence of the dimerizability $a(T)$ (which is defined by the same expression (4.3.26) as in the one-dimensional case) on the Ising variables $\{A_{ij}, B_{ij}\}$ in order to compare the different dimerization patterns.

Again in analogy to the treatment of the dimerized chain (4.1.4), we derive an explicit expression for the dimerizability of the Hamiltonian (4.3.20) for a finite system with $N \times N$ lattice sites and periodic boundary conditions in the following. In contrast to the approach in one dimension though, we do not specify the arrangement of strong and weak couplings on the square lattice, i. e. we formally keep the dependence of $a(T)$ on the numbers $\{A_{ij}, B_{ij}\}$. Another difference is that in two dimensions, we have to introduce two types of local dimer operators

$$D_{ij}^x \equiv \vec{\sigma}_{ij}\vec{\sigma}_{i+1,j}, \qquad D_{ij}^y \equiv \vec{\sigma}_{ij}\vec{\sigma}_{i,j+1}, \tag{4.3.32}$$

because there are two possible orientations of dimers defined on bonds directed along the i- and j-direction. Using these conventions and identifying $H \equiv H(\delta = 0)$ and $A \equiv -\frac{\beta J}{2} \sum_{ij} [A_{ij} D_{ij}^x + B_{ij} D_{ij}^y]$, we can apply the identity (4.3.29) from Par. 4.3.2 (see also App. A.4) to the two-dimensional analog of Eq. (4.3.28). This gives

$$
\begin{aligned}
a(T) = -\frac{1}{\beta^2 N^2} \int_0^\beta d\tau \Bigg\langle & \left(-\frac{\beta J}{2} \sum_{i,j=1}^N [A_{ij} D_{ij}^x(0) + B_{ij} D_{ij}^y(0)] \right) \\
& \times \left(-\frac{\beta J}{2} \sum_{k,l=1}^N [A_{kl} D_{kl}^x(\tau) + B_{kl} D_{kl}^y(\tau)] \right) \Bigg\rangle_{\delta=0} \\
= -\frac{J^2}{4N^2} \int_0^\beta d\tau \sum_{i,j,k,l=1}^N & \left[A_{ij} A_{kl} \left\langle D_{ij}^x(0) D_{kl}^x(\tau) \right\rangle_{\delta=0} + B_{ij} B_{kl} \left\langle D_{ij}^y(0) D_{kl}^y(\tau) \right\rangle_{\delta=0} \right. \\
& \left. + A_{ij} B_{kl} \left\{ \left\langle D_{ij}^x(0) D_{kl}^y(\tau) \right\rangle_{\delta=0} + \left\langle D_{ij}^x(\tau) D_{kl}^y(0) \right\rangle_{\delta=0} \right\} \right].
\end{aligned}
\tag{4.3.33}
$$

Thus as in one dimension, we have expressed the dimerizability in terms of specific structure factors of the dynamical dimer correlations. However, the more important observation is that the result (4.3.33) can be rewritten as the classical Hamilton function of a bilayered system consisting of $2N^2$ Ising spins $\{A_{ij}, B_{ij}\}$ with long-range interactions. Indeed by interchanging the summation and integration in Eq. (4.3.33), we obtain an Ising Hamiltonian

$$
a(T) = \sum_{i,j,k,l=1}^N \left[K_1(k-i, l-j) A_{ij} A_{kl} + K_2(k-i, l-j) B_{ij} B_{kl} + K_3(k-i, l-j) A_{ij} B_{kl} \right],
\tag{4.3.34}
$$

where the coupling constants

$$
K_1(k-i, l-j) \equiv -\frac{J^2}{4N^2} \int_0^\beta d\tau \left\langle D_{ij}^x(0) D_{kl}^x(\tau) \right\rangle_{\delta=0},
\tag{4.3.35}
$$

$$
K_2(k-i, l-j) \equiv -\frac{J^2}{4N^2} \int_0^\beta d\tau \left\langle D_{ij}^y(0) D_{kl}^y(\tau) \right\rangle_{\delta=0},
\tag{4.3.36}
$$

$$
K_3(k-i, l-j) \equiv -\frac{J^2}{4N^2} \int_0^\beta d\tau \left[\left\langle D_{ij}^x(0) D_{kl}^y(\tau) \right\rangle_{\delta=0} + \left\langle D_{ij}^x(\tau) D_{kl}^y(0) \right\rangle_{\delta=0} \right],
\tag{4.3.37}
$$

only depend on the differences of coordinates due to the translational invariance of the uniform Heisenberg model.

In particular, the result (4.3.34) provides a roadmap to determine the dimerization pattern which minimizes the magnetic free energy of the finite system (4.3.20) for small $\delta > 0$:

1. For any fixed temperature $T > 0$ of the quantum system, determine the coupling constants (4.3.35), (4.3.36), and (4.3.37) of the classical Ising model (4.3.34) by evaluating dynamical dimer correlations of the uniform square lattice Heisenberg model. This is done on the basis of the continuous time loop algorithm from Sects. 2.2.4 and 2.2.5. The numerical routines to compute the integrated dimer correlations are identical to those in the one-dimensional case, see also Par. 4.3.2.

2. Extract the configuration of Ising spins $\{A_{ij}, B_{ij}\}$ which minimizes the classical Hamilton function (4.3.34). In practice, this is done numerically by applying classical Monte Carlo

techniques. Note that only configurations with a vanishing total magnetization have to be taken into account due to the constraint (4.3.19). For a detailed description of this part we refer to the following subsection.

At this point we comment shortly on the structure of the coupling constants K_α ($\alpha = 1, 2, 3$) of the Ising Hamiltonian (4.3.34). In contrast to e. g. the definition (3.1.5) of the dimer correlation function G_d for the XXZ chain (see Sect. 3.1), the explicit expressions (4.3.35), (4.3.36), and (4.3.37) for the Ising couplings involve no subtraction of background terms, which are usually expressed by the square of the (site-independent) expectation value of the local exchange energy between adjacent spins on the square lattice. For this reason all the couplings of the Ising model (4.3.34) turn out to be strongly ferromagnetic. However, the ferromagnetic configurations with $A_{ij} = B_{ij} = \pm 1$ for all (i, j) have been excluded from our analysis due to the zero magnetization constraint (4.3.19), because they correspond to a uniform expansion or contraction of the whole lattice. Hence only the deviations from the ferromagnetic background determine the dimerization pattern which is energetically favored.

We close this subsection with some technical remarks on the evaluation of the Ising couplings K_α ($\alpha = 1, 2, 3$). As can be seen from the Eqs. (4.3.35), (4.3.36), and (4.3.37), one basically has to compute three different types of dimer correlations to determine these coupling constants. These are the two-point correlations of each two dimers oriented along the i- and j-direction, respectively, as well as the cross correlations of one dimer oriented along the i- and the second directed along the j-direction. The numerical effort for the computation of these quantities can be minimized by exploiting the periodic boundaries and the fact that the square lattice Heisenberg model with uniform couplings (i. e. $\delta = 0$ in Eq. (4.3.20)) is invariant under a rotation of $\frac{\pi}{2}$ of the lattice. By making use of the definitions (4.3.32), we therefore have

$$\begin{aligned}
\left\langle D_{ij}^y(0) D_{kl}^y(\tau) \right\rangle_{\delta=0} &= \left\langle (\vec{\sigma}_{ij}\vec{\sigma}_{i,j+1})(0)(\vec{\sigma}_{kl}\vec{\sigma}_{k,l+1})(\tau) \right\rangle_{\delta=0} \\
&= \left\langle (\vec{\sigma}_{N-j,i}\vec{\sigma}_{N-j-1,i})(0)(\vec{\sigma}_{N-l,k}\vec{\sigma}_{N-l-1,k})(\tau) \right\rangle_{\delta=0} = \left\langle D_{N-j-1,i}^x(0) D_{N-l-1,k}^x(\tau) \right\rangle_{\delta=0},
\end{aligned} \quad (4.3.38)$$

and

$$\begin{aligned}
\left\langle D_{ij}^x(\tau) D_{kl}^y(0) \right\rangle_{\delta=0} &= \left\langle (\vec{\sigma}_{ij}\vec{\sigma}_{i+1,j})(\tau)(\vec{\sigma}_{kl}\vec{\sigma}_{k,l+1})(0) \right\rangle_{\delta=0} \\
&= \left\langle (\vec{\sigma}_{N-j,i}\vec{\sigma}_{N-j,i+1})(\tau)(\vec{\sigma}_{N-l,k}\vec{\sigma}_{N-l-1,k})(0) \right\rangle_{\delta=0} = \left\langle D_{N-j,i}^y(\tau) D_{N-l-1,k}^x(0) \right\rangle_{\delta=0},
\end{aligned} \quad (4.3.39)$$

where the replacement $(i, j) \to (N-j, i)$ (for (k, l) analogous) in the second step of both equalities is due to a rotation of $\frac{\pi}{2}$ of the lattice. We see that it is sufficient to compute only two different types of expectation values

$$\left\langle D_{ij}^x(0) D_{kl}^x(\tau) \right\rangle_{\delta=0}, \qquad \left\langle D_{ij}^x(0) D_{kl}^y(\tau) \right\rangle_{\delta=0}, \qquad (4.3.40)$$

to determine the coupling constants (4.3.35), (4.3.36), and (4.3.37).

4.3.4. Classical Metropolis algorithm and the optimal dimerization pattern

As has been pointed out in the previous subsection, the dimerized spin model which has the lowest free energy among all Hamiltonians described by the Eqs. (4.3.20) and (4.3.19) can be obtained by

first evaluating the coupling constants K_α ($\alpha = 1, 2, 3$) of the Ising Hamiltonian (4.3.34) for the dimerizability by means of the QMC loop algorithm. Afterwards, one has to determine the classical configuration of Ising spins $\{A_{ij}, B_{ij}\}$ with minimal 'energy' $a(T)$ in the sector of zero magnetization. In this subsection we explain how the latter problem can be solved by applying classical Monte Carlo techniques. The basic idea is to combine the standard Metropolis algorithm (see the introduction 2.1 to Chapt. 2) with some cooling procedure. For example, a similar ansatz has been used in the literature to obtain the classical ground state of Ising-like systems with long-range Coulomb interactions [LEFK94] or competing nearest and next-nearest neighbor couplings [KL04].

To give more details, we assume having computed the couplings (4.3.35), (4.3.36), and (4.3.37) of the Ising Hamiltonian, keeping the temperature T and linear system size N of the square lattice Heisenberg model fixed. We further introduce the temperature t of the Ising model, which − in contrast to temperature T of the quantum system − has no physical meaning and is treated as an auxiliary parameter in this section. To simplify the notation, we only make use of the dimensionless variable $\tilde{t} \equiv t/K_1(0, 0)$ in the following, i. e. the auxiliary temperature is measured in units of the largest coupling constant $K_1(0, 0)$ of the Ising Hamiltonian. We now arbitrarily pick a relatively large value $\tilde{t}_{\max}$ for the temperature of the Ising system. Starting with a randomly chosen configuration of Ising spins which fulfills the constraint of vanishing magnetization (4.3.19), we then apply a certain number of local Metropolis updates (to be specified below) in order to thermalize the classical system. Only the last configuration obtained from this simulation is kept, and serves as the starting configuration for a new Monte Carlo run at an inverse temperature which has been increased by a value of $\Delta(1/\tilde{t})$. Upon repeating this procedure, the system gets cooled down step by step, until at a sufficiently low temperature $\tilde{t}_{\min}$ the configuration of Ising spins remains unchanged during the simulation. This means that the algorithm has converged to a set of Ising spins $\{A_{ij}, B_{ij}\}$ (with zero magnetization) which corresponds to a minimum of the classical 'energy' (4.3.34). Note that in practice, it is necessary to repeat the whole algorithm a couple of times to assure that the resulting configuration is the global minimum of Eq. (4.3.34). However, as the cooling procedure is based on a stepwise reduction of the auxiliary temperature $\tilde{t}$, the algorithm tends to avoid local minima by construction.

Before we focus on the results for the favored dimerization pattern, we give some more details on the local Metropolis updates which are applied during the simulation. A local update consists of two steps. In the first step, we randomly choose two Ising spins among the set of variables $\{A_{ij}, B_{ij}\}$. Note that only pairs of spins with opposite directions are selected to assure that a flip of the two spins maintains the zero magnetization condition (4.3.19). In the second step, a simultaneous spinflip of the two spins is proposed and accepted according to the Metropolis probability (2.1.1) from Sect. 2.1, which becomes

$$p(\mathcal{C} \to \mathcal{C}') = \begin{cases} 1 & \text{if } \Delta a \leq 0, \\ e^{-\Delta a/\tilde{t}} & \text{else.} \end{cases} \tag{4.3.41}$$

Here $\Delta a \equiv a(\mathcal{C}') - a(\mathcal{C})$ is the 'energy' difference of the old and new configurations $\mathcal{C}, \mathcal{C}'$ of Ising spins $\{A_{ij}, B_{ij}\}$ according to Eq. (4.3.34).

We are now in the position to discuss the results of the procedure which has been proposed in this and the previous section. The integrated dynamical dimer correlations of the square lattice
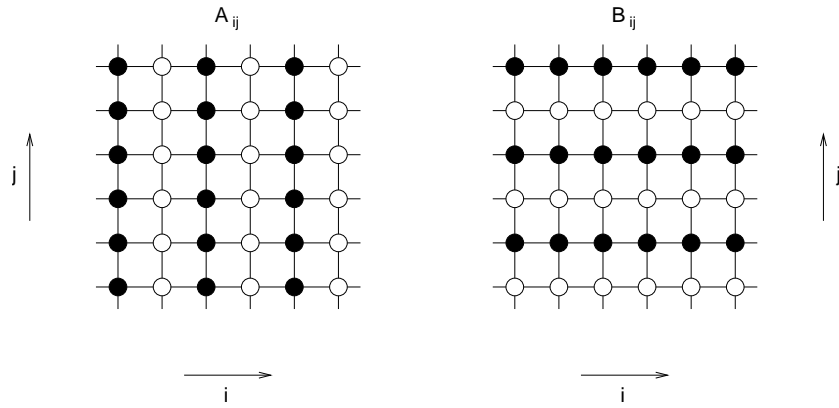
Fig. 4.12.: Visualization of the ground state of the Ising model (4.3.34) with vanishing magnetization for $N = 6$. Open and filled circles correspond to the values ± 1 of the Ising variables $\{A_{ij}\}$ (left panel) and $\{B_{ij}\}$ (right panel). The same pattern was obtained for all temperatures $T = 0.1J, 0.2J, \ldots 4.0J$ and linear system sizes $N = 6, 8, \ldots, 20$ of the quantum system.

Heisenberg model were evaluated for eight different linear system sizes $N = 6, 8, \ldots, 20$ and 40 different temperatures $T = 0.1J, 0.2J, \ldots, 4.0J$. While 2×10^4 Monte Carlo sweeps were skipped for thermalization, a number of 10^6 configurations was evaluated to reach a high accuracy of the QMC estimates. As far as the classical Monte Carlo algorithm is concerned, all simulations were started at an auxiliary temperature of $\tilde{t}_{max} = \frac{1}{2}$, while the other choices were $\Delta(1/\tilde{t}) = \frac{1}{2}$ and $\tilde{t}_{min} = \frac{1}{20}$ for small system sizes $N \leq 16$, and $\Delta(1/\tilde{t}) = \frac{1}{4}$ and $\tilde{t}_{min} = \frac{1}{30}$ in large systems with $N \geq 18$, respectively. At each auxiliary temperature $\tilde{t}$, a number of $10^4 \times N^2$ local updates was applied to reach thermal equilibrium.

For all choices of T and N for the quantum system, one finds that the Metropolis algorithm converges to a configuration of Ising spins which can always be visualized by the same crossing stripe pattern as the one depicted for $N = 6$ in Fig. 4.12. As the result is so robust against variations of temperature and the system size, we therefore conclude that the *plaquette pattern* as shown in the left panel of Fig. 4.4 from Sect. 4.1 (see also Table 4.1 from Par. 4.3.1) corresponds to the lattice modulation which minimizes the dimerizability of the Hamiltonian (4.3.20) and hence the free energy in the vicinity of $\delta = 0$. Furthermore, our result gives evidence that a plaquette-like structure is also the pattern with the lowest ground state energy, because we have included an investigation of the low temperature regime in this section. In particular, this is consistent with the analysis of ground state energies for the plaquette, stair and meander models from Sect. 4.3.1.

4.3.5. Landau theory of the 'spin-Peierls' transition in two dimensions

In the preceeding subsection we have found that for small dimerizations δ, a plaquette-like pattern of strong and weak bonds has the largest gain in the magnetic free energy among the set of models defined by the Eqs. (4.3.20) and (4.3.19). Assuming that the elastic energy loss due to the lattice distortions is given by the same expression (4.3.21) for all the dimerized models, we therefore

conclude that the plaquette model is the proper effective model to describe the magnetism of quasi two-dimensional systems with spin-phonon coupling in the adiabatic limit.

Having determined the correct dimerization pattern, it is straightforward to apply the same ideas which we have used in the context of quasi one-dimensional spin-phonon systems in Sect. 4.3.2, and to establish a Landau theory for the two-dimensional analog of the spin-Peierls transition. This transition can be characterized by the occurrence of a structural instability of the uniform lattice towards a plaquette-like distortion at a certain critical temperature T_c. The order parameter of the transition is the temperature-dependent dimerization $\delta(T)$, which takes finite values below T_c and vanishes at temperatures $T > T_c$. We emphasize that in contrast to the situation in one dimension, this structural phase transition is not accompanied by a magnetic transition, i. e. the magnetic excitation spectrum remains gapless below T_c. This is due to the fact that for $0 < \delta < \delta_c$, the plaquette model has an extended phase with coexisting dimerization and long-range Néel order in the ground state [KKK99b, SKH02] (see also the discussion in Par. 4.1). However, it is conceivable that under certain conditions the system exhibits another transition at a second critical temperature $T_c' < T_c$, where the dimerization $\delta(T)$ exceeds the critical value δ_c of the plaquette model. This means that below T_c', the system has a gapped magnetic excitation spectrum above a non-magnetic ground state which is characterized by short-range magnetic correlations. We will comment on this issue and on the exact value of δ_c in the following subsection.

Here we focus on the structural transition at T_c, following the argumentation from Par. 4.3.2. The critical temperature T_c can be determined if we compare the magnetic free energy gain of $-\frac{1}{2} a_{\mathrm{pl}}(T)\delta^2$ for the plaquette pattern to the elastic energy loss per lattice site, which is given by $K\delta^2$ according to Eq. (4.3.21). Such a comparison yields the condition

$$-a_{\mathrm{pl}}(T_c) = 2K \tag{4.3.42}$$

for T_c, compare the analogous expression (4.3.27) from Par. 4.3.2 in the one-dimensional case. We therefore have to analyze the temperature dependence of the dimerizability a_{pl} given by Eq. (4.3.34) with $A_{ij} = (-1)^i$ and $B_{ij} = (-1)^j$, because according to Table 4.1 from Sect. 4.3.1 these choices correspond to the plaquette pattern. For this set of parameters $\{A_{ij}, B_{ij}\}$ the dimerizability takes an especially simple form. Indeed, by exploiting the identities (4.3.38), (4.3.39) and the translational invariance of the uniform Heisenberg model, one finds

$$a_{\mathrm{pl}}(T) = 2 \sum_{i,j,k,l=1}^{N} K_1(k-i, l-j)(-1)^{i+k}$$
$$= 2N^2 \sum_{x_1,x_2=1}^{N} (-1)^{x_1} K_1(x_1, x_2), \tag{4.3.43}$$

where we have introduced distance coordinates $(x_1, x_2) \equiv (k-i, l-j)$ in the second step (see Eq. (4.3.35) for the definition of K_1).

The temperature dependence of the dimerizability (4.3.43) is given in Fig. 4.13, which shows the QMC data for $-a_{\mathrm{pl}}(T)$ and eight different linear system sizes $N = 10, 12, \ldots, 24$. While for each temperature 2×10^6 configurations were taken for the computation of dimer correlations, a number of 10^5 loop updates was chosen for the thermalization of the algorithm. The curves exhibit
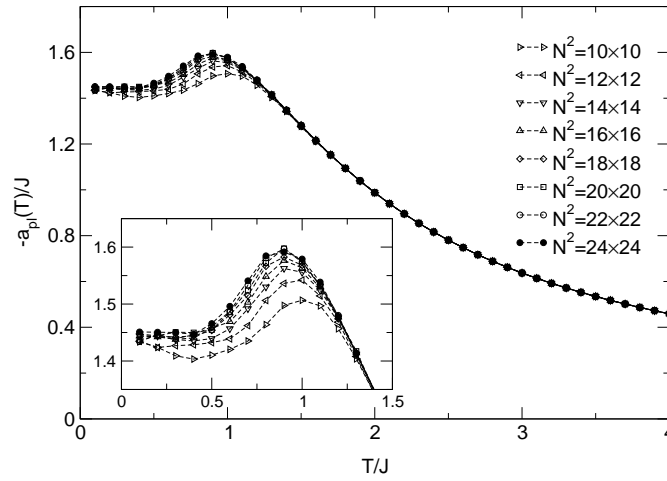
Fig. 4.13.: QMC data for the negative dimerizability of the plaquette model vs. temperature for different linear system sizes $N = 10, 12, \ldots, 24$. The inset shows a magnification of the low temperature regime, where finite-size effects are emphasized. For clarity the datapoints are plotted without errorbars. To gain some insight about the size of the numerical errors, the reader is referred to Fig. 4.14, where the finite-size effect for $T = 0.1J$ and $T = 0.9J$ is investigated. In addition in Fig. 4.15, the curve for the largest system with 24×24 sites is replotted including errrobars.

a fundamentally different behavior as compared to the one-dimensional dimerizability, see Fig. 4.11 from Par. 4.3.2. In one dimension, $-a_{\mathrm{pl}}(T)$ grows monotonously with decreasing temperature, which leads to the characteristic divergence as $T \to 0$. In contrast to this, the corresponding quantity (4.3.43) has a pronounced maximum at $T_{\max} \approx 0.9J$ and stays finite as $T \to 0$.

Evidently both features are generic for the thermodynamic limit, because for the largest values of N the effect of the finite system size (see the inset of Fig. 4.13) is of the same order as the symbol sizes. This statement also holds in the vicinity of $T_{\max}$, where finite-size effects become emphasized. This is demonstrated in Fig. 4.14, where the dependence of the dimerizability on the inverse system size for $T = 0.1J$ and $T = 0.9J$ is shown exemplarily. Keeping the temperature fixed, the numerical estimates for $-a_{\mathrm{pl}}(T)$ scale linearly with $\frac{1}{N^2}$.

Heuristically, the fact that $a_{\mathrm{pl}}(T)$ does not diverge can be understood to reflect a competition of the square lattice Heisenberg model to establish long-range antiferromagnetic or dimer order in the ground state. As has been pointed out in Chapt. 3, the one-dimensional XXX model shows a coexistence of quasi long-range order of both types in the ground state. For this reason the two correlation functions $G_{\parallel/d}$ as defined in Sect. 3.1 decay algebraically at $T = 0$, which is accompanied by a divergence of the corresponding correlation lengths $\xi^{1d}_{\parallel/d}$ as $T \to 0$ (see also the discussion on the behavior of the spin correlation length of the one-dimensional bond coupling model in Par. 4.2.1). According to Eq. (4.3.30), in one dimension $a(T)$ is given by the dynamical structure factor of the dimer correlation function at zero frequency and momentum π (evaluated for the uniform Heisenberg chain), and hence closely related to the dimer correlation length. Thus in a sense the temperature dependence of the dimerizability reflects the divergence of ξ^{1d}_{d}. In two
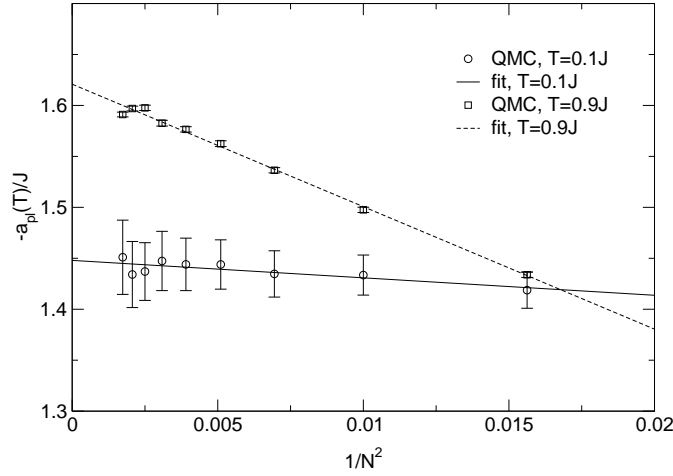
Fig. 4.14.: QMC estimates for the negative dimerizability of the plaquette model vs. $\frac{1}{N^2}$ for $T = 0.1J$ (circles) and $T = 0.9J$ (squares). The straight lines are the results of a linear fit in $\frac{1}{N^2}$.

dimensions, the situation is somewhat different because the square lattice Heisenberg model shows long-range Néel order in the ground state (for a more detailed discussion see Sect. 4.2.2). For this reason we expect the dimer correlation length ξ_d and hence $a_{pl}(T)$ as given by Eq. (4.3.43) to stay finite even at $T = 0$.

In the following we discuss the implications of the condition (4.3.42) for the existence of the structural phase transition described above. In analogy to the approach from Sect. 4.3.2, one can determine T_c by drawing a horizontal line at $-a_{pl} = 2K$ in Fig. 4.13. The critical temperature then corresponds to the first coordinate of the intersection point of the two curves. Applying this scheme, we first observe that for large values $2K \gtrsim 1.6J$ of the elastic constant there is no such intersection point, because the dimerizability stays finite with $-a_{pl}(T) \leq -a_{pl}(T_{max}) \approx 1.6J$ for all $T > 0$. Hence in contrast to the situation in one-dimensional spin-Peierls systems, only for small values of K the free energy gain in the magnetic sector overcompensates the loss in the elastic energy due to the lattice distortions. For $2K \lesssim 1.6J$ the two curves intersect, i. e. there is a structural transition. Interestingly, in the range $1.45J \lesssim 2K \lesssim 1.6J$ there are two solutions of the condition (4.3.42). This might indicate the occurrence of a reentrance of phases (uniform $\rightarrow$ distorted $\rightarrow$ uniform) upon decreasing the temperature. However, this interpretation has to be treated with great care since our analysis does not take into account higher order terms in the Landau expansion (4.3.25) of the free energy density. For even smaller values of $2K \lesssim 1.45J$, there is only one intersection point and hence no such reentrance feature.

For the sake of completeness we also compare the behavior of the dimerizability (4.3.43) for the plaquette lattice to the corresponding curves for a stair- and meander-like lattice distortion. Explicit expressions for $a_{st/me}(T)$ in the latter two cases can be obtained by inserting $A_{ij} = B_{ij} = (-1)^{i+j}$ for the stair and $A_{ij} = (-1)^{i+j}$, $B_{ij} = (-1)^j$ for the meander configuration into Eq. (4.3.34), see
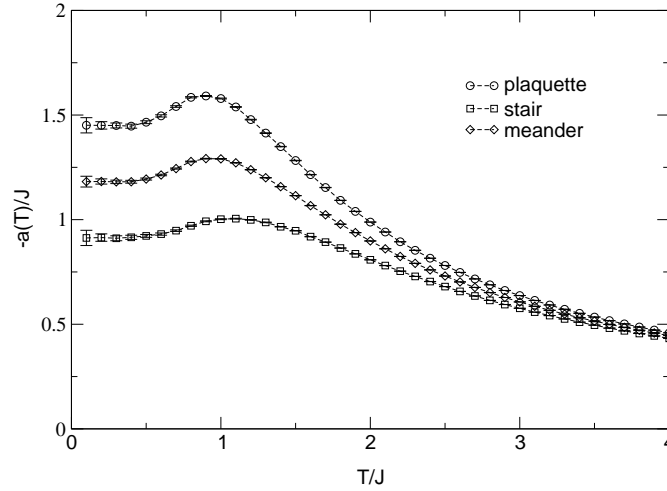
Fig. 4.15.: Comparison of the dimerizability for the plaquette (circles), stair (squares) and meander model (diamonds). The linear system size is $N = 24$.

Table 4.1 from Par. 4.3.1. They read

$$a_{\text{st}}(T) = 2N^2 \sum_{x_1, x_2} (-1)^{x_1 + x_2} K_1(x_1, x_2) \tag{4.3.44}$$

for the stair configuration, while the result for a meander-like pattern is

$$a_{\text{me}}(T) = N^2 \sum_{x_1, x_2} [(-1)^{x_1 + x_2} + (-1)^{x_1}] K_1(x_1, x_2). \tag{4.3.45}$$

We see that as for the plaquette pattern, these expressions only depend on the quantities $K_1(x_1, x_2)$ as defined by Eq. (4.3.35). No additional computational effort is required to determine these numbers. The three curves for a lattice with 24×24 sites are depicted in Fig. 4.15. The findings are completely consistent with our analysis of ground state energies in Sect. 4.3.1. As can be seen from the figure, the gain in the magnetic free energy is largest for the plaquette model, followed by the meander and stair patterns, respectively. As they can be expressed by the same dynamical dimer correlations, all three curves show a local maximum at intermediate temperatures. The position of the maximum, however, depends on the choice of the distortion pattern to a slight degree.

We have not commented on the order of the structural phase transition at T_c so far. To answer the question whether the transition is continuous, we need to analyze the sign of the coefficient

$$b_{\text{pl}}(T) \equiv \left. \frac{\partial^4}{\partial \delta^4} f(T, \delta) \right|_{\delta = 0} \tag{4.3.46}$$

of the fourth order term in the Landau expansion (4.3.25) of the free energy density. A direct evaluation of $b_{\text{pl}}(T)$ would go beyond the scope of this work because it requires the computation of certain dynamical eight-point correlation functions. However, given numerical values for the second order coefficient $a_{\text{pl}}(T)$, it is possible to gain some insight into the behavior of $b_{\text{pl}}(T)$. The argument is based on the observation that for sufficiently small values of δ, one has the relation

$$b_{\text{pl}}(T) \approx \frac{24}{\delta^4} [f(T, \delta) - f_0(T) - \frac{1}{2} a_{\text{pl}}(T) \delta^2], \tag{4.3.47}$$
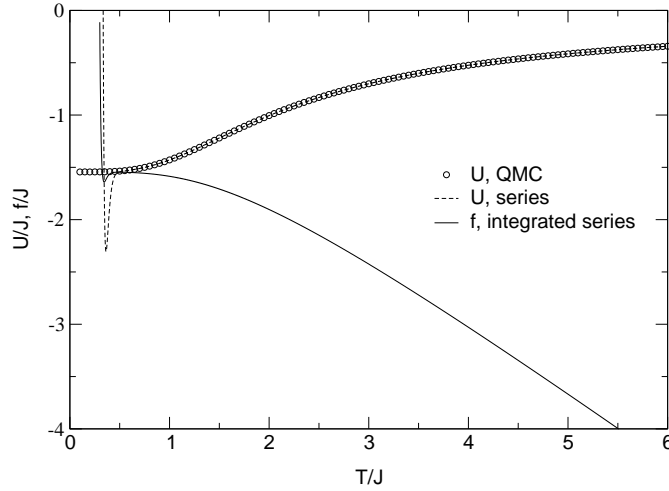
Fig. 4.16.: Illustration of the procedure to determine the free energy of the plaquette model as described in the text. The circles represent the QMC data for the internal energy evaluated in a system with $\delta = 0.5$ and 16×16 lattice sites. The numerical errors are smaller than the symbols. The dashed line is the result obtained by fitting a polynomial (4.3.51) to the QMC data, while the solid curve for the free energy is obtained after integrating this series and subtracting $T \ln 2$ according to Eq. (4.3.50).

where terms $\mathcal{O}(\delta^6)$ have been neglected. From this identity we see that it is possible to analyze $b_{\text{pl}}(T)$ if we calculate the free energies of the uniform Heisenberg model and the plaquette model for one small value of δ in addition to the dimerizability.

At this point we encounter the problem that it is not possible to compute the free energy of a quantum system by means of the QMC method directly. As has been explained in Sect. 4.3.1, it is straightforward though to evaluate the internal energy U for the plaquette model. These QMC estimates can be used to extract numerical estimates for the free energy, although we have to point out that the approach described in the following does not apply to the low temperature regime. We start with the well known relation

$$d\left(\frac{f}{T}\right) = -\frac{U}{T^2}\, dT \tag{4.3.48}$$

from statistical physics. By integrating this equation over the interval $[T, \infty)$, we find

$$\frac{f}{T} = \frac{f}{T}\bigg|_{T \to \infty} + \int_T^\infty \frac{U(t)}{t^2}\, dt. \tag{4.3.49}$$

The constant $\frac{f}{T}\big|_{T \to \infty}$ is just the negative entropy of an ideal paramagnet and hence given by $-\ln 2$. Therefore Eq. (4.3.49) yields

$$f(T) = -T \ln 2 + T \int_T^\infty \frac{U(t)}{t^2}\, dt, \tag{4.3.50}$$

which is the demanded relation between the internal and the free energy of the system.

In practice, numerical estimates for $U(t)$ were computed using the continuous time loop algorithm from Sects. 2.2.4 and 2.2.5, choosing two different values $\delta = 0.25, 0.5$ for the dimerization and

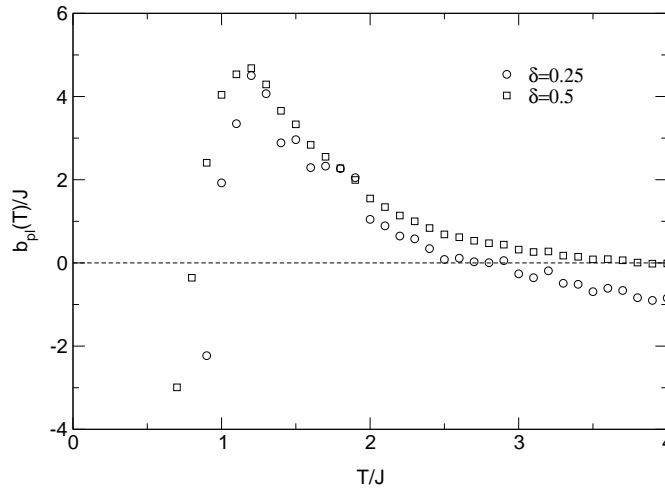Fig. 4.17.: Numerical estimates for the fourth order coefficient (4.3.46) of the Landau expansion (4.3.25) for the plaquette model. The data have been calculated via Eq. (4.3.47) with two different values $\delta = 0.25$ (circles) and $\delta = 0.5$ (squares) of the dimerization.

$N = 16$ for the linear system size. The numbers of loop updates were 2×10^4 for thermalization and 10^6 for the evaluation of expectation values. After fitting a phenomenological high temperature series up to tenth order in $\frac{1}{T}$,

$$U(T) = \sum_{k=1}^{10} \frac{a_k}{T^k}, \tag{4.3.51}$$

to the QMC data with $T/J \in [0.5, 6]$, the integration in Eq. (4.3.50) becomes trivial. For $\delta = 0.5$, the quality of the fit as well as the result for $f(T, \delta)$ after application of the formula (4.3.50) is illustrated in Fig. 4.16. At sufficiently high temperatures $T \gtrsim J$, the procedure yields convincing results. Exactly the same approach is also applied to derive numerical estimates for the free energy $f_0(T)$ of the uniform Heisenberg model with $N = 16$. Here the coefficients a_k obtained from the fit compare well to the corresponding values from the literature which are valid in the thermodynamic limit [Bar91]. In our analysis we nevertheless make use of the fitting parameters, because the numbers from the literature do not take into account finite-size effects.

Given the numerical data for $f_0(T)$, $f(T, \delta)$ and the dimerizability $a_{pl}(T)$ (with $N = 16$), we can now apply the identity (4.3.47) for $\delta = 0.25, 0.5$. The results for $b_{pl}(T)$ are shown in Fig. 4.17. In the temperature range $T \gtrsim J$, where the numbers for the free energies can be trusted, the two curves coincide qualitatively, although there is a systematic shift between the two sets of datapoints. This shift is probably due to the neglect of higher order terms in the expression (4.3.47). The main conclusion we can draw from the figure is that for $T \gtrsim J$, the coefficient $b_{pl}(T)$ takes positive values which means that the structural phase transition at T_c is continuous. However, it is not possible to give reliable errors for the numerical estimates of $b_{pl}(T)$. For this reason one cannot judge whether the occurrence of negative values for $b_{pl}(T)$ at high temperatures (which are deduced from the internal energy data with $\delta = 0.25$) is an artefact of the method described in this subsection. Furthermore, it is not possible to make any statements about the sign of $b_{pl}(T)$ in the

low temperature regime.

4.3.6. Critical dimerization of the plaquette model

In the previous subsection we have pointed out that – in contrast to the situation in one-dimensional spin-Peierls systems – the structural transition at T_c which occurs for $2K \lesssim 1.6J$ does not coincide with a magnetic transition, because for $\delta < \delta_c$ the plaquette model shows long-range antiferromagnetic order in the ground state. Furthermore it has been mentioned that for sufficiently small values of the elastic constant, one cannot exclude the existence of a second magnetic phase transition at $T'_c < T_c$, which would be characterized by the fact that $\delta(T)$ below T'_c exceeds the critical value δ_c of the plaquette lattice.

In principle, the effective dimerization $\delta(T)$ at any temperature $T \leq T_c$ can be derived by minimizing the free energy of the full model which consists of the magnetic Hamiltonian (4.3.20) (with $A_{ij} = (-1)^i$, $B_{ij} = (-1)^j$ for a plaquette-like distortion) and the lattice contribution (4.3.21). Apart from the computation of the dimerizability (4.3.43) this would require to determine the fourth order coefficient (4.3.46) of the Landau expansion (4.3.25) for the plaquette model. Although the estimates shown in Fig. 4.17 provide the possibility to draw conclusions about the sign of $b_{pl}(T)$, they are not reliable enough to perform a quantitative analysis of $\delta(T)$. We are therefore not capable of studying the dependence of T'_c on K. From our analysis of the two-dimensional bond coupling model at $T = 0$ in Sect. 4.2.2, we can only conclude that the values for K have to be very small to encounter a breakdown of the long-range Néel order in the ground state.

It is nevertheless important to have an accurate numerical estimate for δ_c. As has been mentioned in the introduction 4.1 to this chapter, the values for the critical dimerization which have been published in the literature are contradictory. While linear spin wave theory predicts $\delta_c \approx 0.798$ [SKH02], the result $\delta_c \approx 0.30$ from Ref. [KKK99b] based on series expansion techniques seems to be more realistic. In the remainder of this section we derive an independent numerical estimate for δ_c by means of the QMC method. The approach is based on a computation of the staggered magnetization $M_s(\delta)$ in the ground state, which takes finite values for $\delta < \delta_c$ and vanishes for all $\delta \geq \delta_c$.

To determine numerical estimates for $M_s(\delta)$, we can make use of the same ideas which have been applied to the two-dimensional bond coupling model in Par. 4.2.2. For each value of δ, one has to compute the static structure factor (4.2.15) of the two-point spin correlation function (4.2.10) at very low temperatures and for various system sizes. Then one can extract the value of $M_s(\delta)$ in the ground state by extrapolating to the thermodynamic limit according to Eq. (4.2.16). As usual, the spin correlations for four different system sizes $N = 20, 24, 28, 32$ were calculated by means of the continuous time loop algorithm as described in Sects. 2.2.4 and 2.2.5. While the first 2×10^4 Monte Carlo sweeps were skipped to reach thermal equilibrium, 2×10^5 worldline configurations were evaluated. A temperature of $T = 0.04J$ was found to be sufficiently low to avoid systematic errors due to the simulation of finite temperatures.

The values for $M_s(\delta)$ which are obtained in this fashion are plotted in Fig. 4.18. They show the expected behavior, i. e. the staggered magnetization decreases with δ and drops to zero at some critical value in the vicinity of $\delta = 0.29$. Note that the estimate of $M_s = 0.304(1)$ obtained for the
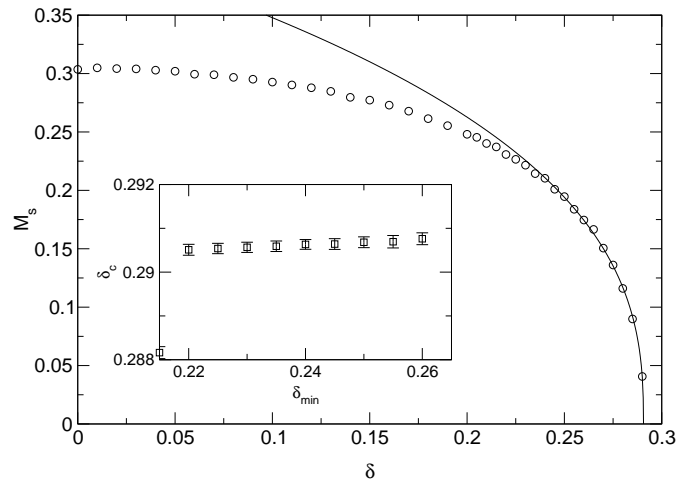
Fig. 4.18.: QMC estimates for the staggered magnetization $M_s(\delta)$ of the plaquette model (circles). The numerical errors are smaller than the size of the circles. The solid line is obtained by fitting the ansatz (4.3.52) to the data with $\delta \in [\delta_{min}, 0.29]$ (here $\delta_{min} = 0.24$ holds). The inset shows the dependence of the fitting parameter δ_c on the left boundary δ_{min} of the fitting interval.

uniform Heisenberg model is in sufficient agreement with the corresponding value of $M_s = 0.3070(3)$ from Ref. [San97]. An accurate number for the critical dimerization can be derived by fitting a phenomenological power law function

$$f(\delta) = c(\delta_c - \delta)^\alpha \tag{4.3.52}$$

with three free parameters c, α, and δ_c to the numerical data with $\delta \in [\delta_{min}, 0.29]$. An example for the quality of the fits with $\delta_{min} = 0.24$ is also given in the figure. As the value for the parameter δ_c depends on the left boundary δ_{min} of the fitting interval, the fitting procedure is applied repeatedly for various choices of δ_{min}. The results for δ_c in dependence of δ_{min} are given in the inset of Fig. 4.18. From this plot, we deduce a value of

$$\delta_c = 0.291(3) \tag{4.3.53}$$

for the critical dimerization of the plaquette model. Note that the numerical errorbars given in the inset of Fig. 4.18 only represent the least-square errors from the fits. In contrast to this, the value of $\Delta\delta_c = 0.003$ in Eq. (4.3.53) is a conservative estimate of the true error which takes into account additional systematic effects like possible deviations from the assumption (4.3.52) for the fitfunction, or the extraction of $M_s(\delta)$ from finite-temperature data for the spin correlations. In conclusion we find that the result (4.3.53) is close to the number given in Ref. [KKK99a]. The estimate obtained from linear spin wave theory, on the other hand, drastically overestimates the exact value of δ_c.

4.4. Spin-lattice coupling and phonon dynamics in quasi two-dimensional systems

In Sect. 4.3, we found that a plaquette-like arrangement of strong and weak bonds on the square lattice has the largest gain in the magnetic free energy among the models defined by the Hamiltonian (4.3.20) with the constraint (4.3.19). Assuming that the elastic energy loss due to the lattice distortions is given by the same contribution (4.3.21) for the whole class of models (4.3.20), we also came to the conclusion that the plaquette model is the proper effective model to describe the magnetism of spin layers with bond coupling in the adiabatic limit. Having determined the dimerization pattern, we were able to establish a Landau theory of the two-dimensional counterpart of the spin-Peierls transition. In contrast to the situation in quasi one-dimensional systems though, this structural phase transition towards a plaquette-like distortion does not affect the magnetic properties of the system. From the experimentalist's point of view, the occurrence of lattice modulations can be studied most conveniently by investigating the temperature dependence of the phonon dispersion curves, which can be measured in neutron or Raman scattering experiments. However, the approach from the preceeding section is not useful to study the influence of the spin-phonon coupling on the lattice dynamics for real materials, where the strongly simplified expression (4.3.21) is not valid.

The aim of this section is to gain a deeper understanding of this issue [ALKW05]. To be more precise, we study three-dimensional cubic systems with a monoatomic unit cell, whose lattice contribution to the total Hamiltonian is given by the general expression

$$H_{\text{dis}} = \sum_{\vec{r}} \frac{\vec{P}_{\vec{r}}^2}{2m} + V(\{\vec{R}_{\vec{r}}\}). \tag{4.4.54}$$

Here $\vec{R}_{\vec{r}}$, $\vec{P}_{\vec{r}}$ are the position and momentum vectors of the magnetic ions with mass m at the lattice sites. In the harmonic approximation, the interaction part $V(\{\vec{R}_{\vec{r}}\})$ of H_{dis} can be written as

$$V(\{\vec{R}_{\vec{r}}\}) = \frac{m}{2} \sum_{\vec{r},\vec{x}} \sum_{\alpha,\beta=x,y,z} G_0^{\alpha\beta}(\vec{x}) u_{\vec{r}}^{\alpha} u_{\vec{r}+\vec{x}}^{\beta}, \tag{4.4.55}$$

where $\vec{u}_{\vec{r}} \equiv \vec{R}_{\vec{r}} - \vec{r}$ is the displacement vector of the ion at lattice site $\vec{r}$. The expression (4.4.55) defines the *dynamical matrix* $G_0(\vec{x}) \equiv \left(G_0^{\alpha\beta}(\vec{x})\right)$ (with $\alpha,\beta = x,y,z$) of the system. In particular, the phonon dispersion relations can be determined from this matrix, because the eigenvalues of its Fourier transform $\hat{G}_0(\vec{q})$ are the squares of the phonon frequencies $\omega_0(\vec{q})$. We emphasize that by introducing G_0, the loss in the elastic energy due to the lattice distortions depends on the type of the lattice modulation, which is a striking difference to the assumption (4.3.21) from the previous section.

In the presence of spin-phonon coupling, one expects that the magnetic degrees of freedom influence the phonon dynamics, i. e. the bare dynamical matrix $G_0(\vec{x})$ has to be modified due to the spin-lattice interaction. In this section, we determine and analyze these corrections by generalizing the ideas from Ref. [CF79] to systems consisting of independent spin layers which are coupled to the three-dimensional phonon system given by Eq. (4.4.54). The magnetic Hamiltonian for the

quasi two-dimensional subsystems reads

$$H = \frac{J}{2} \sum_{i,j=1}^{N} \left[\left(1 + \lambda\{u_{i+1,j}^x - u_{ij}^x\}\right) \vec{\sigma}_{ij}\vec{\sigma}_{i+1,j} + \left(1 + \lambda\{u_{i,j+1}^y - u_{ij}^y\}\right) \vec{\sigma}_{ij}\vec{\sigma}_{i,j+1} \right], \qquad (4.4.56)$$

which is a two-dimensional generalization (with $\lambda = \sqrt{2}g$) of the spin-lattice interaction part of the difference coupling model (4.1.6) from Sect. 4.1. For systems with a monoatomic unit cell, the Hamiltonian (4.4.56) is the simplest non-trivial choice which allows to study the influence of the spin-lattice interaction on the phonon dispersion relations. Following Cross and Fisher [CF79], we apply an adiabatic decoupling to the full lattice problem, dealing with the phonons as the slow and the quantum spins as the fast degrees of freedom. In such a scenario we can replace the displacement operators $\vec{u}_{\vec{r}}$ by their expectation values. Equivalently, we can treat the quantities $u_{ij}^{x/y}$ and $\vec{u}_{\vec{r}}$ in the Eqs. (4.4.56), (4.4.55) as classical variables. This will be assumed for the remainder of this section.

At this point we have to emphasize that the components of the classical vectors $\vec{u}_{\vec{r}}$ take continuous values. Hence in contrast to the analysis of statically dimerized models in the previous section, where only two possible values $\pm\delta$ for the lattice distortions were taken into consideration, the approach from this section enables us to study arbitrary lattice modulations. However, by introducing the spin Hamiltonian (4.4.56) we suggest a mechanism for the spin-phonon interaction which differs fundamentally from the bond coupling mechanism assumed in Sects. 4.2 and 4.3.

In the following subsection, we first determine the contribution of the magnetic Hamiltonian (4.4.56) to the dynamical matrix in leading order of the spin-phonon coupling. In the sequel in Sect. 4.4.2, we analyze the momentum and temperature dependence of this additional term. As in the one-dimensional case, the spin-lattice interaction is found to induce a softening of phonon modes. Determining those phonon modes which are most affected by the spin-phonon coupling provides a tool to specify which types of lattice modulations are energetically favored. In Par. 4.4.3 finally, we specify the lattice potential V in Eq. (4.4.54) and calculate the full dynamical matrix for this simple model. Having determined the dynamical matrix, it is possible to investigate the influence of the spin-phonon coupling on the phonon dynamics, and to discuss under which conditions the system is driven towards a structural instability.

4.4.1. Renormalization of the dynamical matrix

In this subsection we derive an expression which specifies the influence of the spin-phonon coupling as given by Eq. (4.4.56) on the dynamical matrix $G_0(\vec{x})$ defined by the interaction part (4.4.55) of the lattice Hamiltonian (4.4.54). As the system consists of non-interacting magnetic layers which are coupled to the three-dimensional phonon system, one expects that $G_0(\vec{x})$ is only affected for distance vectors $\vec{x} = (x_1, x_2, 0)$ lying in the planes of interacting spins. In addition to this, we observe that the spin Hamiltonian (4.4.56) involves no lattice distortions u_{ij}^z perpendicular to the magnetic layers. Thus it is sufficient to study the modifications of the 2×2 submatrix of $G_0(\vec{x}) = \left(G_0^{\alpha\beta}(\vec{x})\right)$ with $\alpha, \beta = x, y$ in Eq. (4.4.55) for these choices of $\vec{x}$, and the analysis of the impact of the spin-phonon coupling on the phonon dynamics is reduced to an effective two-dimensional problem.

The key idea behind our approach is to follow the argumentation from Sects. 4.3.2 and 4.3.3, and to perform a Landau expansion

$$F(T, \lambda) = F_0(T) + \left.\frac{\partial F}{\partial \lambda}\right|_{\lambda=0} \lambda + \frac{1}{2}\left.\frac{\partial^2 F}{\partial \lambda^2}\right|_{\lambda=0} \lambda^2 + \mathcal{O}(\lambda^3) \tag{4.4.57}$$

of the free energy for the magnetic Hamiltonian (4.4.56), where $F_0(T)$ is the free energy of the square lattice Heisenberg model according to our usual notation. Exploiting the lattice symmetries of the uniform Heisenberg model, the coefficient of the first order term in Eq. (4.4.57) becomes

$$\left.\frac{\partial F}{\partial \lambda}\right|_{\lambda=0} = \frac{J}{2}\langle\vec{\sigma}_{00}\vec{\sigma}_{10}\rangle_{\lambda=0} \sum_{i,j=1}^{N} \left[\{u_{i+1,j}^x - u_{ij}^x\} + \{u_{i,j+1}^y - u_{ij}^y\}\right] = 0, \tag{4.4.58}$$

because the expression between the square brackets vanishes if we assume periodic boundary conditions. We see that the leading contribution of the spin-phonon coupling is given by the second order in the expansion (4.4.57).

In the following we determine the second order coefficient $\left.\frac{\partial^2 F}{\partial \lambda^2}\right|_{\lambda=0}$. To evaluate this quantity, we first note that the model (4.4.56) is formally equivalent to the statically dimerized Hamiltonian (4.3.20) from Sect. 4.3 if we replace

$$\delta \to \lambda, \tag{4.4.59}$$

$$A_{ij} \to \{u_{i+1,j}^x - u_{ij}^x\}, \tag{4.4.60}$$

$$B_{ij} \to \{u_{i,j+1}^y - u_{ij}^y\}. \tag{4.4.61}$$

Hence we can immediately read the demanded result from the expression (4.3.34) for the two-dimensional dimerizability (see Par. 4.3.3), which gives

$$\begin{aligned}
\left.\frac{\partial^2 F}{\partial \lambda^2}\right|_{\lambda=0} = N^2 \sum_{i,j,k,l=1}^{N} \Big[&K_1(k-i, l-j)\{u_{i+1,j}^x - u_{ij}^x\}\{u_{k+1,l}^x - u_{kl}^x\} \\
+ &K_2(k-i, l-j)\{u_{i,j+1}^y - u_{ij}^y\}\{u_{k,l+1}^y - u_{kl}^y\} \\
+ &K_3(k-i, l-j)\{u_{i+1,j}^x - u_{ij}^x\}\{u_{k,l+1}^y - u_{kl}^y\}\Big],
\end{aligned} \tag{4.4.62}$$

where the factor of N^2 in the first line takes into account that the result (4.3.34) stems from an expansion of the free energy density $f(T, \delta)$, while here the total free energy $F(T, \lambda)$ is considered. The numbers K_α ($\alpha = 1, 2, 3$) in the relation (4.4.62) are given by the couplings (4.3.35), (4.3.36), and (4.3.37) from Par. 4.3.3. In the sequel we rewrite the result (4.4.62) by introducing distance coordinates $(x_1, x_2) \equiv (k-i, l-j)$ and again exploiting the periodic boundary conditions, i. e.

$$\begin{aligned}
\left.\frac{\partial^2 F}{\partial \lambda^2}\right|_{\lambda=0} = N^2 \sum_{i,j,x_1,x_2=1}^{N} \Big\{ &u_{ij}^x u_{i+x_1,j+x_2}^x [2K_1(x_1, x_2) - K_1(x_1-1, x_2) - K_1(x_1+1, x_2)] \\
+ &u_{ij}^y u_{i+x_1,j+x_2}^y [2K_2(x_1, x_2) - K_2(x_1, x_2-1) - K_2(x_1, x_2+1)] \\
+ &u_{ij}^x u_{i+x_1,j+x_2}^y [K_3(x_1, x_2) + K_3(x_1+1, x_2-1) \\
&\qquad - K_3(x_1+1, x_2) - K_3(x_1, x_2-1)]\Big\}.
\end{aligned} \tag{4.4.63}$$

The important consequence is that the second order contribution in the expansion (4.4.57) takes the form

$$\frac{1}{2}\frac{\partial^2 F}{\partial\lambda^2}\bigg|_{\lambda=0}\lambda^2 = \frac{m}{2}\sum_{\vec{r},\vec{x}}\sum_{\alpha,\beta=x,y}g^{\alpha\beta}(\vec{x})u_{\vec{r}}^{\alpha}u_{\vec{r}+\vec{x}}^{\beta}. \tag{4.4.64}$$

Here we have introduced the 2×2 matrix $g(\vec{x}) \equiv \left(g^{\alpha\beta}(\vec{x})\right)$ (with $\alpha,\beta = x,y$), whose entries are given by

$$g^{xx}(\vec{x}) = \frac{\lambda^2 N^2}{m}[2K_1(x_1,x_2) - K_1(x_1-1,x_2) - K_1(x_1+1,x_2)], \tag{4.4.65}$$

$$g^{yy}(\vec{x}) = \frac{\lambda^2 N^2}{m}[2K_2(x_1,x_2) - K_2(x_1,x_2-1) - K_2(x_1,x_2+1)], \tag{4.4.66}$$

$$g^{xy}(\vec{x}) = g^{yx}(-\vec{x})$$
$$= \frac{\lambda^2 N^2}{2m}[K_3(x_1,x_2) + K_3(x_1+1,x_2-1) - K_3(x_1+1,x_2) - K_3(x_1,x_2-1)]. \tag{4.4.67}$$

Note that the non-diagonal entries $g^{xy}(\vec{x})$ have the property

$$g^{xy}(\vec{x}) = g^{xy}(-\vec{x}), \tag{4.4.68}$$

which is a consequence of the symmetries of $K_3(\vec{x})$, i. e.

$$K_3(x_1,x_2) = K_3(-x_1+1,x_2) = K_3(x_1,-x_2-1) = K_3(-x_1+1,-x_2-1)$$
$$= K_3(-x_2,x_1-1) = K_3(x_2+1,x_1-1) = K_3(x_2+1,-x_1) = K_3(-x_2,-x_1). \tag{4.4.69}$$

Apparently, the result (4.4.64) has the same structure as the expression (4.4.55). Therefore at finite temperatures and in the leading order of the spin-phonon coupling, the influence of the magnetic degrees of freedom on the lattice dynamics can be expressed if we replace

$$G_0(\vec{x}) \to G(\vec{x}) \equiv G_0(\vec{x}) + g(\vec{x}). \tag{4.4.70}$$

To analyze the influence of the spin-lattice interaction on the phonon dispersion relations, one has to determine the eigenvalues of the corresponding matrix

$$\hat{G}(\vec{q}) = \hat{G}_0(\vec{q}) + \hat{g}(\vec{q}), \tag{4.4.71}$$

where the Fourier transform $\hat{A}(\vec{q})$ of an arbitrary quantity $A(\vec{x})$ is defined by

$$\hat{A}(\vec{q}) \equiv \sum_{\vec{x}} e^{-i\vec{q}\vec{x}} A(\vec{x}). \tag{4.4.72}$$

With this definition, we can immediately determine the entries of $\hat{g}(\vec{q})$ from the real space quantities (4.4.65), (4.4.66), and (4.4.67). The result is

$$\hat{g}^{xx}(\vec{q}) = \frac{2\lambda^2}{m}(1-\cos q_1)\,\tilde{K}_1(\vec{q}), \tag{4.4.73}$$

$$\hat{g}^{yy}(\vec{q}) = \frac{2\lambda^2}{m}(1-\cos q_2)\,\tilde{K}_2(\vec{q}), \tag{4.4.74}$$

$$\hat{g}^{xy}(\vec{q}) = \hat{g}^{yx}(\vec{q}) = \frac{\lambda^2}{4m}\left[(1-e^{iq_1})(1-e^{-iq_2})\,\tilde{K}_3(\vec{q}) + \text{c. c.}\right], \tag{4.4.75}$$

where we have introduced the abbreviation ($\alpha = 1, 2, 3$)

$$\tilde{K}_\alpha(\vec{q}) \equiv N^2 \, \hat{K}_\alpha(\vec{q}) \tag{4.4.76}$$

for the Fourier transformed and rescaled coupling constants (4.3.35), (4.3.36), and (4.3.37) from Par. 4.3.3. Note that the identity (4.4.68) implies that the off-diagonal entries (4.4.75) of $\hat{g}(\vec{q})$ take real values.

Before we investigate the behavior of $\hat{g}(\vec{q})$ in the following subsection, it is instructive to comment on the relation between Eq. (4.4.71) and the corresponding expression (4.1.3) for quasi one-dimensional spin-Peierls systems. According to Refs. [CF79, Pyt74] and to the discussion from Sects. 4.1 and 4.3.2, in one dimension the renormalization of phonon frequencies due to the spin-phonon coupling is given by the polarizability $\Pi(q, \Omega)$ in Eq. (4.1.3). In particular, Π can be expressed via the dynamical structure factor of the two-point dimer correlation function. The result (4.4.71) of this subsection for the two-dimensional problem is the completely analogous expression. On the one hand, we have already mentioned that the eigenvalues of the dynamical matrix $\hat{G}(\vec{q})$ are the squares of the phonon frequencies $\omega(\vec{q})$. On the other hand and according to the relations (4.4.73), (4.4.74), and (4.4.75), we have expressed the entries of the additional contribution $\hat{g}(\vec{q})$ to the bare dynamical matrix $\hat{G}_0(\vec{q})$ by the Fourier transforms of the two-dimensional integrated dynamical dimer correlations. Thus, the matrix $\hat{g}(\vec{q})$ plays the role of the polarizability in Eq. (4.1.3).

4.4.2. Analysis of the spin-phonon contribution

In this subsection we try to gain some insight into the influence of the spin-phonon coupling by analyzing the contribution $\hat{g}(\vec{q})$ to the full dynamical matrix (4.4.71). As has been emphasized in the previous subsection, the entries (4.4.73), (4.4.74), and (4.4.75) of $\hat{g}(\vec{q})$ are given by the rescaled Fourier transforms (4.4.76) of the couplings K_α ($\alpha = 1, 2, 3$) of the effective Ising model (4.3.34) for the dimerizability $a(T)$, see also Sect. 4.3.3. Therefore we can apply the same numerical routines which have been used in the Pars. 4.3.4 and 4.3.5 to calculate $\hat{g}(\vec{q})$. In this and the following subsection and if not otherwise stated, we analyze QMC data for $\hat{g}(\vec{q})$ evaluated in systems with 24×24 lattice sites, taking 10^5 loop updates for thermalization and 2×10^6 configurations for the computation of expectation values. The system size is sufficiently large to keep finite-size effects well under control. For example, this can be seen from the discussion on finite-size effects for the dimerizability $a_{\rm pl}(T)$ of the plaquette model in Par. 4.3.5, which is twice the rescaled Fourier transform $\tilde{K}_1(\pi, 0)$ according to Eq. (4.3.43).

The first conclusion which can be drawn from the calculation of $\hat{g}(\vec{q})$ is that for all temperatures $T = 0.1J, 0.2J, \ldots, 4.0J$, the trace of $\hat{g}(\vec{q})$ vanishes or takes negative values irrespectively of the momentum vector $\vec{q}$. This implies that also the trace of $\hat{G}(\vec{q}) = \hat{G}_0(\vec{q}) + \hat{g}(\vec{q})$ is reduced due to the spin-phonon interaction, which is just the sum $\omega_1^2(\vec{q}) + \omega_2^2(\vec{q})$ of the squares of the two phonon frequencies $\omega_{1/2}(\vec{q})$. The interpretation is that the spin-phonon coupling induces a softening of phonon modes as in the one-dimensional case. The further argumentation is completely analogous to the one from Refs. [Pyt74, CF79], compare also the beginning of Sect. 4.1. When decreasing the temperature of the system at fixed λ (or increasing λ at fixed T), there will be certain phonon
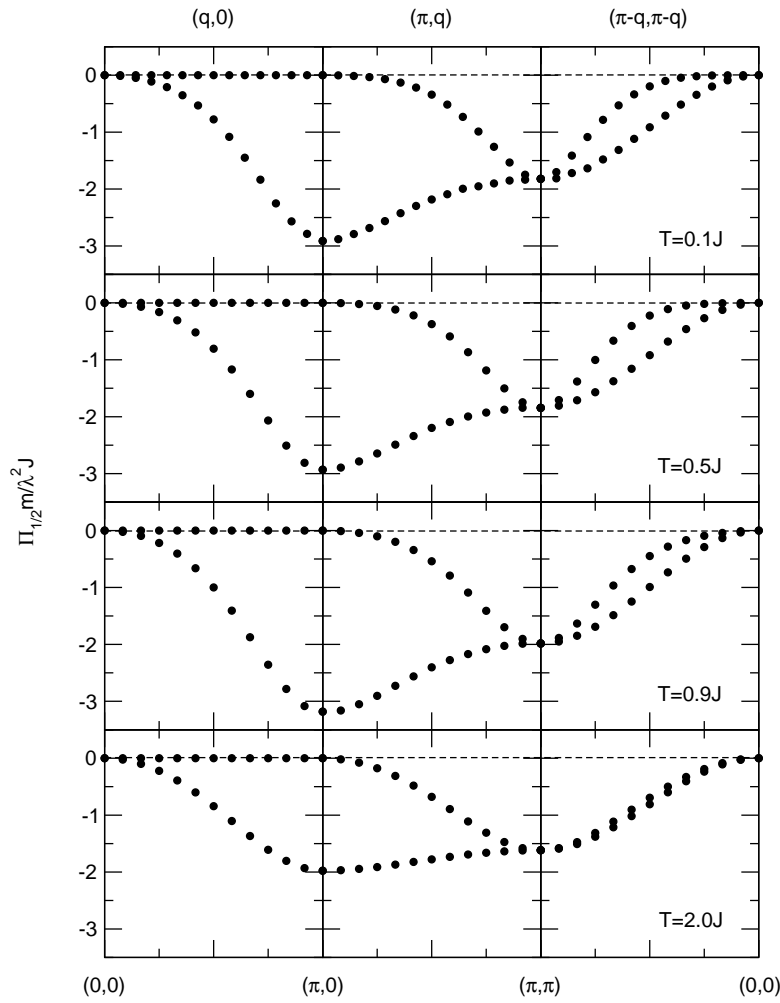
Fig. 4.19.: Eigenvalues $\Pi_{1/2}(\vec{q})$ of the spin-phonon contribution $\hat{g}(\vec{q})$ to the dynamical matrix for a triangular path through $\vec{q}$-space and four different temperatures. For $T = 0.1J$, the linear system size is $N = 28$.

frequencies which are most affected by the spin-lattice interaction. A structural phase transition into a distorted phase is encountered as soon as the renormalized frequency $\omega(\vec{q}_0)$ of a particular phonon which is characterized by the wave vector $\vec{q}_0$ and polarization vector $\vec{p}_0$ turns to zero, because then the system gains energy by macroscopically occupying this phonon mode. Here the polarization vector $\vec{p}_0$ is the corresponding eigenvector of the full dynamical matrix $G(\vec{q}_0)$. In particular, the wave and polarization vectors of the phonon determine the type of lattice modulation which characterizes the distorted phase. Note that in principle in a two-dimensional system, it is possible to occupy two such phonon modes with independent (i. e. orthogonal) polarization vectors at the same time.

In the following we examine the structure of $\hat{g}(\vec{q})$ in more detail by calculating its eigenvalues $\Pi_{1/2}(\vec{q})$, which are plotted along a triangular path in $\vec{q}$-space for four different temperatures in Fig. 4.19. We first see that for all choices of $\vec{q}$, the sum $\Pi_1(\vec{q}) + \Pi_2(\vec{q})$ of the two eigenvalues
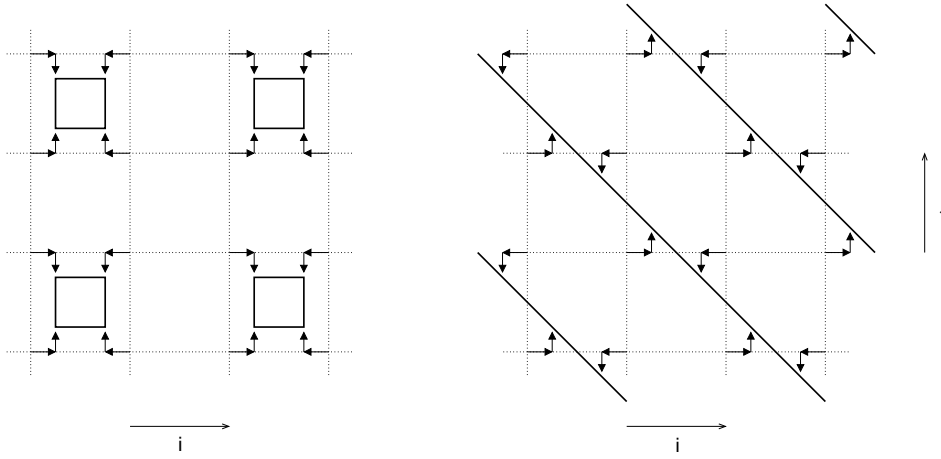
Fig. 4.20.: Illustration of two different types of lattice modulations. Left Panel: A superposition of two phonons with $\vec{q}_1 = (\pi, 0)$, $\vec{p}_1 = (1, 0)$ and $\vec{q}_2 = (0, \pi)$, $\vec{p}_2 = (1, 0)$ reveals a plaquette-like pattern of lattice distortions, which is favored most by the spin-phonon contribution $\hat{g}(\vec{q})$ in Eq. (4.4.71). Right panel: By superposing two phonons with $\vec{q}_1 = (\pi, \pi)$, $\vec{p}_1 = (1, 0)$, and $\vec{q}_2 = (\pi, \pi)$, $\vec{p}_2 = (0, 1)$, one obtains diagonal stripes, which corresponds to an effective magnetic model with a stair-like arrangement of strong and weak bonds.

(i. e. the trace of $\hat{g}(\vec{q})$) indeed vanishes or takes negative values. However, the more important observation is that the curves show a pronounced global minimum at $(\pi, 0)$. Note that for symmetry reasons the analogous feature is found at $(0, \pi)$, which is not shown in the figure. A third characteristic point in $\vec{q}$-space is (π, π), where the two curves for the eigenvalues $\Pi_{1/2}(\vec{q})$ exhibit a local minimum and a saddle point, respectively. A more precise investigation of $\hat{g}(\vec{q})$ at the three points yields:

1. $\vec{q} = (\pi, 0)$:
   Here the matrix $\hat{g}$ reads

$$\hat{g}(\pi, 0) = \frac{2\lambda^2}{m} \begin{pmatrix} a_{\mathrm{pl}}(T) & 0 \\ 0 & 0 \end{pmatrix}, \qquad (4.4.77)$$

   where we have made use of the relation $2\tilde{K}_1(\pi, 0) = a_{\mathrm{pl}}(T)$ according to Eq. (4.3.43) from Par. 4.3.5. Thus the eigenvalues of $\hat{g}(\pi, 0)$ are given by $\Pi_1(\pi, 0) = \frac{2\lambda^2}{m} a_{\mathrm{pl}}(T)$ and $\Pi_2(\pi, 0) = 0$, while the corresponding eigenvectors are $(1, 0)$ and $(0, 1)$, respectively.

2. $\vec{q} = (0, \pi)$:
   In analogy to the point at $\vec{q} = (\pi, 0)$, one obtains

$$\hat{g}(0, \pi) = \frac{2\lambda^2}{m} \begin{pmatrix} 0 & 0 \\ 0 & a_{\mathrm{pl}}(T) \end{pmatrix}, \qquad (4.4.78)$$

   because of the relation $2\tilde{K}_2(0, \pi) = 2\tilde{K}_1(\pi, 0) = a_{\mathrm{pl}}(T)$. We therefore find $\Pi_1(0, \pi) = \frac{2\lambda^2}{m} a_{\mathrm{pl}}(T)$ and $\Pi_2(0, \pi) = 0$, with eigenvectors $(0, 1)$ and $(1, 0)$.

3. $\vec{q} = (\pi, \pi)$:

Here $\hat{g}$ becomes

$$\hat{g}(\pi, \pi) = \frac{2\lambda^2}{m} \begin{pmatrix} a_{\text{st}}(T) & 0 \\ 0 & a_{\text{st}}(T) \end{pmatrix}. \tag{4.4.79}$$

To explain this result we first note that according to the expression (4.3.44) from Sect. 4.3.5, we have the relation $2\tilde{K}_1(\pi, \pi) = 2\tilde{K}_2(\pi, \pi) = a_{\text{st}}(T)$, which has been used for the entries on the diagonal. In addition and according to Eq. (4.4.75), the off-diagonal entries of $\hat{g}(\pi, \pi)$ are proportional to $\tilde{K}_3(\pi, \pi)$, which vanishes because the Fourier transform of the couplings $K_3(x_1, x_2)$ (see Eq. (4.3.37) from Sect. 4.3.3) is the weighted sum of each four equivalent contributions which cancel at (π, π). We therefore find two degenerate eigenvalues $\Pi_{1/2}(\pi, \pi) = \frac{2\lambda^2}{m} a_{\text{st}}(T)$. Again the corresponding eigenvectors are found to be parallel to the coordinate axes, because $\hat{g}(\pi, \pi)$ is diagonal.

It is important to emphasize that we have expressed the global minima $\Pi_1(\pi, 0)$ and $\Pi_1(0, \pi)$ as well as the degenerate eigenvalues $\Pi_{1/2}(\pi, \pi)$ by the dimerizabilities $a_{\text{pl}}(T)$ and $a_{\text{st}}(T)$ of the plaquette and stair model. Hence the temperature dependence of these eigenvalues can be deduced from the two corresponding curves in Fig. 4.15. In particular, this means that the influence of the spin-lattice coupling on the phonon dynamics is largest in the vicinity of the maximum $T_{\text{max}} \approx 0.9J$ of $a_{\text{pl}}(T)$. As can be seen in Fig. 4.19, the eigenvalues of $\hat{g}(\vec{q})$ take their smallest values at this temperature.

Furthermore, our analysis implies that in the leading order in λ, the gain in the magnetic free energy due to the spin-lattice coupling as described by Eq. (4.4.57) is largest for a simultaneous occupation of one phonon with $\vec{q}_1 = (\pi, 0)$ and polarization vector $\vec{p}_1 = (1, 0)$, and a second phonon with $\vec{q}_2 = (0, \pi)$ and orthogonal polarization $\vec{p}_2 = (0, 1)$. Hence the spin-phonon coupling contribution $\hat{g}(\vec{q})$ in Eq. (4.4.71) favors a plaquette-like lattice distortion as illustrated in the left panel of Fig. 4.20. This corresponds with our findings from Sect. 4.3.

However, our result does not mean that a structural transition due to the spin-lattice interaction is always directed towards the plaquette lattice. For a complete investigation of this issue one has to take into account the bare contribution $\hat{G}_0(\vec{q})$ to the dynamical matrix. It is conceivable that under certain conditions the bare phonon frequency $\omega_0(\vec{q}_0)$ at some wave vector $\vec{q}_0 \neq (\pi, 0), (0, \pi)$ is significantly smaller than the corresponding values at $(\pi, 0)$ and $(0, \pi)$. In such a case this phonon mode might vanish first when decreasing T (or alternatively, increasing λ), and a different type of lattice modulation is found. For example, this is likely to occur for the two phonons with $\vec{q}_{0,1/2} = (\pi, \pi)$ and independent polarization vectors $\vec{p}_{0,1} = (1, 0)$ and $\vec{p}_{0,2} = (0, 1)$. Especially at higher temperatures, the two eigenvalues $\Pi_{1/2}(\pi, \pi)$ are close to the global minima at $(\pi, 0)$ and $(0, \pi)$, compare Fig. 4.19. In contrast to the plaquette pattern, a macroscopic occupation of the two (π, π)-phonons leads to the formation of diagonal stripes as illustrated in the right panel of Fig. 4.20. In the language of statically dimerized spin models, this corresponds to a stair-like arrangement of strong and weak bonds.

4.4.3. Analysis of the full dynamical matrix for a simple model

In this subsection we investigate the full dynamical matrix $\hat{G}(\vec{q})$ for a simple choice of the lattice potential $V(\{\vec{R}_{\vec{r}}\})$ in Eq. (4.4.54), i. e. we specify the bare dynamical matrix $\hat{G}_0(\vec{q})$ of the system. The model under consideration, the K-K'-model, is characterized by a harmonic lattice potential which consists of two different types of elastic couplings. While each pair of adjacent lattice ions is subject to a quadratic potential with an elastic constant K, there exists an additional coupling K' between next-nearest neighbors, i. e. over the diagonals of each square on the lattice. The entries of the Fourier transformed bare dynamical matrix for this problem read

$$\hat{G}_0^{xx}(\vec{q}) = \frac{2}{m}[\, K(1 - \cos q_1) + K'(1 - \cos q_1 \cos q_2)\,] \qquad (4.4.80)$$

$$\hat{G}_0^{yy}(\vec{q}) = \frac{2}{m}[\, K(1 - \cos q_2) + K'(1 - \cos q_1 \cos q_2)\,] \qquad (4.4.81)$$

$$\hat{G}_0^{xy}(\vec{q}) = \hat{G}_0^{yx}(\vec{q}) = \frac{2}{m}\, K' \sin q_1 \sin q_2, \qquad (4.4.82)$$

see App. A.5 for a detailed derivation of these expressions.

Having specified the lattice potential, it is possible to calculate the renormalized matrix $\hat{G}(\vec{q})$ by adding the QMC results for $\hat{g}(\vec{q})$ from the preceeding subsection to the bare dynamical matrix $\hat{G}_0(\vec{q})$ which is specified by the formulae (4.4.80), (4.4.81), and (4.4.82). Then the eigenvalues of $\hat{G}(\vec{q})$ correspond to the squares of the renormalized phonon frequencies $\omega_{1/2}(\vec{q})$ of the system.

For a typical choice of coupling constants, the temperature dependence of the resulting curves is shown in Fig. 4.21. As can be seen from the figure, the spin-phonon interaction leads to a significant reduction of particular phonon frequencies upon decreasing the temperature. Corresponding with our findings from the previous subsection, however, the overall size of this phonon softening strongly depends on the momentum vector $\vec{q}$. For example in the vicinity of the center $(0, 0)$ of the first Brillouin zone, the two phonon branches are almost unaffected by the coupling to the spin degrees of freedom. At $(\pi, 0)$ and (π, π), on the other hand, we observe the expected characteristical features. At (π, π), there is a significant reduction of both eigenvalues $\omega_{1/2}^2(\pi, \pi)$ when decreasing the temperature. The most striking feature though occurs at $(\pi, 0)$. While the smaller of the two bare phonon frequencies $\omega_{0,1/2}(\pi, 0)$ is not affected by the spin-phonon coupling, there is an immense reduction of the second frequency when cooling down the system. At a certain intermediate temperature, this originally disadvantaged phonon branch breaks through the unaffected one, and finally turns to zero at a critical temperature T_c slightly above $T = 1.2J$. Note that exactly the same feature is found at $(0, \pi)$, which is expected for symmetry reasons. Evidently, the corresponding polarization vectors are orthogonal and parallel to the coordinate axes, because both $\hat{G}(\pi, 0)$ and $\hat{G}(0, \pi)$ are diagonal matrices. Thus, in accordance with the analysis of $\hat{g}(\vec{q})$ in Par. 4.4.2 we conclude that there is a structural phase transition from the uniform phase at high temperatures to a plaquette phase at $T < T_c$.

An alternative way to obtain this structural transition is to tune the spin-phonon coupling constant λ, while the temperature and the elastic constants K, K' are kept fixed. An example with a fairly small value of the fraction $\frac{K'}{K}$ and $T = 0.1J$ is given in Fig. 4.22, where QMC data for a system with 28×28 sites have been evaluated. The curves look very similar to the ones depicted in Fig. 4.21. While a small value of λ is not sufficient to drive the system into a structural instability,
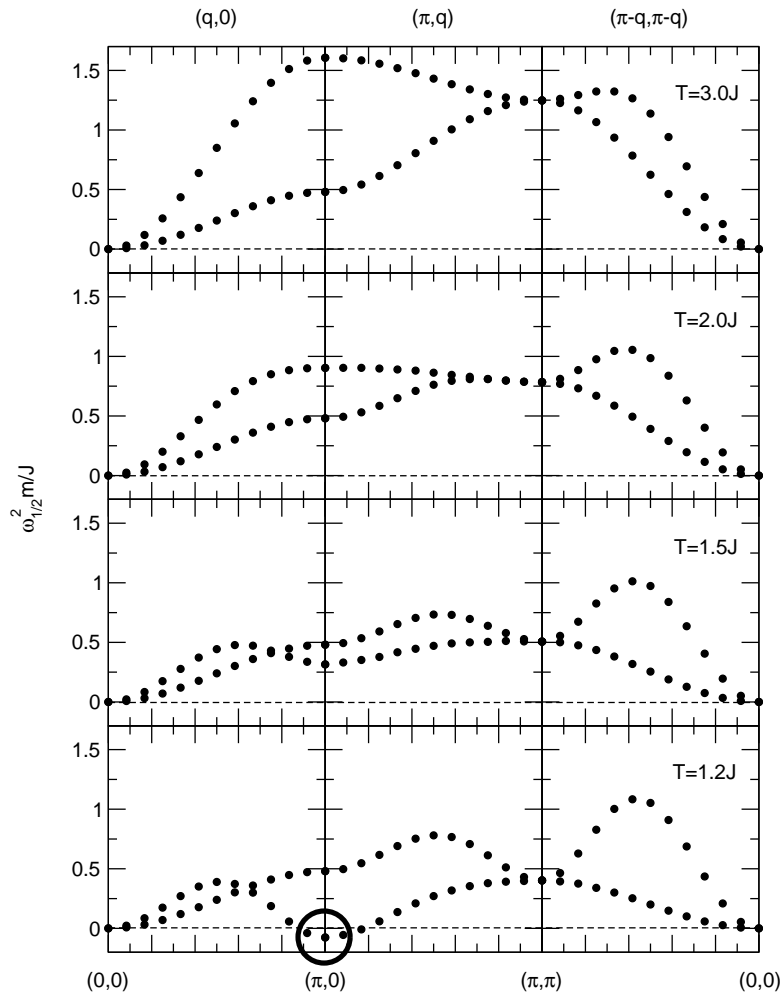
Fig. 4.21.: Eigenvalues $\omega_{1/2}^2(\vec{q})$ of the renormalized dynamical matrix $\hat{G}(\vec{q})$ along a triangular path in $\vec{q}$-space, evaluated for a system with $K = 0.6J$, $\frac{K'}{K} = 0.2$, and $\lambda = 1.0$ at four different temperatures. As indicated by the thick circle in the bottom panel, one of the two eigenvalues at $(\pi, 0)$ changes its sign slightly above $T = 1.2J$, corresponding to a structural instability towards a plaquette-like lattice distortion.

a plaquette-like lattice modulation is found as soon as λ exceeds a certain critical value, which is given by $\lambda_c \approx 0.41$ for this particular choice of coupling constants.

To deduce the exact value of λ_c, we consider the eigenvalues of $\hat{G}(\vec{q})$ at $(\pi, 0)$ (or equivalently, at $(0, \pi)$). The condition for a transition to a plaquette phase is that the smaller eigenvalue of $\hat{G}(\pi, 0)$ vanishes. At $(\pi, 0)$, we have

$$\hat{G}(\pi, 0) = \frac{2}{m} \begin{pmatrix} 2(K + K') + \lambda^2 a_{\mathrm{pl}}(T) & 0 \\ 0 & 2K' \end{pmatrix}, \quad (4.4.83)$$

see also the expression (4.4.77) for $\hat{g}(\pi, 0)$ from the previous subsection. For sufficiently large values of the spin-phonon coupling, the smaller of the two eigenvalues is $\omega_1^2(\pi, 0) = \frac{2}{m}[2(K + K') + \lambda^2 a_{\mathrm{pl}}(T)]$. By setting this number equal to zero, we obtain the critical value $\lambda_{c,\mathrm{pl}}$ for a
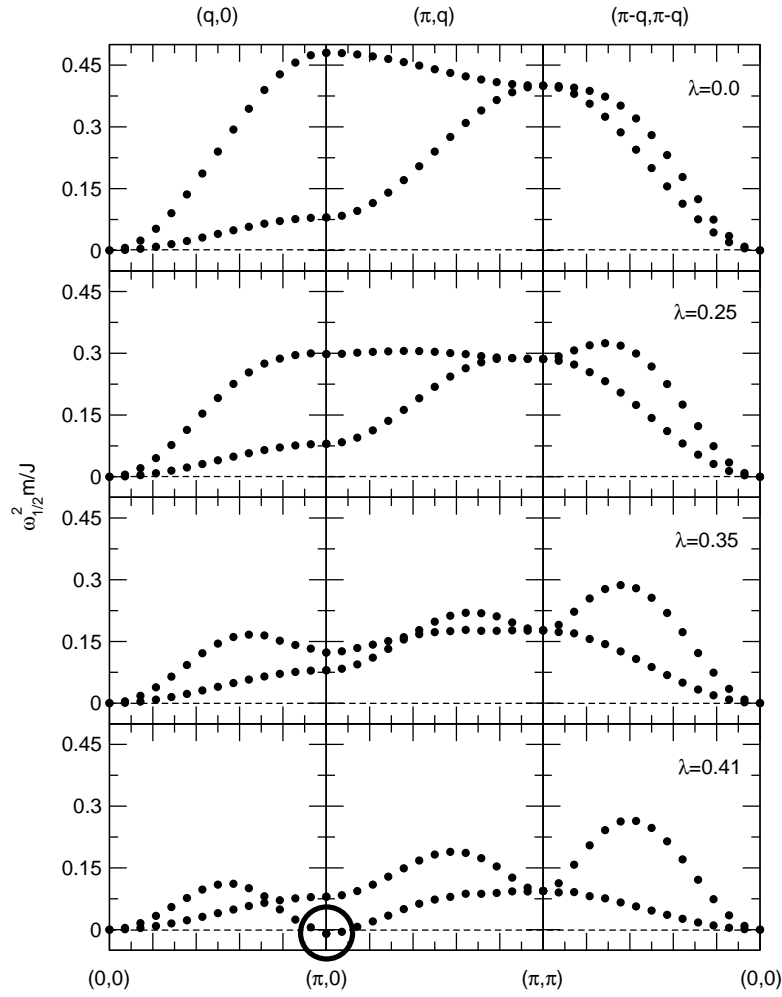
Fig. 4.22.: Squared phonon frequencies $\omega_{1/2}^2(\vec{q})$ in a system with $K = 0.1J$ and a small fraction $\frac{K'}{K} = 0.2$ without spin-phonon coupling (top panel), and three different finite values of λ (lower three panels). The temperature is $T = 0.1J$. At $\lambda \approx 0.41$, there is a structural phase transition to the plaquette phase, because one of the two phonon frequencies at $(\pi, 0)$ (thick circle in the bottom panel) and another one at $(0, \pi)$ turn to zero.

plaquette-like lattice distortion, i. e.

$$\frac{\lambda_{c,pl}^2}{K} = \frac{-2}{a_{pl}(T)} \left(1 + \frac{K'}{K}\right). \tag{4.4.84}$$

In the following we consider the question whether the structural transition is always directed towards the plaquette structure [Web]. As far as the K-K'-model with $\lambda = 0$ is concerned, an examination of $\hat{G}_0(\vec{q})$ implies that the two bare phonon frequencies $\omega_{0,1/2}(\pi, \pi)$ get significantly reduced with respect to the maxima at $(\pi, 0)$ and $(0, \pi)$ if the ratio $\frac{K'}{K}$ is increased. Therefore for sufficiently large values of this fraction, we expect that the renormalized phonon frequencies $\omega_{1/2}(\pi, \pi)$ vanish first when increasing λ. This feature is illustrated in Fig. 4.23, where the eigen-
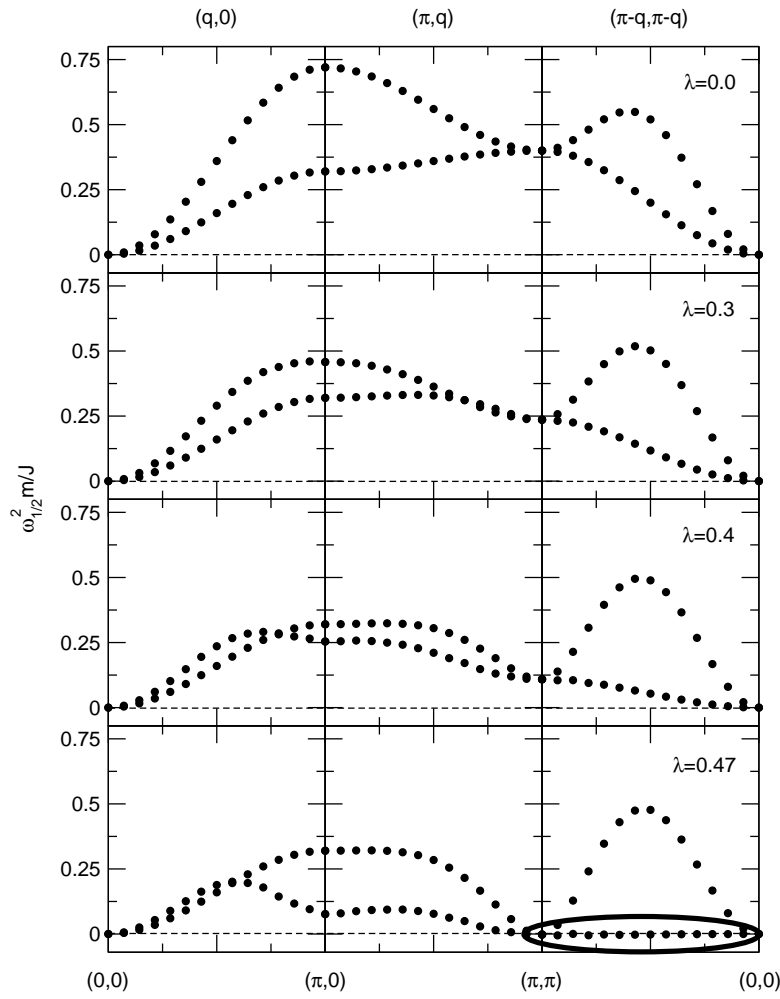
Fig. 4.23.: Eigenvalues of the dynamical matrix $\hat{G}(\vec{q})$ for $K = 0.1J$ and a considerably large value of the ratio $\frac{K'}{K} = 0.8$ at $T = 0.1J$. The comparison of the bare phonon frequencies for $\lambda = 0$ (top panel) to the corresponding curves for $\frac{K'}{K} = 0.2$ (top panel of Fig. 4.22) shows that the two phonon modes at (π, π) are reduced significantly with respect to the maximum at $(\pi, 0)$. When increasing the spin-phonon coupling (lower three panels), the lower of the two phonon branches with $\vec{q} = (q, q)$ gets softened. At $\lambda \approx 0.47$, the corresponding eigenvalues $\omega_1^2(q, q)$ all vanish simultaneously (illustrated by the thick ellipse in the bottom panel).

values of $\hat{G}(\vec{q})$ are plotted for a typical example with $\frac{K'}{K} = 0.8$. Note that again QMC data for a system with $N = 28$ have been evaluated. However, besides the expected feature at (π, π) a whole branch of squared phonon frequencies with wavevectors (q, q) vanishes at the same value $\lambda_c \approx 0.47$ of the spin-phonon coupling. The analogous feature is found on the second diagonal $(q, -q)$ of the Brillouin zone, which is expected for symmetry reasons. Therefore within the numerical accuracy, one cannot judge whether the structural instability can be characterized by the wavevector (π, π) (corresponding to the diagonal stripe pattern as shown in the right panel of Fig. 4.20) or by a particular pair of incommensurate wavevectors (q, q) and $(q, -q)$ with $q \neq \pi$.
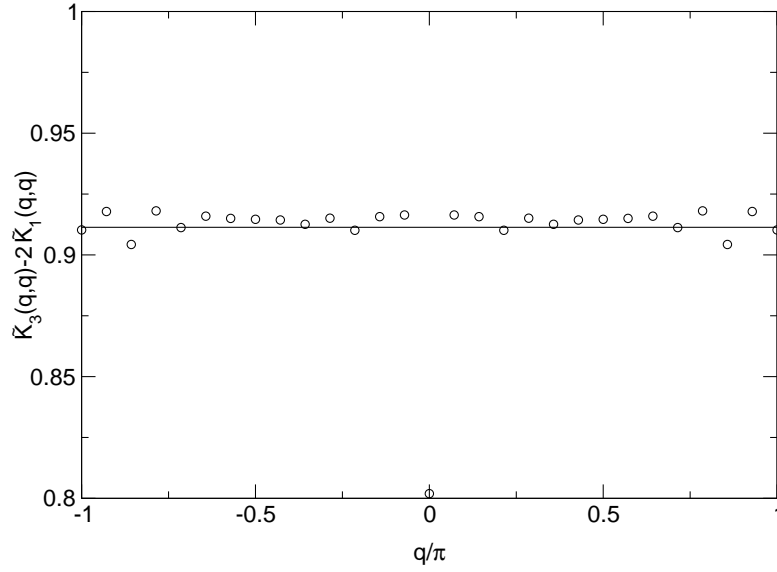
Fig. 4.24.: Numerical estimates for $\tilde{K}_3(q,q) - 2\tilde{K}_1(q,q)$ vs. q evaluated for a system with $N = 28$ at $T = 0.1J$ (circles). The solid line depicts the approximation (4.4.89) to the full Fourier transformed difference.

The fact that for large $\frac{K'}{K}$ a whole branch of phonon frequencies vanishes requires a more detailed analysis. This means that we have to analyze the eigenvalues of $\hat{G}(\vec{q})$ at (q, q) (or equivalently, at $(q, -q)$). For these wavevectors, the renormalized dynamical matrix becomes

$$\hat{G}(q,q) = \frac{2}{m}\begin{pmatrix} [K + \lambda^2\tilde{K}_1(q,q)](1 - \cos q) + K'\sin^2 q & \frac{\lambda^2}{2}\tilde{K}_3(q,q)(1 - \cos q) + K'\sin^2 q \\ \frac{\lambda^2}{2}\tilde{K}_3(q,q)(1 - \cos q) + K'\sin^2 q & [K + \lambda^2\tilde{K}_1(q,q)](1 - \cos q) + K'\sin^2 q \end{pmatrix},$$

$$(4.4.85)$$

where we have used the identity $\tilde{K}_1(q,q) = \tilde{K}_2(q,q)$ which holds for symmetry reasons. For $q = \pi$, this matrix is diagonal with two degenerate eigenvalues $\omega_{1/2}^2(\pi, \pi) = \frac{2}{m}(2K + \lambda^2 a_{\text{st}}(T))$, see also the expression (4.4.79) for $\hat{g}(\pi, \pi)$. For $q \neq \pi$ the degeneracy is lifted, and the lower of the two eigenvalues becomes $\omega_1^2(q,q) = \frac{2}{m}(1 - \cos q)\{K + \lambda^2[\tilde{K}_1(q,q) - \frac{1}{2}\tilde{K}_3(q,q)]\}$. By setting this number equal to zero, we obtain the critical spin-phonon coupling

$$\frac{\lambda_{c,qq}^2}{K} = 2\left[\tilde{K}_3(q,q) - 2\tilde{K}_1(q,q)\right]^{-1} \qquad (4.4.86)$$

for a transition to a distorted phase which is characterized by two independent phonons with wavevectors (q, q) and $(q, -q)$. In particular, the whole phonon branch with momenta (q, q) simultaneously vanishes if the right-hand side of Eq. (4.4.86) does not depend on q. This means

$$\tilde{K}_3(q,q) - 2\tilde{K}_1(q,q) = \text{const} = -2\tilde{K}_1(\pi, \pi) = -a_{\text{st}}(T), \qquad (4.4.87)$$

where the second equality is due to the fact that $\tilde{K}_3(\pi, \pi)$ vanishes. Within the numerical accuracy, the numerical data for $\tilde{K}_1(\vec{q})$ and $\tilde{K}_3(\vec{q})$ obey the condition (4.4.87) at all temperatures. For the system with $N = 28$ and $T = 0.1J$ this is illustrated in Fig. 4.24. Note that it is not possible to

give relieable errorbars for the Fourier transformed difference $\tilde{K}_3(q, q) - 2\tilde{K}_1(q, q)$, because the covariances between the real space structure factors $K_1(\vec{x})$ and $K_3(\vec{x})$ for different distances $\vec{x}$ were not evaluated during the QMC simulations. Thus from the numerical data, it is not possible to judge whether the identity (4.4.87) holds exactly or only approximately.

It is possible though to understand why Eq. (4.4.87) holds at least approximately. We first consider the difference of the real space quantities $K_3(\vec{x}) - 2K_1(\vec{x})$. In real space, the two Ising couplings $K_3(\vec{x})$ and $2K_1(\vec{x})$ quickly decay towards the same constant background at large distances, which is given by the square of the local energy per bond times the inverse temperature of the system. As a result, the difference $K_3(\vec{x}) - 2K_1(\vec{x})$ is strongly peaked around $\vec{x} = 0$. Thus only small distances $\vec{x}$ give a significant contribution to the Fourier transformed difference

$$\tilde{K}_3(q, q) - 2\tilde{K}_1(q, q) = N^2 \sum_{\vec{x}} e^{-iq(x_1 + x_2)} [K_3(\vec{x}) - 2K_1(\vec{x})], \tag{4.4.88}$$

where only the special choice $\vec{q} = (q, q)$ has been considered. From Eq. (4.4.88), we further see that only distances $\vec{x} = (x_1, x_2)$ with $x_1 = -x_2$ give a constant contribution to the Fourier transform. The contributions with $x_1 \neq -x_2$ cancel within the numerical accuracy. By taking into account the peaked structure of $K_3(\vec{x}) - 2K_1(\vec{x})$, we therefore conclude that

$$\tilde{K}_3(q, q) - 2\tilde{K}_1(q, q) \approx N^2 \{K_3(0, 0) + K_3(1, -1) + K_3(-1, 1) - 2[K_1(0, 0) + K_1(1, -1) + K_1(-1, 1)]\} \tag{4.4.89}$$

is a good approximation for the Fourier transformed difference. In the example from Fig. 4.24, the solid line depicts the result of the approximation (4.4.89) which is in good accordance with the numerical data for the full Fourier transformed difference $\tilde{K}_3(q, q) - 2\tilde{K}_1(q, q)$.

We are now in the state to establish the phase diagram of the K-K'-model with spin-phonon coupling at finite temperatures. Our results can be interpreted most easily if we keep T and K fixed. As can be seen from Fig. 4.15 (see Par. 4.3.5), the negative dimerizability $-a_{\rm pl}(T)$ is always larger than the corresponding number $-a_{\rm st}(T)$ for a stair-like lattice distortion. According to the Eqs. (4.4.84) and (4.4.86) (together with (4.4.87)) and for sufficiently small values of $\frac{K'}{K}$, we therefore find the relation $\lambda_{\rm c,pl} < \lambda_{\rm c,qq}$ and thus the plaquette phase for all $\lambda > \lambda_{\rm c,pl}$. In the region of large $\frac{K'}{K}$, on the other hand, the system prefers the phonon branches with wavevectors (q, q) and $(q, -q)$ as soon as λ exceeds $\lambda_{\rm c,qq}$, because in contrast to Eq. (4.4.84) the expression (4.4.86) does not depend on K'. The phase segragation line between the two distorted phases can be deduced by equating the right-hand sides of the two conditions (4.4.84) and (4.4.86) (together with (4.4.87)), which yields

$$\frac{K'}{K} = \frac{a_{\rm pl}(T)}{a_{\rm st}(T)} - 1. \tag{4.4.90}$$

The phase diagram for $T = 0.1J$ which is obtained from QMC results for $a_{\rm pl/st}(T)$ in a system with 28×28 spins is shown in Fig. 4.25. We emphasize that the examination of $\hat{G}(\vec{q})$ for arbitrary wavevectors $\vec{q}$ gives no evidence for the existence of further phases in the phase diagram of the K-K'-model with spin-phonon coupling.

On the basis of the three expressions (4.4.84), (4.4.86), and (4.4.90) it is also possible to discuss the influence of the temperature on the phase diagram of the system. The T-dependence of the parameters $\frac{-2}{a_{\rm pl}(T)}$, $\frac{-2}{a_{\rm st}(T)}$ and $\frac{a_{\rm pl}(T)}{a_{\rm st}(T)} - 1$, which enter the three equations for the phase segregation
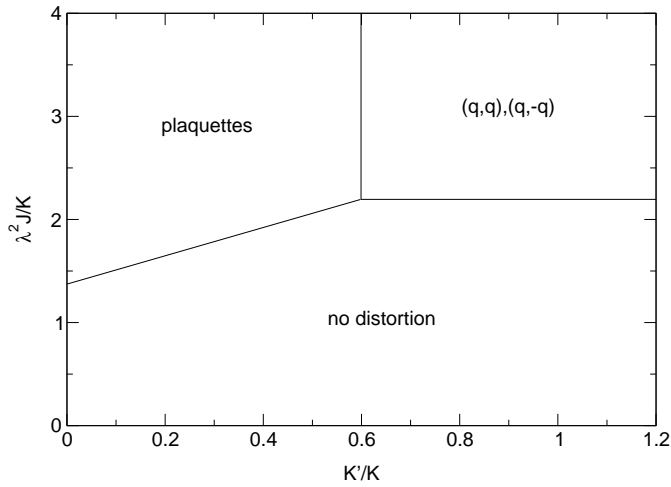
Fig. 4.25.: Phase diagram of the K-K'-model with spin-phonon coupling determined from QMC data for $a_{\mathrm{pl/st}}(T)$ for $T = 0.1J$ and $N = 28$. The transition lines between the undistorted and the two distorted phases are given by the expressions (4.4.84) and (4.4.86) (together with Eq. (4.4.87)), while the phase segragation line between the plaquette and the incommensurate phase (characterized by wavevectors (q, q) and $(q, -q)$) is obtained from Eq. (4.4.90).

lines, is given in Table 4.2. To obtain a structural phase transition at higher temperatures, one has to increase λ (or decrease K) significantly as compared to the low temperature regime, which is an expected feature. A more interesting point is that the largest extension (with respect to the ordinate axis in Fig. 4.25) of the two distorted phases is found at temperatures close to the maximum $T_{\mathrm{max}} \approx 0.9J$ of the curve for $-a_{\mathrm{pl}}(T)$ (or the corresponding temperature $T_{\mathrm{max}} \approx 1.1J$ where $-a_{\mathrm{st}}(T)$ takes its maximum), see the Figs. 4.13 and 4.15. Thus in principle and in accordance with the investigation of the statically dimerized plaquette model in Sect. 4.3.5, a reentrance (uniform $\rightarrow$ distorted $\rightarrow$ uniform) of phases is conceivable for certain values of the coupling constants. However, this interpretation has to be taken with great care because we do not take into account higher order terms in the Landau expansion (4.4.57) from Par. 4.4.1, which correspond to anharmonic contributions to the phonon dynamics. Another major influence of the temperature on the phase diagram is that the segragation line between the plaquette and the incommensurate phases is shifted towards smaller values of $\frac{K'}{K}$ upon increasing T.

We close this chapter with a couple of remarks concerning the applicability of the approach from this section. Due to the adiabatic treatment of the lattice degrees of freedom, we have neglected the kinetic energy contribution of the lattice ions to the total Hamiltonian, which is the sum of Eqs. (4.4.54) and (4.4.56). For this reason the phonon dispersion curves as shown in the Figs. 4.21, 4.22, and 4.23 contain a systematic error which enters especially at higher energies, and therefore have to be handled carefully if compared to experimental data. In any case, for a direct comparison to the experiment one would have to take into account that the unit cell of real quasi two-dimensional substances contains a considerably large number of interacting lattice ions. For this reason one cannot expect that the simple K-K'-model correctly describes the full

T/J	$\frac{-2J}{a_{pl}}$	$\frac{-2J}{a_{st}}$	$\frac{a_{pl}}{a_{st}} - 1$	T/J	$\frac{-2}{a_{pl}}$	$\frac{-2}{a_{st}}$	$\frac{a_{pl}}{a_{st}} - 1$
0.1	1.37	2.20	0.60	2.1	2.13	2.56	0.21
0.2	1.38	2.19	0.59	2.2	2.24	2.65	0.19
0.3	1.38	2.20	0.59	2.3	2.34	2.74	0.17
0.4	1.38	2.18	0.58	2.4	2.45	2.84	0.16
0.5	1.36	2.17	0.59	2.5	2.56	2.94	0.15
0.6	1.34	2.15	0.61	2.6	2.67	3.04	0.14
0.7	1.30	2.11	0.63	2.7	2.79	3.15	0.13
0.8	1.26	2.06	0.63	2.8	2.90	3.26	0.12
0.9	1.26	2.02	0.60	2.9	3.02	3.37	0.11
1.0	1.27	2.00	0.58	3.0	3.14	3.47	0.11
1.1	1.30	1.99	0.53	3.1	3.26	3.58	0.10
1.2	1.35	2.00	0.48	3.2	3.38	3.69	0.09
1.3	1.41	2.03	0.43	3.3	3.50	3.81	0.09
1.4	1.48	2.07	0.40	3.4	3.62	3.92	0.08
1.5	1.56	2.11	0.35	3.5	3.74	4.03	0.08
1.6	1.65	2.18	0.32	3.6	3.87	4.15	0.07
1.7	1.73	2.24	0.29	3.7	3.99	4.27	0.07
1.8	1.83	2.31	0.26	3.8	4.11	4.39	0.07
1.9	1.92	2.39	0.24	3.9	4.24	4.50	0.06
2.0	2.02	2.48	0.22	4.0	4.36	4.62	0.06

Table 4.2.: QMC estimates for the parameters $\frac{-2}{a_{pl}(T)}$, $\frac{-2}{a_{st}(T)}$ and $\frac{a_{pl}(T)}{a_{st}(T)} - 1$, which govern the expressions (4.4.84), (4.4.86), and (4.4.90) for the phase segregation lines in the phase diagram of the K-K'-model with spin-phonon coupling. For $T = 0.1J$, the dimerizabilities $a_{pl/st}(T)$ were evaluated in a system with 28×28 sites (compare also the phase diagram 4.25), while the linear system size was $N = 24$ for all $T > 0.1J$.

phonon branches of the magnetic ions for this class of materials. However, we do expect that the softening of phonon modes is well described within the adiabatic approach. In particular and regardless of the details of the microscopic model for the lattice potential, the results from this section imply that the phonon frequencies at wavevectors $(\pi, 0)$, $(0, \pi)$ and (π, π) are strongly affected by the spin-lattice interaction. The occurrence of lattice distortions characterized by incommensurate wavevectors is also conceivable. For this reason it seems worthwhile to search for these symptoms of the spin-phonon coupling in experimental data. As for the quasi one-dimensional $CuGeO_3$ though, the adiabatic limit is not realized in the undoped parent compounds of the high temperature superconductors like e. g. La_2CuO_4 [Web]. Indeed, the neutron diffraction data for a number of cuprates have been successfully described by an empirical model without introducing a coupling between the spin and lattice degrees of freedom [CRPP95].

As far as the K-K'-model is concerned, we emphasize that we have not made any statements about the ground state phase diagram of the system, because the Landau expansion (4.4.57) of the

free energy is only applicable at finite temperatures. Furthermore, we were not able to examine the order of the transitions between the different phases in Fig. 4.25, although in Sect. 4.3.5 we have found some indications that the transition from the uniform to the plaquette phase is continuous. Another issue which remains unsolved is the question whether the spin-lattice interaction can drive the system into a paramagnetic phase. While such a feature can be excluded if e. g. the system favors a stair-like magnetic structure [SKH02], it remains possible in the plaquette region of the phase diagram 4.25.

5. Conclusions

5.1. Summary

This thesis deals with the properties of correlation functions in low-dimensional quantum antiferromagnets. In particular, it is demonstrated that the analysis of finite temperature correlations provides an instrument to examine both thermodynamic and ground state properties of this class of spin systems. The thesis consists of three main parts. Chapter 2 deals with the loop algorithm as the basic numerical instrument which is used in this work. In Chapt. 3, this method is applied to study the equal time spin and dimer correlation functions of the spin-$\frac{1}{2}$ XXZ chain. The third main part in Chapt. 4 is dedicated to the square lattice spin-$\frac{1}{2}$ Heisenberg model with spin-phonon coupling.

The numerical data which are examined in this dissertation were computed by means of the loop algorithm, which is described in Chapt. 2. The loop algorithm is a quantum Monte Carlo (QMC) technique. Quantum Monte Carlo in general is a numerical method based on stochastic decisions to determine the finite-temperature properties of quantum many body systems. As the method is non-perturbative, it does not suffer from systematic truncation errors. For this reason the numerical estimates for thermal expectation values are exact up to a statistical error which reflects the limited access of CPU time in a computer simulation. Furthermore and in contrast to other numerical approaches like DMRG, the method is not obstructed by the dimensionality of the system. Finite-size effects are well under control, because considerably large system sizes can be treated.

The loop algorithm in particular is based on a path integral representation of the partition function. Due to the general applicability of this construction, it can be formulated for a large class of spin models. The major advantage of the algorithm is that it allows for global loop updates of the spin degrees of freedom, leading to a substantial reduction of autocorrelation times. A description of the loop algorithm for the one-dimensional XXZ model is given in Sect. 2.2. In this case, one can formulate the algorithm directly in continuous time. This removes the systematic error which comes from the artificial discretization of Trotter time in the construction of the path integral. The generalization to the two-dimensional Heisenberg model on a square lattice is straightforward, including the case of bond disorder, i. e. bond-dependent antiferromagnetic spin exchange. In Sect. 2.3, it is shown that the loop algorithm can be extended to the Heisenberg model coupled to dispersionless Einstein phonons. For this bond-coupling model both in one and two spatial dimensions, one has to modify the loop update procedure by introducing additional local updates for the phonon degrees of freedom. However, this extension is at the expense of there being no simple way to remove the artificial discretization of Trotter time. Section 2.4 deals with the evaluation

of correlation functions and reliable numerical error bars. The expectation values of both diagonal and off-diagonal operators with respect to the chosen basis of the Hilbert space are computed most efficiently within the framework of improved estimators.

In Chapt. 3, the loop algorithm is applied to examine the equal time spin and dimer correlations of the quantum critical XXZ chain in the low temperature regime. This model is of particular importance because it is realized in a couple of substances like e. g. $SrCuO_3$. Furthermore, as it is integrable by means of the Bethe ansatz, the model serves as a reference system in the field of quantum magnetism. Certain analytical expressions for the longitudinal and transversal spin correlations have been derived in the literature. However, it has not yet been possible to evaluate these expressions for intermediate and large distances. The long distance properties of spin and dimer correlations both at low finite temperatures and at absolute zero are nevertheless well understood due to a combination of conformal field theory and Bethe ansatz results.

Section 3.2 gives a detailed survey of the asymptotic properties of correlation functions in conformal invariant theories, where primary fields play a crucial part. In leading order, the two-point correlators of arbitrary fields in the ground state are found to decay algebraically. The corresponding powers are given by the anomalous dimensions of the primary fields involved. Likewise, the same quantities govern the correlation length of the exponential decay which is predicted at low finite temperatures. In particular, conformal field theory predicts a smooth crossover from the behavior at low temperatures to the corresponding expressions in the ground state. The application of the findings from the conformal approach to the special case of the critical XXZ chain is reviewed in Sect. 3.3, where the asymptotic expressions for the decay of the two-point spin and dimer correlations are given explicitly. The same section also contains a survey of additional field theoretical results concerning the longitudinal and transversal spin correlation functions. These are the correlation amplitudes and the leading algebraic and logarithmic corrections to asymptotic scaling in the ground state.

The Monte Carlo estimates for the three different correlation functions at finite temperatures are examined in Sect. 3.3. The analysis is restricted to the repulsive gapless region $0 \leq \Delta \leq 1$ of the model. A chain length of $N = 1000$ is found to be sufficiently large to make statements about the thermodynamic limit even at very low temperatures $T \geq 0.02J$. The numerical data clearly demonstrate that the expressions from the conformal approach correctly describe the crossover from the low temperature regime to the ground state. Deviations from asymptotic scaling at finite temperatures are investigated. Furthermore, an extrapolation of these results to zero temperature allows to study algebraic and logarithmic corrections in the ground state. As far as the longitudinal and transversal spin correlations are concerned, the correct correlation exponents of the leading and subleading orders are extracted from the numerical data. In addition, independent numerical estimates for the correlation amplitudes are determined and compared to previous analytical and numerical results. For $0 \leq \Delta < 1$ and zero temperature, it is discussed to what extent the algebraic corrections obtained by Lukyanov and Terras coincide with the data at intermediate distances. As far as the corresponding logarithmic corrections in the isotropic XXX chain are concerned, the perturbative results from the literature are found to describe the numerical estimates very precisely down to small distances. In the case of the dimer correlation function, it is possible to deduce

the correct correlation exponents of the leading order from the Monte Carlo data for values of the anisotropy parameter which are not too large. Reliable estimates for the correlation amplitudes for all $0 \leq \Delta < 1$ are determined by analyzing the deviations from asymptotic scaling. For $\Delta = 1$, these deviations are found to be consistent with the exponent of $-\frac{3}{2}$ for the multiplicative logarithmic correction in the ground state.

The square lattice Heisenberg model coupled to phonons is investigated in Chapt. 4. This system is of special interest, because the two-dimensional Heisenberg model describes the magnetic properties of the undoped parent compounds of the high temperature superconductors such as $LaCu_2O_4$. Although the interaction between spin and lattice degrees of freedom is generic to all magnetic materials, there is only a fragmentary knowledge of the impact of the spin-phonon coupling on substances with a quasi two-dimensional magnetic structure.

In Sect. 4.2, the loop algorithm is applied to examine the spin correlations of the two-dimensional bond coupling model for two different choices $g = 0.1J$, $\omega = 8J$, and $g = \omega = 0.67J$ of coupling constants. In one dimension, the first system shows quasi long-range antiferromagnetic order in the ground state, while the second is strongly dimerized. The fundamentally different orders in the ground state are reflected in the temperature dependence of the spin correlation length at low finite temperatures. As far as the two-dimensional model is concerned, an analogous analysis implies that the large value of the spin-phonon coupling for the second system is not sufficient to destroy the long-range Néel order of the square lattice Heisenberg model. Besides the characteristic exponential growth of the spin correlation length upon decreasing the temperature, this interpretation is strongly supported by a finite-size scaling analysis of the correlation length in systems with up to 24×24 lattice sites. Nevertheless the spin-phonon coupling weakens the antiferromagnetic order in the ground state. This conclusion is drawn from an analysis of the staggered magnetization at zero temperature, which is obtained by studying the static structure factor of the spin correlation function at very low temperatures. For $g = \omega = 0.67J$, the value of the staggered magnetization is found to be reduced with respect to the unperturbed Heisenberg model.

Section 4.3 deals with statically dimerized Heisenberg models as the effective spin models to describe the magnetism of distorted spin layers with spin-phonon coupling in the adiabatic limit. These systems are studied most conveniently by means of the loop algorithm in continuous time. In a first step, the plaquette, stair and meander models are considered as those three models which are characterized by a minimal 2×2 unit cell and alternating bonds along each linear chain of the square lattice. Numerical estimates for the ground state energies are deduced from low temperature data for the internal energies in systems with a maximum size of 32×32 spins. In the whole range $0 < \delta \leq 1$, the plaquette pattern has the largest energy gain due to the dimerization as compared to the other two dimerized models. In the sequel, the case of arbitrary dimerization patterns is discussed, i. e. all the different possibilities of distributing an equal number of strong and weak bonds on the square lattice. By considering the second order term in a Landau expansion of the free energy in δ for this general case, the problem of determining the optimal configuration of dimerized bonds is mapped to an effective Ising model with long-range interactions. These coupling constants are given by the integrated dimer correlations of the uniform Heisenberg model, which were computed for linear system sizes $N \leq 20$ and 40 different temperatures of the quantum

system. An application of classical Monte Carlo techniques to this Ising model always yields a plaquette configuration as the energetically favored dimerization pattern. Under the assumption that the loss in the elastic energy due to the lattice distortions is identical for the whole class of dimerized models, it is then possible to establish a Landau theory for the two-dimensional analog of the spin-Peierls transition. This is a structural phase transition from the uniform to the plaquette-distorted lattice upon cooling down the system. In contrast to the situation in quasi one-dimensional systems, the Monte Carlo estimates for the two-dimensional 'dimerizability' in systems with maximum 24×24 spins give no evidence for a divergence of this quantity at low temperatures. This means that the structural transition only occurs for small values $K \lesssim 0.8J$ of the elastic constant. The analysis of the dimerizability also provides an instrument to determine the critical temperature of the transition, which is likely to be continuous according to an investigation of the free energy of the plaquette model at intermediate and high temperatures. The question whether the spin-phonon coupling can drive the system to a paramagnetic ground state remains an open issue. Such a transition is conceivable, because the plaquette model exhibits a quantum phase transition from an antiferromagnetically ordered to a spin gapped phase. The critical dimerization can be determined by studying the staggered magnetization of the plaquette model in the ground state. An analysis of the static structure factor of the spin correlations analogous to the approach for the bond coupling model yields a critical value of $\delta_c = 0.291$.

The influence of the spin-phonon coupling on the phonon dynamics is examined in Sect. 4.4, where a difference coupling mechanism between the spin and lattice degrees of freedom is assumed. In an adiabatic treatment of the phonons and in an expansion up to the second order of the spin-phonon coupling constant λ, the spin-lattice interaction leads to a renormalization $\hat{G}_0 \rightarrow \hat{G}_0 + \hat{g}$ of the bare dynamical matrix which is specified by the particular lattice model. The entries of the spin-phonon contribution $\hat{g}$ are given by certain structure factors of the dimer correlations of the square lattice Heisenberg model, and hence accessible to the continuous time loop algorithm. The numerical analysis of the matrix $\hat{g}$ for lattices with maximum 28×28 sites at various temperatures implies that the phonon branches at momentum $(\pi, 0)$ and $(0, \pi)$ are most affected by the spin-lattice interaction. This reflects the tendency of the system to establish a plaquette pattern of lattice distortions. However, the spin-phonon coupling also has a significant impact on the two phonon modes at (π, π). This kind of lattice modulation corresponds to the formation of diagonal stripes and hence a stair-like arrangement of strong and weak bonds in an effective magnetic model. The occurrence of lattice instabilities is investigated in more detail for a special choice of the bare dynamical matrix. For this K-K'-model, a significant phonon softening at $(\pi, 0)$, $(0, \pi)$ and (π, π) is found upon decreasing the temperature or alternatively, increasing the spin-phonon coupling. A thorough investigation of these features allows to examine the phase diagram of the system. Both the occurrence of the transition and the type of lattice modulations in the low temperature phase depend on the specific values of the elastic constants K and K'. Regardless of the temperature, a distorted phase only exists for sufficiently large values of the fraction $\frac{\lambda^2}{K}$. The plaquette structure can only be established for small numbers of the ratio $\frac{K'}{K}$. When increasing this ratio, two phonon branches with momentum (q, q) and $(q, -q)$ are found to vanish simultanously when increasing $\frac{\lambda^2}{K}$.

5.2. Outlook

As far as the quantum critical XXZ chain is concerned, it remains a major challenge to evaluate the exact analytical expressions for the spin correlation functions from the literature. For this reason further numerical investigations in this system are indispensable. The approach from Chapt. 3 can be directly applied to study the low-temperature correlations in the gapless attractive region $-1 < \Delta < 0$ of the phase diagram. In particular, this should lead to a better understanding of the deviations from asymptotic scaling as predicted by conformal field theory. The QMC method is also useful to examine the spin correlations at intermediate and high temperatures, where the results from conformal field theory are not valid.

The knowledge of the properties of the dimer correlation function is even more uncomplete due to a lack of analytical expressions. Similarly to the case of spin correlations, the loop algorithm or related QMC techniques can be used to study this correlation function in the region $-1 < \Delta < 0$, and at intermediate and high temperatures for general values of Δ. Other numerical approaches like DMRG allow for a direct computation of the dimer correlations in the ground state. Such data can serve for an independent analysis of the deviations from asymptotic scaling at absolute zero, which can be compared to the findings from this dissertation.

A wide field which has only been touched in this thesis is the issue of dynamical correlations of the XXZ chain. These are of particular interest because they can be measured in scattering experiments. The QMC method, however, only provides direct access to Euclidean dynamical quantities. Thus an application of DMRG or exact complete diagonalization seems to be more promising in this context.

For the square lattice Heisenberg model coupled to phonons there remain a couple of unresolved questions. As far as the two-dimensional bond coupling model is concerned, it is desirable to investigate the regime with very large spin-phonon coupling. This is especially important to give a definite answer to the question whether an increasing spin-phonon coupling can lead to a breakdown of long-range magnetic order in the ground state. In addition to this, the occurrence of lattice distortions should be investigated to establish the ground state phase diagram of the system. However, especially in the case of large spin-phonon coupling the modified loop algorithm which has been applied in this dissertation severely suffers from autocorrelation effects. For this reason the development of alternative QMC techniques seems to be helpful to cope with these problems.

Another promising way to gain more insight into the influence of the spin-phonon coupling is to consider the statically dimerized plaquette model. In principle, the continuous time loop algorithm provides access to the coefficients of the fourth and higher order terms in the Landau expansion of the free energy of this system, because arbitrary n-point correlation functions of the uniform Heisenberg model can be evaluated. Having determined the coefficient of the fourth order, a more detailed discussion on the structural phase transition from the uniform to the plaquette phase is possible. In particular, one should be able to determine the temperature dependence of the dimerization in the distorted phase. As a consequence, the analysis under which conditions the dimerization exceeds the critical value δ_c becomes feasible. Furthermore, an unambiguous result for the sign of the fourth order coefficient would allow to determine the order of the transition.

Evidently, the search for substances with a quasi two-dimensional magnetic structure is required,

which show a structural phase transition driven by the spin-phonon coupling. To find experimental evidence for the presence of a strong spin-lattice interaction, one has to identify those phonon modes of the magnetic ions which show an anomalous softening behavior. Having found such a substance, it is possible to calculate theoretical phonon dispersion curves which can be compared to the experimental data. The adiabatic approach from Sect. 4.4 directly applies to this problem, because it is not restricted to the simple special case of the K-K'-model. In practice, one has to establish the bare dynamical matrix for the specific solid by modelling the lattice degrees of freedom in a realistic fashion. Then it is straightforward to determine the full renormalized dynamical matrix by making use of the QMC data from this thesis, and hence to deduce the desired renormalized phonon frequencies.

A. Appendix

A.1. Plaquette weights for the XXZ model

In this section we give a detailed derivation of the expressions (2.2.8),(2.2.9), and (2.2.10) for the plaquette weights (2.2.7) of the XXZ model. In a simplified notation this means that we have to calculate matrix elements

$$\langle s_1 s_2 | e^{-\beta H_{\mathsf{plaq}}/M} | s_1' s_2' \rangle, \tag{A.1.1}$$

with

$$H_{\mathsf{plaq}} = \frac{J}{2}(\sigma_1^x \sigma_2^x + \sigma_1^y \sigma_2^y + \Delta \sigma_1^z \sigma_2^z). \tag{A.1.2}$$

Introducing the permutation operator P_{12} which interchanges the spins on site 1 and site 2, we can make use of the identity

$$\sigma_1^x \sigma_2^x + \sigma_1^y \sigma_2^y = (1 - \sigma_1^z \sigma_2^z) P_{12} \tag{A.1.3}$$

in the Taylor expansion

$$e^{-\beta H_{\mathsf{plaq}}/M} = \sum_{k=0}^{\infty} \frac{(-1)^k}{k!} \left(\frac{\beta J}{2M}\right)^k [(1 - \sigma_1^z \sigma_2^z) P_{12} + \Delta \sigma_1^z \sigma_2^z]^k. \tag{A.1.4}$$

We now simplify the square bracket in this expression, which becomes

$$[(1 - \sigma_1^z \sigma_2^z) P_{12} + \Delta \sigma_1^z \sigma_2^z]^k =$$

$$\sum_{m=0}^{k} \binom{k}{m} (1 - \sigma_1^z \sigma_2^z)^m P_{12}^m \Delta^{k-m} (\sigma_1^z \sigma_2^z)^{k-m} =$$

$$\sum_{m=0}^{k} \binom{k}{m} (1 - \sigma_1^z \sigma_2^z)^m \Delta^{k-m} (\sigma_1^z \sigma_2^z)^{k-m} \frac{1}{2} \{1 + (-1)^m + P_{12}[1 - (-1)^m]\} =$$

$$\frac{1}{2}(1 + P_{12}) [(1 - \sigma_1^z \sigma_2^z) + \Delta \sigma_1^z \sigma_2^z]^k + \frac{1}{2}(1 - P_{12}) [(\sigma_1^z \sigma_2^z - 1) + \Delta \sigma_1^z \sigma_2^z]^k \tag{A.1.5}$$

due to the identity $P_{12}^2 = 1$. Again we consider the square brackets, i. e.

$$[(1 - \sigma_1^z \sigma_2^z) + \Delta \sigma_1^z \sigma_2^z]^k = [\sigma_1^z \sigma_2^z (\Delta - 1) + 1]^k =$$

$$\sum_{m=0}^{k} \binom{k}{m} (\Delta - 1)^m (\sigma_1^z \sigma_2^z)^m 1^{k-m} =$$

$$\sum_{m=0}^{k} \binom{k}{m} (\Delta - 1)^m 1^{k-m} \frac{1}{2} \{1 + (-1)^m + \sigma_1^z \sigma_2^z [1 - (-1)^m]\} =$$

$$\frac{1}{2}(1 + \sigma_1^z \sigma_2^z) \Delta^k + \frac{1}{2}(1 - \sigma_1^z \sigma_2^z)(2 - \Delta)^k, \tag{A.1.6}$$

and

$$[(\sigma_1^z \sigma_2^z - 1) + \Delta \sigma_1^z \sigma_2^z]^k = \frac{1}{2}(1 + \sigma_1^z \sigma_2^z)\Delta^k + \frac{1}{2}(1 - \sigma_1^z \sigma_2^z)(-2 - \Delta)^k \tag{A.1.7}$$

in an analogous fashion (here we have $(\sigma_{1/2}^z)^2 = 1$). Therefore we find for the expression (A.1.5)

$$[(1 - \sigma_1^z \sigma_2^z)P_{12} + \Delta \sigma_1^z \sigma_2^z]^k =$$

$$\frac{1}{2}(1 + \sigma_1^z \sigma_2^z)\Delta^k + \frac{1}{4}(1 + P_{12})(1 - \sigma_1^z \sigma_2^z)(2 - \Delta)^k + \frac{1}{4}(1 - P_{12})(1 - \sigma_1^z \sigma_2^z)(-2 - \Delta)^k, \tag{A.1.8}$$

and thus for Eq. (A.1.4)

$$e^{-\beta H_{\text{plaq}}/M} =$$

$$\frac{1}{2}e^{-\beta J\Delta/2M}(1 + \sigma_1^z \sigma_2^z) + \frac{1}{4}e^{\beta J\Delta/2M}[e^{-\beta J/M}(1 + P_{12})(1 - \sigma_1^z \sigma_2^z) + e^{\beta J/M}(1 - P_{12})(1 - \sigma_1^z \sigma_2^z)]. \tag{A.1.9}$$

We now apply this identity to the basis states of the system, and obtain

$$e^{-\beta H_{\text{plaq}}/M}|++\rangle = e^{-\beta J\Delta/2M}|++\rangle,$$

$$e^{-\beta H_{\text{plaq}}/M}|+-\rangle = \frac{1}{2}e^{\beta J\Delta/2M}[e^{-\beta J/M}(|+-\rangle + |-+\rangle) + e^{\beta J/M}(|+-\rangle - |-+\rangle)],$$

$$e^{-\beta H_{\text{plaq}}/M}|-+\rangle = \frac{1}{2}e^{\beta J\Delta/2M}[e^{-\beta J/M}(|+-\rangle + |-+\rangle) + e^{\beta J/M}(|+-\rangle - |-+\rangle)],$$

$$e^{-\beta H_{\text{plaq}}/M}|--\rangle = e^{-\beta J\Delta/2M}|--\rangle. \tag{A.1.10}$$

We therefore have for the non-vanishing matrix elements

$$\langle++|e^{-\beta H_{\text{plaq}}/M}|++\rangle = \langle--|e^{-\beta H_{\text{plaq}}/M}|--\rangle = e^{-\beta J\Delta/2M}, \tag{A.1.11}$$

$$\langle+-|e^{-\beta H_{\text{plaq}}/M}|-+\rangle = \langle-+|e^{-\beta H_{\text{plaq}}/M}|+-\rangle = e^{\beta J\Delta/2M}\sinh(-\beta J/M), \tag{A.1.12}$$

$$\langle+-|e^{-\beta H_{\text{plaq}}/M}|+-\rangle = \langle-+|e^{-\beta H_{\text{plaq}}/M}|-+\rangle = e^{\beta J\Delta/2M}\cosh(\beta J/M). \tag{A.1.13}$$

These are the expressions (2.2.8),(2.2.9), and (2.2.10) except for the minus sign in the argument of the sinh in the second line. The sign is removed when considering the matrix elements of the unitarily transformed Hamiltonian

$$\tilde{H}_{\text{plaq}} \equiv \sigma_2^z H_{\text{plaq}} \sigma_2^z, \tag{A.1.14}$$

which are given by

$$\langle s_1 s_2 |e^{-\beta \tilde{H}_{\text{plaq}}/M}|s_1' s_2'\rangle =$$

$$\sum_{k=0}^{\infty} \frac{(-1)^k}{k!}\left(\frac{\beta}{M}\right)^k \langle s_1 s_2 |(\sigma_2^z H_{\text{plaq}} \sigma_2^z)^k|s_1' s_2'\rangle =$$

$$\sum_{k=0}^{\infty} \frac{(-1)^k}{k!}\left(\frac{\beta}{M}\right)^k \langle s_1 s_2 |\sigma_2^z (H_{\text{plaq}})^k \sigma_2^z|s_1' s_2'\rangle =$$

$$s_2 s_2' \sum_{k=0}^{\infty} \frac{(-1)^k}{k!}\left(\frac{\beta}{M}\right)^k \langle s_1 s_2 |(H_{\text{plaq}})^k|s_1' s_2'\rangle =$$

$$s_2 s_2' \langle s_1 s_2 |e^{-\beta H_{\text{plaq}}/M}|s_1' s_2'\rangle. \tag{A.1.15}$$

Note that in the second step again the identity $(\sigma_2^z)^2 = 1$ was used. Hence the unitary transformation only changes the sign of the matrix elements (A.1.12) as desired.

A.2. Plaquette weights for the bond coupling model

In this part we derive the Eqs. (2.3.47), (2.3.48), and (2.3.49) for the plaquette weights (2.3.45) of the bond coupling model. Simplifying our notation as in App. A.1, we have to calculate the matrix elements

$$\langle s_1 s_2 n | e^{-\beta H_{\text{plaq}}/M} | s_1' s_2' n' \rangle, \tag{A.2.16}$$

with

$$H_{\text{plaq}} = \frac{J}{2}(\vec{\sigma}_1 \vec{\sigma}_2 - c)(1 + g[a^\dagger + a]). \tag{A.2.17}$$

Note that by introducing the constant c in the bond Hamiltonian (A.2.17), we have generalized the case described in Sect. 2.3.1 where we have $c = 1$ for the summands H_i of H_{sp} in (2.3.39). We will set $c = 1$ at the end of this section. As for the plaquette weights of the XXZ model, we first expand $\exp(-\beta H_{\text{plaq}}/M)$ in a power series and find

$$\langle s_1 s_2 n | e^{-\beta H_{\text{plaq}}/M} | s_1' s_2' n' \rangle =$$
$$\sum_{k=0}^{\infty} \frac{(-1)^k}{k!} \left(\frac{\beta J}{2M} \right)^k \langle s_1 s_2 | (\vec{\sigma}_1 \vec{\sigma}_2 - c)^k | s_1' s_2' \rangle \langle n | (1 + g[a^\dagger + a])^k | n' \rangle. \tag{A.2.18}$$

By making use of the permutation operator P_{12} of the spins on site 1 and site 2 and the identity $\vec{\sigma}_1 \vec{\sigma}_2 = 2P_{12} - 1$, we can simplify

$$(\vec{\sigma}_1 \vec{\sigma}_2 - c)^k = (2P_{12} - 1 - c)^k = 2^k \left(P_{12} - \frac{1}{2}[1 + c] \right)^k =$$

$$2^k \sum_{m=0}^{k} \binom{k}{m} P_{12}^m \left(-\frac{1}{2} \right)^{k-m} (1 + c)^{k-m} \quad \overset{(P_{12}^2 = 1)}{=}$$

$$2^k \sum_{m=0}^{k} \binom{k}{m} \left(-\frac{1}{2} \right)^{k-m} (1 + c)^{k-m} \frac{1}{2} \{ 1 + (-1)^m + P_{12}[1 - (-1)^m] \} =$$

$$2^{k-1} \left[(1 + P_{12}) \sum_{m=0}^{k} \binom{k}{m} [-\frac{1}{2}(1 + c)]^{k-m} + (1 - P_{12}) \sum_{m=0}^{k} \binom{k}{m} (-1)^m [-\frac{1}{2}(1 + c)]^{k-m} \right] =$$

$$\frac{1}{2} \left[(1 + P_{12})(1 - c)^k + (1 - P_{12})(-3 - c)^k \right]. \tag{A.2.19}$$

This implies

$$\langle s_1 s_2 n | e^{-\beta H_{\text{plaq}}/M} | s_1' s_2' n' \rangle =$$

$$\frac{1}{2} \left[\langle s_1 s_2 | 1 + P_{12} | s_1' s_2' \rangle \sum_{k=0}^{\infty} \frac{(-1)^k}{k!} \left(\frac{\beta J}{2M} \right)^k (1 - c)^k \langle n | (1 + g[a^\dagger + a])^k | n' \rangle \right.$$

$$\left. + \langle s_1 s_2 | 1 - P_{12} | s_1' s_2' \rangle \sum_{k=0}^{\infty} \frac{(-1)^k}{k!} \left(\frac{\beta J}{2M} \right)^k (-3 - c)^k \langle n | (1 + g[a^\dagger + a])^k | n' \rangle \right] =$$

$$\frac{1}{2} \left[(\delta_{s_1 s_1'} \delta_{s_2 s_2'} + \delta_{s_1 s_2'} \delta_{s_2 s_1'}) \langle n | e^{\eta_1(1 + g[a^\dagger + a])} | n' \rangle + (\delta_{s_1 s_1'} \delta_{s_2 s_2'} - \delta_{s_1 s_2'} \delta_{s_2 s_1'}) \langle n | e^{\eta_2(1 + g[a^\dagger + a])} | n' \rangle \right] =$$

$$\frac{1}{2} \left[(\delta_{s_1 s_1'} \delta_{s_2 s_2'} + \delta_{s_1 s_2'} \delta_{s_2 s_1'}) A(g, \eta_1, n, n') + (\delta_{s_1 s_1'} \delta_{s_2 s_2'} - \delta_{s_1 s_2'} \delta_{s_2 s_1'}) A(g, \eta_2, n, n') \right], \tag{A.2.20}$$

where we have introduced

$$A(g, \eta, n, n') \equiv \langle n | e^{\eta(1+g[a^\dagger + a])} | n' \rangle, \qquad (A.2.21)$$

and the abbreviations $\eta_1 \equiv \frac{\beta J}{2M}(c-1)$ and $\eta_2 \equiv \frac{\beta J}{2M}(c+3)$. We now have to calculate A. We first consider the simple special case $g\eta = 0$, for which one obtains

$$A(g, \eta, n, n') = e^\eta \langle n | n' \rangle = e^\eta \delta_{n, n'}. \qquad (A.2.22)$$

Otherwise we can make use of

$$e^{g\eta(a^\dagger + a)} = e^{g\eta a^\dagger} e^{g\eta a} e^{-\frac{1}{2}[g\eta a^\dagger, g\eta a]} = e^{g\eta a^\dagger} e^{g\eta a} e^{\frac{1}{2}g^2 \eta^2}, \qquad (A.2.23)$$

and find

$$A(g, \eta, n, n') = \langle n | e^{\eta(1+g[a^\dagger + a])} | n' \rangle = e^\eta e^{\frac{1}{2}g^2 \eta^2} \langle n | e^{g\eta a^\dagger} e^{g\eta a} | n' \rangle =$$

$$e^{\eta(1+\frac{1}{2}\eta g^2)} \sum_{k=0}^\infty \frac{(g\eta)^k}{k!} \langle n | e^{g\eta a^\dagger} a^k | n' \rangle =$$

$$e^{\eta(1+\frac{1}{2}\eta g^2)} \sum_{k=0}^{n'} \frac{(g\eta)^k}{k!} \left(\prod_{i=0}^{k-1} \sqrt{n'-i} \right) \langle n | e^{g\eta a^\dagger} | n'-k \rangle =$$

$$e^{\eta(1+\frac{1}{2}\eta g^2)} \sum_{k=0}^{n'} \frac{(g\eta)^k}{k!} \left(\prod_{i=0}^{k-1} \sqrt{n'-i} \right) \sum_{l=0}^\infty \frac{(g\eta)^l}{l!} \langle n | (a^\dagger)^l | n'-k \rangle =$$

$$e^{\eta(1+\frac{1}{2}\eta g^2)} \sum_{k=0}^{n'} \sum_{l=0}^\infty \frac{(g\eta)^k}{k!} \frac{(g\eta)^l}{l!} \left(\prod_{i=0}^{k-1} \sqrt{n'-i} \right) \left(\prod_{j=0}^{l-1} \sqrt{n'-k+j+1} \right) \langle n | n'-k+l \rangle. \quad (A.2.24)$$

Since we have $\langle n | n'-k+l \rangle = \delta_{n, n'-k+l}$ we can evaluate the sum over l, which leads to

$$A(g, \eta, n, n') =$$

$$e^{\eta(1+\frac{1}{2}\eta g^2)} \sum_{k=\max\{0, n'-n\}}^{n'} \frac{(g\eta)^k}{k!} \frac{(g\eta)^{n-n'+k}}{(n-n'+k)!} \left(\prod_{i=0}^{k-1} \sqrt{n'-i} \right) \left(\prod_{j=0}^{n-n'+k-1} \sqrt{n'-k+j+1} \right) =$$

$$e^{\eta(1+\frac{1}{2}\eta g^2)} \sqrt{n! n'!} \sum_{k=\max\{0, n'-n\}}^{n'} \frac{(g\eta)^{n-n'+2k}}{k!(n-n'+k)!(n'-k)!}. \qquad (A.2.25)$$

Together with the relation (A.2.22), this is the result (2.3.50) from Sect. 2.3.1. We can now set $c = 1$, which implies $\eta_1 = 0$ and $\eta_2 = \frac{2\beta J}{M} \equiv \eta$. Inserting these findings into Eq. (A.2.20), we finally get six non-vanishing matrix elements

$$\langle + + n | e^{-\beta H_i/M} | + + n' \rangle = \langle - - n | e^{-\beta H_i/M} | - - n' \rangle = \delta_{n, n'}, \qquad (A.2.26)$$

$$\langle + - n | e^{-\beta H_i/M} | - + n' \rangle = \langle - + n | e^{-\beta H_i/M} | + - n' \rangle = -\frac{1}{2}[A(g, \eta, n, n') - \delta_{n, n'}], \qquad (A.2.27)$$

$$\langle + - n | e^{-\beta H_i/M} | + - n' \rangle = \langle - + n | e^{-\beta H_i/M} | - + n' \rangle = \frac{1}{2}[A(g, \eta, n, n') + \delta_{n, n'}]. \qquad (A.2.28)$$

Except for the minus sign in the second line, these are the results (2.3.47), (2.3.48), and (2.3.49). In complete analogy to the calculation for the XXZ model, this sign can be removed by considering the matrix elements of the unitarily transformed Hamiltonian (A.1.14) of (A.2.17), see also App. A.1.

A.3. Measurement rules for four-point correlation functions

In this section, we make use of the relation (2.4.74) from Sect. 2.4.3 and derive measurement rules for those four-point correlators which are needed for the evaluation of dimer correlations $\langle D_i(\tau_1) D_j(\tau_2) \rangle$. Here the dimer operator $D_i(\tau_1)$ is defined by $D_i(\tau_1) \equiv \vec{\sigma}_i(\tau_1) \vec{\sigma}_{i+1}(\tau_1) \equiv \vec{\sigma}_{x_1} \vec{\sigma}_{x_2}$ (for $D_j(\tau_2)$ analogously), i. e. according to our notation from Sects. 2.4.2 and 2.4.3 the indices x_1 and x_2 denote spacetime points on the $(1+1)$-dimensional checkerboard lattice for the XXZ model. Due to the identity $\vec{\sigma}_{x_1} \vec{\sigma}_{x_2} = 2(S_{x_1}^+ S_{x_2}^- + S_{x_1}^- S_{x_2}^+) + \sigma_{x_1}^z \sigma_{x_2}^z$, we have

$$
\begin{aligned}
D_i(\tau_1) D_j(\tau_2) = {} & \sigma_{x_1}^z \sigma_{x_2}^z \sigma_{y_1}^z \sigma_{y_2}^z \\
& + 2 \left[\sigma_{x_1}^z \sigma_{x_2}^z S_{y_1}^+ S_{y_2}^- + \sigma_{x_1}^z \sigma_{x_2}^z S_{y_1}^- S_{y_2}^+ + S_{x_1}^+ S_{x_2}^- \sigma_{y_1}^z \sigma_{y_2}^z + S_{x_1}^- S_{x_2}^+ \sigma_{y_1}^z \sigma_{y_2}^z \right] \\
& + 4 \left[S_{x_1}^+ S_{x_2}^- S_{y_1}^+ S_{y_2}^- + S_{x_1}^+ S_{x_2}^- S_{y_1}^- S_{y_2}^+ + S_{x_1}^- S_{x_2}^+ S_{y_1}^+ S_{y_2}^- + S_{x_1}^- S_{x_2}^+ S_{y_1}^- S_{y_2}^+ \right],
\end{aligned} \tag{A.3.29}
$$

and hence we have to determine measurement rules for four-point correlations of the type

$$
\langle \sigma_v^z \sigma_w^z \sigma_x^z \sigma_y^z \rangle, \tag{A.3.30}
$$

$$
\langle S_v^+ S_w^- \sigma_x^z \sigma_y^z \rangle, \tag{A.3.31}
$$

$$
\langle S_v^+ S_w^- S_x^+ S_y^- \rangle, \tag{A.3.32}
$$

with general spacetime indices v, w, x, y. As has been mentioned in Par. 2.4.3, there are only two possibilities to obtain a non-vanishing contribution to these expectation values. One situation is that the four spins s_v, s_w, s_x, s_y group into two pairs of spins which belong to two different loops. The second possibility is that the spins all belong to one single loop.

We start with the correlation function (A.3.30). Since the corresponding operator is diagonal with respect to the basis of the Hilbert space, we can argue in an analogous way to our approach for the longitudinal two-point correlations in Sect. 2.4.2. One immediately finds

$$
\langle \sigma_v^z \sigma_w^z \sigma_x^z \sigma_y^z \rangle \rightarrow
\begin{cases}
s_v s_w s_x s_y & \text{if the spins group into two pairs belonging to different loops,} \\
s_v s_w s_x s_y & \text{if the four spins all belong to one single loop,} \\
0 & \text{else.}
\end{cases} \tag{A.3.33}
$$

The identical result can also be derived from relation (2.4.74) by evaluating the relevant traces.

s_x	s_y	one-loop contribution from $S_x^+ \sigma_y^z$	one-loop contribution from $S_x^+ S_y^+$
+1	+1	$\mathrm{Tr}\,(\sigma^+ \sigma^z) = 0$	$\mathrm{Tr}\,(\sigma^+ \sigma^+) = 0$
-1	-1	$\mathrm{Tr}\,(\sigma^- \sigma^z) = 0$	$\mathrm{Tr}\,(\sigma^- \sigma^-) = 0$
+1	-1	$\mathrm{Tr}\,(\sigma^+ \sigma^x \sigma^z \sigma^x) = 0$	$\mathrm{Tr}\,(\sigma^+ \sigma^x \sigma^- \sigma^x) = 0$
-1	+1	$\mathrm{Tr}\,(\sigma^- \sigma^x \sigma^z \sigma^x) = 0$	$\mathrm{Tr}\,(\sigma^- \sigma^x \sigma^+ \sigma^x) = 0$

Table A.1.: Evaluation of the trace over a single loop for the cases that $S_x^+ \sigma_y^z$ and $S_x^+ S_y^+$ act on the two spins s_x, s_y.

We now consider expectation values of the type (A.3.31). For the two-loop contributions, there are two different cases. The first is that the four spins group into pairs (s_v, s_w) and (s_x, s_y). Then for the first pair, we have to evaluate the trace over a loop where two matrices $\sigma^{\pm}$ (depending on the value of the spin variables s_v, s_w) have been inserted. Similarly, for the second pair the trace over a loop after the insertion of two σ^z matrices has to be determined. We have already derived the results in Table 2.1 in the context of two-point correlations, see Sect. 2.4.3. Hence the total contribution is given by the product $\frac{1}{2}s_x s_y$. In the second case we have the two distributions $(s_v, s_x), (s_w, s_y)$ and $(s_v, s_y), (s_w, s_x)$, respectively. Here the relevant traces over the individual loops both vanish. The case that the two operators S^+, σ^z are applied to two spins lying on the same loop is considered in Table A.1. The one-loop contributions depend on the order in which the four spins are traversed by the loop. For example, if we assume that all four spins have the same value $+1$ and that they are stringed according to $s_v \rightarrow s_x \rightarrow s_w \rightarrow s_y$, we have to evaluate

$$\frac{1}{2}\text{Tr } (\sigma^+ \sigma^z \sigma^- \sigma^z) = -\frac{1}{2} = -\frac{1}{2}s_x s_y. \tag{A.3.34}$$

As usual, the prefactor $\frac{1}{2}$ takes into account the normalization factor $\frac{1}{2}$ from Eq. (2.4.74). Observing that there are $2^4 = 16$ different spin configurations and six possibilities to line up the four spins, we have to perform such a calculation in 96 different cases. As a result one finds that there are only two different contributions $\pm \frac{1}{2}s_x s_y$, where the sign depends on the order in which the four spins are traversed by the loop. Adding an additional factor of $(-1)^{g+h}$ (g, h are the spatial components of the indices v, w) for the influence of the unitary transformation (2.2.11) from Sect. 2.2.1 for both one- and two-loop contributions, we finally obtain

$$\langle S_v^+ S_w^- \sigma_x^z \sigma_y^z \rangle \rightarrow \begin{cases} (-1)^{g+h} s_x s_y & \text{if the spins group into two pairs } (s_v, s_w), (s_x, s_y) \\ & \text{belonging to different loops,} \\ (-1)^{g+h} s_x s_y & \text{if the spins belong to a single loop and are traversed} \\ & \text{according to } s_v \rightarrow s_w \rightarrow s_x \rightarrow s_y, \ s_v \rightarrow s_w \rightarrow s_y \rightarrow s_x \\ & \text{(or the reversed orders),} \\ (-1)^{g+h+1} s_x s_y & \text{if the spins belong to a single loop and are traversed} \\ & \text{according to } s_v \rightarrow s_x \rightarrow s_w \rightarrow s_y \text{ (or reversed),} \\ 0 & \text{else.} \end{cases}$$

$$\tag{A.3.35}$$

At last we consider correlations of the type (A.3.32). As for the correlation function (A.3.31), we have to distinguish between two cases for the two-loop contributions. If the four spins group into pairs $(s_v, s_w), (s_x, s_y)$ or $(s_v, s_y), (s_w, s_x)$, we find two factors of the same type that we have determined in Table 2.1 for the two-point function $\langle S_x^+ S_y^- \rangle$. Therefore the total contribution is $(\frac{1}{2})^2 = \frac{1}{4}$. In the case that the pairs are $(s_v, s_x), (s_w, s_y)$, there is no contribution because the action of two operators S^+ to different spins belonging to the same loop yields vanishing traces, see also Table A.1. For the one-loop contributions, we only have to calculate a single trace as before. In the example given in the context of the correlations (A.3.31), the relevant trace is

$$\frac{1}{2}\text{Tr } (\sigma^+ \sigma^+ \sigma^- \sigma^-) = 0. \tag{A.3.36}$$

Again such a calculation has to be done in 96 different cases. We find that the results only take two different values, namely a vanishing contribution (as in our example) or the value of $\frac{1}{2}$, which depends on the order in which the four spins are traversed by the loop. We finally have to include an additional prefactor $(-1)^{g+h+i+j}$ which accounts for the influence of the unitary transformation (2.2.11), where g, h, i, j are the spatial components of the spacetime indices v, w, x, y. Thus in summary, we have

$$
\langle S_v^+ S_w^- S_x^+ S_y^- \rangle \to
\begin{cases}
(-1)^{g+h+i+j}\frac{1}{4} & \text{if the spins group into two pairs } (s_v, s_w), (s_x, s_y) \text{ or} \\
& (s_v, s_y), (s_w, s_x) \text{ belonging to different loops,} \\
(-1)^{g+h+i+j}\frac{1}{2} & \text{if the spins belong to a single loop and are traversed} \\
& \text{according to } s_v \to s_w \to s_y \to s_x \text{ (or the reversed order),} \\
0 & \text{else.}
\end{cases}
$$

(A.3.37)

A.4. A useful identity for the calculation of dimerizabilities

In this section we prove the identity (compare Eq. (A.4.38) from Par. 4.3.2)

$$
\frac{\partial^2}{\partial \delta^2}\bigg|_{\delta=0} \text{Tr } e^{-\beta H + \delta A} = \frac{Z}{\beta} \int_0^\beta d\tau \, \langle A(0) A(\tau) \rangle,
$$

(A.4.38)

which is used for the calculation of dimerizabilities in Sects. 4.3.2 and 4.3.3. Here A is an arbitrary operator which does not necessarily commute with H. The partition function Z as well as the expectation values on the right-hand side are defined with respect to the unperturbed Hamiltonian H, and the time-dependence of $A(\tau)$ is given by a translation in imaginary time direction as defined by Eq. (2.4.67), see Par. 2.4.1.

We start with the right-hand side of Eq. (A.4.38). Making use of the definition (2.4.67), we find

$$
\frac{Z}{\beta} \int_0^\beta d\tau \, \langle A(0) A(\tau) \rangle =
$$

$$
\frac{Z}{\beta} \int_0^\beta d\tau \frac{1}{Z} \text{Tr} \left(A e^{-\tau H} A e^{(\tau - \beta)H} \right) =
$$

$$
\frac{1}{\beta} \int_0^\beta d\tau \, \text{Tr} \left[A \left(\sum_{k=0}^\infty \frac{(-\tau)^k}{k!} H^k \right) A \left(\sum_{l=0}^\infty \frac{(\tau - \beta)^l}{l!} H^l \right) \right] =
$$

$$
\frac{1}{\beta} \int_0^\beta d\tau \, \text{Tr} \left[A \sum_{k=0}^\infty \sum_{l=0}^k \frac{(-\tau)^l}{l!} \frac{(\tau - \beta)^{k-l}}{(k-l)!} H^l A H^{K-l} \right] =
$$

$$
\frac{1}{\beta} \text{Tr} \left[A \sum_{k=0}^\infty \sum_{l=0}^k \frac{(-1)^l}{l!(k-l)!} \left(\int_0^\beta d\tau \, \tau^l (\tau - \beta)^{k-l} \right) H^l A H^{k-l} \right],
$$

(A.4.39)

where we have inserted the Taylor representation of the exponential function in the third line, followed by an application of the Cauchy formula for the product of two infinite series. Evaluating the integral

$$
\int_0^\beta d\tau \, \tau^l (\tau - \beta)^{k-l} = (-1)^{k-l} \beta^{k+1} \frac{(k-l)!\,l!}{(k+1)!},
$$

(A.4.40)

the expression (A.4.39) becomes

$$\frac{Z}{\beta} \int_0^\beta d\tau \, \langle A(0)A(\tau) \rangle =$$

$$\text{Tr} \left[A \sum_{k=0}^\infty \frac{(-\beta)^k}{(k+1)!} \sum_{l=0}^k H^l A H^{k-l} \right] =$$

$$\text{Tr} \left[A \sum_{k=1}^\infty \frac{1}{k!} \sum_{l=1}^k (-\beta H)^{l-1} A (-\beta H)^{k-l} \right] =$$

$$\text{Tr} \left[A \sum_{k=1}^\infty \frac{1}{k!} \sum_{l=1}^k (-\beta H + \delta A)^{l-1} A (-\beta H + \delta A)^{k-l} \right]\bigg|_{\delta=0} =$$

$$\frac{\partial}{\partial \delta}\bigg|_{\delta=0} \text{Tr} \left[A \sum_{k=0}^\infty \frac{1}{k!} (-\beta H + \delta A)^k \right] =$$

$$\frac{\partial}{\partial \delta}\bigg|_{\delta=0} \text{Tr} \left(A \, e^{-\beta H + \delta A} \right) = \frac{\partial^2}{\partial \delta^2}\bigg|_{\delta=0} \text{Tr} \, e^{-\beta H + \delta A} \tag{A.4.41}$$

due to the cyclic invariance of the trace symbol. The result (A.4.41) is the left-hand side of Eq. (A.4.38).

A.5. Derivation of the bare dynamical matrix $\hat{G}_0$ for the K-K'-model

In this appendix we derive the expressions (4.4.80), (4.4.81), and (4.4.82) for the entries of the dynamical matrix $\hat{G}_0(\vec{q})$ of the K-K'-model, see Par. 4.4.3. We start with the general expression for the harmonic potential between two lattice ions at lattice sites $\vec{r}$, $\vec{r}'$,

$$V(\vec{R}_{\vec{r}} - \vec{R}_{\vec{r}'}) = \frac{K_0}{2} \left[\frac{\vec{r} - \vec{r}'}{|\vec{r} - \vec{r}'|} (\vec{u}_{\vec{r}} - \vec{u}_{\vec{r}'}) \right]^2, \tag{A.5.42}$$

where K_0 is the elastic constant which defines the energy scale of the interaction. As far as the K-K'-model is concerned , the total lattice potential consists of the two parts

$$V(\{\vec{R}_{\vec{r}}\}) = V_{\text{NN}}(\{\vec{R}_{\vec{r}}\}) + V_{\text{NNN}}(\{\vec{R}_{\vec{r}}\}), \tag{A.5.43}$$

where V_{NN} is the sum of the potentials between pairs of the nearest neighbors (coupling K), and V_{NNN} contains all contributions of pairs of the next-nearest neighbors (coupling constant K'). According to Eq. (A.5.42), the total contribution of the nearest neighbor terms is

$$V_{\text{NN}}(\{\vec{R}_{\vec{r}}\}) = \frac{1}{2} \sum_{i,j=1}^N \frac{K}{2} \bigg\{ \left[\begin{pmatrix} 1 \\ 0 \end{pmatrix} (\vec{u}_{ij} - \vec{u}_{i+1,j}) \right]^2 + \left[\begin{pmatrix} -1 \\ 0 \end{pmatrix} (\vec{u}_{ij} - \vec{u}_{i-1,j}) \right]^2$$

$$+ \left[\begin{pmatrix} 0 \\ 1 \end{pmatrix} (\vec{u}_{ij} - \vec{u}_{i,j+1}) \right]^2 + \left[\begin{pmatrix} 0 \\ -1 \end{pmatrix} (\vec{u}_{ij} - \vec{u}_{i,j-1}) \right]^2 \bigg\}, \tag{A.5.44}$$

where the lattice constant has been set to one as usual, and the global factor of $\frac{1}{2}$ takes into account that the contribution of each pair of neighboring ions is counted twice in the summation.

In the following we evaluate the vector products in the squared brackets and determine the squares of the resulting expressions. For example under the assumption of periodic boundary conditions, the first squared bracket from Eq. (A.5.44) gives

$$\frac{1}{2} \sum_{i,j=1}^{N} \frac{K}{2} \left[\begin{pmatrix} 1 \\ 0 \end{pmatrix} (\vec{u}_{ij} - \vec{u}_{i+1,j}) \right]^2 = \frac{K}{2} \sum_{i,j=1}^{N} \left[(u_{ij}^x)^2 - u_{ij}^x u_{i+1,j}^x \right]. \tag{A.5.45}$$

Comparing this result to the relation (4.4.55) from Sect. 4.4, we find that the selected term contributes to the following entries of the real space dynamical matrix $G_0(\vec{x})$:

$$G_0^{xx}(\vec{x} = (0,0)) \rightarrow \frac{K}{m}, \qquad G_0^{xx}(\vec{x} = (1,0)) \rightarrow -\frac{K}{m}. \tag{A.5.46}$$

For the other three summands in the expression (A.5.44), we can proceed in an analogous fashion. We receive the following non-vanishing contributions to the entries of the matrix $G_0(\vec{x})$:

$$G_{0,\text{NN}}^{xx}(0,0) = \frac{2K}{m}, \tag{A.5.47}$$

$$G_{0,\text{NN}}^{xx}(1,0) = G_{0,\text{NN}}^{xx}(-1,0) = -\frac{K}{m}, \tag{A.5.48}$$

$$G_{0,\text{NN}}^{yy}(0,0) = \frac{2K}{m}, \tag{A.5.49}$$

$$G_{0,\text{NN}}^{yy}(0,1) = G_{0,\text{NN}}^{yy}(0,-1) = -\frac{K}{m}. \tag{A.5.50}$$

With these numbers, it is possible to calculate the Fourier transform $\hat{G}_{0,\text{NN}}(\vec{q})$ of $G_{0,\text{NN}}(\vec{x})$ according to Eq. (4.4.72), see Par. 4.4.1. The result is

$$\hat{G}_{0,\text{NN}}^{xx}(\vec{q}) = \frac{2K}{m}(1 - \cos q_1), \tag{A.5.51}$$

$$\hat{G}_{0,\text{NN}}^{yy}(\vec{q}) = \frac{2K}{m}(1 - \cos q_2), \tag{A.5.52}$$

$$\hat{G}_{0,\text{NN}}^{xy}(\vec{q}) = \hat{G}_{0,\text{NN}}^{yx}(\vec{q}) = 0, \tag{A.5.53}$$

which also reflects the elementary symmetries of the square lattice. For the lattice potential V_{NNN} in Eq. (A.5.43) the way of proceeding is completely analogous. The relation (A.5.44) is replaced by

$$V_{\text{NNN}}(\{\vec{R}_{\vec{r}}\}) = \frac{1}{2} \sum_{i,j=1}^{N} \frac{K'}{2} \left\{ \left[\frac{1}{\sqrt{2}} \begin{pmatrix} 1 \\ 1 \end{pmatrix} (\vec{u}_{ij} - \vec{u}_{i+1,j+1}) \right]^2 + \left[\frac{1}{\sqrt{2}} \begin{pmatrix} -1 \\ -1 \end{pmatrix} (\vec{u}_{ij} - \vec{u}_{i-1,j-1}) \right]^2 \right.$$

$$\left. + \left[\frac{1}{\sqrt{2}} \begin{pmatrix} 1 \\ -1 \end{pmatrix} (\vec{u}_{ij} - \vec{u}_{i+1,j-1}) \right]^2 + \left[\frac{1}{\sqrt{2}} \begin{pmatrix} -1 \\ 1 \end{pmatrix} (\vec{u}_{ij} - \vec{u}_{i-1,j+1}) \right]^2 \right\}. \tag{A.5.54}$$

Again we have to evaluate the squared vector products. Now we find the following non-vanishing contributions to the entries of the real space dynamical matrix $G_0(\vec{x})$:

$$G_{0,\text{NNN}}^{xx}(0,0) = \frac{2K'}{m}, \tag{A.5.55}$$

$$G_{0,\text{NNN}}^{xx}(1,1) = G_{0,\text{NNN}}^{xx}(-1,-1) = G_{0,\text{NNN}}^{xx}(1,-1) = G_{0,\text{NNN}}^{xx}(-1,1) = -\frac{K'}{2m}, \tag{A.5.56}$$

$$G_{0,\text{NNN}}^{yy}(0,0) = \frac{2K'}{m}, \tag{A.5.57}$$

$$G_{0,\text{NNN}}^{yy}(1,1) = G_{0,\text{NNN}}^{yy}(-1,-1) = G_{0,\text{NNN}}^{yy}(1,-1) = G_{0,\text{NNN}}^{yy}(-1,1) = -\frac{K'}{2m}, \tag{A.5.58}$$

$$G_{0,\text{NNN}}^{xy}(1,1) = G_{0,\text{NNN}}^{xy}(-1,-1) = -G_{0,\text{NNN}}^{xy}(1,-1) = -G_{0,\text{NNN}}^{xy}(-1,1) = -\frac{K'}{2m}, \tag{A.5.59}$$

$$G_{0,\text{NNN}}^{yx}(1,1) = G_{0,\text{NNN}}^{yx}(-1,-1) = -G_{0,\text{NNN}}^{yx}(1,-1) = -G_{0,\text{NNN}}^{yx}(-1,1) = -\frac{K'}{2m}. \tag{A.5.60}$$

Then the calculation of the Fourier transform $\hat{G}_{0,\text{NNN}}(\vec{q})$ of $G_{0,\text{NNN}}(\vec{x})$ yields

$$\hat{G}_{0,\text{NNN}}^{xx}(\vec{q}) = \hat{G}_{0,\text{NNN}}^{yy}(\vec{q}) = \frac{2K'}{m}(1 - \cos q_1 \cos q_2), \tag{A.5.61}$$

$$\hat{G}_{0,\text{NNN}}^{xy}(\vec{q}) = \hat{G}_{0,\text{NNN}}^{yx}(\vec{q}) = \frac{2K'}{m} \sin q_1 \sin q_2. \tag{A.5.62}$$

By adding the matrices $\hat{G}_{0,\text{NN}}(\vec{q})$ defined by the Eqs. (A.5.51), (A.5.52), (A.5.53), and $\hat{G}_{0,\text{NNN}}(\vec{q})$ with entries (A.5.61) and (A.5.62), respectively, we finally obtain the results (4.4.80), (4.4.81), and (4.4.82) from Sect. 4.4.3, i. e. the desired result for the bare dynamical matrix $\hat{G}_0(\vec{q})$ of the K-K'-model.

Bibliography

[AG00]   J.V. Alvarez and C. Gros, *On the evaluation of the specific heat and general off-diagonal n-point correlation functions within the loop algorithm*, Eur. Phys. J. B **15** (2000), 641.

[AGSZ89] I. Affleck, D. Gepner, H.J. Schulz, and T. Ziman, *Critical behvior of spin-S Heisenberg antiferromagnetic chains - analytic and numerical results*, J. Phys. A **22** (1989), 511.

[Ait02]   C.H. Aits, *Quanten-Monte-Carlo-Untersuchungen effektiver Spinmodelle mit Spin-Phonon-Kopplung*, diploma thesis (in German), Universität zu Köln, 2002.

[AL03]   C.H. Aits and U. Löw, *Thermodynamic properties of the two-dimensional S=1/2 Heisenberg antiferromagnet coupled to bond phonons*, Phys. Rev. B **68** (2003), 184416.

[AL05]   C.H. Aits and U. Löw, *Conformal invariance and correlation functions in the antiferromagnetic S=1/2 XXZ chain – a quantum Monte Carlo study*, to be published, 2005.

[ALKW05] C.H. Aits, U. Löw, A. Klümper, and W. Weber, *Structural instabilities of layered magnetic systems beyond the Einstein phonon approximation*, to be published, 2005.

[And52]   P.W. Anderson, *An approximate quantum theory of the antiferromagnetic ground state*, Phys. Rev. **86** (1952), 694.

[And63]   P.W. Anderson, *Theory of magnetic exchange interactions - exchange in insulators and semiconductors*, Solid State Phys. **14** (1963), 99.

[And87]   P.W. Anderson, *The resonating valence bond state in La_2CuO_4 and superconductivity*, Science **235** (1987), 1196.

[AO00]   A. Al-Omari, *Spin-Peierls dimerization of a s=1/2 Heisenberg antiferromagnet on a square lattice*, J. Phys. Soc. Jpn. **69** (2000), 3387.

[Aue94]   A. Auerbach, *Interacting electrons and quantum magnetism*, pp. 21–28, Springer-Verlag, New York Berlin Heidelberg, 1994.

[Bar91]   T. Barnes, *The 2d Heisenberg antiferromagnet in high-T_C superconductivity*, Int. J. Mod. Phys. C **2** (1991), 659.

[Bax82]   R. J. Baxter, *Exactly solved models in statistical mechanics*, pp. 127–179, Academic Press, London New York, 1982.

[BB05]   W. Barford and R.J. Bursill, *Peierls transition in the quantum spin-Peierls model*, preprint, **cond-mat**/0506133, 2005.

[BBGW98] B.B. Beard, R.J. Birgeneau, M. Greven, and U.-J. Wiese, *Square-lattice Heisenberg antiferromagnet at very large correlation lengths*, Phys. Rev. Lett. **80** (1998), 1742.

[BCW98]   R. Brower, S. Chandrasekharan, and U.-J. Wiese, *Green's functions from quantum cluster algorithms*, Physica A **261** (1998), 520.

[Bet31]   H.A. Bethe, *Zur Theorie der Metalle. I. Eigenwerte und Eigenfunktionen der linearen Atomkette*, Z. Phys. **71** (1931), 205.

[BM86]   J.G. Bednorz and K.A. Müller, *Possible high-T_C superconductivity in the Ba-La-Cu-O system*, Z. Phys. B **64** (1986), 189.

[BMH99]   R.J. Bursill, R.H. McKenzie, and C.J. Hamer, *Phase diagram of a Heisenberg spin-Peierls model with quantum phonons*, Phys. Rev. Lett. **83** (1999), 408.

[BPZ84]   A.A. Belavin, A.M. Polyakov, and A.B. Zamolodchikov, *Infinite conformal symmetry in two-dimensional quantum field theory*, Nucl. Phys. B **241** (1984), 333, and references therein.

[Büh03]   A. Bühler, *High temperature series expansions for spin- and spin-phonon-systems*, PhD thesis, Universität zu Köln, 2003.

[BUO04]   A. Bühler, G.S. Uhrig, and J. Oitmaa, *Thermodynamics of a spin-1/2 chain coupled to Einstein phonons*, Phys. Rev. B **70** (2004), 214429.

[BW96]   B.B. Beard and U.-J. Wiese, *Simulations of discrete quantum systems in continuous Euclidean time*, Phys. Rev. Lett. **77** (1996), 5130.

[BWL$^+$96] M. Braden, G. Wilkendorf, J. Lorenzana, M. Aïn, G.J. McIntyre, M. Behruzi, G. Heger, G. Dhalenne, and A. Revcolevschi, *Structural analysis of CuGeO$_3$: Relation between nuclear structure and magnetic interaction*, Phys. Rev. B **54** (1996), 1105.

[Car86]   J.L. Cardy, *Operator content of two-dimensional conformally invariant theories*, Nucl. Phys. B **270** (1986), 186.

[Car90]   J.L. Cardy, *Conformal invariance and statistical mechanics*, Les Houches 1988: Fields, strings and critical phenomena (E. Brézin and J. Zinn-Justin, eds.), North Holland, Amsterdam Oxford New York Tokyo, 1990, pp. 169–246, and references therein.

[Car96]   J.L. Cardy, *Scaling and renormalization in statistical physics*, pp. 52–55, Cambridge University Press, Cambridge New York Melbourne, 1996.

[CCE95]   G. Castilla, S. Chakravarty, and V.J. Emery, *Quantum magnetism of CuGeO$_3$*, Phys. Rev. Lett. **75** (1995), 1823.

[CEF$^+$95] S. Caracciolo, R.G. Edwards, S.J. Ferreira, A. Pelissetto, and A.D. Sokal, *Extrapolating Monte Carlo simulations to infinite volume: finite-size scaling at $\frac{\xi}{L} \gg 1$*, Phys. Rev. Lett. **74** (1995), 2969.

[CEPS95]   S. Caracciolo, R.G. Edwards, A. Pelissetto, and A.D. Sokal, *Asymptotic scaling in the two-dimensional O(3) σ model at correlation length 10^5*, Phys. Rev. Lett. **75** (1995), 1891.

[CF79]   M.C. Cross and D.S. Fisher, *A new theory of the spin-Peierls transition with special relevance to the experiments on TTFCuBDT*, Phys. Rev. B **19** (1979), 402.

[CHN89]   S. Chakravarty, B.I. Halperin, and D.R. Nelson, *Two-dimensional quantum Heisenberg anti-ferromagnet at low temperatures*, Phys. Rev. B **39** (1989), 2344.

[CL83]   J.J. Cullen and D.P. Landau, *Monte Carlo studies of one-dimensional quantum Heisenberg and XY models*, Phys. Rev. B **27** (1983), 297.

[CRPP95]   S.L. Chaplot, W. Reichardt, L. Pintschovius, and N. Pyka, *Common interatomic potential model for the lattice dynamics of several cuprates*, Phys. Rev. B **52** (1995), 7230.

[DM90]   H.-Q. Ding and M.S. Makivić, *Spin correlations of 2d quantum antiferromagnet at low temperatures and a direct comparison with neutron-scattering experiments*, Phys. Rev. Lett. **64** (1990), 1449.

[DM91]   H.-Q. Ding and M.S. Makivić, *Two-dimensional spin-1/2 Heisenberg antiferromagnet: A quantum Monte Carlo study*, Phys. Rev. B **43** (1991), 3562.

[DOB$^+$81] P.M. Duxbury, J. Oitmaa, M.N. Barber, A. van der Bilt, K.O. Joung, and R.L. Carlin, *Transverse susceptibility of the one-dimensional antiferromagnetic XY model. Application to Cs_2CoCl*, Phys. Rev. B **24** (1981), 5149.

[Egg96a] S. Eggert, *Accurate determination of the exchange constant in Sr_2CuO_3 from recent theoretical results*, Phys. Rev. B **53** (1996), 5116.

[Egg96b] S. Eggert, *Numerical evidence for multiplicative logarithmic corrections from marginal operators*, Phys. Rev. B **54** (1996), R9612.

[ELM93] H.G. Evertz, G. Lana, and M. Marcu, *Cluster algorithm for vertex models*, Phys. Rev. Lett. **70** (1993), 875.

[Eve01] H.G. Evertz, *The loop algorithm*, Numerical methods for lattice quantum many-body problems (D.J. Scalapino, ed.), Addison Weasly, Reading, MA, 2001, **cond-mat**/9707221, and references therein.

[EYB$^+$88] Y. Endoh, K. Yamada, R.J. Birgeneau, D.R. Gabbe, H.P. Jenssen, M.A. Kastner, C.J. Peters, P.J. Picone, T.R. Thurston, J.M. Tranquada, G. Shirane, Y. Hidaka, M. Oda, Y. Enomoto, M. Suzuki, and T. Murakami, *Static and dynamic spin correlations in pure and doped La_2CuO_4*, Phys. Rev. B **37** (1988), 7443.

[FM99] K. Fabricius and B.M. McCoy, *Quantum-classical crossover in the spin-1/2 XXZ chain*, Phys. Rev. B **59** (1999), 381.

[FQS84] D. Friedan, Z. Qiu, and S. Shenker, *Conformal invariance, unitarity, and critical exponents in two dimensions*, Phys. Rev. Lett. **52** (1984), 1575.

[FT81] L.D. Faddeev and L.A. Takhtajan, *What is the spin of a spin-wave*, Phys. Lett. A **85** (1981), 375.

[FW00] S. Feldkemper and W. Weber, *Superexchange via cluster states: Calculations of spin-phonon coupling constants for $CuGeO_3$*, Phys. Rev. B **62** (2000), 3816.

[Gin90] P. Ginsparg, *Applied conformal field theory*, Les Houches 1988: Fields, strings and critical phenomena (E. Brézin and J. Zinn-Justin, eds.), North Holland, Amsterdam Oxford New York Tokyo, 1990, pp. 1–168, and references therein.

[GK96] W. Geertsma and D. Khomskii, *Influence of side groups on $90°$ superexchange: A modification of the Goodenough-Kanamori-Anderson rules*, Phys. Rev. B **54** (1996), 3011.

[GKS04] F. Göhmann, A. Klümper, and A. Seel, *Integral representations for correlation functions of the XXZ chain at finite temperature*, J. Phys. A **37** (2004), 7625.

[GLG$^+$00] M. Grove, P. Lemmens, G. Güntherodt, B.C. Sales, F. Büllesfeld, and W. Assmus, *Magnetoelastic coupling and spin excitations in the spin-gap system $(VO)_2P_2O_7$: A Raman scattering study*, Phys. Rev. B **61** (2000), 6126.

[GNT$^+$97] A.W. Garrett, S.E. Nagler, D.A. Tennant, B.C. Sales, and T. Barnes, *Magnetic excitations in the $S=1/2$ alternating chain compound $(VO)_2P_2O_7$*, Phys. Rev. Lett. **79** (1997), 745.

[GO86] P. Goddard and D. Olive, *Kac-Moody and Virasoro algebras in relation to quantum physics*, Int. J. Mod. Phys. A **1** (1986), 303, and references therein.

[Goo55] J.B. Goodenough, *Theory of the role of covalence in the perovskite-type manganites $[La,M(II)]MnO_3$*, Phys. Rev. **100** (1955), 564.

[GS89] T. Giamarchi and H.J. Schulz, *Correlation functions of one-dimensional quantum systems*, Phys. Rev. B **39** (1989), 4620.

[Gut63] M.C. Gutzwiller, *Effect of correlation on the ferromagnetism of transition metals*, Phys. Rev. Lett. **10** (1963), 159.

[Han62] D.C. Handscomb, *Monte Carlo method in quantum statistical mechanics*, Proc. Cambridge Philos. Soc. **58** (1962), 594.

[HF98] T. Hikihara and A. Furusaki, *Correlation amplitude for the S=1/2 XXZ spin chain in the critical region: Numerical renormalization-group study of an open chain*, Phys. Rev. B **58** (1998), R583.

[HF01] T. Hikihara and A. Furusaki, *Spin correlations in the two-leg antiferromagnetic ladder in a magnetic field*, Phys. Rev. B **63** (2001), 134438.

[HF04] T. Hikihara and A. Furusaki, *Correlation amplitudes for the spin-$\frac{1}{2}$ XXZ chain in a magnetic field*, Phys. Rev. B **69** (2004), 064427.

[HHM95] K.A. Hallberg, P. Horsch, and G. Martínez, *Numerical renormalization-group study of the correlation functions of the antiferromagnetic spin-1/2 Heisenberg chain*, Phys. Rev. B **52** (1995), R719.

[HKS$^+$79] S. Huizinga, J. Kommandeur, G.A. Sawatzky, B.T. Thole, K. Kopinga, W.J.M. de Jonge, and J. Roos, *Spin-Peierls transition in N-methyl-N-ethyl-morpholinium-ditetracyanoquinodimethanide [MEM-(TCNQ)$_2$]*, Phys. Rev. B **19** (1979), 4723.

[HSH$^+$95] K. Hirota, G. Shirane, Q.J. Harris, Q. Feng, R.J. Birgeneau, M. Hase, and K. Uchinokura, *Characterization of the structural and magnetic fluctuations near the spin-Peierls transition in CuGeO$_3$*, Phys. Rev. B **52** (1995), 15412.

[HSSB81] J.E. Hirsch, D.J. Scalapino, R.L. Sugar, and R. Blankenbecler, *Efficient Monte Carlo procedure for systems with fermions*, Phys. Rev. Lett. **47** (1981), 1628.

[HTU93] M. Hase, I. Terasaki, and K. Uchinokura, *Observation of the spin-Peierls transition in linear Cu^{2+} (spin-1/2) chains in an inorganic compound CuGeO$_3$*, Phys. Rev. Lett. **70** (1993), 3651.

[Hub63] J. Hubbard, *Electron correlations in narrow energy bands*, Proc. Roy. Soc. A **276** (1963), 238.

[HZ93] F.D.M. Haldane and M.R. Zirnbauer, *Exact calculation of the ground-state dynamical spin correlation function of a S=1/2 antiferromagnetic Heisenberg chain with free spinons*, Phys. Rev. Lett. **71** (1993), 4055.

[JBJ$^+$76] I.S. Jacobs, J.W. Bray, H.R. Hart Jr., L.V. Interrante, J.S. Kasper, G.D. Watkins, D.E. Prober, and J.C. Bonner, *Spin-Peierls transitions in magnetic donor-acceptor compounds of tetrathiafulvalene (TTF) with bisdithiolene metal-complexes*, Phys. Rev. B **14** (1976), 3036.

[JH05] C. Jia and J.H. Han, *Valence-bond-solid order in antiferromagnets with spin-lattice coupling*, preprint, **cond-mat**/0505573, 2005.

[JJGJ87] D.C. Johnston, J.W. Johnson, D.P. Goshorn, and A.J. Jacobsen, *Magnetic susceptibility of (VO)$_2$P$_2$O$_7$: A one-dimensional spin-1/2 Heisenberg antiferromagnet with a ladder spin configuration and a singlet ground state*, Phys. Rev. B **35** (1987), 219.

[Kan59] J. Kanamori, *Superexchange interaction and symmetry properties of electron orbitals*, J. Phys. Chem. Solids **10** (1959), 87.

[Kat62] S. Katsura, *Statistical mechanics of the anisotropic linear Heisenberg model*, Phys. Rev. **127** (1962), 1508.

[KBI93] V.E. Korepin, N.M. Bogoliubov, and A.G. Izergin, *Quantum inverse scattering method and correlation functions*, pp. 63–79,502–516, Cambridge University Press, Cambridge New York Melbourne, 1993, and references therein.

[KBM+03]   V. Kataev, J. Baier, A. Möller, L. Jongen, G. Meyer, and A. Freimuth, *Orbital order in the low-dimensional quantum spin system TiOCl probed by ESR*, Phys. Rev. B **68** (2003), 140405(R).

[KF87]   K. Kuboki and H. Fukuyama, *Spin-Peierls transition with competing interactions*, J. Phys. Soc. Jpn. **56** (1987), 3126.

[KFL+97]   K.M. Kojima, Y. Fudamoto, M. Larkin, G.M. Luke, J. Merrin, B. Nachumi, Y.J. Uemura, N. Motoyama, H. Eisaki, S. Uchida, K. Yamada, Y. Endoh, S. Hosoya, B.J. Sternlieb, and G. Shirane, *Reduction of ordered moment and Néel temperature of quasi-one-dimensional antiferromagnets Sr_2CuO_3 and Ca_2CuO*, Phys. Rev. Lett. **78** (1997), 1787.

[KGM96]   D. Khomskii, W. Geertsma, and M. Mostovoy, *Elementary excitations, exchange interaction and spin-Peierls transition in $CuGeO_3$*, Czech. Journ. of Physics **46** (1996), 3239.

[KH04]   N. Kawashima and K. Harada, *Recent developments of world-line Monte Carlo methods*, J. Phys. Soc. Jpn. **73** (2004), 1379, and references therein.

[KKK99a]   A. Koga, S. Kumada, and N. Kawakami, *Quantum phase transitions in two-dimensional spin systems with ladder, plaquette and mixed-spin structures*, J. Phys. Soc. Jpn. **68** (1999), 2373.

[KKK99b]   A. Koga, S. Kumada, and N. Kawakami, *Two-dimensional quantum spin systems with ladder and plaquette structures*, J. Phys. Soc. Jpn. **68** (1999), 642.

[KL99]   R.W. Kühne and U. Löw, *Thermodynamical properties of a spin-1/2 Heisenberg chain coupled to phonons*, Phys. Rev. B **60** (1999), 12125.

[KL04]   D. Khomskii and U. Löw, *Superstructures at low spin-high spin transitions*, Phys. Rev. B **69** (2004), 184401.

[Klü93]   A. Klümper, *Thermodynamics of the anisotropic spin-1/2 Heisenberg chain and related quantum chains*, Z. Phys. B: Condens. Matter **91** (1993), 507.

[Klü98]   A. Klümper, *The spin-1/2 Heisenberg chain: Thermodynamics, quantum criticality and spin-Peierls exponents*, Eur. Phys. J. B **5** (1998), 677.

[KMST02]   N. Kitanine, J.M. Maillet, N.A. Slavnov, and V. Terras, *Spin-spin correlation functions of the XXZ-1/2 Heisenberg chain in a magnetic field*, Nucl. Phys. B **641** (2002), 487.

[KRS99]   A. Klümper, R. Raupach, and F. Schönfeld, *Finite temperature density-matrix-renormalization-group investigation of the spin-Peierls transition in $CuGeO_3$*, Phys. Rev. B **59** (1999), 3612.

[KSTS04]   G. Kato, M. Shiroishi, M. Takahashi, and K. Sakai, *Third-neighbour and other four-point correlation functions of spin-1/2 XXZ chain*, J. Phys. A **37** (2004), 5097.

[KTP+02]   U. Kuhlmann, C. Thomsen, A.V. Prokofiev, F. Büllesfeld, E. Uhrig, and W. Assmus, *Phonon anomalies in the two phases of the low-dimensional spin compound $(VO)_2P_2O_7$*, Phys. Rev. B **66** (2002), 064420.

[KU00]   C. Knetter and G.S. Uhrig, *Perturbation theory by flow equations: dimerized and frustrated S=1/2 chain*, Eur. Phys. J. B **13** (2000), 209.

[Kühne01]   R.W. Kühne, *Thermodynamics of Heisenberg chains coupled to phonons*, PhD thesis, Universität Dortmund, 2001.

[Lan50]   C. Lanczos, *An iteration method for the solution of the eigenvalue problem of linear differential and integral operators*, J. Res. Natl. Bur. Stand. **45** (1950), 255.

[LCC$^+$04] P. Lemmens, K.Y. Choi, G. Caimi, L. Degiorgi, N.N. Kovaleva, A. Seidel, and F.C. Chou, *Giant phonon softening in the pseudogap phase of the quantum spin system TiOCl*, Phys. Rev. B **70** (2004), 134429.

[LCG$^+$84] R. Laversanne, C. Coulon, B. Gallois, J.P. Pouget, and R. Moret, *Structural and electrical properties of ($TMTTF)_2MF_6$ salts (M=P,As,Sb) – role of the anions*, J. Phys. (France) Lett. **45** (1984), L393.

[LCV$^+$05] P. Lemmens, K.Y. Choi, R. Valenti, T. Saha-Sagupta, E. Abel, Y.S. Lee, and F.C. Chou, *Spin gap formation in the quantum spin systems TiOX, X=Cl and Br*, New J. Phys. **7** (2005), 74.

[LEFK94] U. Löw, V.J. Emery, K. Fabricius, and S.A. Kivelson, *Study of an Ising model with competing long- and short-range interactions*, Phys. Rev. Lett. **72** (1994), 1918.

[LHS$^+$94] J.E. Lorenzo, K. Hirota, G. Shirane, J.M. Tranquada, M. Hase, K. Uchinokura, H. Kojima, I. Tanaka, and Y. Shibuya, *Soft longitudinal modes in spin-singlet $CuGeO_3$*, Phys. Rev. B **50** (1994), 1278.

[LL79] L.D. Landau and E.M. Lifschitz, *Lehrbuch der Theoretischen Physik V – Statistische Physik Teil 1*, pp. 423–490, Akademie Verlag, Berlin, 1979.

[LP75] A. Luther and I. Peschel, *Calculation of critical exponents in two dimensions from quantum field-theory in one dimension*, Phys. Rev. B **12** (1975), 3908.

[LRP$^+$93] Q. Liu, S. Ravy, J.P. Pouget, C. Coulon, and C. Bourbonnais, *Structural fluctuations and spin-Peierls transitions revisited*, Synth. Met. **56** (1993), 1840.

[LSM61] E. Lieb, T. Schultz, and D. Mattis, *Two soluble models of an antiferromagnetic chain*, Ann. Phys. **16** (1961), 407.

[LT03] S. Lukyanov and V. Terras, *Long-distance asymptotics of spin-spin correlation functions for the XXZ spin chain*, Nucl. Phys. B **654** (2003), 323.

[Luk99] S. Lukyanov, *Correlation amplitude for the XXZ spin chain in the disordered regime*, Phys. Rev. B **59** (1999), 11163.

[LZ97] S. Lukyanov and A. Zamolodchikov, *Exact expectation values of local fields in the quantum sine-Gordon model*, Nucl. Phys. B **493** (1997), 571.

[Maz89] S. Mazumdar, *Coment on "Peierls instability in the two-dimensional half-filled Hubbard model"*, Phys. Rev. B **39** (1989), 12324.

[McC68] B.M. McCoy, *Spin correlation functions of the X-Y model*, Phys. Rev. **173** (1968), 531.

[MFFM85] A. Maaroufi, S. Flandrois, G. Fillion, and J.P. Morand, *Magnetic instabilities in TMTTF salts*, Mol. Cryst. Liq. Cryst. **119** (1985), 311.

[MRR$^+$53] N. Metropolis, A.W. Rosenbluth, M.N. Rosenbluth, A.H. Teller, and E. Teller, *Equation of state calculations by fast computing machines*, J. Chem. Phys. **21** (1953), 1087.

[MW66] N.D. Mermin and H. Wagner, *Absence of ferromagnetism or antiferromagnetism in one- or two-dimensional isotropic Heisenberg models*, Phys. Rev. Lett. **17** (1966), 1133.

[OC04] E. Orignac and R. Chitra, *Mean-field theory of the spin-Peierls transition*, Phys. Rev. B **70** (2004), 214436.

[OM00] J. Orenstein and A.J. Mills, *Advances in the physics of high-temperature superconductivity*, Science **288** (2000), 468.

[ON92]   K. Okamoto and T. Nomura, *Fluid-dimer critical point in $S = \frac{1}{2}$ antiferromagnetic Heisenberg chain with next nearest neighbor interactions*, Phys. Lett. A **169** (1992), 433.

[PBA$^+$98] A.V. Prokofiev, F. Büllesfeld, W. Assmus, H. Schwenk, D. Wichert, U. Löw, and B. Lüthi, *Magnetic properties of the low dimensional spin system $(VO)_2P_2O_7$: ESR and susceptibility*, Eur. Phys. J. B **5** (1998), 313.

[Pei55]   R. E. Peierls, *Quantum theory of solids*, pp. 108–112, Oxford University Press, Oxford, 1955.

[PMC$^+$82] J.P. Pouget, R. Moret, R. Comes, K. Bechgaard, J.M. Fabre, and L. Giral, *X-ray diffuse-scattering study of some $(TMTSF)_2X$ and $(TMTTF)_2X$ salts*, Mol. Cryst. Liq. Cryst. **79** (1982), 129.

[PST98a]   N.V. Prokof'ev, B.V. Svistunov, and I.S. Tupitsyn, *Exact, complete, and universal continuous-time worldline Monte Carlo approach to the statistics of discrete quantum systems*, Sov. Phys.-JETP **87** (1998), 310.

[PST98b]   N.V. Prokof'ev, B.V. Svistunov, and I.S. Tupitsyn, *"Worm" algorithm in quantum Monte Carlo simulations*, Phys. Lett. A **238** (1998), 253.

[Pyt74]   E. Pytte, *Peierls instability in Heisenberg chains*, Phys. Rev. B **10** (1974), 4637.

[RBU01]   C. Raas, A. Bühler, and G. S. Uhrig, *Effective spin models for spin-phonon chains by flow equations*, Eur. Phys. J. B **21** (2001), 369.

[RHD83]   M. Roger, J.H. Hetherington, and J.M. Delrieu, *Magnetism in solid ^3He*, Rev. Mod. Phys. **55** (1983), 1.

[RKS00]   R. Raupach, A. Klümper, and F. Schönfeld, *Pressure dependence and non-universal effects of microscopic couplings on the spin-Peierls transition in $CuGeO_3$*, Eur. Phys. J. B **17** (2000), 51.

[RLUK02]   C. Raas, U. Löw, G.S. Uhrig, and R.W. Kühne, *Spin-phonon chains with bond coupling*, Phys. Rev. B **65** (2002), 144438.

[RY88]   J.D. Reger and A.P. Young, *Monte Carlo simulations of the spin-1/2 Heisenberg antiferromagnet on a square lattice*, Phys. Rev. B **37** (1988), 5978.

[Sac00]   S. Sachdev, *Quantum criticality: Competing ground states in low dimensions*, Science **288** (2000), 475.

[Sac03]   S. Sachdev, *Order and quantum phase transitions in the cuprate superconductors*, Rev. Mod. Phys. **75** (2003), 913.

[San97]   A.W. Sandvik, *Finite-size scaling of the ground-state parameters of the two-dimensional Heisenberg model*, Phys. Rev. B **56** (1997), 11678.

[San98a]   A.W. Sandvik, *Critical temperature and the transition from quantum to classical order parameter fluctuations in the three-dimensional Heisenberg antiferromagnet*, Phys. Rev. Lett. **80** (1998), 5196.

[San98b]   A.W. Sandvik, *Stochastic series expansion method with operator-loop update*, Phys. Rev. B **59** (1998), R14157.

[SC99]   A.W. Sandvik and D.K. Campbell, *Spin-Peierls transition in the Heisenberg chain with finite-frequency phonons*, Phys. Rev. Lett. **83** (1999), 195.

[SDVRG04]   T. Saha-Dasgupta, R. Valenti, H. Rosner, and C. Gros, *TiOCl, an orbital-ordered system?*, Europhys. Lett. **67** (2004), 63.

[Sen03]   P. Sengupta, *Néel to spin-Peierls transition in the ground state of quasi-1D Heisenberg model coupled to bond phonons*, preprint, **cond-mat**/0307746, 2003.

[SFS89]   R.R. Singh, M.E. Fisher, and R. Shankar, *Spin-1/2 antiferromagnetic XXZ chain: New results and insights*, Phys. Rev. B **39** (1989), 2562.

[SK91]   A.W. Sandvik and J. Kurkijärvi, *Quantum Monte Carlo simulation method for spin systems*, Phys. Rev. B **43** (1991), 5950.

[SKH02]   J. Sirker, A. Klümper, and K. Hamacher, *Ground-state properties of two-dimensional dimerized Heisenberg models*, Phys. Rev. B **65** (2002), 134409.

[SKU04]   K.P. Schmidt, C. Knetter, and G.S. Uhrig, *Spectral properties of the dimerized and frustrated $S = 1/2$ chain*, Phys. Rev. B **69** (2004), 104417.

[SMC$^+$03] A. Seidel, C.A. Marianetti, F.C. Chou, G. Ceder, and P.A. Lee, *S=1/2 chains and spin-Peierls transition in TiOCl*, Phys. Rev. B **67** (2003), 020405(R).

[SMK77]   M. Suzuki, S. Miyashita, and A. Kuroda, *Monte Carlo simulation of quantum spin systems I*, Prog. Theor. Phys. **58** (1977), 1377.

[SS02]   O.F. Syljuåsen and A.W. Sandvik, *Quantum Monte Carlo with directed loops*, Phys. Rev. E **66** (2002), 046701, and references therein.

[SSB00]   P. Sun, D. Schmeltzer, and A.R. Bishop, *Analytic approach to the one-dimensional spin-Peierls system in the entire frequency range*, Phys. Rev. B **62** (2000), 11308.

[SSC97]   A.W. Sandvik, R.R.P. Singh, and D.K. Campbell, *Quantum Monte Carlo in the interaction representation: Application to a spin-Peierls model*, Phys. Rev. B **56** (1997), 14510.

[SSC03]   P. Sengupta, A.W. Sandvik, and D.K. Campbell, *Peierls transition in the presence of finite-frequency phonons in the one-dimensional extended Peierls-Hubbard model at half-filling*, Phys. Rev. B **67** (2003), 245103.

[SST05]   J. Sato, M. Shiroishi, and M. Takahashi, *Correlation functions of the spin-1/2 anti-ferromagnetic Heisenberg chain: exact calculation via the generating function*, preprint, **hep-th**/0507290, 2005.

[Suz76]   M. Suzuki, *Relationship between d-dimensional quantal spin systems and (d+1)-dimensional Ising systems*, Prog. Theor. Phys. **56** (1976), 1454.

[Suz85]   M. Suzuki, *General correction theorems on decomposition formulas of exponential operators and extrapolation methods for quantum Monte-Carlo simulations*, Phys. Lett. A **113** (1985), 299.

[Tak99]   M. Takahashi, *Thermodynamics of one-dimensional solvable models*, pp. 34–66,117–144,152–157, Cambridge University Press, Cambridge New York Melbourne, 1999, and references therein.

[TEM01]   S. Trebst, N. Elstner, and H. Monien, *Renormalization of the spin-Peierls transition due to phonon dynamics*, Europhys. Lett. **56** (2001), 268.

[TH88]   S. Tang and J.E. Hirsch, *Peierls instability in the two-dimensional half-filled Hubbard model*, Phys. Rev. B **37** (1988), 9546.

[TH89]   S. Tang and J.E. Hirsch, *Reply to "Comment on 'Peierls instability in the two-dimensional half-filled Hubbard model'"*, Phys. Rev. B **39** (1989), 12327.

[Thi58]   W. Thirring, *A soluble relativistic field theory*, Ann. Phys. **3** (1958), 91.

[TN00]   Y. Tokura and N. Nagaosa, *Orbital physics in transition-metal oxides*, Science **288** (2000), 462.

[Tro59]   H.F. Trotter, *On the product of semi-groups of operators*, Proc. Am. Math. Soc. **10** (1959), 545.

[TW04]   M. Troyer and U.-J. Wiese, *Computational complexity and fundamental limitations to fermionic quantum Monte Carlo simulations*, preprint,**cond-mat**/0408370, 2004.

[Uhr98]   G.S. Uhrig, *Nonadiabatic approach to spin-Peierls transitions via flow equations*, Phys. Rev. B **57** (1998), R14004.

[UN98]   G.S. Uhrig and B. Normand, *Magnetic properties of $(VO)_2P_2O_7$ from frustrated interchain coupling*, Phys. Rev. B **58** (1998), R14705.

[Voj03]   M. Vojta, *Quantum phase transitions*, Rep. Prog. Phys. **66** (2003), 2069.

[Web]   W. Weber, private communication.

[Weg94]   F.J. Wegner, *Flow equations for Hamiltonians*, Ann. Phys. (Leipzig) **3** (1994), 77.

[Wei95]   S. Weinberg, *The quantum theory of fields I*, pp. 306–314, Cambridge University Press, Cambridge New York Melbourne, 1995.

[WFK98]   G. Wellein, H. Fehske, and A. P. Kampf, *Peierls dimerization with non-adiabatic spin-phonon coupling*, Phys. Rev. Lett. **81** (1998), 3956.

[WGB99]   R. Werner, C. Gros, and M. Braden, *Microscopic spin-phonon coupling constants in $CuGeO_3$*, Phys. Rev. B **59** (1999), 14356.

[Whi92]   S.R. White, *Density matrix formulation for quantum renormalization groups*, Phys. Rev. Lett. **69** (1992), 2863.

[Whi93]   S.R. White, *Density-matrix algorithms for quantum renormalization groups*, Phys. Rev. B **48** (1993), 10345.

[WWF99]   A. Weiße, G. Wellein, and H. Fehske, *Quantum lattice fluctuations in a frustrated Heisenberg spin-Peierls chain*, Phys. Rev. B **60** (1999), 6566.

[YK02]   Q.S. Yuan and T. Kopp, *Coexistence of bond-order wave and antiferromagnetism in a two-dimensional half-filled Peierls-Hubbard model*, Phys. Rev. B **65** (2002), 085102.

[YKE$^+$89] K. Yamada, K. Kakurai, Y. Endoh, T.R. Thurston, M.A. Kastner, R.J. Birgeneau, G. Shirane, Y. Hidaka, and T. Murakami, *Spin dynamics in the two-dimensional quantum antiferromagnet La_2CuO_4*, Phys. Rev. B **40** (1989), 4557.

[YNK$^+$99] T. Yamauchi, Y. Narumi, J. Kikuchi, Y. Ueda, K. Tatani, T.C. Kobayashi, K. Kindo, and K. Motoya, *Two gaps in $(VO)_2P_2O_7$: Observation using high-field magnetization and NMR*, Phys. Rev. Lett. **83** (1999), 3729.

[YNK01]   Q.S. Yuan, T. Nunner, and T. Kopp, *Imperfect nesting and Peierls instability for a two-dimensional tight-binding model*, Eur. Phys. J. B **22** (2001), 37.

[YSSH83]   H. Yoshizawa, G. Shirane, H. Shiba, and K. Hirakawa, *Neutron scattering study of a one-dimensional XY antiferromagnet Cs_2CoCl_4*, Phys. Rev. B **28** (1983), 3904.

[YY66a]   C.N. Yang and C.P. Yang, *Ground-state energy of a Heisenberg-Ising lattice*, Phys. Rev. **147** (1966), 303.

[YY66b]   C.N. Yang and C.P. Yang, *One-dimensional chain of anisotropic spin-spin interactions. I. Proof of Bethe's hypothesis for ground state in a finite system*, Phys. Rev. **150** (1966), 321.

[YY66c]   C.N. Yang and C.P. Yang, *One-dimensional chain of anisotropic spin-spin interactions. II. Properties of the ground-state energy per lattice site for an infinite system*, Phys. Rev. **150** (1966), 327.

[ZP88]   F.C. Zhang and P. Prelovsek, *Dimerization in the two-dimensional Hubbard model*, Phys. Rev. B **37** (1988), 1569.

Abstract

In this thesis the quantum Monte Carlo loop algorithm is applied to study the properties of correlation functions in low-dimensional quantum antiferromagnets. Two different types of lattice models are investigated. The first system is the quantum critical XXZ chain. The second class of models emerges when coupling the square lattice Heisenberg model to phonons.

The quantum Monte Carlo method provides direct access to the finite-temperature properties of these non-frustrated quantum spin systems. The numerical estimates for thermal expectation values are exact up to a statistical error which reflects the limited amount of CPU time in a computer simulation. The loop algorithm in particular is based on global loop updates for the spin degrees of freedom, substantially reducing autocorrelation effects. In the case of pure spin models, the algorithm can be directly formulated in the limit of continuous Trotter time. The expectation values of both diagonal and off-diagonal operators are computed efficiently within the framework of improved estimators.

The method is first used to study the two-point spin and dimer correlation functions of the quantum critical XXZ chain at low temperatures. Here a comprehensive survey is given of the long distance properties of the correlations, which are obtained by a combination of conformal field theory and the Bethe ansatz. Starting from these asymptotic expressions, the crossover from the finite-temperature to the ground state behavior is investigated. The Monte Carlo data are used to extract numerical estimates for the correlation amplitudes, which are compared to previous analytical or numerical results. The deviations from asymptotic scaling at low finite temperatures and intermediate distances are examined. The results are also used to study the algebraic and logarithmic corrections in the ground state.

The loop algorithm is further applied to compute the spin correlations of the square lattice Heisenberg model coupled to dispersionless Einstein phonons. The low temperature data allow to examine the magnetic order in the ground state. Further insight into the influence of the spin-phonon coupling is gained by studying statically dimerized Heisenberg models in two dimensions, which are viewed as the effective models to describe the magnetism of layered spin-phonon systems in the adiabatic limit. Here the quantum Monte Carlo technique is used to determine the specific pattern of dimerized bonds which has the largest gain in the magnetic energy. A direct comparison of ground state energies is only possible for a small number of dimerized systems. For this reason an alternative approach is developed, which allows to study a significantly larger class of models. Starting from a Landau expansion of the free energy, this amounts to a computation of specific structure factors of the dimer correlations of the uniform Heisenberg model. As a consequence, a Landau theory for the two-dimensional counterpart of the spin-Peierls transition is established. The adiabatic approach also applies to the Heisenberg model coupled to dispersive phonons. In this case the data for the dimer correlations are used to study the impact of the spin-phonon coupling on the phonon dispersion relations. In particular, the softening of phonon modes is investigated, which is relevant for experimental studies on substances with a quasi two-dimensional magnetic structure.

Deutsche Zusammenfassung

In der vorliegenden Arbeit werden die Eigenschaften von Korrelationsfunktionen in niedrigdimensionalen Quanten-Antiferromagneten mit Hilfe des Quanten-Monte-Carlo-Loop-Algorithmus untersucht. Dabei werden zwei unterschiedliche Typen von Gittermodellen behandelt. Das erste System ist das quantenkritische eindimensionale XXZ-Modell. Die zweite Klasse von Modellen entsteht durch Kopplung des Heisenberg-Modells auf dem Quadratgitter an phononische Freiheitsgrade.

Die thermodynamischen Eigenschaften dieser nichtfrustrierten Quantenspinsysteme sind im Rahmen der Quanten-Monte-Carlo-Methode direkt zugänglich. Die Methode liefert numerisch exakte Daten für thermische Erwartungswerte, die mit einem statistischen Fehler behaftet sind, der die Beschränkungen in der Laufzeit von Computersimulationen widerspiegelt. Der Loop-Algorithmus im Speziellen zeichnet sich durch ein globales Update-Schema der Spinfreiheitsgrade aus, was zu einer substantiellen Reduktion von Autokorrelationseffekten führt. Bei der Anwendung auf reine Spinmodelle ist eine direkte Formulierung im Limes kontinuierlicher Trotterzeit möglich. Erwartungswerte sowohl diagonaler als auch nicht-diagonaler Operatoren lassen sich effizient im Rahmen sog. Improved Estimators berechnen.

Die Methode wird zunächst auf die quantenkritische XXZ-Kette angewandt, deren Spin- und Dimerkorrelationsfunktionen bei tiefen Temperaturen untersucht werden. Dieser Teil beinhaltet eine ausführliche Übersicht über die Eigenschaften der Korrelationen bei großen Abständen, die sich aus einer Kombination von konformer Feldtheorie und Bethe-Ansatz-Ergebnissen ergeben. Angewandt auf die Monte-Carlo-Daten, ermöglichen die asymptotischen Ausdrücke eine Analyse des Übergangs vom Regime tiefer Temperaturen in den Grundzustand. Zudem werden unabhängige Zahlenwerte für die Korrelationsamplituden bestimmt und mit älteren numerischen oder analytischen Ergebnissen verglichen. Abweichungen vom asymptotischen Verhalten bei tiefen Temperaturen und mittleren Abständen werden diskutiert. Diese Ergebnisse ermöglichen auch eine Untersuchung algebraischer und logarithmischer Korrekturen im Grundzustand.

Der Loop-Algorithmus dient weiterhin zur Berechnung der Spin-Korrelationen des Heisenberg-Modells auf dem Quadratgitter mit Kopplung an dispersionslose Einstein-Phononen. Die Tieftemperaturdaten erlauben insbesondere eine Analyse der magnetischen Ordnung im Grundzustand. Der Einfluss der Spin-Phonon-Kopplung wird zudem im Rahmen statisch dimerisierter Heisenberg-Modelle untersucht. Diese Systeme dienen als effektive magnetische Modelle zur Beschreibung geschichteter Spin-Phonon-Systeme im adiabatischen Limes. Die Quanten-Monte-Carlo-Methode ermöglicht die Bestimmung derjenigen Anordnung dimerisierter Kopplungen, die zur größten Absenkung der magnetischen Energie führt. Ein direkter Vergleich von Grundzustandsenergien ist dabei nur für eine kleine Anzahl verschiedener Dimerisierungsmuster möglich. Aus diesem Grunde wird ein alternativer Zugang entwickelt, der den Vergleich einer großen Klasse von dimerisierten Modellen zulässt. Ausgehend von einer Landau-Entwicklung der freien Energie, erfordert dieser Ansatz die Berechnung bestimmter Strukturfaktoren der Dimerkorrelationen des nicht-dimerisierten Heisenberg-Modells. Die im Folgenden aufgestellte Landau-Theorie für das zweidimensionale Analogon des Spin-Peierls-Übergangs basiert auf denselben Daten. Das zweidimensionale Heisenberg-Modell mit Kopplung an dispersive Phononen wird ebenfalls im Rahmen der adiabatischen Näherung untersucht. Hier ermöglichen die numerischen Daten für die Dimer-Korrelationen eine Analyse

des Einflusses der Spin-Phonon-Kopplung auf die Phononen-Dispersionsrelationen. Dabei wird insbesondere das sog. Softening bestimmter Schwingungsmoden untersucht, was von besonderer Relevanz für Experimente an Materialien mit einer quasi-zweidimensionalen magnetischen Struktur ist.

Danksagung

Zunächst möchte ich mich bei Frau Priv. Doz. Dr. Ute Löw für die Vergabe und Betreuung dieser Arbeit bedanken. Ohne unsere intensiven Diskussionen wäre diese Dissertation wohl nicht zu Stande gekommen. Zudem bin ich durch ihre Unnachgiebigkeit, vermeintlich sichere Ergebnisse lieber einmal mehr zu überprüfen, vor so manchem Fehler bewahrt worden.

Ein weiteres Dankeschön geht an Prof. E. Müller-Hartmann, der meine Arbeit in den vergangenen Jahren kritisch begleitet hat. Vor allem seine zahlreichen Diskussionsbeiträge während der Mitarbeiterseminare haben wesentliche Impulse zu dieser Dissertation gegeben.

Des Weiteren danke ich Prof. A. Klümper, der zahlreiche grundlegende Ideen zum Kapitel über Spinsysteme mit Spin-Phonon-Kopplung beigetragen hat. Auch bei Prof. W. Weber möchte ich mich für wesentliche Anregungen zu diesem Teil bedanken. Beiden gilt insbesondere mein Dank für die fruchtbare Zusammenarbeit an unserem gemeinsamen Paper.

Prof. H. G. Evertz danke ich für anregende Diskussionen über Monte-Carlo-Verfahren und besonders über den Loop-Algorithmus.

Bedanken möchte ich mich auch bei Prof. M. Braden für die Begutachtung dieser Arbeit, sowie bei Prof. H. Tjeng für die Übernahme des Prüfungsvorsitzes.

Weiterer Dank gebührt Robert Schmitz und Prof. E. Müller-Hartmann für das aufmerksame Korrekturlesen dieser Arbeit. Meiner Patentante Gillian Schreiber sowie ihrem Ehemann Jochen danke ich für die detaillierte Durchsicht der Dissertation in sprachlicher Hinsicht.

Ein großes Dankeschön geht an Carsten Raas, der mir mit zahlreichen Tipps insbesondere bei Computerproblemen geholfen hat. Ihm sowie Robert Schmitz, Thomas Koethe, Sebastian Kirschner, Michal Karski, und Philip Greulich danke ich auch für die angenehme und produktive Arbeitsatmosphäre in Zimmer 104 mit wechselnder Belegung. Das sehr gute kollegiale Verhältnis auch zu Kai Schmidt, Alexander Reischl, Sebastien Dusuel und Alexander Bühler führte zu zahlreichen privaten Kontakten, die ich sehr schätze. Moralische Unterstützung innerhalb des Instituts wurde mir ebenfalls durch meine alten Freunde Erik Dahlmann und Jan Müller zuteil.

Die kontinuierliche Unterstützung meiner Eltern nicht nur bei der Entstehung dieser Arbeit, sondern schon während des gesamten Physikstudiums, ist überhaupt nicht wegzudenken. Über euer Interesse an meiner Arbeit, aber auch eure tatkräftige Hilfe in allen Lebenslagen freue ich mich sehr.

Das letzte Jahr, insbesondere die Phase des Aufschreibens, wäre mir ohne Jessica wohl nicht so leicht gefallen. Ich bin überglücklich, dass ich Dich gefunden habe.

Gewidmet ist diese Arbeit meinem lieben Patenonkel Hinrich Stapelfeld, der im Januar dieses Jahres leider plötzlich verstorben ist. Ich weiß, dass er sich sehr über die Fertigstellung meiner Doktorarbeit gefreut hätte.

Erklärung

Ich versichere, dass ich die von mir vorgelegte Dissertation selbständig angefertigt, die benutzten Quellen und Hilfsmittel vollständig angegeben und die Stellen der Arbeit – einschließlich Tabellen, Karten, und Abbildungen –, die anderen Werken im Wortlaut oder dem Sinn nach entnommen sind, in jedem Einzelfall als Entlehnung kenntlich gemacht habe; dass diese Dissertation noch keiner anderen Fakultät oder Universität zur Prüfung vorgelegen hat; dass sie – abgesehen von unten angegebenen Teilpublikationen – noch nicht veröffentlicht worden ist sowie, dass ich eine solche Veröffentlichung vor Abschluss des Promotionsverfahrens nicht vornehmen werde. Die Bestimmungen dieser Promotionsordnung sind mir bekannt. Die von mir vorgelegte Dissertation ist von Frau Privat-Dozent Dr. Ute Löw betreut worden.

Köln, den 19. Dezember 2005

Teilpublikationen

- C .H. Aits und U. Löw, *Thermodynamic properties of the two-dimensional S=1/2 Heisenberg antiferromagnet coupled to bond phonons*, Phys. Rev. B **68** (2003), 184416.

Lebenslauf

Persönliche Daten:

Name	Carsten Hinrich Aits
Geburtstag	07.10.1976
Geburtsort	Wermelskirchen
Familienstand	ledig
Staatsangehörigkeit	deutsch
Anschrift	Fuchsstr. 20, 50823 Köln

Schulbildung:

1982	Grundschule Am Steinberg Remscheid
1982-1986	Katholische Grundschule Am Stadion Remscheid-Lennep
1986-1995	Städtisches Röntgen-Gymnasium Remscheid-Lennep
1995	Abschluss: Allgemeine Hochschulreife

Wehrdienst:

Juli 1995 - Sept. 1995	Grundausbildung beim Luftwaffenausbildungsregiment in Roth
Okt. 1995 - Juni 1996	Fernmeldesektor 114 in Much/Köln

Studium:

WS 1996/1997	Immatrikulation an der Universität zu Köln, Studiengang: Physik, Diplom
Juli 1998	Vordiplom Physik
WS 1998/1999 - SS 1999	Auslandsstudium an der Universiteit Utrecht, Niederlande
Juli 2001	Beginn der Diplomarbeit bei Priv.-Doz. Ute Löw am Institut für Theoretische Physik, Universität zu Köln
Sept. 2002	Abschluss: Diplom Physik
seit Sept. 2002	Promotion in theoretischer Physik bei Priv.-Doz. Ute Löw

Arbeitsverhältnisse:

Okt. 1999 - Feb. 2001	Studentische Hilfskraft am Mathematischen Institut, Universität zu Köln
Apr. 2001 - Aug. 2002	Studentische Hilfskraft am Institut für Theoretische Physik, Universität zu Köln
seit Sept. 2002	Wissenschaftlicher Mitarbeiter am Institut für Theoretische Physik, Universität zu Köln